AN EXPERIMENTAL INVESTIGATION OF LAMINAR AND TURBULENT MIXING OF COMPRESSIBLE JETS AT LOW REYNOLDS NUMBERS

A THESIS

Presented to

The Faculty of the Division of Graduate

Studies and Research

By

Dale Edward Jensen

In Partial Fulfillment

of the Requirements for the Degree

Doctor of Philosophy in the School of Mechanical Engineering

Georgia Institute of Technology

February, 1974

AN EXPERIMENTAL INVESTIGATION OF LAMINAR AND TURBULENT MIXING OF COMPRESSIBLE JETS AT LOW REYNOLDS NUMBERS

Approved:

Stephen L. Dickerson, Chairman

Prateen V. Desai

Carl V. Justus

Date approved by Chairman: 1/18/79

ACKNOWLEDGMENTS

I wish to extend my appreciation to the faculty and staff of the School of Mechanical Engineering whose assistance was invaluable throughout the course of this investigation.

I am especially grateful to my advisor, Dr. Stephen L. Dickerson, who first conceived of this research topic and whose patience and encouragement made the completion of this research possible. I wish to thank Dr. Prateen V. Desai and Dr. Carl G. Justus for their suggestions and guidance. A special note of thanks goes to Dr. Walter O. Carlson, Dr. Howard M. McMahon and Dr. Gene T. Colwell for their assistance as members of the thesis committee.

I am indebted to Daniel C. Anderson, a fellow student and co-designer of the experimental apparatus, and to John W. Davis and Joseph G. Doyal for their aid in construction and assembly of the equipment.

I wish to thank my wife, Mary, who typed the first draft and proof read this thesis. Her patience and support made this effort possible.

TABLE OF CONTENTS

Page

ACKNOWLEDGMENTS ii

LIST OF TABLES vi

LIST OF ILLUSTRATIONS x

SUMMARY xv

NOMENCLATURE xvii

Chapter

I. INTRODUCTION 1

Motivation for this Research
Objectives for this Research
Thesis Organization
Literature Review
Plane Jet
Jet Interaction
Jet Impingement upon a Receiver

II. EQUIPMENT AND INSTRUMENTATION 113

Experimental Model
Vacuum Pump
Support Equipment
Instrumentation

III. PROCEDURE 134

Preliminary Considerations
Calibration of the Anemometer and
Associated Instrumentation
Experimental Procedure

IV. FREE JET EXPERIMENTS 144

Experimental Data
Free Jet Structure
Comparison of Experimental Data to Previous Studies
Free Jet Data Correlations

Chapter Page

V. JET INTERACTION EXPERIMENTS 207

Experimental Data
Jet Deflection Angle
Control Port Flow Rate
Estimation of the Supply Nozzle Mass Flow Rate

VI. JET RECEIVER IMPINGEMENT EXPERIMENTS. 226

Experimental Data
Computation of the Open Load Flow Rate
Computation of the Blocked Load Pressure
Experimental Results

VII. CONCLUSIONS AND SUGGESTIONS FOR FURTHER RESEARCH. . . . 245

Conclusion
Suggestions for Further Research

Appendix

A. ANEMOMETER CALIBRATION. 252

B. CALCULATION OF STEADY STATE AND FLUCTUATING COMPONENTS OF VELOCITY. 259

Calculation of Steady State Velocity
Uncertainty in Steady State Velocity Measurements
Calculation of the Fluctuating Component of Velocity
Uncertainty in Fluctuating Component of Velocity Measurements

C. FREE JET DATA 269

Flow Conditions
Free Jet Velocity Data
Free Jet Static Pressure Measurements
Free Jet Velocity Vector Measurements

D. JET INTERACTION DATA. 302

Flow Conditions
Jet Deflection Data
Deflected Jet Static Pressure Measurements
Deflected Jet Velocity Vector Measurements

Appendix Page

E. JET RECEIVER IMPINGEMENT DATA 320

Flow Conditions
Receiver Interaction Data

F. DERIVATION OF FREE JET MOMENTUM AND MASS FLOW INTEGRALS. 334

Momentum Integral
Mass Flow Integral

G. ESTIMATION OF THE SUPPLY NOZZLE MASS FLOW RATE. 343

Momentum Integral
Mass Flow Integral
Calculation of Nozzle Flow Rate

H. SAMPLE CALCULATIONS 350

Calculation of Free Jet Parameters
Calculation of Jet Deflection Angle
Calculation of Power Nozzle Mass Flow Rate
Calculation of Open Load Flow Rate and Blocked Load Pressure Recovery

I. COMPUTER PROGRAM FOR JET PARAMETERS 360

LITERATURE CITED 375

VITA 377

LIST OF TABLES

Table		Page
1.	Comparison of Measured and Computed Maximum Pressure and Flow Recoveries	109
2.	Tabulation of Jet Width Parameters for Example 1.	195
3.	Tabulation of Jet Width Parameters for Example 2.	200
4.	Tabulation of Error Between Measured Values of Centerline Velocity and Data Correlation Predictions.	204
5.	Comparison of Measured and Computed Power Nozzle Mass Flow Rates	223
6.	Uncertainty in Steady State Velocity Measurements	262
7.	Percentage Uncertainty in Root Mean Square Velocity Measurements.	267
8.	Experimental Free Jet Conditions.	273
9.	Free Jet Velocity Measurements; R_e = 47.7, M = 0.591, $\bar{u}_0$ = 645 ft./sec..	274
10.	Free Jet Velocity Measurements; R_e = 64.2, M = 0.416, $\bar{u}_0$ = 463 ft./sec..	275
11.	Free Jet Velocity Measurements; R_e = 109, M = 0.67, $\bar{u}_0$ = 725 ft./sec.	277
12.	Free Jet Velocity Measurements; R_e = 152, M = 0.885, $\bar{u}_0$ = 930 ft./sec..	279
13.	Free Jet Velocity Measurements; R_e = 142, M = 0.457, $\bar{u}_0$ = 507 ft./sec..	279
14.	Free Jet Velocity Measurements; R_e = 255, M = 0.761, $\bar{u}_0$ = 811 ft./sec..	280
15.	Free Jet Velocity Measurements; R_e = 336, M = 0.956, $\bar{u}_0$ = 985 ft./sec..	282
16.	Free Jet Velocity Measurements; R_e = 262, M = 0.347, $\bar{u}_0$ = 389 ft./sec..	284

Table — Page

17. Free Jet Velocity Measurements; R_e = 325, M = 0.426, $\bar{u}_0$ = 468 ft./sec.. 285

18. Free Jet Velocity Measurements; R_e = 515, M = 0.646, $\bar{u}_0$ = 701 ft./sec.. 287

19. Free Jet Velocity Measurements; R_e = 359, M = 0.24, $\bar{u}_0$ = 270 ft./sec. 289

20. Free Jet Velocity Measurements; R_e = 558, M = 0.368, $\bar{u}_0$ = 410 ft./sec.. 289

21. Free Jet Velocity Measurements; R_e = 705, M = 0.458, $\bar{u}_0$ = 507 ft./sec.. 290

22. Free Jet Velocity Measurements; R_e = 546, M = 0.183, $\bar{u}_0$ = 206 ft./sec.. 291

23. Free Jet Velocity Measurements; R_e = 645, M = 0.216, $\bar{u}_0$ = 244 ft./sec.. 293

24. Free Jet Static Pressure Measurements; R_e = 336, M = 0.956, $\bar{u}_0$ = 985 ft./sec.. 295

25. Free Jet Static Pressure Measurements; R_e = 325, M = 0.426, $\bar{u}_0$ = 468 ft./sec.. 296

26. Free Jet Static Pressure Measurements; R_e = 705, M = 0.458, $\bar{u}_0$ = 507 ft./sec.. 297

27. Free Jet Velocity Vector Measurements; R_e = 336, M = 0.956, $\bar{u}_0$ = 985 ft./sec.. 298

28. Free Jet Velocity Vector Measurements; R_e = 325, M = 0.426, $\bar{u}_0$ = 468 ft./sec.. 300

29. Free Jet Velocity Vector Measurements; R_e = 705, M = 0.458, $\bar{u}_0$ = 507 ft./sec.. 301

30. Experimental Jet Interaction Conditions 305

31. Deflected Jet Velocity Measurements; R_e = 114, M = 0.691, $\mathring{m}_i$ = 0.00544 lbm./min. 306

32. Deflected Jet Velocity Measurements; R_e = 155, M = 0.892, $\mathring{m}_i$ = 0.00796 lbm./min. 308

Table — Page

33. Deflected Jet Velocity Measurements; R_e = 252, M = 0.763, $\dot{m}_i$ = 0.0120 lbm./min.. 308

34. Deflected Jet Velocity Measurements; R_e = 341, M = 0.970, $\dot{m}_i$ = 0.01586 lbm./min. 309

35. Deflected Jet Velocity Measurements; R_e = 326, M = 0.434, $\dot{m}_i$ = 0.01640 lbm./min. 310

36. Deflected Jet Velocity Measurements; R_e = 534, M = 0.662, $\dot{m}_i$ = 0.02796 lbm./min. 312

37. Deflected Jet Velocity Measurements; R_e = 546, M = 0.183, $\dot{m}_i$ = 0.0292 lbm./min.. 313

38. Deflected Jet Velocity Measurements; R_e = 700, M = 0.222, $\dot{m}_i$ = 0.0388 lbm./min.. 314

39. Deflected Jet Static Pressure Measurements; R_e = 341, M = 0.97, $\dot{m}_i$ = 0.01440 lbm./min.. 316

40. Deflected Jet Static Pressure Measurements; R_e = 326, M = 0.434, $\dot{m}_i$ = 0.01574 lbm./min. 317

41. Deflected Jet Velocity Vector Measurements; R_e = 341, M = 0.97, $\dot{m}_i$ = 0.01440 lbm./min.. 318

42. Deflected Jet Velocity Vector Measurements; R_e = 326, M = 0.434, $\dot{m}_i$ = 0.01574 lbm./min. 319

43. Experimental Jet Receiver Impingement Conditions. 322

44. Receiver Interaction Measurements; R_e = 107, M = 0.653, $\dot{m}_i$ = 0.00532 lbm./min. 323

45. Receiver Interaction Measurements; R_e = 252, M = 0.763, $\dot{m}_i$ = 0.0120 lbm./min.. 325

46. Receiver Interaction Measurements; R_e = 530, M = 0.657, $\dot{m}_i$ = 0.0276 lbm./min.. 328

47. Receiver Interaction Measurements; R_e = 566, M = 0.368, $\dot{m}_i$ = 0.03045 lbm./min. 330

48. Receiver Interaction Measurements; R_e = 549, M = 0.184, $\dot{m}_i$ = 0.0293 lbm./min.. 332

Table

Page

49. Computer Program Input Variables. 363

50. Computer Program Output Variables 364

LIST OF ILLUSTRATIONS

Figure		Page
1.	Description of the Prandtl Mixing Length Concept.	12
2.	Free Jet Boundary Flow.	17
3.	Fully Developed Free Jet Flow	17
4.	Representation of a Plane Turbulent Jet	25
5.	Mean Velocity Distribution in a Half Jet (σ = 12.0) from Reference [7]	28
6.	Lateral Distribution of Mean and Fluctuating Velocities in a Half Jet (x = 54.3 centimeters) from Reference [7] . .	29
7.	Jet Width for a Turbulent Incompressible Jet from Reference [8]	31
8.	Centerline Velocity Decay for a Turbulent Incompressible Jet from Reference [8].	31
9.	Turbulent X-Stress and Static Pressure Profiles for the Transition Region from Reference [8].	33
10.	Mean Velocity Profiles for the Fully Turbulent Region from Reference [8].	35
11.	Turbulent X-Stress Profiles for the Fully Turbulent Region from Reference [8]	36
12.	Static Pressure Profiles for the Fully Turbulent Region from Reference [8]	37
13.	Sketch of Differential Control Volume for Free Jet Model of Olson and Miller [13].	45
14.	Comparison of Centerline Velocity Decay for a Compressible and Incompressible Turbulent Jet	51
15.	Comparison of Jet Spread Rate for a Compressible and Incompressible Turbulent Jet.	51
16.	Mean Velocity Profiles for the Compressible Turbulent Flow of a Plane Jet from Reference [13]	53

Figure		Page
17.	Velocity Profiles for a Laminar Incompressible Jet from Reference [18]	60
18.	Centerline Velocity Decay for a Laminar Incompressible Jet from Reference [18]	60
19.	Velocity Distributions for the Mixing of a Uniform Stream of Compressible Fluid with Surrounding Fluid from Reference [19]	64
20.	Centerline Velocity Decay for Low Reynolds Number Compressible Jets from Reference [21]	67
21.	Jet Spread Rate for Low Reynolds Number Compressible Jets from Reference [21]	67
22.	Centerline Velocity Decay for Low Reynolds Number Compressible Jets from Reference [21]	68
23.	Jet Spread Rate for Low Reynolds Number Compressible Jets from Reference [21]	68
24.	Neutral Stability for the "Pseudolaminar Jet" from Reference [23]	80
25.	Neutral Stability Contours for the Incompressible Flow of a Laminar Jet from Reference [18]	80
26.	Sketch of a Proportional Fluid Amplifier	83
27.	Sketch of Control Port Geometry	87
28.	Schematic Representation of Control Flow Components	91
29.	Nonlinear Jet Receiver Interaction Geometry	100
30.	Linearized Jet Receiver Interaction Geometry	104
31.	Pressure-Flow Characteristics for a Circular Jet Impinging on a Receiver from Reference [29]	107
32.	Physical Model for the "Cowl" Streamline Concept	111
33.	Experimental Model Sketch	114
34.	Nozzle Block Sketch	116
35.	Receiver-Diffuser Sketch	118

Figure Page

36. Photograph of Experimental Model. 120

37. Experimental Apparatus Diagram. 122

38. Sketch of Static Pressure Probe 124

39. Velocity Direction Sensor 126

40. Velocity Sensors. 127

41. Thermocouple Probe. 129

42. Instrumentation Photographs 132

43. Comparison of Present Flow Regime to Previous Investigations. 145

44. Centerline Velocity Decay Rate Data 147

45. Time-Average and Fluctuating Velocity Data for R_e = 546, M = 0.183 148

46. Time-Average and Fluctuating Velocity Data for R_e = 325, M = 0.426 149

47. Time-Average and Fluctuating Velocity Data for R_e = 255, M = 0.761 150

48. Time-Average Velocity Data for R_e = 64.2, M = 0.416 151

49. Comparison of Centerline Velocity Decay Data from the Present Investigation to Data from other Flow Regimes 155

50. Comparison of Time-Average Characteristics from the Present Research to Data from Reference [21]. 158

51. Comparison of Jet Width Data from the Present Research to Data from other Flow Regimes 160

52. Comparison of Gaussian Distribution to Time-Average Velocity Profiles for R_e = 109, M = 0.67. 163

53. Comparison of Core Region Fluctuating Velocity Profiles from the Present Research to Data of Reference [8]. 165

54. Comparison of Developed Region Fluctuating Velocity Profiles from the Present Research to Data of Reference [8] 166

Figure		Page
55.	Transition Conditions from Laminar to Turbulent Flow. . . .	168
56.	Comparison of Free Jet Static Pressure Distributions from the Present Research to Data from Reference [8]. . . .	171
57.	Free Jet Longitudinal Time-Average Velocity Distribution. .	175
58.	Free Jet Representation	178
59.	Graphical Presentation of Expressions for x_c/b, y_c/b and c_v	181
60.	Graphical Presentation of Expression for x_0/b	183
61.	Graphical Presentation of Centerline Velocity in the Transition Region	184
62.	Graphical Presentation of Centerline Velocity in the Turbulent Regime.	186
63.	Graphical Presentation of Dimensionless Profile Width at x/b = 1/4.	188
64.	Graphical Presentation of Momentum Power Series Function. .	189
65.	Comparison of Correlation to Centerline Velocity Data for R_e = 64.2, M = 0.416.	194
66.	Comparison of Correlation to Time-Average Velocity Profiles for R_e = 64.2 and M = 0.416.	196
67.	Comparison of Correlation to Centerline Velocity Data for R_e = 325 and M = 0.426	201
68.	Comparison of Correlation to Time-Average Velocity Profiles for R_e = 325 and M = 0.426	203
69.	Comparison of Predicted Values of Jet Deflection Angle to Experimental Data.	209
70.	Comparison of Predicted and Measured Time-Average Velocity Profiles in a Deflected Jet.	210
71.	Graphical Presentation of Free Jet Mass Flow Rate Function	214
72.	Comparison of Predicted and Measured Values of Control Port Mass Flow Rate	216

Figure Page

73. Graphical Presentation of Nozzle Exit Momentum Function . . 219

74. Graphical Presentation of Nozzle Exit Mass Flow Rate Function 222

75. Receiver Mass Flow Rate and Pressure Recovery Characteristics for R_e = 107, M = 0.653 and θ_r = 0° 232

76. Comparison of Measured and Predicted Values of Receiver Characteristics for R_e = 107, M = 0.653 and θ_r = 0° 233

77. Comparison of Measured and Predicted Values of Receiver Characteristics for R_e = 252, M = 0.763 and θ_r = 0° 236

78. Comparison of Measured and Predicted Values of Receiver Characteristics for R_e = 566, M = 0.368 and θ_r = 0° 237

79. Comparison of Measured and Predicted Values of Receiver Characteristics for R_e = 107, M = 0.653, x_r/b = 5.5 and θ_r = 10°. 239

80. Comparison of Measured and Predicted Values of Receiver Characteristics for R_e = 252, M = 0.763, x_r/b = 5.5 and θ_r = 10°. 241

81. Comparison of Measured and Predicted Values of Receiver Characteristics for R_e = 566, M = 0.368, x_r/b = 5.5 and θ_r = 10°. 242

82. Anemometer Calibration Curve for P_m = 5.0 mm. hg. 260

SUMMARY

The subject of this research is the experimental investigation of bounded rectangular jets in the low Reynolds number compressible flow regime. Both a single and two perpendicular interacting jets are considered. Limited information is also presented on the interaction of these jets with a diffuser. The flow fields in this study were created by providing a rarefied flow of air through the experimental model with a vacuum pump. The limits of the present investigation based on conditions at the centerline of the nozzle exit are

$$0.2 \leq M \leq 0.95$$

$$50 \leq R_e \leq 700$$

$$5 \times 10^{-4} \leq K_n \leq 2 \times 10^{-2}$$

This study involves conditions in the lower continuum and upper transitional flow regime assuming a Knudsen number of 10^{-2} (based on conditions at the nozzle exit) is the boundary between these flows.

In the single jet studies measurements were made of the decay of the centerline velocity. At several downstream stations the fluctuating velocity profiles, the time-averaged velocity profiles, the angle of the velocity vector and the static pressure profiles across the jet were determined. Fifteen flow cases were examined in this study. The investigation demonstrated both the laminar and turbulent mixing process were present in this regime. The origin

and propagation of turbulence as well as its effect on the jet flow field are described both qualitatively and quantitatively. Data from the present investigations are compared to experimental and analytical results from other flow regimes and differences noted. Semi-empirical correlation equations were developed to describe various jet parameters. These expressions describe the steady state velocity field in terms of Reynolds and Mach number and nondimensional location in the jet.

Measurements have been carried out on the interaction of two perpendicular jets. These experimental results are presented. A simple control volume model for the interaction process has been formulated for small deflection angles. It provides a description of the jet deflection and mass flow rates for the two nozzles. Empirical equations obtained from the single jet study have been incorporated to complete the interaction model. The experimental measurements are in satisfactory agreement with the analysis. This demonstrates that the jet interaction process is not significantly affected by molecular effects at a Knudsen number of 1×10^{-2}.

Experimental studies were performed to determine the output flow and pressure resulting from the interaction of a jet flow upon a simple receiver and diffuser. Attempts to predict pressure flow characteristics with existing theories using the free jet data correlation have produced mixed results. This is attributed to the lack of a good analytical model of the interaction of a skewed nonuniform velocity profile with a receiver, and the growth of boundary layers on the top and bottom plates of the experimental model negating the two-dimensional assumptions made in these calculations.

NOMENCLATURE

b = width of power jet's nozzle, in.

b_m = width of power jet's mixing zone, in.

c = sonic velocity, ft./sec.

c_T = sonic velocity based on upstream stagnation temperature, ft./sec.

c_v = velocity coefficient

C_p = constant pressure specific heat, BTU/lbm.°R

d = width of inlet to the receiver, in.

e = receiver offset distance from supply nozzle centerline, in.

h = height of power jet, in.

J = momentum per unit height, lbf./in.

J_∞ = momentum per unit height of power jet, lbf./in.

k = ratio of specific heats

K_n = Knudsen number

ℓ = arc length through which power jet is deflected at receiver inlet, in.

$\dot{m}_a$ = atmospheric flow component, lbm./sec.

$\dot{m}_c$ = control port mass flow rate, lbm./sec.

$\dot{m}_e$ = power jet entrained mass flow rate component, lbm./sec.

$\dot{m}_i$ = power nozzle mass flow rate, lbm./sec.

$\dot{m}_r$ = receiver open load mass flow rate, lbm./sec.

$\dot{m}_{re}$ = returned power jet mass flow rate component, lbm./min.

M = Mach number

p = static pressure, lbf./in.^{2}

P_B = receiver blocked load pressure recovery, lbf./in.^{2}

P_m = model static pressure, lbf./in.^{2}

P_r = receiver pressure recovery, lbf./in.^{2}

P_T = stagnation pressure in power jet reservoir, lbf./in.^{2}

P_1 = control port pressure, lbf./in.^{2}

r = distance in radial direction, in.

R = radius of curvature of power jet, in.

$\bar{R}$ = gas constant, ft.lbf./lbm.°R

R_e = Reynolds number

s = distance along jet's centerline in interaction region, in.

t = time, sec.

T = temperature, °R

T_T = power jet's total temperature, °R

$\bar{u}$ = time-averaged velocity component in axial direction, ft./sec.

u' = fluctuating velocity component, ft./sec.

$\bar{u}_c$ = power jet's centerline velocity, ft./sec.

$\bar{u}_i$ = velocity calculated using isentropic flow, ft./sec.

$\bar{u}_0$ = velocity at centerline of nozzle exit plane, ft./sec.

$\bar{v}$ = time-averaged velocity component normal to jet's centerline, ft./sec.

v' = fluctuating velocity component, ft./sec.

V = speed of vector component of velocity, ft./sec.

x = streamwise distance coordinate, in.

x_c = potential core length, in.

x_r = distance from intersection of supply and control port centerlines to receiver inlet, in.

x_s = distance to beginning of turbulent regime, in.

x_0 = transition parameter, in.

X = control port width, in.

y = distance normal to jet centerline, in.

y_c = potential core width, in.

y_e = control port setback from centerline of supply nozzle, in.

y* = distance from centerline to one percent point on jet's velocity profile, in.

z = distance from jet's centerline to edge of control port, in.

α = jet deflection angle as it crosses edge of control port, deg.

δ = distance between centerline of jet and centerline of nozzle, in.

η = nondimensional velocity profile shape factor

θ = power jet's deflection angle, deg.

θ_r = receiver offset angle from power nozzle centerline, deg.

μ = viscosity, lbf.sec./ft.^{2}

ρ = density, lbm./ft.^{3}

τ_1 = nondimensional exit plane shape factor

CHAPTER I

INTRODUCTION

Motivation for this Research

Numerous analytical and experimental studies have been made of free and interacting jet flows. These investigations have considered conditions which may be separated into either the high Reynolds number compressible and incompressible flow regime or the low Reynolds number incompressible flow regime. Motivation for the study of jets from these two regimes historically has stemmed from their purely scientific as well as practical importance. High Reynolds number jet flows have been the subject of numerous investigations since this is the simplest flow situation in which a turbulent mechanism controls the diffusion process in the fluid. Also, there exist many practical applications which involve these flows, for example, nozzles and ejectors. Low Reynolds number incompressible jets have been mainly of scientific interest due to the lack of practical applications for such devices.

Between the high Reynolds number turbulent flow regime and the low Reynolds number laminar incompressible flow regime lie a class of free jet flows which have been mainly ignored. No information on the compressible jet mixing process at low Reynolds numbers is available at present. Furthermore, the only information concerning these flows which is presently available is a limited quantity of mean velocity distribution data within the jet. This absence of information has historically

been the result of the lack of practical applications for jet devices which would be very small when operated at near atmospheric pressures. However, contributing to this lack of research may be the difficulties associated with the analytical modeling of the transition from laminar to turbulent flow in this regime and the making of precise measurements of the flow fields.

Technical advancements primarily in the last decade have provided motivation for the study of low Reynolds number compressible flows. This interest has been aroused chiefly from the development of pneumatic fluidic devices. These devices make use of single and interacting bounded jet flows to perform logic, amplify signals and to control processes. Present and anticipated future applications of these devices require them to operate at sea level, in high altitude aircraft and even in space. There is also a wide variation in physical sizes for these devices. Elements with power nozzle widths as large as several inches and as small as a few thousands of an inch have been constructed. Even smaller miniaturized fluidic elements have been proposed for signal processing devices. It is anticipated that these miniaturized fluidic elements would improve speed of response and lower quiescent flow.

Free and interacting jet analytical models and data have been used extensively in the design of fluidic devices. In the proportional fluid amplifier, for example, researchers have proposed that its complicated flow field can be approximated by three independent jet problems, and thus, each can be analyzed separately. These three

problems are the interaction of the control and supply jets, the propagation of the combined control and supply jet flows through the device and the impingement of these jet flows on the devices receiver and its ultimate output flow and pressure. Investigators and designers of relatively large fluidic elements have relied heavily on turbulent free jet information for mathematically modeling the undisturbed and interacting jets in these devices. Smaller devices and elements which function at low ambient pressures, however, utilize jet flows which are well below those reported to have fully turbulent characteristics. There is only a small amount of recent data and no analytical or empirical jet flow models to aid the design of these devices. The lack of experimental data and analytical models for the low Reynolds number compressible flow regime has provided the motivation for this research.

Objectives for this Research

The purpose of this research is to investigate free and interacting rectangular jets in the compressible low Reynolds number flow regime. It is anticipated that this research will serve two basic purposes. The first is to study jet flows in a regime which previously has not been investigated and compare these data to existing theories and experimental data. The second is to organize this information so that it may be used in the design of fluidic elements and other jet devices.

An extensive experimental program was performed to obtain information on low Reynolds number compressible jets. The flow fields in this study were created by providing a rarefied flow of air through

the experimental model with a vacuum pump. Measurements were carried out on the distribution of average velocity, velocity fluctuations and static pressure throughout a jet. Measurements were actually taken along the jet centerline and along several paths perpendicular to the jet centerline. Both a free jet and two perpendicular intersecting jets are considered. Limited experiments were performed upon the interaction of these jets with a receiver. The limits of the present investigation based on conditions at the centerline of the nozzle exit are

$$0.2 \leq M \leq 0.95$$

$$50 \leq R_e \leq 700$$

$$5\text{x}10^{-4} \leq K_n \leq 2\text{x}10^{-2}$$

This study involves conditions in the lower continuum and upper transitional flow regime assuming a Knudsen number of 10^{-2} (based on conditions at the nozzle exit) is the boundary between these flows. The flow regime considered in this research corresponds approximately to fluidic devices using air with atmosphere venting pressure and nozzle width variations of 0.005 in. $\geq$ b $\geq$ 0.0001 in. This flow regime includes devices which are presently operational as well as devices which would possess very much smaller flow passages.

Thesis Organization

An extensive review of literature pertinent to single and interacting jets is presented in the remainder of Chapter I. It should be

noted that this long section may be passed over at the discretion of the reader. The presentation of results from the present research begins in Chapter II with the description of the experimental apparatus. Procedures and methods employed in the experimental investigations are discussed in Chapter III. Chapters IV through VI present, respectively, the results of the free jet investigation, jet interaction investigation and jet receiver interaction investigation. The conclusions resulting from these investigations along with recommendations for further research are presented in Chapter VII.

Literature Review

In the subsequent sections analytical theories and experimental data will be reviewed which are pertinent to the present investigation. Since the findings of the present research are to be presented in three portions, literature relevant to these results will be reviewed in the same manner.

Plane Jet

Experimental investigations have demonstrated that the flow structure of the plane jet is very different when turbulence exists as compared to when the flow is laminar. Likewise, the analytical techniques employed to determine the flow field vary for compressible flow versus incompressible flow and for laminar flow versus turbulent flow. These differences in techniques have resulted in plane jet analytical investigations being divided into five categories

1. turbulent incompressible plane jet

2. turbulent compressible plane jet
3. laminar incompressible plane jet
4. laminar compressible plane jet
5. transition from laminar to turbulent flow in a plane jet

Reynolds number and Mach number based on conditions at the jet exhaust nozzle have been universally assumed as the parameters which divide the first four flow regimes. The fifth regime consists of jets transcending from laminar to turbulent flow.

This review will follow historical precedent and separate analytical and experimental results into the five preceding categories. It will be limited to the case of interest, that is, to the plane subsonic situation where there is no variation of total temperature between the jet and surrounding fluid at rest.

Turbulent Incompressible Plane Jet

Actual flows at high Reynolds numbers are characterized by a phenomenon known as "turbulence." In such a flow, the apparent steady motion of fluids is only steady in so far as the temporal mean values of the velocities and the pressure are concerned; in reality, velocities and pressures are subjected to random fluctuations. In this case the velocity and pressure distributions, and especially the energy losses, are determined mainly by the turbulent fluctuations.

In the flow of a plane jet at high Reynolds numbers, it is known that only near the exit of the nozzle is the flow laminar or streamline flow, but far downstream the flow in the jet is turbulent.

The essential characteristic of this turbulent motion is that the fluctuations are random in nature. Hence, the logical solution of the turbulent jet problems appears to be the application of methods of statistical mechanics. But such an application is difficult, because both the nature and elementary units and the expressions for probability are unknown. However, it is desirable to have some sort of theory as a guide for experimental results. Several semi-empirical theories, sometimes known as phenomenological theories, of fully developed turbulent flow have been developed. The best known of these is the Prandtl mixing length hypothesis which will be reviewed in a later section. The application of these theories to predicting the mean velocity field in two turbulent plane jet flow problems has been quite successful.

A necessary prerequisite to a review of analytical solutions for the mean velocity profiles in the fully developed portions of the plane jet is a discussion of the appropriate differential equations describing turbulent flow. It should be pointed out that the fundamental differential equations describing laminar flow (the Navier-Stokes equations) are invalid for turbulent flow. However, the Reynolds equations of motion which do describe the turbulent mixing of an incompressible fluid may be derived from the Navier-Stokes equations [1]. The Reynolds equations will be developed for a two-dimensional steady flow field in the following section.

Formulation of Reynolds Equations of Motion. In describing a turbulent flow in mathematical terms, it is convenient to separate it into a mean motion and a fluctuating, or eddying motion. The time-average of the u-component of velocity will be denoted by $\bar{u}$ and its

fluctuating component of velocity by u'. The following relations may be written for the velocity components and pressure:

$$u = \bar{u} + u' \quad ; \quad v = \bar{v} + v' \quad ; \quad p = \bar{p} + p' \tag{1}$$

The time-averages of the variables are formed at a fixed point in space and are given by

$$\bar{u} = 1/t_1 \int_{t_0}^{t_0+t_1} u \, dt \tag{2}$$

It is understood that the mean values are taken over a sufficiently long interval of time, t_1, for them to be independent of time. Consequently, by definition the time-averages of the fluctuating components are equal to zero.

It is useful to list several rules of operating on mean time-averages which will be required later. If f and g are two dependent variables whose mean values are to be formed and if q denotes one of the independent variables x and y, then the following rules apply:

$$\bar{f} = \bar{\bar{f}} \quad ; \quad \overline{f + g} = \bar{f} + \bar{g} \tag{3}$$

$$\overline{\bar{f} \cdot g} = \bar{f} \cdot \bar{g}$$

$$\overline{\frac{\partial f}{\partial q}} = \frac{\partial \bar{f}}{\partial q} \quad ; \quad \overline{\int f \, dq} = \int \bar{f} \, dq$$

It is now possible to derive the Reynolds' equations. The object of this derivation is to determine the equations of motion which must be satisfied by the time-averages of the velocity components $\bar{u}$

and $\bar{v}$ and the pressure $\bar{p}$. The Navier-Stokes equations for incompressible two-dimensional steady flow are

$$\rho \left[\frac{\partial(u^2)}{\partial x} + \frac{\partial(uv)}{\partial y}\right] = -\frac{\partial p}{\partial x} + \mu \nabla^2 u \tag{4}$$

$$\rho \left[\frac{\partial(vu)}{\partial x} + \frac{\partial(v^2)}{\partial y}\right] = -\frac{\partial p}{\partial y} + \mu \nabla^2 v$$

$$\frac{\partial u}{\partial x} + \frac{\partial v}{\partial y} = 0$$

The decomposition of the velocity and pressure from equation (1) may now be introduced into the preceding expression. The equation of motion which must be satisfied by the time-average of the variables may then be determined by averaging equation (4) term by term

$$\rho \left[\overline{\frac{\partial(\bar{u}+u')^2}{\partial x}} + \overline{\frac{\partial(\bar{u}+u')(\bar{v}+v')}{\partial y}}\right] = -\overline{\frac{\partial(\bar{p}+p')}{\partial x}} + \overline{\mu \nabla^2(\bar{u}+u')} \tag{5}$$

$$\rho \left[\overline{\frac{\partial(\bar{v}+v')(\bar{u}+u')}{\partial x}} + \overline{\frac{\partial(\bar{v}+v')^2}{\partial y}}\right] = -\overline{\frac{\partial(\bar{p}+p')}{\partial y}} + \overline{\mu \nabla^2(\bar{v}+v')}$$

$$\overline{\frac{\partial(\bar{u}+u')}{\partial x}} + \overline{\frac{\partial(\bar{v}+v')}{\partial y}} = 0$$

If the averaging process is carried out on the preceding equations in accordance with the rules in expression (3) and a simplification from continuity is made, the resulting expressions are

$$\rho\left(\bar{u}\frac{\partial\bar{u}}{\partial x}+\bar{v}\frac{\partial\bar{u}}{\partial y}\right)=-\frac{\partial\bar{p}}{\partial x}+\mu\nabla^2\bar{u}-\rho\left(\frac{\partial\overline{u'^2}}{\partial x}+\frac{\partial\overline{u'v'}}{\partial y}\right) \tag{6}$$

$$\rho\left(\bar{u}\frac{\partial\bar{v}}{\partial x}+\bar{v}\frac{\partial\bar{v}}{\partial y}\right)=-\frac{\partial\bar{p}}{\partial y}+\mu\nabla^2\bar{v}-\rho\left(\frac{\partial\overline{u'v'}}{\partial x}+\frac{\partial\overline{v'^2}}{\partial y}\right)$$

$$\frac{\partial\bar{u}}{\partial x}+\frac{\partial\bar{v}}{\partial y}=0$$

The preceding results are identical to those of the Navier-Stokes equations if the velocity components and pressure u, v and p are replaced by their time-averages except for the quadratic terms in turbulent velocity. These additional terms may be interpreted as components of a stress tensor. If this analogy is introduced into expression (6), the Reynolds equations are

$$\rho\left(\bar{u}\frac{\partial\bar{u}}{\partial x}+\bar{v}\frac{\partial\bar{u}}{\partial y}\right)=-\frac{\partial\bar{p}}{\partial x}+\mu\nabla^2\bar{u}+\left(\frac{\partial\sigma_x}{\partial x}+\frac{\partial\tau_{xy}}{\partial y}\right) \tag{7}$$

$$\rho\left(\bar{u}\frac{\partial\bar{v}}{\partial x}+\bar{v}\frac{\partial\bar{v}}{\partial y}\right)=-\frac{\partial\bar{p}}{\partial y}+\mu\nabla^2\bar{v}+\left(\frac{\partial\tau_{xy}}{\partial x}+\frac{\partial\sigma_y}{\partial y}\right)$$

$$\frac{\partial\bar{u}}{\partial x}+\frac{\partial\bar{v}}{\partial y}=0$$

The components of the stress tensor due to the turbulent velocity components are

$$\begin{pmatrix}\sigma_x & \tau_{xy}\\ \tau_{xy} & \sigma_y\end{pmatrix}=-\begin{pmatrix}\rho\overline{u'^2} & \rho\overline{u'v'}\\ \rho\overline{u'v'} & \rho\overline{v'^2}\end{pmatrix} \tag{8}$$

It may be concluded that the components of the mean velocity of turbulent flow satisfy the same equations as for laminar flow, except that the laminar stresses must be increased by additional stresses. These additional stresses are known as apparent or virtual stresses of turbulent flow or Reynolds stresses. These stresses are added to the ordinary viscous terms in laminar flow and have a similar influence on the flow field; it is often said that they are caused by eddy viscosity.

Expressions (7) and (8) constitute the starting point for the mathematical determination of the turbulent flow field. Although the time-averaged values of the turbulent velocity fluctuations may be interpreted as components of a stress tensor, this interpretation does not lead to a mathematical solution as in the case of laminar flow. Viscosity in laminar flow is a property of the fluid and may be determined experimentally, whereas, in turbulent flow eddy viscosity is dependent on the flow field itself. Expressions (7) and (8) cannot be used to evaluate the mean flow as long as the relationships between the mean and the turbulent velocity components are not known. This relationship can only be determined empirically [2].

Prandtl Mixing Length Theory. A number of phenomenological theories exist which relate the mean and fluctuating components of velocity in turbulent flow. Perhaps the best known of these is the Prandtl mixing length theory whose fundamental concepts will be reviewed for the case of parallel flow. In this simple flow situation the mean velocity varies only from streamline to streamline; the

principal direction of flow is assumed to be parallel to the x-axis. The mean components of velocity may be written as

$$\bar{u} = \bar{u}(y) \quad ; \quad \bar{v} = 0 \tag{9}$$

This type of flow can be found in a channel for which measurements of the turbulent velocity components indicate the only non-zero stress component from expression (8) is

$$\tau_{xy} = \tau = -\rho\overline{u'v'} \tag{10}$$

Prandtl proposed that in the turbulent flow field, fluid particles coalesce into lumps which move together for a given traversed length, both in the longitudinal and in the transverse direction, retaining their momentum parallel to the x-direction. He postulated that a lump of fluid which comes, for example, from a layer at $(y_1-\ell_1)$ and has a velocity $\bar{u}(y_1-\ell_1)$ is displaced a distance ℓ_1 in the transverse direction to the layer at y_1; see Figure 1.

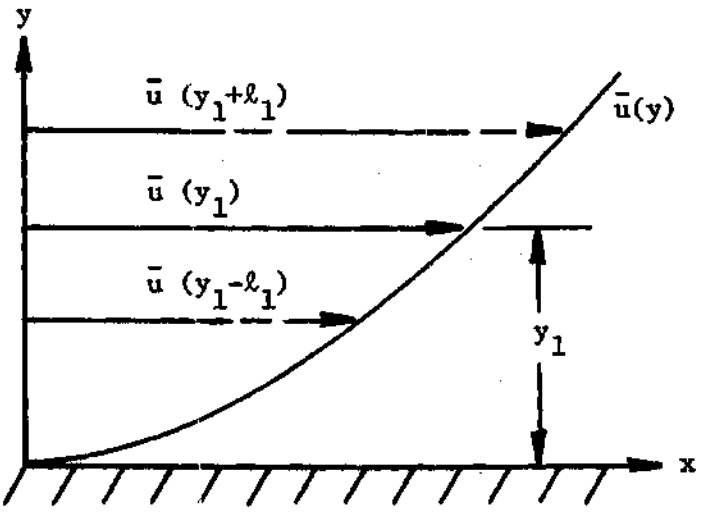

Figure 1. Description of the Prandtl Mixing Length Concept

The distance ℓ_1 is the Prandtl mixing length. The lump of fluid retains its original momentum from the layer at $(y_1-\ell_1)$; thus its velocity in the new lamina at y_1 is smaller than the velocity prevailing there. This difference in velocity between lamina is then

$$\Delta u_1 = \bar{u}(y_1) - \bar{u}(y_1-\ell_1) = \ell_1 \frac{\Delta \bar{u}}{\Delta y} = \ell_1 \left(\frac{d\bar{u}}{dy}\right)_{y_1} \tag{11}$$

The preceding expression may be obtained by developing $\bar{u}(y_1-\ell_1)$ in a Taylor series and neglecting higher order terms. Similarly, a lump of fluid which comes from the $(y_1+\ell_1)$ lamina to the y_1 lamina would possess a velocity which exceeds its surrounding by

$$\Delta u_2 = \bar{u}(y_1+\ell_1) - \bar{u}(y_1) = \ell_1 \left(\frac{d\bar{u}}{dy}\right)_{y_1} \tag{12}$$

The velocity differences caused by the transverse motion of fluid particles can be regarded as the turbulent velocity components at y_1. Hence, we can calculate the time-average of the absolute value of the velocity fluctuation in the x-direction and obtain

$$\overline{|u'|} = \frac{1}{2}\left(|\Delta u_1| + |\Delta u_2|\right) = \ell_1 \left|\left(\frac{d\bar{u}}{dy}\right)_{y_1}\right| \tag{13}$$

Prandtl assumed that velocity fluctuations in the transverse or y-direction originate in the following way: Consider two lumps of fluid meeting in a lamina at y_1, the slower one from $(y_1-\ell_1)$ and the faster one from $(y_1+\ell_1)$. Under these circumstances the lumps will collide and diverge sideways. This is equivalent to the existence of a fluctuating velocity component in both directions with respect to the

layer at y_1. This argument implies that the transverse component v' is of the same order of magnitude as u' and thus we may write

$$\overline{|v'|} = \text{const} \cdot \overline{|u'|} = \text{const} \cdot \ell_1 \frac{d\bar{u}}{dy} \tag{14}$$

In order to determine the expression for shearing stress found in equation (10), it is necessary to consider the mean value of $\overline{u'v'}$ a little closer. It follows from the preceding model that lumps which arrive at layer y_1 with a positive value of v' (upwards from below) produce "mostly" a negative u'; so that the product u'v' is negative. Lumps with a negative value of v' (downward from above) produce "mostly" a positive value of u' and again the product u'v' is negative. The qualifying word "mostly" indicates the appearance of particles with u' of opposite sign is not excluded, however, is less frequent. Hence, we can assume

$$\overline{u'v'} = - c_1 \overline{|u'|} \cdot \overline{|v'|} \tag{15}$$

Inserting equations (13) and (14) into (15) yields

$$\overline{u'v'} = - \text{const} \cdot \ell_1^2 \left|\frac{d\bar{u}}{dy}\right| \frac{d\bar{u}}{dy} \tag{16}$$

It should be noted that the constant in the preceding expression also contains c_1. This constant may be included into the still unknown mixing length and we may write

$$\overline{u'v'} = - \ell_1^2 \left|\frac{d\bar{u}}{dy}\right| \frac{d\bar{u}}{dy} \tag{17}$$

Consequently, the shearing stress from equation (10) becomes

$$\tau = \rho \, \ell_1^2 \left|\frac{d\bar{u}}{dy}\right| \frac{d\bar{u}}{dy} \tag{18}$$

An expression for the virtual kinematic viscosity becomes

$$\varepsilon = \ell_1^2 \left|\frac{d\bar{u}}{dy}\right| \tag{19}$$

Prandtl's result in expression (18) for the turbulent shearing stress is unsatisfactory in that the virtual kinematic viscosity, ε, vanishes at points where $\frac{d\bar{u}}{dy}$ equal zero (i.e., at points of maximum and minimum velocity). This is certainly not the case because turbulent mixing does not vanish at points of maximum velocity. As an example, hot wire anemometer data have demonstrated the turbulent mixing process exists at the centerline of high Reynolds number jets. In order to counter this problem, Prandtl established a simpler equation for the virtual kinematic viscosity. This expression is valid only for free turbulent flow and was derived from extensive experimental data. Prandtl assumed that the lumps of fluid which move in a transverse direction during turbulent mixing are of the same order of magnitude as the width of the turbulent mixing zone. The virtual kinematic viscosity is formed by multiplying the maximum difference in the mean flow velocity by a length which is assumed to be proportional to the width, b_m, of the mixing zone. Thus

$$\varepsilon = \psi_1 \, b_m \, (\bar{u}_{max} - \bar{u}_{min}) \tag{20}$$

Here ψ_1 denotes a dimensionless number to be determined experimentally. It follows that ε remains constant over the whole width of every cross-section, whereas the hypothesis in expression (19) implies that virtual

kinematic viscosity varies even if the mixing length were assumed to be constant [3].

Analytical Solutions to Turbulent Plane Jet Problems. In the preceding sections, the mathematical tools have been developed for the solution of two problems involved in the flow field of an incompressible turbulent plane jet. These problems are that of the free jet boundary and the fully developed free jet flow. The solutions to these two flow problems have been assumed to describe, respectively, the time-average velocity profiles in the core region and the fully developed turbulent flow region in a plane jet; see Figure 4.

The free jet boundary problem occurs when a fluid is discharged from a nozzle or orifice into a fluid medium at rest; see Figure 2. The discontinuity in the velocities of the jet and surrounding medium is unstable and gives rise to a zone of turbulent mixing downstream of the point where the streams first meet. The width of this mixing region increases in the downstream direction.

A fully developed turbulent flow occurs at some distance downstream of the nozzle of a free jet; see Figure 3. In this region of flow, the jet has traveled far enough downstream from the nozzle exit for the time-averaged velocity profiles through the jet to become similar.

Before proceeding to integrate the Reynolds equations for the cases of interest, an estimate will be made of the increase of the width of the mixing zone and the decrease of height of the velocity profile with increasing distance x. The following account is based on one by Prandtl.

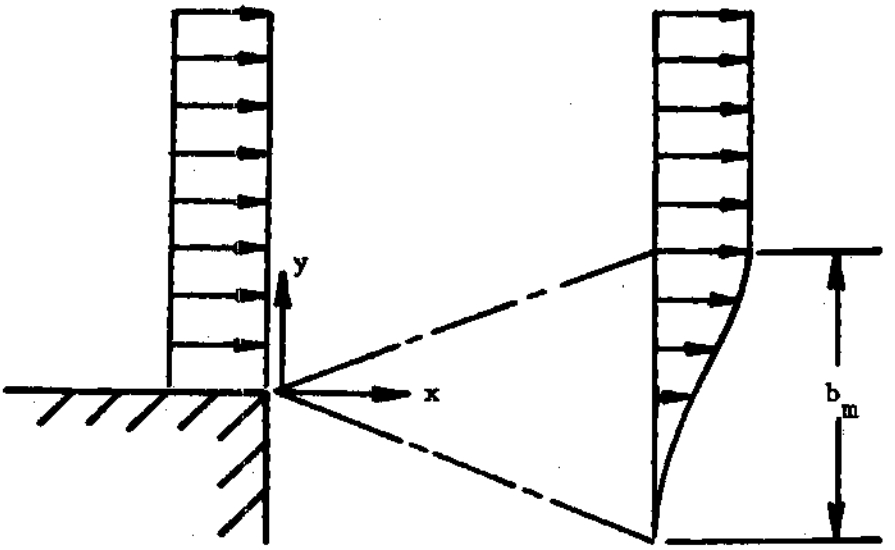

Figure 2. Free Jet Boundary Flow

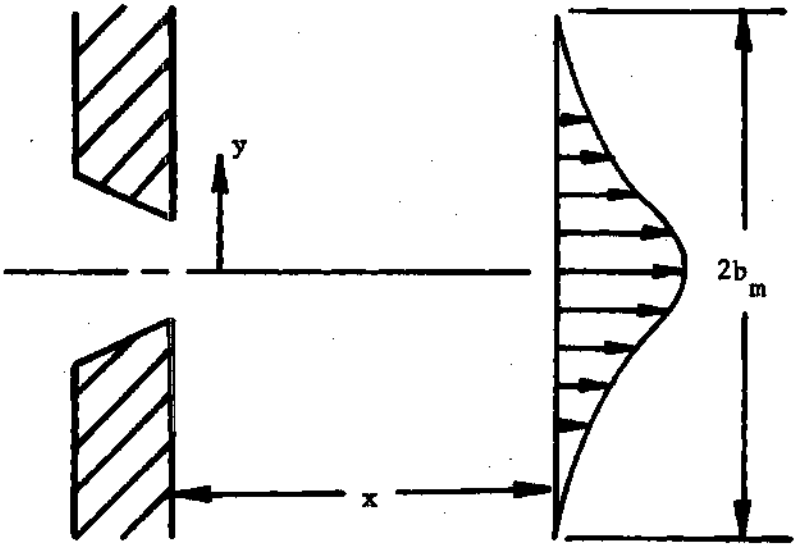

Figure 3. Fully Developed Free Jet Flow

It may be assumed for a turbulent jet that the mixing length, ℓ_1, is proportional to the mixing zone width, b_m.

$$\ell_1/b_m = \beta = \text{const} \tag{21}$$

In addition, the rate of increase of the mixing zone width with time is proportional to the transverse velocity v'.

$$\frac{Db_m}{Dt} \sim v' \tag{22}$$

Here D/Dt denotes the substantive derivative, so that $\frac{D}{Dt} = u\frac{\partial}{\partial x} + v\frac{\partial}{\partial y}$. Also, $v' \sim \ell_1 \frac{d\bar{u}}{dy}$ from expression (14) may be substituted into the previous equation

$$\frac{Db_m}{Dt} \sim \ell_1 \frac{\partial \bar{u}}{\partial y} \tag{23}$$

The mean value of $\partial\bar{u}/\partial y$ taken over the mixing zone may be assumed to be approximately proportional to $\bar{u}_{max}/b_m$. Thus

$$\frac{Db_m}{Dt} = \text{const} \cdot \ell_1 \cdot \bar{u}_{max}/b_m \tag{24}$$

Introducing equation (21) into the preceding expression gives

$$\frac{Db_m}{Dt} = \text{const} \cdot \beta \cdot \bar{u}_{max} = \text{const} \cdot \bar{u}_{max} \tag{25}$$

Evaluating the substantive derivative for b_m produces

$$\bar{u}_{max}\frac{db_m}{dx} = \text{const} \cdot \bar{u}_{max} \tag{26}$$

The preceding expression indicates the mixing zone width is proportional to downstream distance x for both the jet boundary and the fully developed jet flow.

$$b_m = \text{const} \cdot x \tag{27}$$

The decay of centerline velocity in a fully developed jet may be determined if the momentum of the jet is assumed to be conserved (this assumption will be examined in more detail in the section describing experimental studies of free turbulent plane jets). The momentum per unit height is

$$J = \rho \int \bar{u}^2 \, dy = \text{const} \tag{28}$$

It may also be assumed that the integrand in the preceding expression may be approximated by

$$\int_0^{b_m} \bar{u}^2 \, dy = \text{const} \cdot \bar{u}^2_{max} \, b_m \tag{29}$$

Thus, expression (28) becomes

$$J/\rho = \text{const} \cdot \bar{u}^2_{max} \, b_m \tag{30}$$

Introducing the expression for the mixing zone in equation (27), yields

$$\bar{u}_{max} = \text{const} \cdot \frac{1}{\sqrt{x}} \sqrt{J/\rho} \tag{31}$$

Free Jet Boundary. A summary of the solution for the time-averaged velocity distribution in a free jet boundary follows. With reference to Figure 2, the more general case will be considered where

at $x = 0$ there is a meeting of two streams whose constant velocities are U_1 and U_2, respectively; it being assumed that $U_1 > U_2$. Downstream of the point of encounter the streams will form a mixing zone whose width increases proportionally to x. The x-component of momentum and the continuity equation from expression (7) may be written as

$$\rho \left(\bar{u} \frac{\partial \bar{u}}{\partial x} + \bar{v} \frac{\partial \bar{u}}{\partial y} \right) = - \frac{\partial \bar{p}}{\partial x} + \mu \nabla^2 \bar{u} - \rho \frac{\partial \overline{u'^2}}{\partial x} - \rho \frac{\partial \overline{u'v'}}{\partial y} \tag{32}$$

$$\frac{\partial \bar{u}}{\partial x} + \frac{\partial \bar{v}}{\partial y} = 0$$

The term $\mu \nabla^2 \bar{u}$ in the preceding expression represents laminar friction and may be neglected for the present situation, since turbulent friction dominates the flow field. It will be assumed that the pressure is constant and that turbulent fluctuations in the x-direction are small in the flow fields of both the jet boundary and the fully developed jet flow. This assumption will be verified and considered in more detail in the section of experimental studies to follow. Thus expression (32) reduces to

$$\rho \left(\bar{u} \frac{\partial \bar{u}}{\partial x} + \bar{v} \frac{\partial \bar{u}}{\partial y} \right) = - \rho \frac{\partial \overline{u'v'}}{\partial y} = \frac{\partial \tau}{\partial y} \tag{33}$$

$$\frac{\partial \bar{u}}{\partial x} + \frac{\partial \bar{v}}{\partial y} = 0$$

The previous set of equations was first solved by Tollmien [4] who made use of Prandtl's hypothesis in the form of expression (18). He also assumed the mixing length remained constant over the mixing zone. We shall review here the mathematical simpler solution due to Görtler [5] who bases it on Prandtl's hypothesis in expression (20). Expression

(33) based on Prandtl's second assumption becomes

$$\left(\bar{u}\frac{\partial\bar{u}}{\partial x}+\bar{v}\frac{\partial\bar{u}}{\partial y}\right)=\frac{1}{\rho}\frac{\partial\tau}{\partial y}=\frac{\partial(\epsilon\frac{\partial\bar{u}}{\partial y})}{\partial y} \tag{34}$$

$$\frac{\partial\bar{u}}{\partial x}+\frac{\partial\bar{v}}{\partial y}=0$$

If the virtual kinematic viscosity is assumed constant across the mixing zone, then

$$\left(\bar{u}\frac{\partial\bar{u}}{\partial x}+\bar{v}\frac{\partial\bar{u}}{\partial y}\right)=\epsilon\frac{\partial^2\bar{u}}{\partial y^2} \tag{35}$$

Putting $b_m = c_1 x$ from expression (27) where c_1 is some constant, the virtual kinematic viscosity becomes

$$\epsilon = \psi_1 c_1 x (U_1-U_2) \tag{36}$$

It may be assumed that the velocity profiles of $\bar{u}$ and $\bar{v}$ are similar functions of y/x. Putting $\xi = \sigma y/x$ we can satisfy the equation of continuity by the adoption of the stream function $\psi = xUF(\xi)$ where $U = 1/2(U_1+U_2)$. Then, $\bar{u} = U\sigma F'(\xi)$ and expression (35) leads to the following differential equation for $F(\xi)$:

$$F''' + 2\tau^2 FF'' = 0 \tag{37}$$

where the value of τ is

$$\tau = \frac{1/2}{\sqrt{\psi_1 c_1 \left(\frac{U_1-U_2}{U_1+U_2}\right)}} \tag{38}$$

The boundary conditions are $\xi = \pm \infty$; $F'(\xi) = 1 \pm \lambda$. Görtler solved expression (37) by assuming a power-series expansion of the form

$$\tau F(\xi) = F_0(\xi) + \lambda F_1(\xi) + \lambda^2 F_2(\xi) + \cdots \tag{39}$$

with $F_0 = \xi$. Substituting expression (39) into (38) and arranging in ascending powers of λ, we obtain a system of differential equations which is solved by recursion. The first of these is

$$F_1''' + 2 \xi F_1'' = 0 \tag{40}$$

with the boundary conditions $F_1'(\xi) = \pm 1$ at $\xi = \pm \infty$. The solution of expression (40) is given by the error function

$$F_1'(\xi) = \operatorname{erf}(\xi) = \frac{2}{\sqrt{\pi}} \int_0^{\xi} e^{-z^2} \, dz \tag{41}$$

The contributions of the succeeding terms of equation (39) are negligible, thus the solution is

$$\bar{u} = \frac{U_1 + U_2}{2} \left[1 + \frac{U_1 - U_2}{U_1 + U_2} \operatorname{erf}(\xi) \right] \tag{42}$$

$$\xi = \sigma y / x$$

The single arbitrary constant σ in the preceding expression must be evaluated from experimental data.

Fully Developed Plane Jet. The mean velocity distribution in a two-dimensional turbulent jet was first calculated by Tollmien [4] who made use of Prandtl's first mixing length hypothesis of equation (18). However, as in the case of the free boundary we will review the

mathematically simpler solution due to Görtler [5]. In the plane jet problem similar simplifying assumptions will be made to the equations of motion, that is viscous friction will be neglected, pressure is assumed constant in the flow field and turbulent fluctuations in the x-direction are neglected. The simplified equations of motion are

$$\bar{u}\frac{\partial \bar{u}}{\partial x} + \bar{v}\frac{\partial \bar{u}}{\partial y} = \varepsilon \frac{\partial^2 \bar{u}}{\partial y^2} \tag{43}$$

$$\frac{\partial \bar{u}}{\partial x} + \frac{\partial \bar{v}}{\partial y} = 0$$

The rate of increase of the jet mixing zone, b_m, is assumed to be proportional to x. The virtual kinematic viscosity from Prandtl's second hypothesis, expression (20), then becomes

$$\varepsilon = \psi_1 b_m \bar{u}_c \tag{44}$$

where $\bar{u}_c$ denotes the centerline velocity and ψ_1 is some arbitrary constant. As in the case of the jet boundary, the velocity profiles of $\bar{u}$ and $\bar{v}$ may be assumed to be similar to η_1 where $\eta_1 = \sigma y/x$. The equation of continuity in expression (43) may be satisfied by adopting a stream function. Writing the x-momentum equation in (43) in terms of the stream function, results in an ordinary differential equation in terms of functions of the stream function, $F(\eta_1)$, and its derivatives. Integrating that differential equation leads to the final solution to this problem

$$\bar{u} = \bar{u}_c \operatorname{sech}^2 (\eta_1) \tag{45}$$

$$\bar{v} = \bar{u}_c/2\sigma \left[2\eta_1 \operatorname{sech}^2 (\eta_1) - \tanh (\eta_1)\right]$$

$$\eta_1 = \sigma y/x$$

$$\bar{u}_c = \bar{u}_1 \left(\frac{x}{x_1}\right)^{-1/2}$$

$\bar{u}_c$ in the preceding expression denotes the centerline velocity at some arbitrary distance x from the nozzle. The centerline velocity at some fixed distance from the nozzle x_1 is $\bar{u}_1$. The arbitrary constant σ in the expression above must be evaluated from experimental data. It is interesting to note that the form of the solution for $\bar{u}$ and $\bar{v}$ for the turbulent plane jet is identical to that for the laminar plane jet. The profile similarity parameters for these two cases, however, are different [6].

Experimental Investigations of Plane Incompressible Turbulent Jets. A general explanation of the flow structure observed in a turbulent fluid jet can be made with reference to Figure 4. The fluid jet is discharged from a nozzle with a uniform velocity. The pronounced velocity gradient between the fluid jet at the nozzle walls and the surrounding fluid will result in a turbulent lateral mixing process which progresses both inward and outward from the efflux section. The fluid within the jet is gradually decelerated and fluid from the surrounding region is gradually accelerated or entrained. This mixing process on either side of the potential core gradually reduces its width until it is completely eliminated. The point at which the two

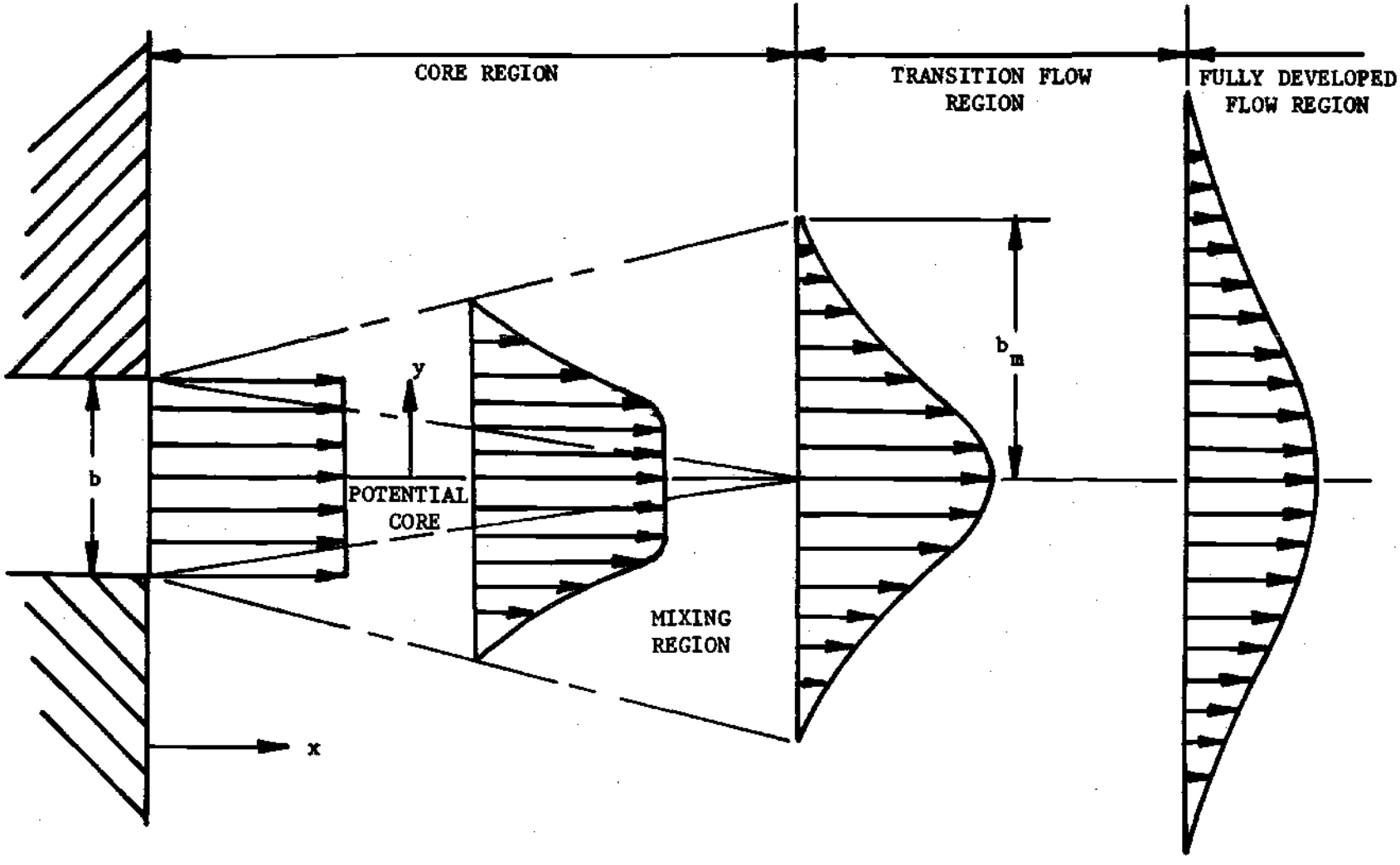

Figure 4. Representation of a Plane Turbulent Jet

mixing zones intersect is the end of the core region. Following the core region is the transition flow region. In this regime the time-average velocity profiles are progressing toward similarity. At the end of the transition flow region, the jet's velocity profiles have obtained similarity and a fully developed turbulent flow exists.

Liepmann and Laufer [7] have made an extensive experimental investigation of the time-average and fluctuating velocity field in a plane turbulent free mixing region. The free mixing zone is assumed to correspond to a half jet in the core region; see Figure 4. The free mixing region in their investigation was created by allowing a jet of air to emerge from a nozzle and mix with still air on one of its boundaries. The other boundaries were solid walls. The nozzle width of the apparatus was 19.05 centimeters with an aspect ratio of 8:1. The Reynolds number at which this study was conducted was 460,000 based on the width of a corresponding free jet situation where the nozzle width would be 38.1 centimeters. The Mach number of this study was 0.052.

Measurements of the time-average and fluctuating field have indicated the boundary layer at the mouth of the jet was only 0.1 centimeters thick and was laminar. The mixing zone was found to be laminar from $x = 0$ to $x = 6$ centimeters, however, beyond that point turbulence existed in the mixing zone. Experimental measurements of the time-average velocity field had demonstrated that fully developed turbulent velocity profiles were obtained only for a distance exceeding approximately 30 centimeters downstream of the nozzle.

In a comparison of the measured velocity profiles in the mixing zone's fully developed region, Liepmann and Laufer had found that by appropriate choice of the experimental constant σ both the theory based on constant mixing length (Tollmien) and the one based on constant exchange coefficient (Görtler) could be made to agree with the measured velocity distribution. Figure 5 shows that for $\sigma = 12.0$ the agreement with Tollmien's velocity profile is fairly good; while for $\sigma = 11.0$ Görtler's velocity profile is better approximated. As a matter of fact, an error integral curve (Görtler's first approximation and the one reviewed in the preceding section) gives a reasonable agreement with measured values.

Measurements of the longitudinal and lateral components of the velocity fluctuations were carried out at several stations in the flow. These data indicated that the profiles of the fluctuating components of velocity had attained similarity at approximately 30 centimeters downstream of the nozzle. Their study thus indicated the time-average velocity profiles as well as the fluctuating velocity attained similarity at approximately the same distance downstream of the nozzle. Shown in Figure 6 is time-average and fluctuating components of velocity at one location in the flow field. The velocity profiles are nondimensionalized by θ_1 which is the momentum thickness given by

$$\theta_1 = \int_{-\infty}^{\infty} \bar{u}/\bar{u}_0 \left(1 - \frac{\bar{u}}{\bar{u}_0}\right) dy \qquad (46)$$

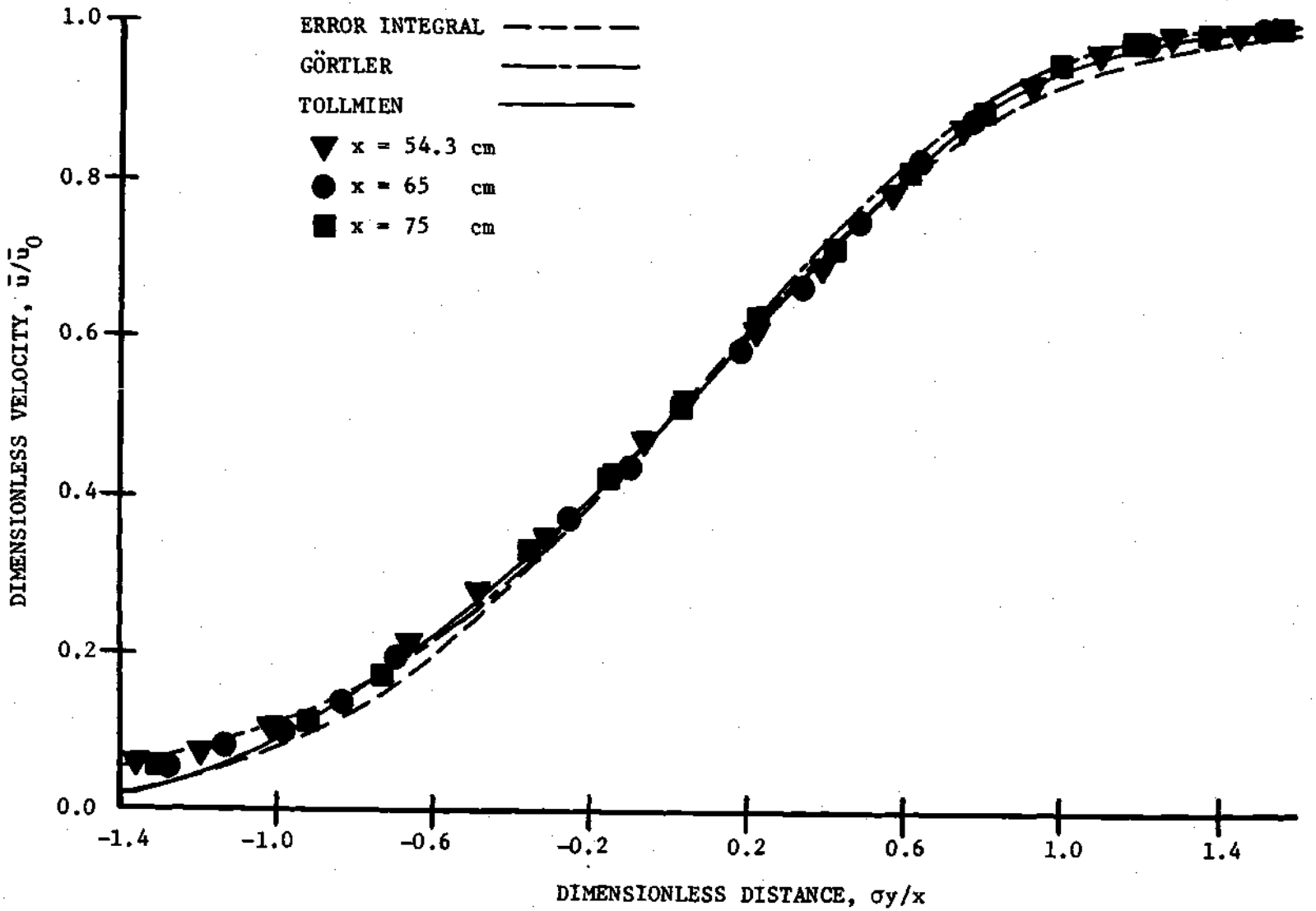

Figure 5. Mean Velocity Distribution in a Half Jet (σ=12.0) from Reference [7]

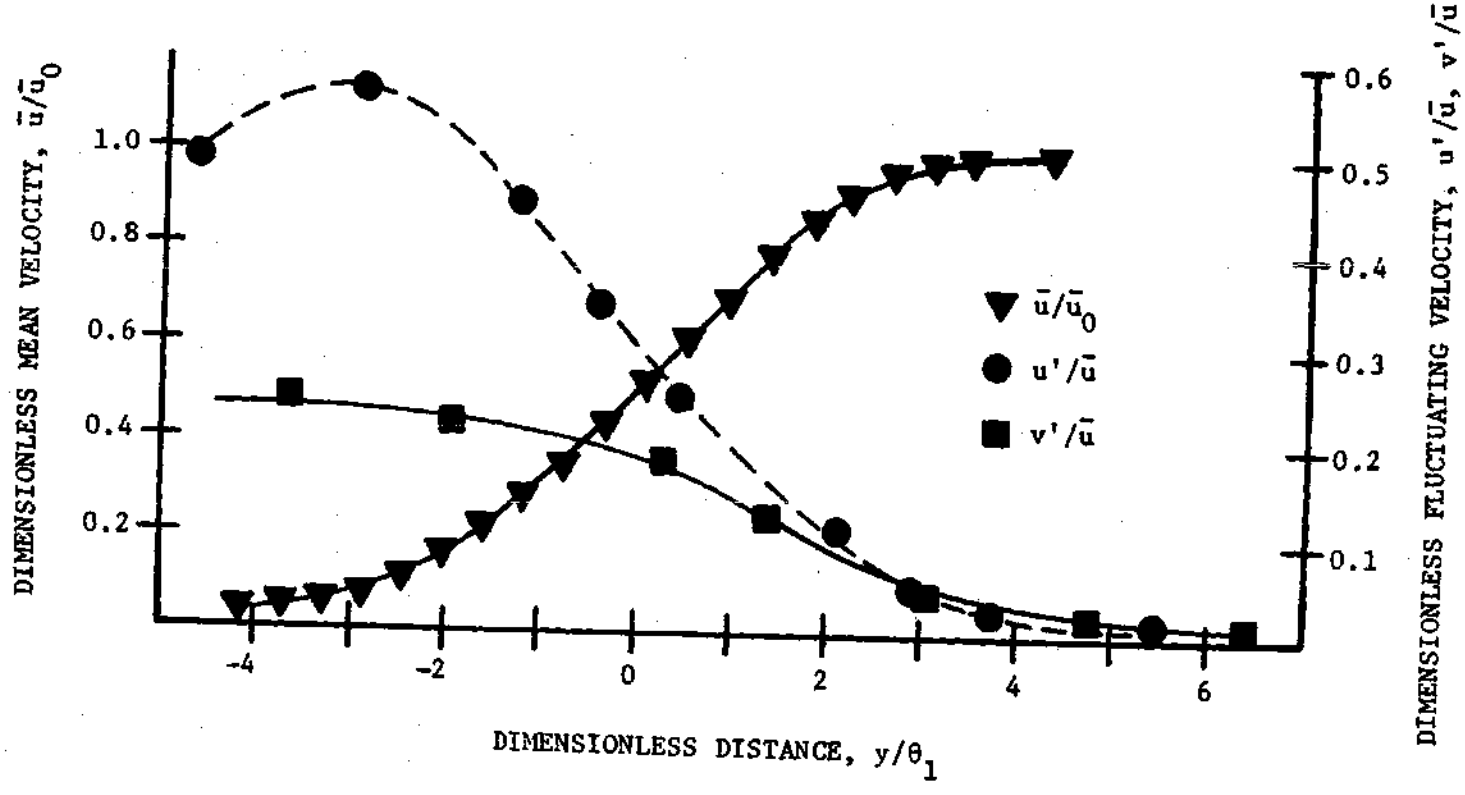

Figure 6. Lateral Distribution of Mean and Fluctuating Velocities in a Half Jet (x=54.3 centimeters) from Reference [7]

From the measured correlation coefficient and the components of the turbulent fluctuations, Liepmann and Laufer have calculated the turbulent shear stress. The mixing length and exchange coefficient were then computed from the turbulent shear stress and the measured velocity profile. These results indicated both the exchange coefficient and mixing length vary across the mixing zone. Thus the hypothesis used by Görtler and Tollmien in the solution of this problem is in error, even though their resulting time-average velocity profiles are in good agreement with data.

An extensive experimental investigation has been made of the structure of a free turbulent plane jet issuing into a fluid at rest by Miller and Comings [8]. Measurements were made of the time-average velocity, the fluctuating velocity and the static pressure within the jet. The measurements performed with air were at a reported Reynolds number of 17,800, based on the width of the nozzle, and a Mach number of 0.063. A nozzle of aspect ratio 40:1 was employed to insure a two-dimensional flow field.

Jet width as a function of downstream distance is shown in Figure 7. The author's definition of jet width may be ascertained from Figure 10. From the velocity distribution in this figure, the jet width is the lateral distance to the point where the velocity is 67 per cent of the centerline velocity. The jet width is approximately constant for the first four nozzle widths downstream. Further downstream a transition to linear spread with distance was observed. From $x/b = 7$ to the farthest measurement station, the jet width, b_m, is proportional

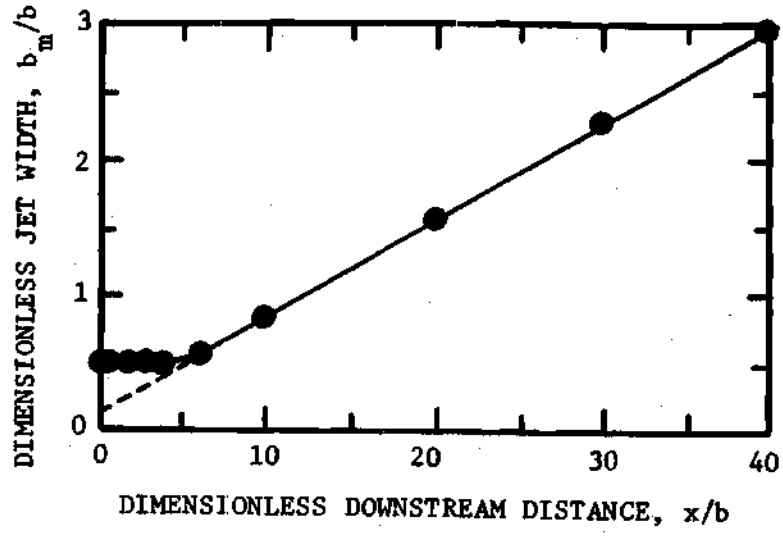

Figure 7. Jet Width for a Turbulent Incompressible Jet from Reference [8]

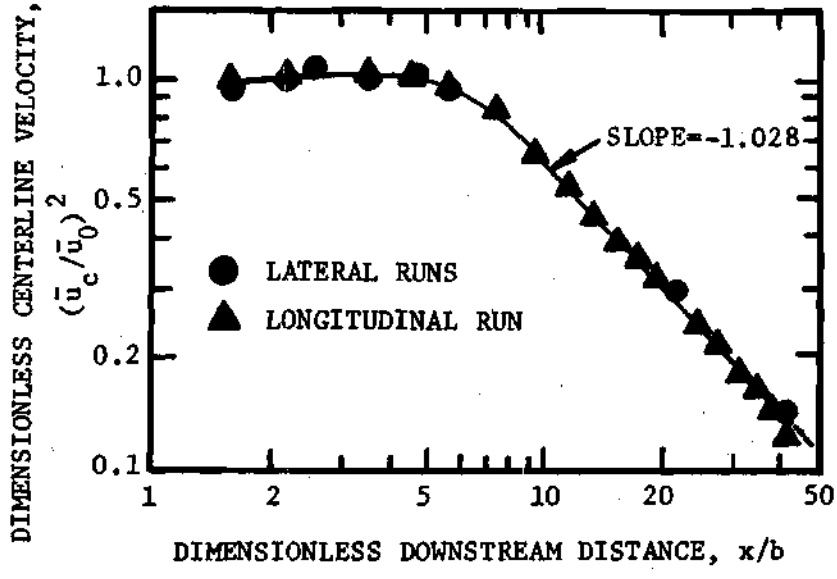

Figure 8. Centerline Velocity Decay for a Turbulent Incompressible Jet from Reference [8]

to x. It should be pointed out that the analytical solutions for the free boundary and the fully developed jet both predict the mixing zone grows proportional to downstream distance x.

The decay curve for the centre-plane velocity (squared) appears in Figure 8. The straight portion of the curve for $x/b \geq 7$ has a slope of -1.028 as compared to a slope of -1 predicted by the analytical solution for a fully developed turbulent plane jet. From these data it would appear the potential core exists some five nozzle widths downstream of the nozzle. Centerplane velocity data by Albertson [9] are in good agreement with Figure 8. Albertson's study which was performed for Reynolds number range of $13{,}000 \geq R_e \geq 1500$ indicated a constant core length of 5.2 nozzle widths.

The behavior of the centerline velocity decay and jet spread with distance from the nozzle defines two distinct flow regimes. The authors of this research had defined the flow region up to $x/b = 7$ as the transition region, and the distance beyond as the fully developed region. These two regions were considered separately.

Miller and Comings report making measurements of the lateral distributions of $\bar{u}$, $\overline{u'^2}$, and $\bar{p}$ at several stations in the transition region. Data for $\overline{u'^2}$ and $\bar{p}$ are shown in Figure 9. Unfortunately, time-average velocity profiles are not reported for this region. Hot wire anemometer data indicated a region of low turbulence level ($\sqrt{\overline{(u'^2)}} \,/\, \bar{u} \leq 0.05$) which existed downstream from the nozzle was contained in a wedge whose vertex fell on the centre-plane at $x/b = 2.5$ and whose base coincided with the nozzle mouth. A positive static

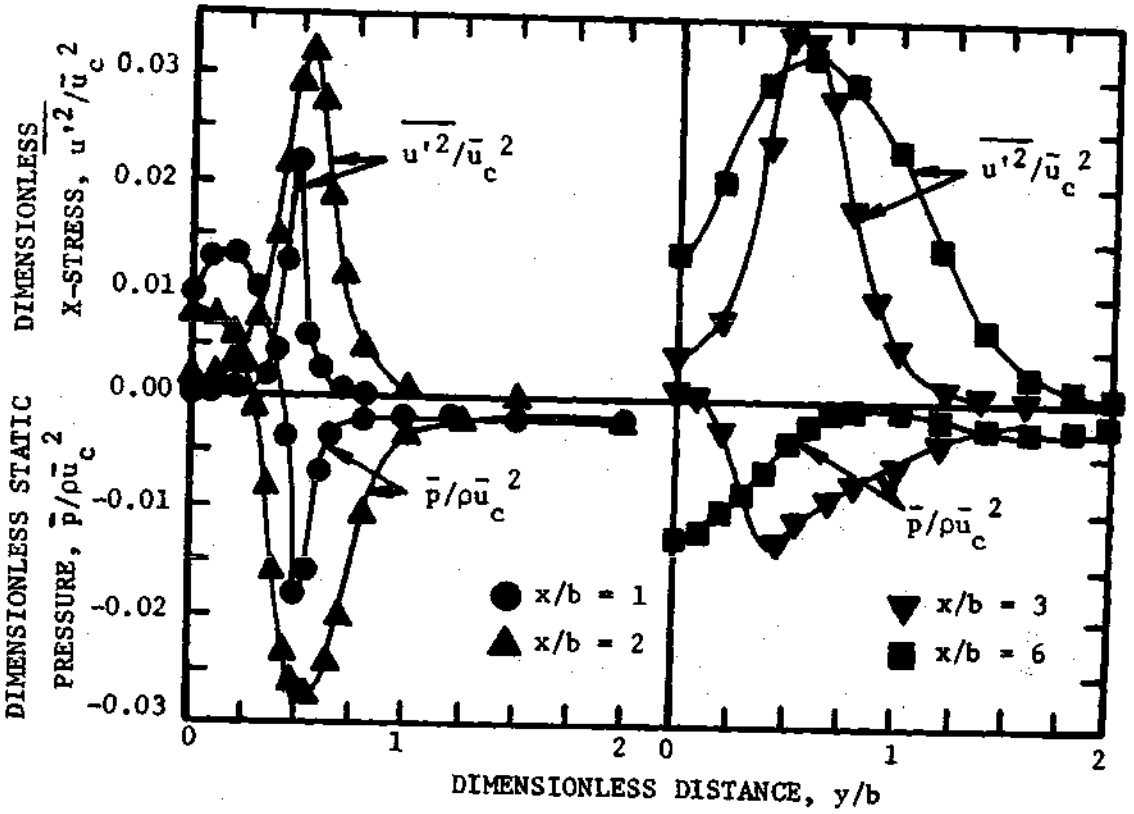

Figure 9. Turbulent X-Stress and Static Pressure Profiles for the Transition Region from Reference [8]

pressure ridge, straddling the centre-plane and decaying rapidly with x, was found within the "potential wedge." This ridge is attributed to the persistence of the pressure distribution created within the nozzle.

Outside this potential wedge all measured static pressures were negative. Particularly striking were the static pressure trenches appearing on each side of the potential wedge starting at $x/b = 0.8$ and finally merging at the centre-plane at $x/b = 5.0$.

The corresponding turbulence x-stress profiles of Figure 9 show the development of turbulence in the high shear regions on either side of the potential wedge. A close negative correspondence is noted between the static pressure and turbulent fluctuations in the x-direction at $x/b = 1$ and 2, however, this correspondence is seen to deteriorate at stations farther downstream.

Lateral distributions of $\bar{u}$, $\overline{u'^2}$ and $\bar{p}$ at several stations in the fully developed regime are shown in Figures 10, 11 and 12. In each case the lateral distance y is nondimensionalized by the jet width parameter, b_m, in Figure 7. The distributions of the time-average velocity $\bar{u}$ demonstrate the similarity of the mean velocity profiles in this region. Theoretical velocity profiles for this region by Görtler; see equation (45), and Reichardt are in agreement with measured data. However, Görtler's solution appears to be in appreciable error near the jet boundary while Reichardt's expression fits the data through the entire profile.

The most striking feature of the turbulent x-stress profile and the pressure distributions in the fully developed region is their lack

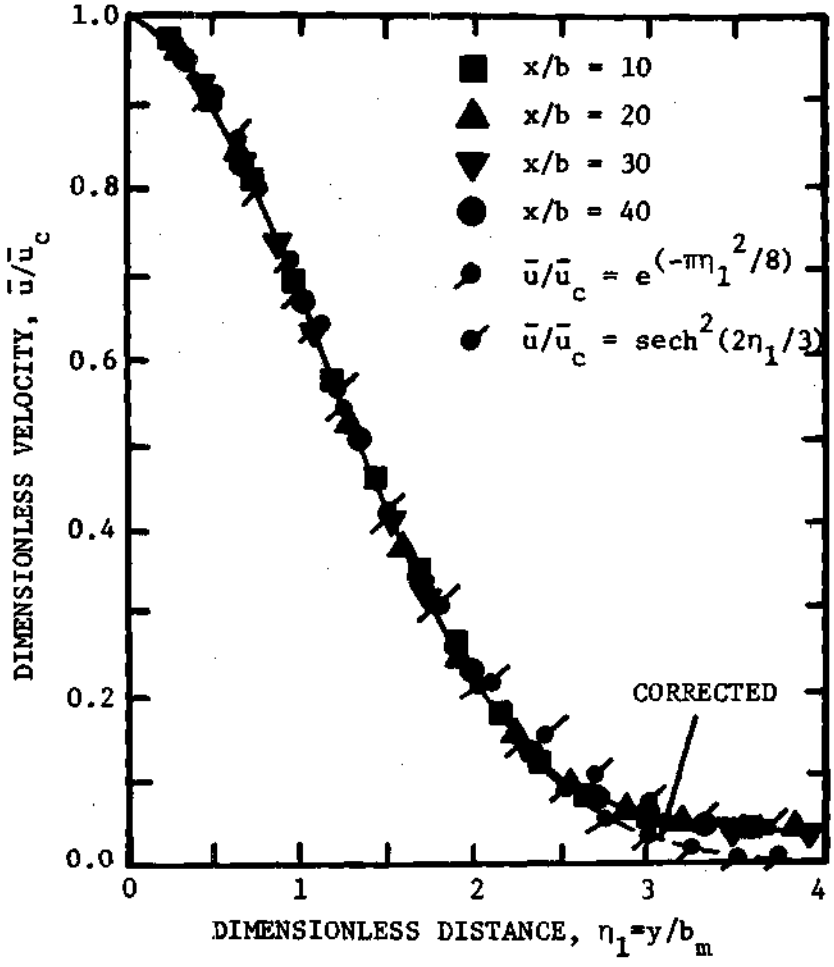

Figure 10. Mean Velocity Profiles for the Fully Turbulent Region from Reference [8]

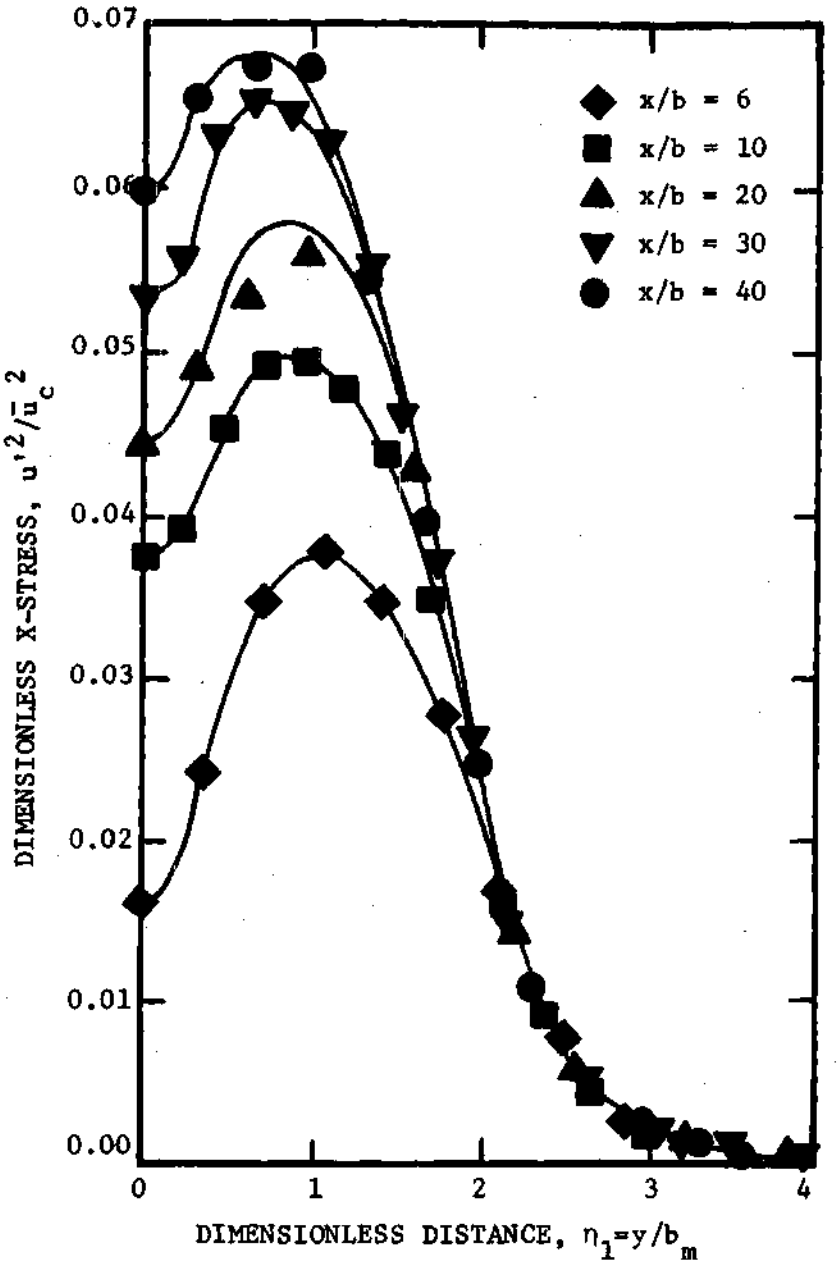

Figure 11. Turbulent X-Stress Profiles for the Fully Turbulent Region from Reference [8]

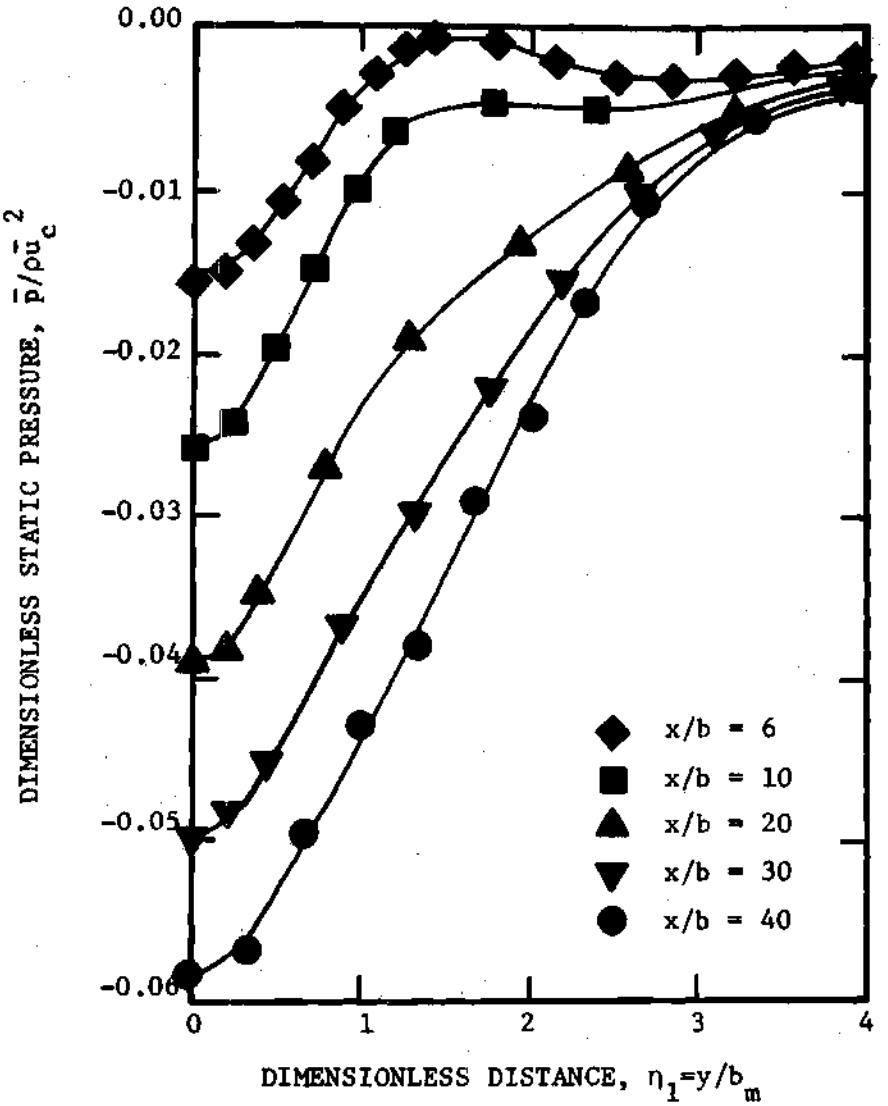

Figure 12. Static Pressure Profiles for the Fully Turbulent Region from Reference [8]

of similarity; see Figures 11 and 12. Although the time-average velocity profile has obtained similarity in approximately seven nozzle widths, the fluctuating velocity field is still developing at 40 nozzle widths downstream. It would appear, however, that similarity is being approached.

The preceding data indicate a negative static pressure field exists throughout the turbulent region in the two-dimensional free jet. The close correspondence between static pressure deficiency and turbulent x-stress component suggests that the static pressure deficiency is a manifestation of the presence of turbulence.

The magnitude of this negative static pressure distribution is of the same order of magnitude, but opposite in sign to the turbulent fluctuations in the x-direction. Thus, the neglecting of the terms $-\frac{\partial \bar{p}}{\partial x}$ and $-\rho \frac{\partial \overline{u'^2}}{\partial x}$ in expression (32) is justified. The magnitude of the pressure forces in the plane turbulent jet are small in comparison to the x-component of momentum, and thus the common assumption of conservation of momentum in that direction is justified.

Turbulent Compressible Plane Jet

For the turbulent flow of a compressible fluid, the effect of variation of density upon the fluctuating and time-average flow properties cannot be neglected. Thus for high speed flows a description of a plane jet becomes much more difficult. In the study of turbulent compressible plane jets, besides the correlation of velocity components, we must also consider the correlation of velocity and density and pressure and velocity. Since there is not a statistical theory of the

turbulent shear flow of an incompressible fluid yet, the knowledge of the turbulent flow of a compressible fluid is that much more meager. However, with some plausible assumptions, it is possible to extend some of the semi-empirical theories of turbulent flow of an incompressible fluid to the case of a compressible fluid. At least for engineering purposes the effect of compressibility on the mean velocity distribution can be determined [10].

Formulation of Equations of Motion for the Compressible Flow of a Turbulent Plane Jet. A prerequisite to a review of the plane compressible turbulent jet is a discussion of the equations of motion describing the flow field. As in the previous case of turbulent incompressible flow, the starting point of the mathematical description will be the Navier-Stokes equations. The momentum equation in the x-direction and the continuity equation for the case of a plane compressible steady flow neglecting the effects of viscosity, body forces and pressure variations is

$$\rho u \frac{\partial u}{\partial x} + \rho v \frac{\partial u}{\partial y} = 0 \tag{47}$$

$$\frac{\partial \rho u}{\partial x} + \frac{\partial \rho v}{\partial y} = 0$$

If the flow properties are separated into their mean and fluctuating components, then the dependent variables in the preceding expression become

$$\rho = \rho' + \bar{\rho} \quad ; \quad u = u' + \bar{u} \quad ; \quad v = v' + \bar{v} \tag{48}$$

The equations of motion describing the time-average quantities $\bar{u}$, $\bar{v}$ and $\bar{\rho}$ can be determined by inserting expression (48) into expression (47) and averaging term by term. The resulting equation for the x-component of momentum is

$$\overline{\rho'u'\frac{\partial u'}{\partial x}} + \overline{\rho'u'}\frac{\partial \bar{u}}{\partial x} + \bar{u}\overline{\rho'\frac{\partial u'}{\partial x}} + \bar{\rho}\overline{u'\frac{\partial u'}{\partial x}} + \bar{\rho}\bar{u}\frac{\partial \bar{u}}{\partial x} \tag{49}$$

$$+ \overline{\rho'v'\frac{\partial u'}{\partial y}} + \overline{\rho'v'}\frac{\partial \bar{u}}{\partial y} + \bar{v}\overline{\rho'\frac{\partial u'}{\partial y}} + \bar{\rho}\overline{v'\frac{\partial u'}{\partial y}} + \bar{\rho}\bar{v}\frac{\partial \bar{u}}{\partial y} = 0$$

The expression for continuity is

$$\frac{\partial \bar{\rho}\bar{u}}{\partial x} + \frac{\partial \bar{\rho}\bar{v}}{\partial y} + \frac{\overline{\partial(\rho'u')}}{\partial x} + \frac{\overline{\partial(\rho'v')}}{\partial y} = 0 \tag{50}$$

By a comparison of the order of magnitude of the terms in expression (49), that equation may be reduced to

$$\bar{\rho}\bar{u}\frac{\partial \bar{u}}{\partial x} + \bar{\rho}\bar{v}\frac{\partial \bar{u}}{\partial y} + \overline{\rho'v'}\frac{\partial \bar{u}}{\partial y} + \bar{\rho}\overline{v'\frac{\partial u'}{\partial y}} = 0 \tag{51}$$

Equations (50) and (51) along with an energy equation and an equation of state make up a description of the flow field for a plane compressible turbulent jet. It should be pointed out that the solution to this set of equations is much more difficult than in the turbulent incompressible case. This added complexity stems from the correlations between velocity components as well as density and velocity contained in these equations.

For the incompressible flow case a phenomenological theory was used to describe the correlation between the fluctuating components of velocity, and thus the equations of motion were reduced to a solvable

form. In the present situation an additional semi-empirical relationship for density must be employed.

If Taylor's modified vorticity transport theory is employed to describe the fluctuating velocity component in the x-direction, then we may write

$$\frac{\partial u'}{\partial y} = \Delta\omega = \ell_1 \frac{\partial}{\partial y}\left(\frac{\partial \bar{u}}{\partial y}\right) \tag{52}$$

The preceding result is identical to that for Prandtl's first mixing length hypothesis if the mixing length is considered constant.

Density fluctuations may be assumed to be analogous to velocity fluctuations. Thus, the fluctuating component of density is defined in terms of the steady component of density as

$$\rho' = \ell_\rho \frac{\partial \bar{\rho}}{\partial y} \tag{53}$$

where ℓ_ρ in the previous expression is the density mixing length. Inserting relations (52) and (53) into equation (51) and simplifying, results in

$$\bar{\rho}\bar{u} \frac{\partial \bar{u}}{\partial x} + \bar{\rho}\bar{v} \frac{\partial \bar{u}}{\partial y} = \epsilon \left[\frac{\partial}{\partial y}\left(\bar{\rho} \frac{\partial \bar{u}}{\partial y}\right) + (E_1 - 1) \frac{\partial \bar{\rho}}{\partial y} \frac{\partial \bar{u}}{\partial y}\right] \tag{54}$$

E_1 in the previous equation is equal to the ratio of density mixing length to velocity mixing length. The virtual kinematic viscosity, ϵ, is given by $\epsilon = -\overline{\ell_1 v'}$.

In ordinary analysis it may be assumed that $E_1 = 1$, but for hypersonic flow E_1 should be assigned a value larger than unity.

Inserting $E_1 = 1$ into (54), gives

$$\bar{\rho}\bar{u}\frac{\partial \bar{u}}{\partial x} + \bar{\rho}\bar{v}\frac{\partial \bar{u}}{\partial y} = \varepsilon \frac{\partial}{\partial y}\left(\bar{\rho}\frac{\partial \bar{u}}{\partial y}\right) \tag{55}$$

Equation (55) represents the starting point of the analysis of the turbulent compressible plane jet for moderate speeds [11].

Analytical Solutions of the Compressible Flow of a Plane Turbulent Jet by Abramovich. Abramovich [12] used Prandtl's assumption that the mixing length across each section of the jet is constant and reduced equation (55) to

$$\bar{\rho}\bar{u}\frac{\partial \bar{u}}{\partial x} + \bar{\rho}\bar{v}\frac{\partial \bar{u}}{\partial y} = 2c_1^2 x^2 \frac{\partial \bar{u}}{\partial y}\frac{\partial}{\partial y}\left(\bar{\rho}\frac{\partial \bar{u}}{\partial y}\right) \tag{56}$$

It was also assumed that the velocity, temperature and density profiles in the jet mixing region are similar, thus

$$\bar{u} = u_0 f(\eta_1) \quad ; \quad \bar{T} = T_0 \theta_1(\eta_1) \quad ; \quad \bar{\rho} = \rho_0 K(\eta_1) \tag{57}$$

$\bar{T}$ in the previous expression is mean temperature and f, θ_1 and K are functions of η_1 only. The profile similarity parameter is given by $\eta_1 = y/\alpha_1 x$. The subscript 0 in (57) refers to some reference state. Introducing the stream function

$$\psi = \alpha_1 x \rho_0 u_0 F(\eta_1) \tag{58}$$

which satisfies the continuity equation when $\overline{\rho' u'}$ and $\overline{\rho' v'}$ are neglected in comparison to $\bar{\rho}\,\bar{u}$ and $\bar{\rho}\,\bar{v}$, respectively, Abramovich obtained the differential equation

$$F''' = - F + \frac{\partial}{\partial \eta_1} \left(\frac{K'}{K} F'\right) \tag{59}$$

For the case of high subsonic flow of an ideal gas, Abramovich assumed that for the unheated jet (the condition where the jet's stagnation temperature is equal to the temperature of the surrounding fluid) no heat transfer existed between the fluid in the jet and the surrounding medium. The heat content of the fluid in the jet is uniquely associated with the flow velocities, thus

$$C_p(\bar{T}-T_0) = J_m/2g \ (u_0^2-\bar{u}^2) \tag{60}$$

In (60) J_m is the heat equivalent of mechanical work. For the assumption of constant pressure in the jet the density function becomes

$$K = \frac{\bar{\rho}}{\rho_0} = \frac{T_0}{\bar{T}} = \frac{1}{1 + \frac{k-1}{2} M_0^2 \left[1 - \left(\frac{\bar{u}}{u_0}\right)^2\right]} \tag{61}$$

Inserting equation (61) into (59) and integrating numerically results in the final solution to this problem. Adam's method was used by Abramovich.

Abramovich found that the effect of compressibility upon the properties of jet mixing due to high speed up to $M_0 = 1$ is negligible. The qualitative results of this solution indicate with an increase of velocity the non-dimensional values of the frictional stresses decrease, the width of the mixing zone decreases and the velocity field is slightly deformed.

Experimental Studies of the Compressible Flow of a Plane Turbulent Jet. Olson and Miller [13] made an investigation of high Reynolds number compressible plane jets. In their study measurements were made of the time-average velocity profiles at a number of downstream stations for both subsonic and supersonic flow cases. Only the results from the subsonic regime will be considered in this review. It is appropriate to indicate that the measurements of the steady state velocity field made by these authors could not indicate the existence of turbulence. However, because of the high Reynolds number of this flow study (approximately 120,000 based on nozzle width), it would be assumed that the turbulent mechanism controls the jet diffusion process.

Experimental velocity profiles in the x-direction for the mixing region were found to fit a Gaussian distribution, as was the case for the turbulent incompressible jet by Albertson [9]. Using this distribution for the mixing region and assuming the jet's momentum in the direction of flow is conserved, the authors formulated a semi-empirical correlation of their data. A short summary of their data correlation will follow.

Considering the differential control volume shown in Figure 13 which lies between the jet centerline and the location where the velocity is equal to one-half of the centerline velocity, the change of momentum in the x-direction can be expressed as

$$\frac{d}{dx}\left[\rho_0 u_0^2 h_i + \int_0^{\xi^*} \rho u^2 d\xi\right] = \left[u^* \frac{d}{dx}\left(\rho_0 u_0 h_i + \int_0^{\xi^*} \rho u d\xi\right)\right] + \tau^* \qquad (62)$$

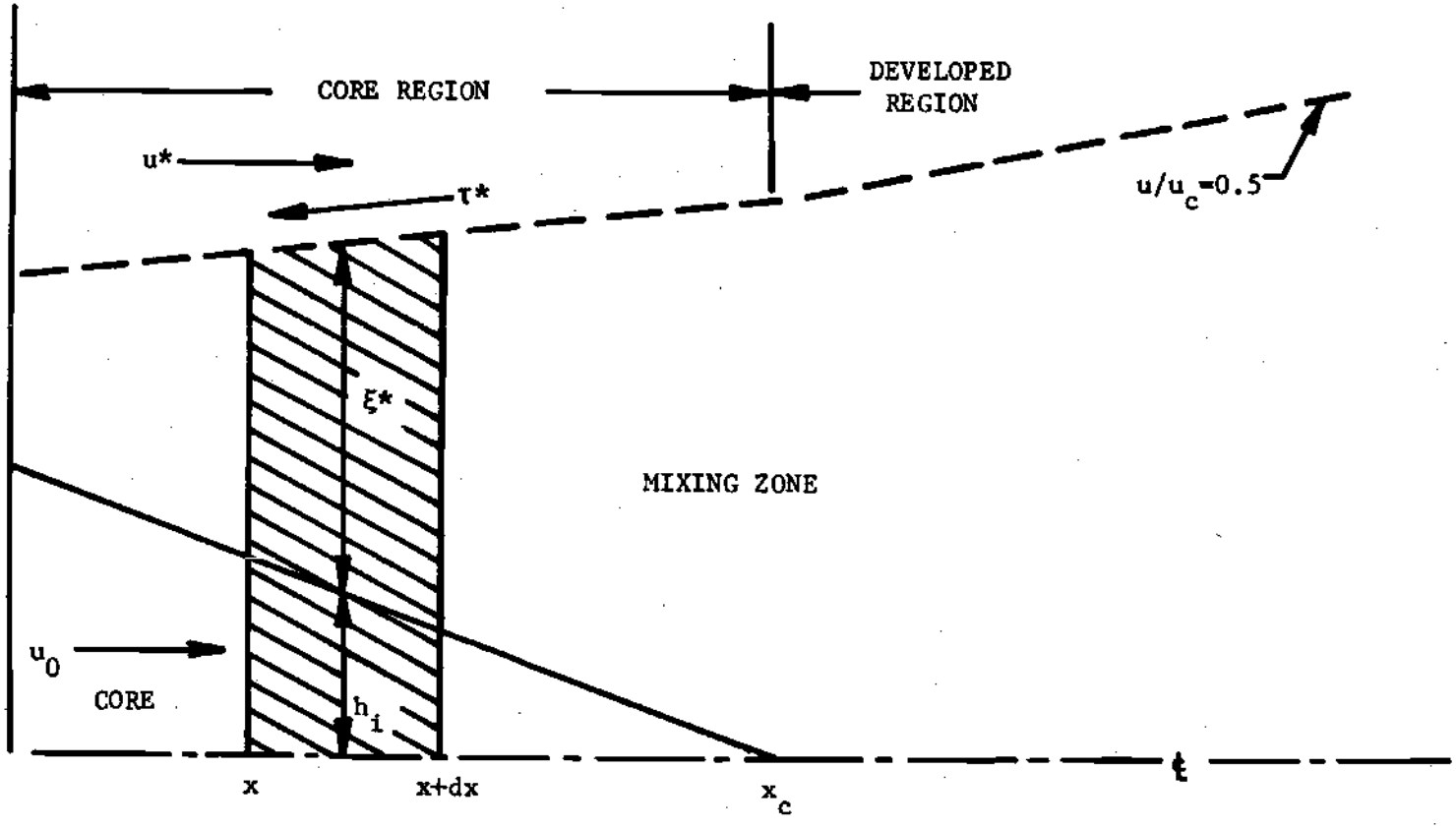

Figure 13. Sketch of Differential Control Volume for Free Jet Model of Olson and Miller [13]

It should be noted that the variables in (62) represent the time-average components. The preceding expression can be derived from (55) if the fluctuating components of the continuity equation $\overline{\rho' u'}$ and $\overline{\rho' v'}$ are neglected in comparison to $\bar{\rho}\,\bar{u}$ and $\bar{\rho}\,\bar{v}$, respectively.

The authors assumed Prandtl's second mixing length hypothesis of equation (20) to describe the shear stress. That is, the virtual kinematic viscosity is constant across the mixing zone. The shear stress in (62) based on this assumption can be expressed as

$$\tau^* = \rho^* \varepsilon \left.\frac{du}{dy}\right|_{\xi=\xi^*} = 0.5\, K_s \rho^* \xi^* u_c \left.\frac{du}{dy}\right|_{\xi=\xi^*} \tag{63}$$

K_s is a constant referred to as the shear stress constant and u_c is the jet centerline velocity. Substituting (63) into (62) and nondimensionalizing, yields

$$\frac{d}{dx}\left[\xi^* \int_0^1 \frac{\rho u^2}{\rho_0 u_0^2}\, d\left(\frac{\xi}{\xi^*}\right)\right] - 0.5\, U \frac{d}{dx}\left[\xi^* \int_0^1 \frac{\rho u}{\rho_0 u_0}\, d\left(\frac{\xi}{\xi^*}\right)\right] \tag{64}$$

$$+ \frac{dh_1}{dx}(1-0.5\, U) = \frac{\rho^* K_s \xi^*}{2\rho_c u_c}\left(\left.\frac{du}{dy}\right|_{\xi=\xi^*}\right)\frac{\rho_c}{\rho_0} U^2$$

where $U = u_c/u_0$.

Assuming the velocity profiles in the mixing zone to have a Gaussian distribution, then the velocity distribution is

$$u/u_c = e^{-B_1(\xi/\xi^*)^2} \tag{65}$$

$$B_1 = 0.6931 \quad \text{for} \quad u/u_c = 0.5 \quad \text{at} \quad \xi/\xi^* = 1$$

From the ideal gas equation of state, assuming isobaric conditions with no heat transfer between the jet and the surrounding fluid, the density ratio becomes

$$\frac{\rho}{\rho_0} = \left\{1 + \frac{k-1}{2} M_0^2 \left[1 - \left(\frac{u}{u_0}\right)^2\right]\right\}^{-1} \tag{66}$$

Evaluating the shear stress for the velocity distribution in expression (65) and inserting the expression for density in (66), reduces equation (64) to

$$\frac{d\left[\frac{\xi^*}{b} f_1(U)\right]}{d(x/b)} - 0.5\ U \frac{d\left[\frac{\xi^*}{b} f_2(U)\right]}{d(x/b)} + \frac{dh_i}{dx}(1-0.5\ U) = -K_s f_3(U) \tag{67}$$

The conservation of x-momentum expression for the control volume is

$$\rho_0 u_0^2 h_i + \xi^* \int_0^\infty \rho u^2\, d\left(\frac{\xi}{\xi^*}\right) = \rho_0 u_0^2 h_0 \tag{68}$$

Dividing by $\rho_0 u_0^2$ and normalizing with respect to b, the nozzle width, simplifies (68) to

$$\frac{\xi^*}{b} = \frac{1 - h_i/h_0}{2 f_4(U)} \tag{69}$$

The function $f_4(U)$ in the preceding expression is only dependent on initial jet Mach number M_0. For the core region, $f_1(U)$, $f_2(U)$ and $f_3(U)$ found in expression (67) are also only dependent on initial jet Mach number. Differentiating (ξ^*/b) in expression (69) and inserting

into (67) and integrating that equation, yields

$$\frac{h_i}{h_0} = 1 - \frac{x/b}{x_c/b} \tag{70}$$

The preceding expression is valid only if the shear stress constant K_s does not vary with x. It also assumes no initial boundary layers at the exit plane of the jet's nozzle. Substituting equation (70) into (69), gives

$$\xi^*/b = \frac{\frac{x}{b} \Big/ \frac{x_c}{b}}{2f_4(U)} \tag{71}$$

Substituting (71) into (67) and rearranging, yields

$$\frac{x_c}{b} = \frac{C_2}{K_s} \tag{72}$$

where C_2 is a function of $f_1(U)$, $f_2(U)$, $f_3(U)$ and $f_4(U)$.

In summary for the core region of flow, if the value of the shear stress constant K_s is known then the nondimensional core length (x_c/b) may be calculated from expression (72). The nondimensional distance to the point where $u = 0.5u_c$ and the core width may then be calculated for any downstream station from expressions (71) and (70), respectively. The velocity field in the core is thus defined with the addition of the assumed velocity profile in expression (65).

For the developed region, equation (67) must be solved numerically in the following manner. Equation (69) if $h_1 = 0$ becomes

$$\frac{\xi^*}{b} = \frac{1}{2f_4(U)} \tag{73}$$

Substituting (73) into equation (67) where again $h_i = 0$, yields

$$\frac{d\,[g_1(U)]}{d(x/b)} - 0.5\ U\ \frac{d\,[g_2(U)]}{d(x/b)} = -K_s f_3(U) \tag{74}$$

Expression (74) may be rewritten as

$$\left\{\frac{d\,[g_1(U)]}{dU} - 0.5\ U\ \frac{d\,[g_2(U)]}{dU}\right\} \frac{dU}{d(\frac{x}{b})} = -K_s f_3(U) \tag{75}$$

The previous expression can be simplified by defining

$$F(U) = \frac{g_1'(U) - 0.5\ U\ g_2'(U)}{f_3(U)} \tag{76}$$

The derivatives $g_1'(U)$ and $g_2'(U)$ can be determined graphically. Equation (75) thus becomes

$$F(U)\ dU = -K_s d(x/b) \tag{77}$$

The previous equation may be integrated from the end of the core to any arbitrary downstream position. If the shear stress constant K_s is assumed to be a nonvarying in the developed region, then this integration yields

$$\int_1^U F(U)\ dU = -K_s \left[\frac{x}{b} - \frac{x_c}{b}\right] \tag{78}$$

where $\int_1^U F(U)\ dU$ can be determined numerically.

In summary for the developed region of flow, if the value of the shear stress constant K_s is known then the distance from the core to some arbitrary point U may be evaluated from (78). In this manner the jet's centerline velocity can be determined as a function of downstream distance. The function $f_4(U)$ can be calculated at each downstream station and then (ξ^*/b) may be calculated from (73). The velocity field in the developed region is thus defined with the addition of the assumed velocity profile in expression (65).

Pertinent experimental results taken from the research of Olson and Miller are shown in Figures 14 through 16. Depicted in Figure 14 is centerline velocity decay data as a function of nondimensional downstream distance for two compressible flow cases; also plotted on this graph is similar data for the incompressible case by Miller and Comings [8]. A check of these data in the fully developed regime indicates in each case the centerline velocity decays fit the -1/2 power law profile predicted by turbulent incompressible flow theory. The only marked difference between the centerline decay data from References [13] and [8] appears to be a slightly longer core region for the flow cases from Olson's investigation. This effect may be the result, however, of the higher Reynolds number flow conditions in the compressible jet study, since Olson's investigation demonstrated core length decreased with increasing Mach number.

The spread of the free jet mixing zone in the downstream direction for a compressible and incompressible flow case is shown in Figure 15. The distance from the jet centerline to the location where

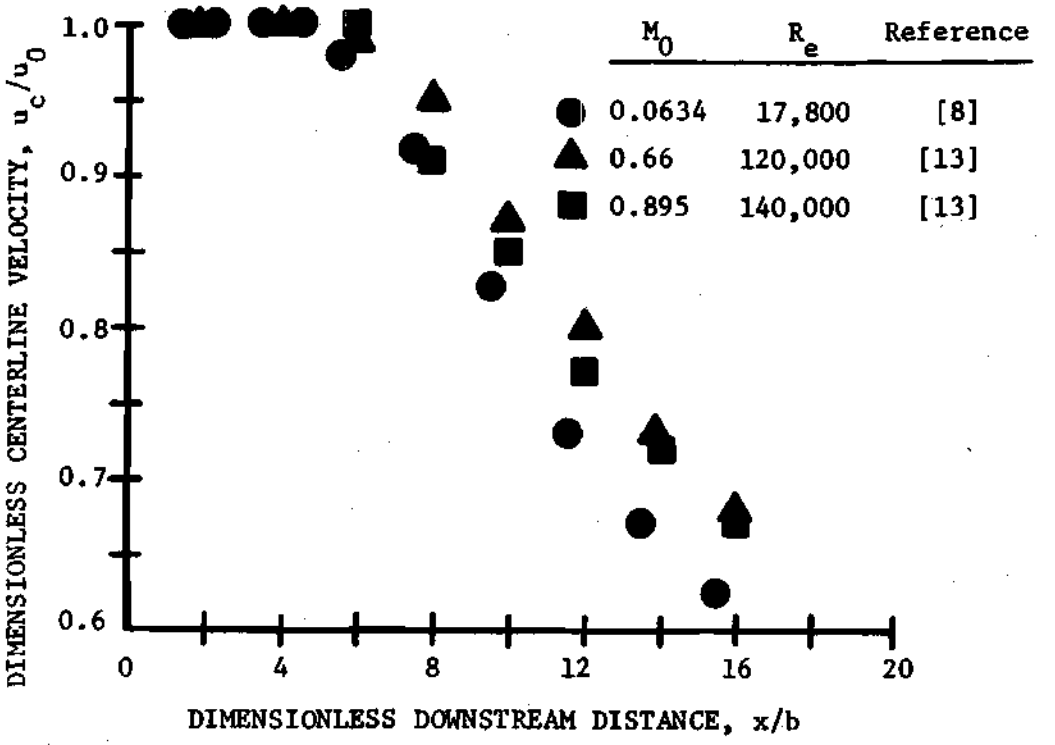

Figure 14. Comparison of Centerline Velocity Decay for a Compressible and Incompressible Turbulent Jet

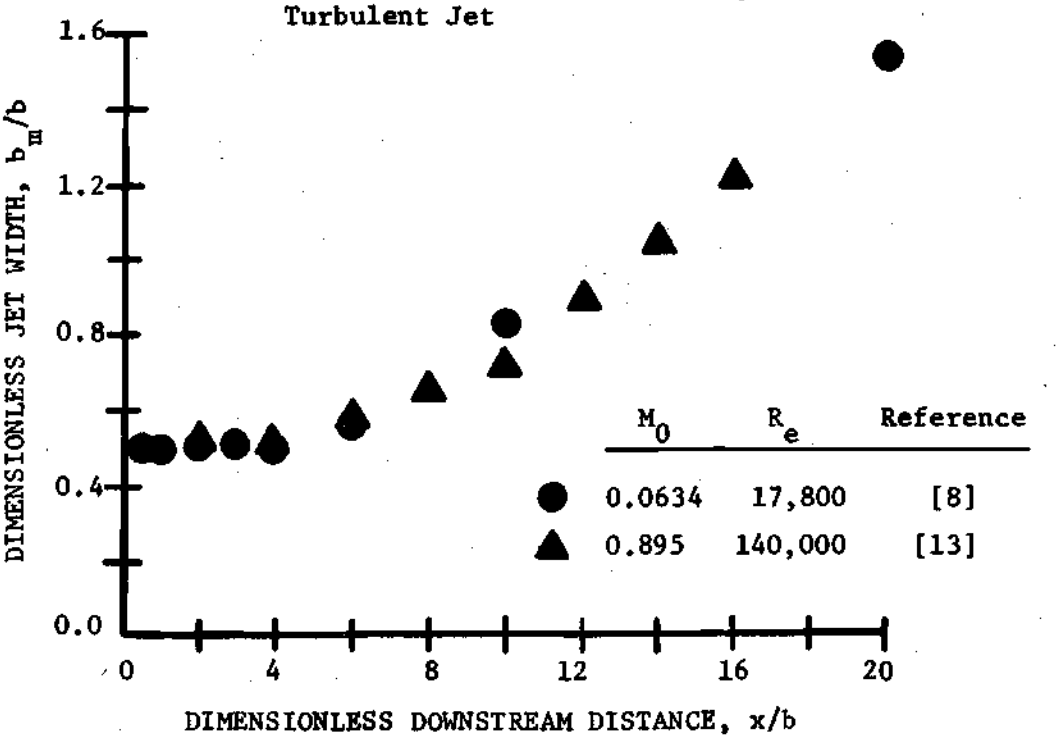

Figure 15. Comparison of Jet Spread Rate for a Compressible and Incompressible Turbulent Jet

$u/u_c = 0.67$ is defined as b_m. For the incompressible flow case this data was taken from the research of Miller and Comings; see Figure 7. The data for the compressible case were obtained from Figure 16. These data indicate essentially the same spreading rates for the compressible and incompressible free jet. In both cases the spreading rate is proportional to downstream distance in the fully developed regime.

Folded free jet velocity profiles, which were obtained by Olson and Miller at a jet Reynolds number of 140,000 based on nozzle width and a Mach number of 0.895, are shown in Figure 16. The curves drawn through these data represent the Gaussian velocity distribution computed via the previously described correlation. In order to produce a better fit of their correlation to experimental data, the authors found it necessary to define a different shear stress constant K_s for the core and developed regime. As may be seen from the data, their correlation is in fair agreement in these regimes. However, for the transition region between the two the fit is poorer. Thus, it would appear that the shear stress constant K_s should vary with downstream distance at least in the transition regime in order to provide the best fit to the experimental data.

The experimental results of Olson and Miller verify the analytical predictions of Abramovich, that is the effect of compressibility on free jet mixing up to $M_0 = 1$ tend to be negligible. It would also appear that Olson and Miller's correlation technique for the subsonic jet is somewhat complicated. If the free jet momentum is conserved,

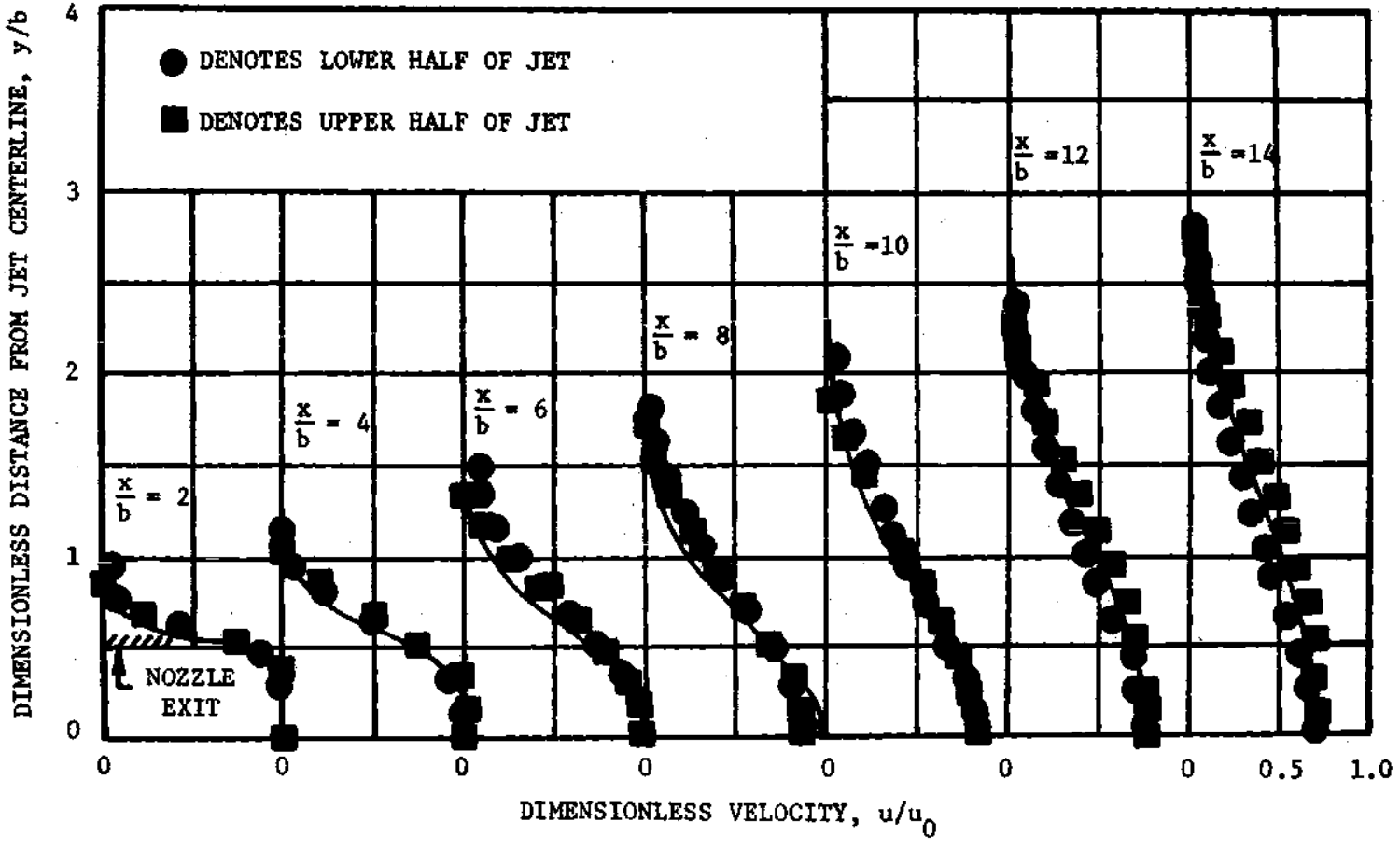

Figure 16. Mean Velocity Profiles for the Compressible Turbulent Flow of a Plane Jet from Reference [13]

the flow is isonenergetic and the velocity profile in the mixing region is Gaussian; the only quantities required to define the velocity field in the x-direction are the core length and centerline velocity decay. Their data has indicated the centerline velocity decay fits the - 1/2 power law profile for the fully developed region. The core length for a wide range of turbulent flow conditions is essentially constant. Thus, the dependence on the shear stress constant K_s is not required to describe the flow field.

Laminar Incompressible Plane Jet

In the flow of a plane jet, it is well known that at least near the nozzle exit plane the flow is laminar or streamline. It is also known that for relatively low Reynolds numbers this laminar structure may persist for some distance downstream of the nozzle. Experimental evidence suggests that the structure of a laminar jet is essentially unstable and thus the laminar mixing zone must always transcend to turbulence. In this section of the literature review the completely laminar incompressible jet will be reviewed. The transition from laminar to turbulent flow will be considered in a later section.

Analytical Solution for Laminar Incompressible Flow in a Free Jet Boundary. A sketch of a free jet boundary may be found in Figure 2. In this flow situation two parallel streams of respective velocities U_1 and U_2 meet at the edge of a nozzle. The velocity discontinuity between the streams produces a mixing zone which spreads downstream of the nozzle. It is often assumed that this problem represents a half jet in the core region.

A summary of the solution to this problem according to Pai [14] follows. It will be assumed that no initial boundary layers exist at the nozzle exit plane.

The appropriate differential equations describing the free jet boundary may be derived from the Navier-Stokes equations; expression (4). The equation of x-momentum for a steady plane flow neglecting body forces and assuming no pressure variations in the mixing zone is

$$u \frac{\partial u}{\partial x} + v \frac{\partial u}{\partial y} = \nu \left(\frac{\partial^2 u}{\partial x^2} + \frac{\partial^2 u}{\partial y^2} \right) \tag{79}$$

For the jet mixing zone the boundary layer assumptions may be applied, that is $u >> v$ and $\frac{\partial}{\partial y} >> \frac{\partial}{\partial x}$. Thus equation (79) reduces to

$$u \frac{\partial u}{\partial x} + v \frac{\partial u}{\partial y} = \nu \frac{\partial^2 u}{\partial y^2} \tag{80}$$

The continuity equation for this case from (4) is

$$\frac{\partial u}{\partial x} + \frac{\partial v}{\partial y} = 0 \tag{81}$$

Equations (80) and (81) are the appropriate differential equations describing plane laminar incompressible jet mixing. It should be noted that these equations are identical to those for turbulent incompressible flow if the kinematic viscosity, ν, is replaced by the virtual kinematic viscosity of turbulent motion, ε; see expression (34). The present set of equations for the laminar case are solved in a fashion identical to those for the turbulent case. The solution for the distribution of the x-component of velocity is

$$u = \frac{U_1 + U_2}{2}\left[1 + \frac{U_1 - U_2}{U_1 + U_2}\,\mathrm{erf}\,(\xi)\right] \tag{82}$$

$$\xi = \sqrt{U/\nu x}\;\frac{y}{2}$$

$$U = \frac{U_1 + U_2}{2}$$

It is apparent that the velocity distribution expressions in the laminar and turbulent case are identical, however, the respective profile similarity parameters are different. The spread of the mixing zone in a laminar jet boundary is proportional to the $\sqrt{x}$, while for the turbulent case it is proportional to x.

Analytical Solution for Laminar Incompressible Flow in a Fully Developed Free Jet. A sketch of a fully developed free jet flow may be found in Figure 3. In this flow situation the plane jet has traversed a sufficient distance downstream of the nozzle for the velocity profiles within the mixing zone to become similar. In this regime of velocity profile similarity the flow is referred to as fully developed.

Schlichting [15] and later Bickley [16] determined the solution to this problem. They assumed the slot from which the jet issued was infinitely narrow and the jet momentum was finite. If the flow field is assumed to be plane and steady with no variation in pressure, the differential equations describing the developed jet are equations (80) and (81). The appropriate boundary conditions are

$$v = 0 \;;\; \frac{\partial u}{\partial y} = 0 \qquad \text{at} \quad y = 0 \tag{83}$$

$$u = 0 \qquad \text{at} \quad y = \infty$$

It again should be noted that the equations describing the fully developed laminar incompressible jet are identical to those for the turbulent case if the kinematic viscosity, ν, is replaced by the virtual kinematic viscosity of turbulent motion, ε; see expression (43). The present set of equations for the laminar case are solved in an identical manner to those for the turbulent case. The solution for the velocity distribution in the jet is

$$u = 0.4543 \, (J_\infty^2/\rho^2 \nu x)^{1/3} \, \text{sech}^2 \, (\eta_1) \tag{84}$$

$$v = 0.5503 \, (J_\infty \nu/\rho x^2)^{1/3} \, [2\eta_1 \, \text{sech}^2 \, (\eta_1) - \tanh \, (\eta_1)]$$

$$\eta_1 = 0.2752 \, (J_\infty/\rho\nu^2)^{1/3} \, (y/x^{2/3})$$

J_∞ in the previous expression is the free jet momentum per unit height. A comparison of the results for the fully developed laminar jet found in expression (84) and the fully developed turbulent case found in expression (45), shows the solution to be of identical form. The respective profile similarity parameters and centerline velocity decay parameters, however, are different. The spread of the mixing zone for the laminar fully developed jet is proportional to $x^{2/3}$ while for the turbulent case it is proportional to x. The centerline velocity decay for the laminar case is proportional to $x^{-1/3}$ while for the turbulent situation is proportional to $x^{-1/2}$.

Experimental Studies of the Laminar Incompressible Flow of a Plane Jet. Andrade [17] made an experimental investigation of a plane water jet issuing into the same fluid medium at rest. He obtained

velocity profiles by a photographic technique for several stations in the flow field for a Reynolds number range based on nozzle width of approximately 10 to 30. The nearest station at which he obtained data was some 44 nozzle widths downstream, while the farthest station was approximately 177 nozzle widths downstream. Andrade found that his experimental data were in agreement with theoretical predictions of equation (84) if a virtual origin behind the nozzle exit plane was assumed for the jet. This assumption eliminates the difficulty associated with the theoretical jet issuing from an infinitely thin channel. It would be expected, however, that the theoretical result would be in appreciable error near the nozzle exit. Unfortunately, no data are presented for locations near the nozzle exit plane. The non-dimensional distance behind the nozzle as a function of Reynolds number proposed by Andrade for the virtual origin of flow is

$$x/b = 0.65\ R_e \tag{85}$$

Chanaud and Powell [18] made an experimental investigation of the laminar incompressible flow of a jet of air issuing into the same medium at rest. Their experimental apparatus allowed air to pass through a parallel sided nozzle 7.5 centimeters long, of rectangular cross section one millimeter by 30 centimeters. This nozzle length was sufficient to ensure a parabolic exit velocity profile. Velocity profiles in the jet were obtained via a hot wire anemometer for a Reynolds number range of $15 \leq R_e \leq 240$. These Reynolds numbers were computed based on nozzle mass flow rate and nozzle width.

A comparison of experimental data from the research of Chanaud to analytical predictions for the fully developed incompressible flow of a laminar jet are found in Figures 17 and 18. Shown in Figure 17 is x-component of velocity data for a flow of Reynolds number of 68 compared to the theoretical prediction of expression (84). For each downstream position the value of η_1, the profile similarity parameter, was chosen in order to give the best fit to the data. It is apparent that even near the slot exit the predicted hyperbolic secant profile is in agreement with data. The experimental velocity profile, however, would appear to be somewhat broader than the analytical prediction.

A comparison of centerline velocity decay data to analytical prediction is shown in Figure 18. These curves are compared on an equal exit-momentum basis since Bickley's solution was for a line source. As may be seen, the curves do not fit well but do have similar trends far downstream of the slot. The use of a virtual origin proposed by Andrade, that is expression (85), will not provide a better fit for the higher Reynolds number cases for locations near the nozzle.

Experimental evidence indicates Bickley's solution may be approached some distance downstream of the nozzle for the laminar jet. The transition region from the nozzle exit to fully developed laminar flow appears to increase in length with higher Reynolds numbers.

Laminar Compressible Plane Jet

For the high velocity flow of a laminar plane jet, the effects of variations of density, temperature and viscosity must be taken into account. The addition of these variables to the analysis of the flow

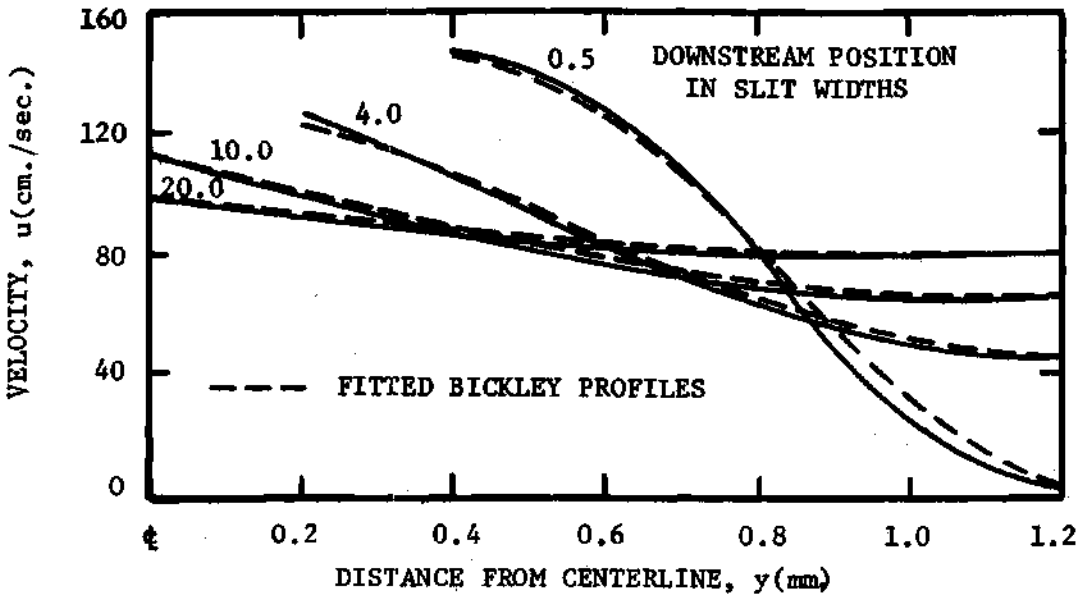

Figure 17. Velocity Profiles for a Laminar Incompressible Jet from Reference [18]

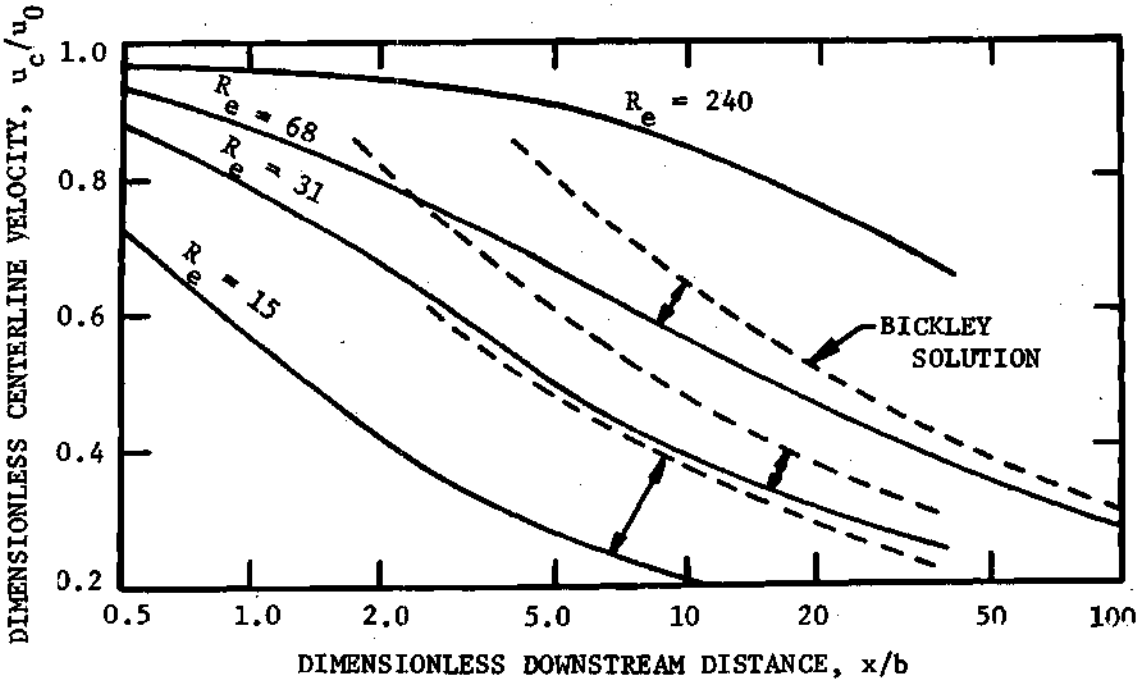

Figure 18. Centerline Velocity Decay for a Laminar Incompressible Jet from Reference [18]

field complicates the mathematical solution to the plane jet problem. This difficulty arises because an energy equation and an equation of state must be considered along with the expression for x-momentum and the continuity equation.

Analytical Solutions to the Two-Dimensional Laminar Jet Mixing of a Compressible Fluid. Chapman [19] analytically determined the velocity distribution resulting from laminar compressible mixing in a free jet boundary. In this flow situation a uniform stream emerging from a nozzle is allowed to mix with a region of fluid at rest; see Figure 2. A summary of this solution follows.

The analysis of this problem is based on the assumptions that the flow field is steady and two-dimensional. It may be further assumed that there is no variation of pressure in the mixing region and that the effect of body forces are negligible. The boundary layer assumptions may also be applied to the jet mixing zone, that is $u >> v$ and $\frac{\partial}{\partial y} >> \frac{\partial}{\partial x}$.

The differential equation describing the momentum in the x-direction obtained from the compressible form of the Navier-Stokes equation is

$$\rho u \frac{\partial u}{\partial x} + \rho v \frac{\partial u}{\partial y} = \frac{\partial}{\partial y} \left(\mu \frac{\partial u}{\partial y}\right) \tag{86}$$

The continuity equation for this case is

$$\frac{\partial(\rho u)}{\partial x} + \frac{\partial(\rho v)}{\partial y} = 0 \tag{87}$$

By employing the previous assumptions, the complete differential equation representing the balance of energy in viscous compressible flow reduces to

$$\rho u \frac{\partial (C_p T)}{\partial x} + \rho v \frac{\partial (C_p T)}{\partial y} = \frac{\partial}{\partial y} \left(K_t \frac{\partial T}{\partial y} \right) + \mu \left(\frac{\partial u}{\partial y} \right)^2 \tag{88}$$

For a given gas the variation of μ and C_p with temperature is known, hence, the foregoing system of three partial differential equations is completed by the equation of state for a region of constant pressure

$$T/T_\infty = \rho_\infty/\rho \tag{89}$$

The subscript ∞ in the previous expression represents conditions at the uniform stream's exit plane.

In order to solve the above set of equations, Chapman made the further assumptions

$$C_p = \text{const} \tag{90}$$

$$P_R = C_p \mu/K_t = 1$$

$$\mu/\mu_\infty = C_1 (T/T_\infty)^n$$

The second of these is often made in calculating boundary layer flows when only the velocity profile is desired. The difference between the mixing layer velocity distributions for $P_R = 1$ and $P_R = 0.73$ is assumed to be small.

The consequence of the assumption of $P_R = 1$ is that the temperature becomes only a function of velocity. The following relationship

between velocity and temperature satisfies both expressions (86) and (88):

$$T = A + Bu - (u^2/2C_p) \tag{91}$$

where A and B are constants determined by the boundary conditions. Since the temperature determines the density, expression (91) also provides a means for calculating the density as a function of the velocity.

In order to satisfy the continuity equation, Chapman introduced a stream function. The velocity components in terms of this stream function are

$$u = \frac{\rho_\infty}{\rho}\frac{\partial \psi}{\partial y} \quad ; \quad v = -\frac{\rho_\infty}{\rho}\frac{\partial \psi}{\partial x} \tag{92}$$

Since the requirements of conservation of energy are fulfilled by expression (91), and conservation of mass by (92), the only equation left to be solved is the momentum equation. By assuming the velocity profiles in the mixing region are similar, it is possible to reduce the momentum equation (86) to an ordinary non-linear differential equation. This equation may be converted to an integral equation and solved by the method of successive approximation.

The velocity distribution in the mixing region as a function of the profile similarity parameter is shown in Figure 19. These data were calculated for several free stream Mach numbers. The profile similarity parameter η_1 may be written as

$$y\sqrt{\frac{u_\infty}{\nu_\infty x}} = \frac{y}{x}\sqrt{\frac{u_\infty x}{\nu_\infty}} = \frac{y}{x}\sqrt{R_e} \tag{93}$$

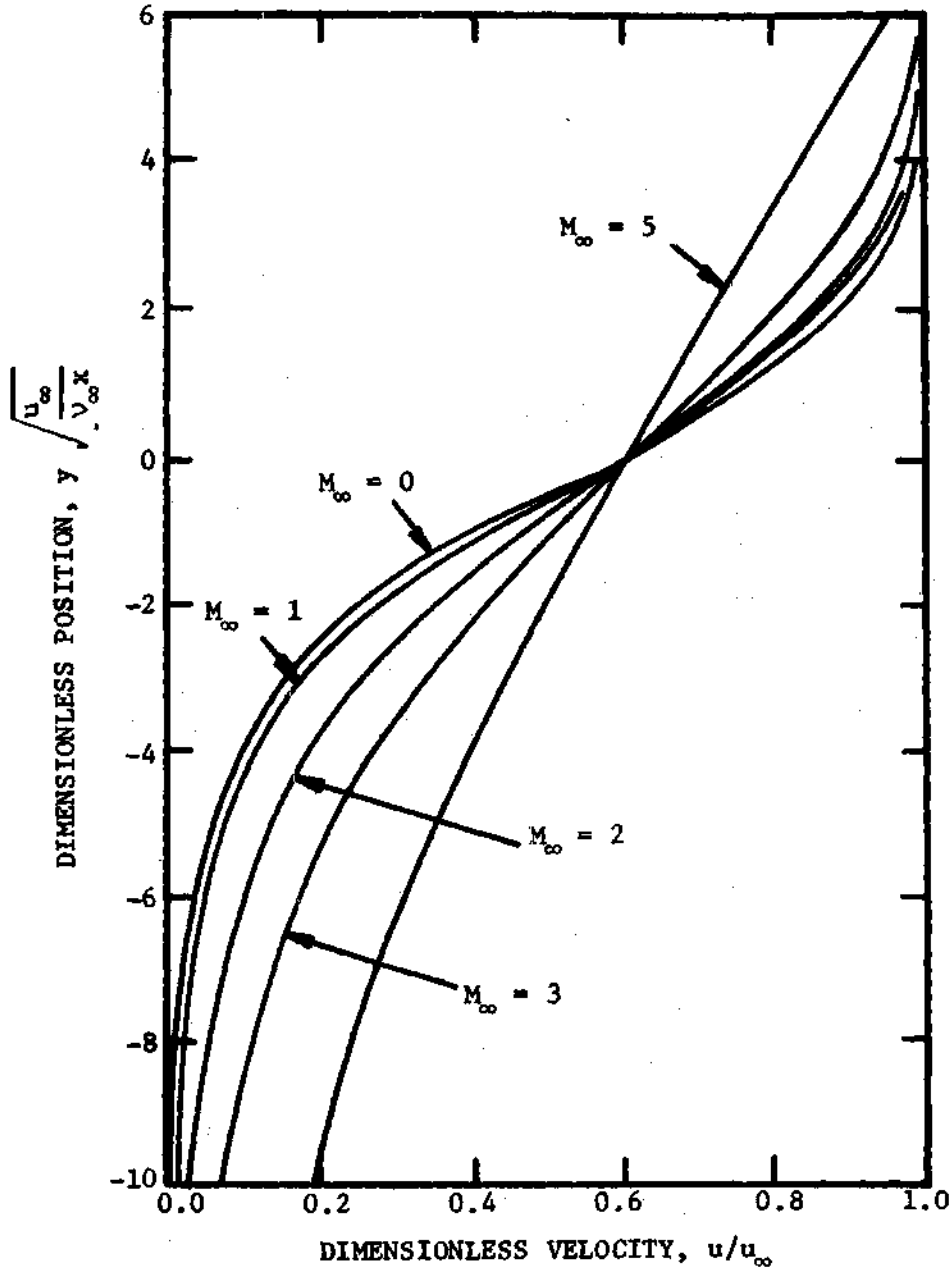

Figure 19. Velocity Distributions from the Mixing of a Uniform Stream of Compressible Fluid with Surrounding Fluid from Reference [19]

Thus at constant Reynolds number based on length, the information in Figure 19 indicates the mixing layer width grows with free stream Mach number. Chapman suggested that the rate of growth of the mixing layer with Mach number is approximately

$$\delta_M/\delta_{M=0} = 1 + 0.11\ M_\infty^2 \tag{94}$$

where δ_M in the previous expression represents the distance between the points where $u = 0.01\ u_\infty$ and $u = 0.99\ u_\infty$. It may be observed from Figure 19 that the effect of compressibility up to a Mach number of unity has a relatively minor influence on the velocity profile. This conclusion is in agreement with the predictions of Abramovich [12] for turbulent flow.

Pai [20] used a similar method to determine the velocity distribution for the laminar compressible mixing of a fully developed plane jet. His analysis concluded that the properties of jet mixing depended mainly on the momentum of the jet. Thus an increase in velocity which also tends to increase density would increase the jet momentum and, consequently, reduce the jet mixing zone width.

Studies of the Low Reynolds Number Flow of a Compressible Fluid Jet by Anderson. Anderson [21] made an experimental investigation of low Reynolds number compressible jet flows in connection with his thesis on jet wall attachment. A Reynolds number range of from approximately 11,000 to 200 based on nozzle width and maximum exit plane velocity was considered in this research. Studies were made of both subsonic and supersonic flows, however, only the results for the subsonic case will be reviewed.

The experimental jet flow was created by allowing air at a low total upstream pressure to expand through a fixed rectangular nozzle which was 0.2 inches wide with an aspect ratio of five. The nozzle exit was formed by two circular arcs 0.25 inches in radius. Downstream of the nozzle exit plane was a large rectangular chamber which was evacuated by a high volumetric displacement vacuum pump. The different flow conditions in this research were created by independently varying the jet's upstream total pressure and exhaust ambient pressure.

Measurements were made of the x-component of the steady state velocity in the jet via an impact pressure probe. The probe was 1/16 inch in outside diameter and was designed in order to yield accurate pressure measurements in low Reynolds number flows. It should be pointed out that the impact pressure measurements made by Anderson are incapable of indicating whether the flow is laminar or turbulent. However, it is anticipated based upon the studies of a turbulent incompressible jet by Miller and Comings [8] and laminar incompressible jets by Chanaud and Powell [18] that the range of Reynolds numbers considered in this research would border both high Reynolds number turbulent jet flows as well as low Reynolds number laminar jet flows.

Experimental results indicating the effect of Reynolds number and Mach number on the jet's centerline velocity decay and spread rate are shown in Figures 20 through 23. The jet width, b_m, in Figures 21 and 23 is defined as the distance from the jet's centerline to the point where the velocity is 67 percent of its centerline value. The information in these figures was computed from data found in Tables 10 through

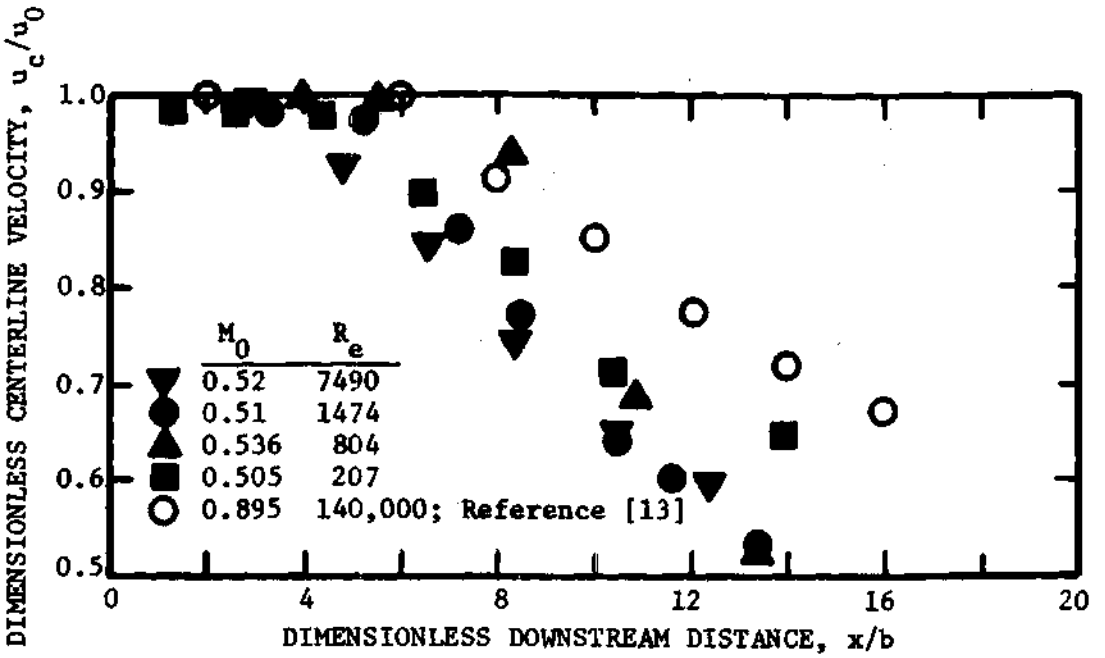

Figure 20. Centerline Velocity Decay for Low Reynolds Number Compressible Jets from Reference [21]

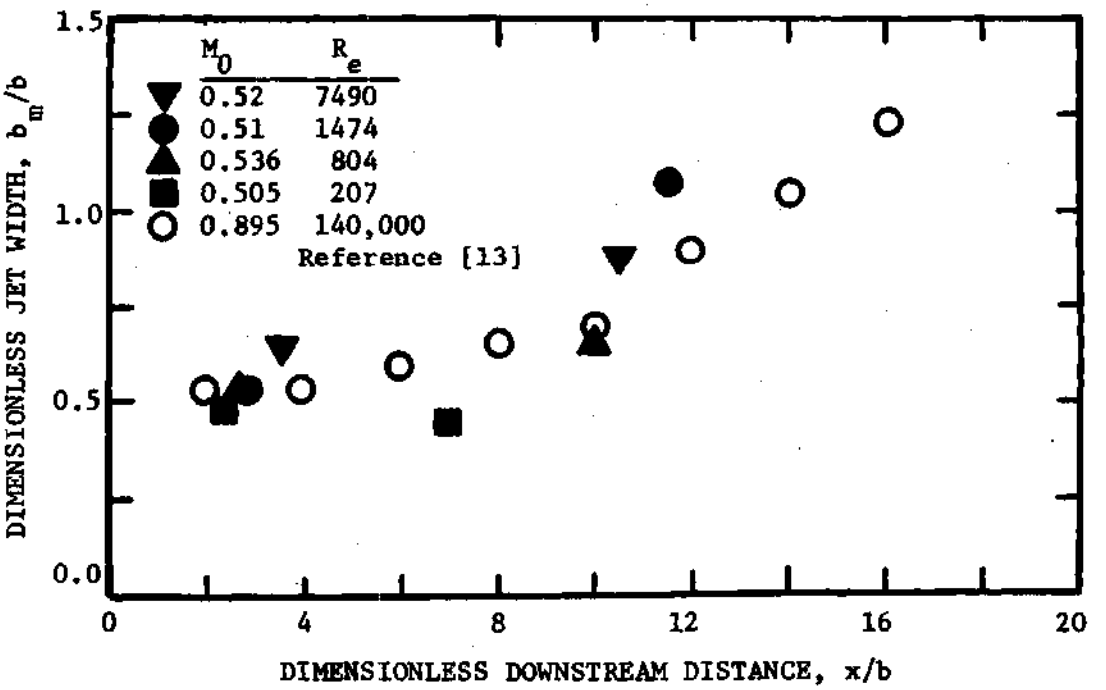

Figure 21. Jet Spread Rate for Low Reynolds Number Compressible Jets from Reference [21]

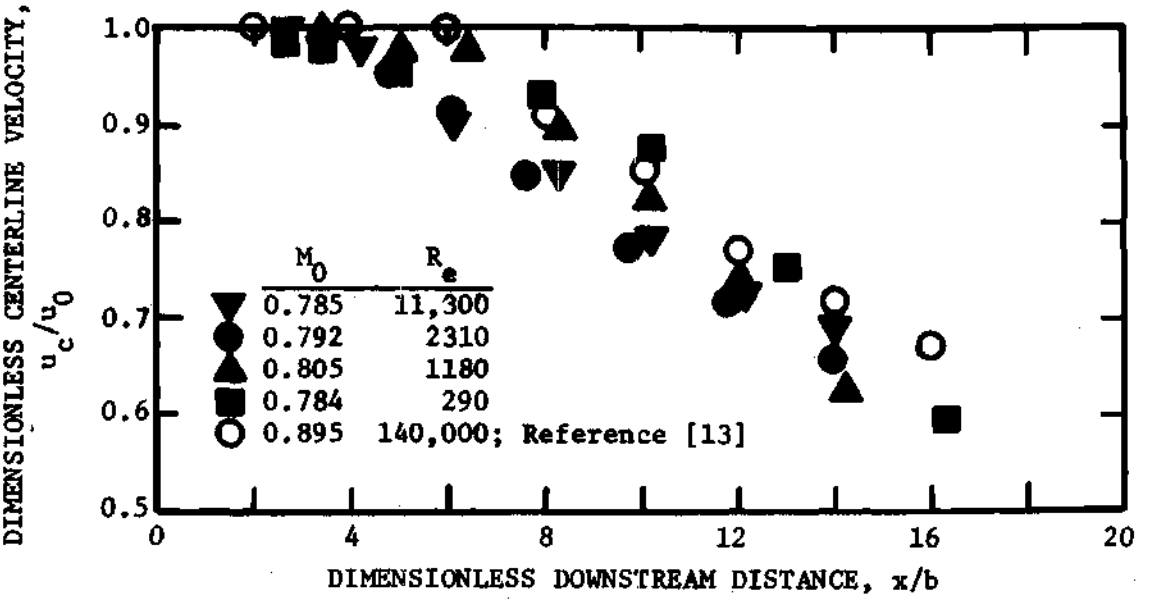

Figure 22. Centerline Velocity Decay for Low Reynolds Number Compressible Jets from Reference [21]

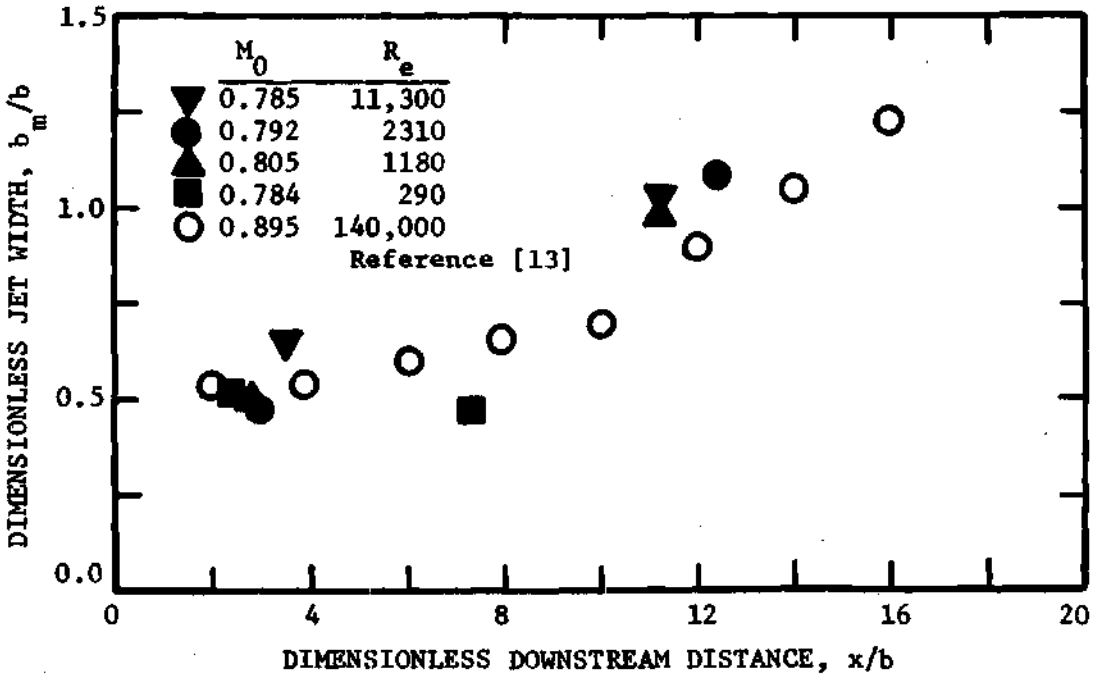

Figure 23. Jet Spread Rate for Low Reynolds Number Compressible Jets from Reference [21]

18 in Anderson's thesis. In Figures 20 and 21 the approximate Mach number of the jet at the centerline of its exit plane is 0.5, while in Figures 22 and 23 the Mach number is approximately 0.8. Also shown in these figures for comparison is similar data for a plane turbulent compressible jet from the studies of Olson and Miller [13]; see Figures 14 and 15.

The data in Figures 20 through 23 indicate several general trends as to the effect of variation of Reynolds number and Mach number on a free jet in this low Reynolds number compressible flow regime. Firstly, the data demonstrate that as the free jet's Reynolds number is decreased from its maximum value, the core length increases until some intermediate value of Reynolds number is attained. At this intermediate value of Reynolds number the core length reaches a maximum and further reductions of the Reynolds number then result in a reduction in core length. For very low values of Reynolds number it would appear that the jet's potential core is very short or non-existent. It would also appear that the effect of Mach number on core length is negligible. It is interesting to note that the core lengths measured by Anderson even at relatively high values of Reynolds number tend to be somewhat shorter than those reported by Olson or Albertson [9]. Experimental error associated with the relative sizes of the impact probe and the jet nozzle could explain this observation. Since the nozzle width was 0.2 inch and the probe diameter was 1/16 inch, it would be expected, based on the skewed profiles impacting the probe near the end of the core, that velocity measurements would indicate a shorter core length than actually existed.

Secondly, the centerline velocity decay rate of the jet would appear to be a function of both Mach number and Reynolds number. The experimental data demonstrate that as the Mach number increases the centerline velocity decay rate decreases. It is interesting to note that Olson's studies did not exhibit this characteristic for the case of the turbulent compressible flow of a plane jet. Anderson's results also demonstrate that as the Reynolds number decreases the centerline velocity decay rate also decreases. This trend would be expected since at a sufficiently low Reynolds number the flow would be laminar, and a laminar jet is known to have a lower centerline velocity decay rate in comparison to a turbulent jet. The magnitude of the centerline velocity decay rates from this flow regime would appear to be somewhat larger than those reported for the adjacent high Reynolds number turbulent flow regime or the low Reynolds number laminar regime. Both Olson and Miller [13] and Miller and Comings [8] found that the centerline velocity decay rate for a high Reynolds number turbulent jet fit a -1/2 power law distribution. Anderson's data for the higher Reynolds number conditions exhibits a somewhat larger centerline velocity decay rate. For example, at a Reynolds number of 7490 and a Mach number of 0.52 the centerline velocity decay is best fit by a -0.593 power law distribution. Chanaud and Powell [18] found that the centerline velocity decay rate of a laminar incompressible plane jet tends to approach asymptotically a -1/3 power law distribution. Anderson's results for the lower Reynolds number conditions would tend to exhibit a higher decay rate. For example, the centerline velocity decay at a Reynolds number of 207 and a Mach number of 0.52 is best fitted by a -0.416 power law distribution.

Thirdly, the spread of the jet width, b_m, would tend to indicate this parameter is primarily a function of Reynolds number since no apparent Mach number dependence is observed in the data. It should be pointed out, however, that velocity distributions and thus jet width were measured for two downstream positions for each of the flow conditions in this study. Thus, observations upon the effect of flow conditions on this parameter are tentative. The experimental data do indicate that the jet's spread rate increases with larger Reynolds number. This conclusion is in qualitative agreement with centerline velocity decay data presented previously. It should be noted that for the higher Reynolds number conditions studied by Anderson the jet spread rate is somewhat larger than that reported by Olson and Miller or Miller and Comings (linear spread with distance) for the case of turbulent jets. For the lower Reynolds number conditions, however, essentially no jet spread rate is detected near the nozzle. The jet width at locations near the exit plane is less than one-half the supply nozzle width. Thus, it could be again concluded that either no potential core exists or it is very short for these low Reynolds number conditions.

Anderson found that the experimental velocity profiles from his research could be fitted to a Gaussian distribution. Using this distribution for the mixing zone, he employed the correlation procedure of Olson to describe the flow in the developed region of flow.

Transition from Laminar to Turbulent Flow in a Plane Jet

The transition process from laminar to turbulent flow is one of the most interesting and often investigated problems of fluid mechanics.

Our present knowledge of this process suggests transition can result as a consequence of two effects. It has been found that for large Reynolds numbers a flow will be unstable for infinitesimal disturbances which grow exponentially resulting in transition. But it is also known that if the outside disturbance is large enough it may cause transition at a much lower Reynolds number than at that due to the basic instability of the flow. As a consequence of the complexity of this phenomena, it is not possible to describe completely the transition process in a plane jet. However, the study of the stability of the flow field to a small disturbance yields both qualitative and quantitative information on transition. A discussion of this topic according to Schlichting [22] follows.

Theory of Stability of Laminar Flows. Efforts to explain theoretically the process of transition were initiated many decades ago; they have led to success only recently. These theoretical investigations are based on the assumption that laminar flows are affected by certain small disturbances; in the case of the plane jet these disturbances may originate at the nozzle exit plane. The theory endeavors to follow up in time the behavior of such disturbances when they are superimposed on the main flow, bearing in mind that their exact form still remains to be determined. The decisive question is whether the disturbances increase or die out with time. If the disturbances decay with time, the main flow is considered stable; on the other hand, if the disturbances increase with time the flow is considered unstable, and there exists the possibility of transition.

A short summary of the derivation of the differential equation describing the stability of a laminar flow will follow. It is assumed in this derivation that the flow field is two-dimensional and incompressible. It will be further assumed that the flow is parallel, that is the mean component of velocity in the y-direction is zero. It is appropriate to point out that this assumption is necessary in order to reduce the complexity of the resulting differential equation of stability.

It may be assumed that the velocity components and the pressure can be separated into a mean flow (whose stability constitutes the subject of the investigation) and into a disturbance superimposed on it. For the case of parallel flow these variables are

$$u = U + u' \quad ; \quad v = v' \quad ; \quad p = P + p' \tag{95}$$

Substituting the previous relations into the Navier-Stokes equations for two-dimensional incompressible flow and neglecting quadratic terms in the disturbance velocity components, result in

$$\frac{\partial u'}{\partial t} + U \frac{\partial u'}{\partial x} + v' \frac{\partial U}{\partial y} + \frac{1}{\rho} \frac{\partial P}{\partial x} + \frac{1}{\rho} \frac{\partial p'}{\partial x} = \nu \left(\frac{d^2 U}{dy^2} + \nabla^2 u' \right) \tag{96}$$

$$\frac{\partial v'}{\partial t} + U \frac{\partial v'}{\partial x} + \frac{1}{\rho} \frac{\partial P}{\partial y} + \frac{1}{\rho} \frac{\partial p'}{\partial y} = \nu \nabla^2 v'$$

$$\frac{\partial u'}{\partial x} + \frac{\partial v'}{\partial y} = 0$$

If the mean flow itself satisfies the Navier-Stokes equations, the above may be simplified to

$$\frac{\partial u'}{\partial t} + U \frac{\partial u'}{\partial x} + v' \frac{\partial U}{\partial y} + \frac{1}{\rho} \frac{\partial p'}{\partial x} = \nu \nabla^2 u' \qquad (97)$$

$$\frac{\partial v'}{\partial t} + U \frac{\partial v'}{\partial x} + \frac{1}{\rho} \frac{\partial p'}{\partial y} = \nu \nabla^2 v'$$

$$\frac{\partial u'}{\partial x} + \frac{\partial v'}{\partial y} = 0$$

The mean laminar flow in the x-direction is assumed to be influenced by a disturbance which is composed of a number of discrete partial fluctuations, each of which is said to consist of a wave which is propagated in the x-direction. As it has already been assumed that the flow is two-dimensional, it is possible to introduce a stream function $\psi(x,y,t)$, thus integrating the equation of continuity in expression (97). The stream function representing a single oscillation of the disturbance is assumed to be of the form

$$\psi(x,y,t) = \phi_1(y)\, e^{i\alpha_1(x-c_1 t)} \qquad (98)$$

Any arbitrary disturbance is assumed expanded in a Fourier series, each of whose terms represent such a partial oscillation. In equation (98) the wave number, α_1, is a real quantity and $\lambda = 2\pi/\alpha_1$ is the wave length of the disturbance. The quantity c_1 is complex,

$$c_1 = c_r + i\, c_i \qquad (99)$$

c_r is the velocity of the wave in the x-direction whereas c_i determines the degree of amplification or damping. The disturbances are damped if $c_i < 0$, whereas for $c_i > 0$ instability sets in.

Introducing the stream function defined in expression (98) into the equations of motion found in expression (97), after the elimination of pressure, results in the following ordinary, fourth order, differential equation for $\phi_1(y)$

$$(U-c_1)(\phi_1''-\alpha_1^2\phi_1) - U''\phi_1 = \frac{-i}{\alpha_1 R_e}(\phi_1''''-2\alpha_1^2\phi_1''+\alpha_1^4\phi_1) \qquad (100)$$

The previous expression has been nondimensionalized in that all lengths have been divided by a suitable reference length, and all velocities have been divided by the maximum velocity of the main flow. In the case of the free jet, the length quantity is the mixing region width, b_m, and the centerline velocity, u_c, is the maximum velocity in the flow. The prime denotes differentiation with respect to (y/b_m) and the Reynolds number is defined as

$$R_e = \frac{u_c\, b_m}{\nu} \qquad (101)$$

Expression (100) is the fundamental differential equation of laminar stability theory which forms the point of departure for a stability analysis. It is commonly referred to as the Orr-Sommerfeld equation.

Solution to the Orr-Sommerfeld Equation for the Plane Jet. The Orr-Sommerfeld equation was derived for parallel flow and thus it would appear that it cannot be employed in determining the stability of a plane incompressible jet. However, a stability analysis can be made of a "pseudolaminar jet." That is, the jet's velocity distribution in the y-direction may be employed in the calculation of the

solution of the Orr-Sommerfeld equation. Thus in effect the velocity variation in the x-direction for a plane jet is neglected except for its effects on local Reynolds number. This same procedure has been used with excellent results to predict the transition of the boundary layer on a flat plate and, consequently, a precedent for its application on boundary layer type flows is established.

Curle [23] in his solution to the "pseudolaminar jet" made use of the velocity profiles predicted by Bickley [16] for a plane incompressible free jet; see expression (84). The velocity distribution in the y-direction employed in the calculation is

$$u = u_c \operatorname{sech}^2 (y/b_m) \tag{102}$$

$$u_c = 0.4543 \, (J_\infty^2/\rho^2 \nu x)^{1/3}$$

$$b_m = 3.633 \, (\rho \nu^2 x^2/J_\infty)^{1/3}$$

The preceding expression represents a finite momentum jet originating from a line source. In order to correct for this inconsistency between the mathematical model and reality, Curle assumed the virtual line source was located upstream of the real nozzle exit plane. Andrade's expression found in equation (85) was used for the location of the virtual origin as a function of Reynolds numbers.

The parameters used in the analysis to nondimensionalize the Orr-Sommerfeld equation are given in expression (102). The local value of Reynolds number defined in (101) is

$$R_e = 1.651 \left[\frac{J_\infty (x+x_0)}{\rho \nu^2}\right]^{1/3} \tag{103}$$

$$x_0 = 0.65\ b\ R_e\Big|_{x=0}$$

It should be noted that the local free jet Reynolds number defined above increases proportional to $x^{1/3}$.

Curle's solution for the stability of the "pseudolaminar jet" is found in Figure 24. Shown in this figure as a function of α_1 and Reynolds number is the locus of points of neutral stability which divides the regions of stable and unstable disturbances. The point on this curve at which the Reynolds number has its smallest value (tangent parallel to the α_1-axis) is of great interest since it indicates that value of Reynolds number below which all individual oscillations decay, whereas above that value at least some are amplified. As may be seen for the plane jet the region in which the flow is completely stable is approximately below a Reynolds number of 5.5. For Reynolds numbers above this critical value the jet is only stable for disturbances with a high value of wave number (short wave length disturbances).

It is appropriate at this point to consider the transition process of a hypothetical plane jet in accordance with Curle's results. Near the nozzle exit plane the hypothetical jet may possess a local Reynolds number less than the critical value and thus would be stable to all disturbances in the flow field. As the jet progresses downstream the local Reynolds number increases proportional to $x^{1/3}$, and

thus the flow will eventually become unstable to certain wave length disturbances. It would be expected that in any flow field disturbances of all wave lengths no matter how minute would be present. Thus once the jet crosses over into the unstable region, outside disturbances would be magnified and transition to turbulent flow will eventually ensue.

The preceding description introduces an important parameter to transition, that is "degree of disturbance" in the surrounding flow field. If the surroundings possess a high level of turbulent intensity, it would be expected that disturbances imposed on the free jet would be much larger and thus the points of instability to disturbances and transition to turbulence would be much closer.

Sensitivity of the Plane Laminar Jet to Disturbances. Unfortunately, an experimental verification of Curle's stability analysis has not been performed. This is due to the difficulties associated with determining stability as a function of distance along the stream as well as establishing the low surrounding turbulence levels required in the experimental study. An interesting investigation of the sensitivity of a plane jet to finite disturbances has been performed by Chanaud [18]. This study does provide a qualitative verification of the results of Curle.

In Chanaud's experimental model a plane jet of water was allowed to flow through a rectangular nozzle of width 0.25 inches and height 6.0 inches. This water jet was disturbed by plates moving sinusoidally in a direction perpendicular to the flow. The amplitude

and frequency of the oscillations were carefully recorded. The effect of the disturbances on the stability of the jet was observed visually by injecting dye into the flow.

Shown in Figure 25 are curves of neutral stability for this research plotted as a function of Reynolds number and Strouhal number. The Reynolds number is based on the mean velocity u_m at the nozzle exit and the nozzle width, b. The Strouhal number is defined as

$$S = fb/u_m \tag{104}$$

f in the previous expression represents the frequency of the oscillations. The half amplitude of the oscillations shown in the preceding figure is a_1. Neutral stability was defined by the authors as the condition of unchanging amplitude of barely detectable waves lying between about four and 10 slitwidths downstream of the nozzle.

The experimental data shown in Figure 25 exhibit several features qualitatively predicted by stability theory. Firstly, there does appear to be a critical Reynolds number below which the jet is stable to any disturbance frequency. This critical value of Reynolds number, however, is found to be a function of disturbance amplitude. Secondly, the theory predicts that the upper boundary of the unstable region is at almost constant Strouhal number (constant α_1) except where it drops sharply near the critical Reynolds number. Thirdly, although it proved impossible for the authors to obtain meaningful data for the lower boundary of the unstable region (long wave length disturbances), it may be concluded that if it exists it must lie close to the Reynolds number axis even at comparatively low Reynolds numbers.

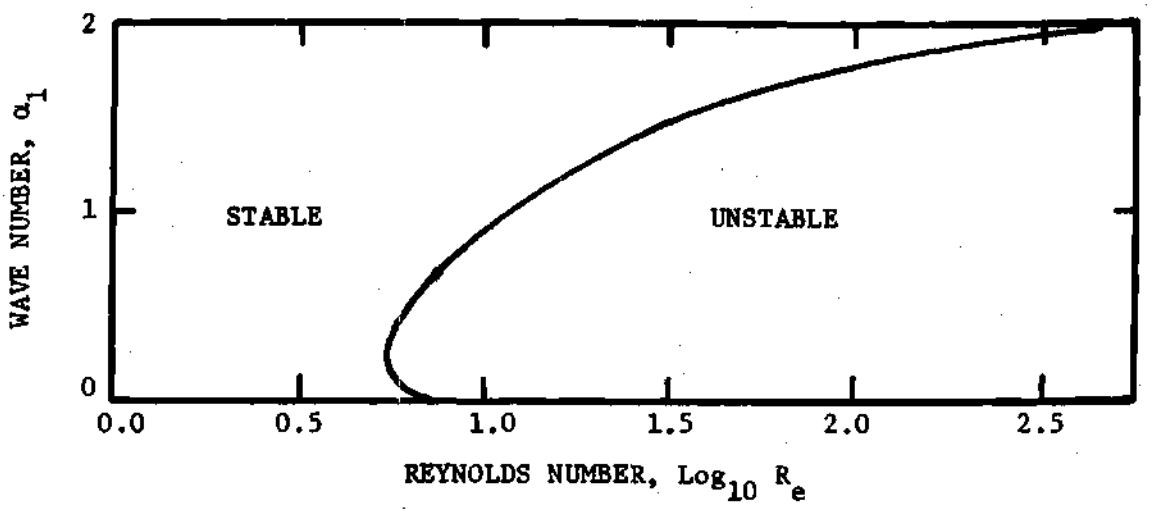

Figure 24. Neutral Stability Contours for the "Pseudolaminar Jet" from Reference [23]

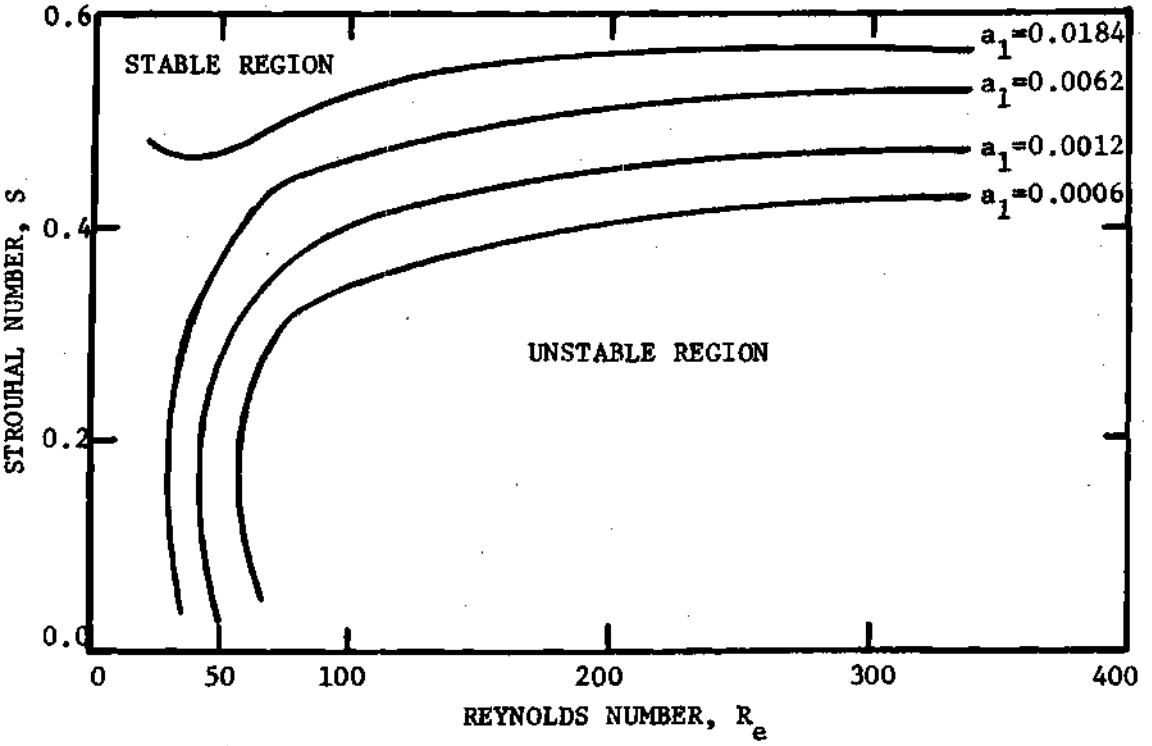

Figure 25. Neutral Stability Contours for the Incompressible Flow of a Laminar Jet from Reference [18]

The authors of this research also report their observation of the turbulent transition of an undisturbed jet of water. If the water jet was not deliberately disturbed it was found to travel an appreciable distance before any disturbance became of visible magnitude. These disturbances, once visible, grow extremely rapidly. They would always be of very long wave length (small α_1). Chanaud proposed that these disturbances were of such a small spatial rate of amplification that they only became visible after traveling a long distance when they entered into a region of high instability. Chanaud further proposed that these disturbances may originate at the orifice and play a dominant role in transition.

Measurements of the steady state velocity profiles in a laminar incompressible jet of air indicated the hyperbolic secant distribution predicted by Bickley tends to fit the experimental data; see Figure 17. However, centerline velocity decay results, especially at higher values of Reynolds number, are in poor agreement with Bickley's predictions; see Figure 18. Thus Curle's use of the hyperbolic secant distribution in calculating the curve of neutral stability would appear to be justified; although, assuming the local value of Reynolds number grows proportional to $x^{1/3}$ is not justified.

The Effect of Compressibility on the Stability of a Plane Jet. For the case of high velocity flows, the effect of compressibility on the stability of a laminar jet must be considered. This necessitates the addition of density and temperature to an already difficult mathematical analysis. As a result of this complication, a solution to the

problem of the stability of a plane jet of compressible fluid has not been achieved. However, if the fluid is assumed to be inviscid, qualitative results can be attained on the effect of Mach number on stability.

Pai [24] analyzed the stability of a plane jet flow of inviscid compressible fluid. He found that for symmetrical subsonic disturbances as the Mach number of the jet increased, the value of the wave number, α_1, for neutral stability decreased. This would have the effect of moving the locus of neutral stability toward the Reynolds number axis in Figure 24. At a sufficiently high Mach number the flow was found to be completely stable to all disturbances. For the case of no heat transfer this value of critical Mach number was given as approximately 2.5.

Jet Interaction

The interaction process involving two or more jet flows has been the subject of numerous recent investigations. This interest has been aroused chiefly from the development of fluidic elements. These devices which make use of single and interacting bounded jet flows are utilized in performing logic, amplifying signals and controlling processes. An example of the application of the jet interaction process in a fluidic device may be seen in the proportional fluid amplifier shown in Figure 26. It can be observed in this sketch that the two control streams exert normal forces on the supply jet. These forces which result from the momentum and pressure of the control streams act to deflect the supply jet. It has been found experimentally that as

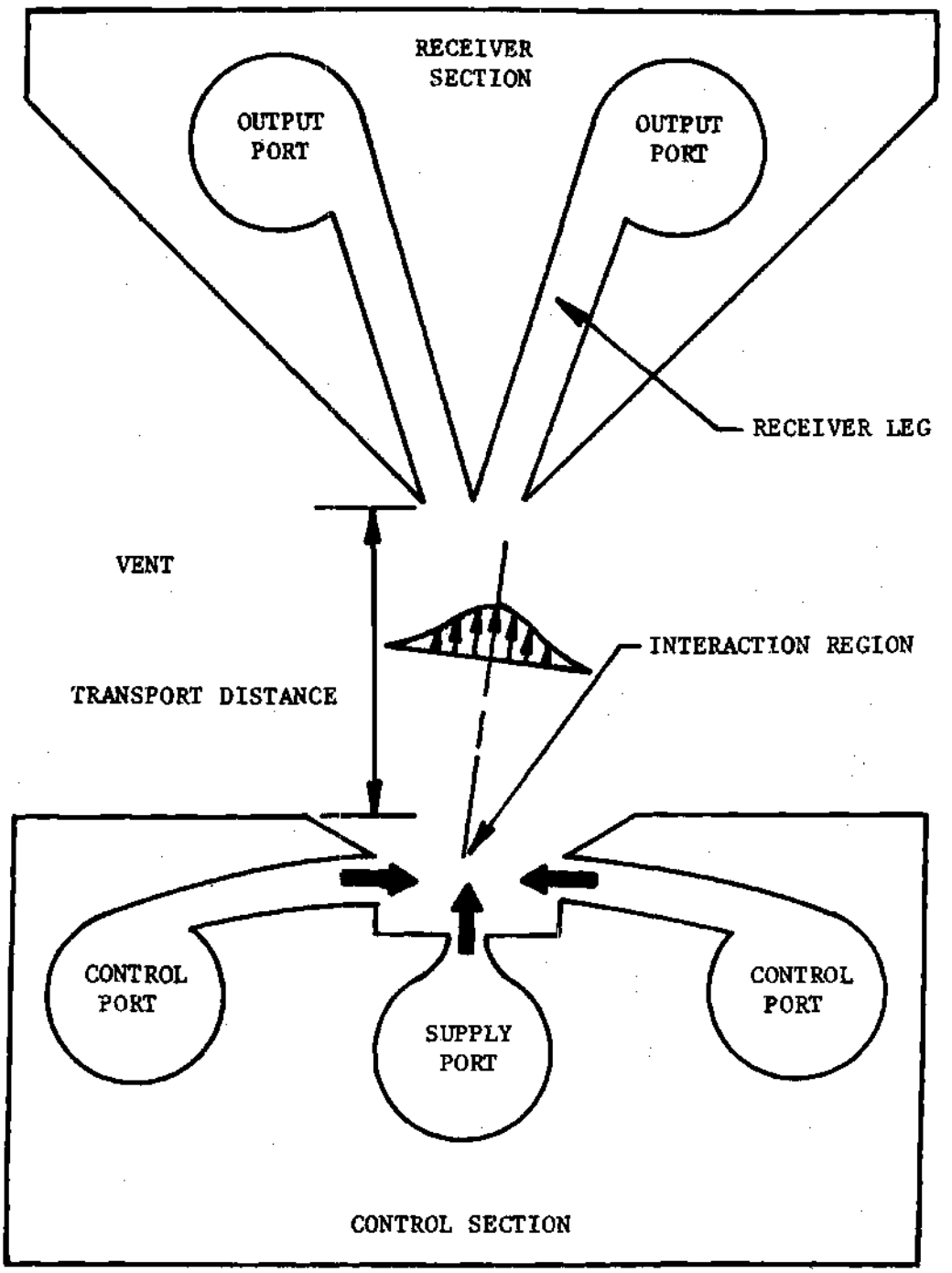

Figure 26. Sketch of a Proportional Fluid Amplifier

the control streams interact with the power jet, they tend to merge into the power jet. This merging process accelerates the outer edge of the supply jet while decelerating the control jets. Thus it is to be expected that the combined streams would exhibit a distorted velocity profile, at least, near the interaction region. However, downstream of the interaction zone, a smoothing process on the profile takes place as a result of diffusion with the surrounding fluid at rest. This smoothed jet flow ultimately impinges upon a receiver section which is located downstream of the control section. In the receiver the velocity profile of the jet is converted to an output pressure and flow.

It is obvious that a description of the interaction process is required if the performance of this device is to be predicted. In particular, the deflection angle of the combined jets as a function of the supply and control port pressure as well as a description of the combined jet's velocity profile are required.

Experimental studies by Moynihon and Reilly [25] have demonstrated that a summation of momentum and static pressure forces on a control volume drawn around the interaction region is adequate to describe the deflection angle of the supply jet. It was found that the deflected power jet appeared to originate from the intersection of the ports centerlines. Even though such an analysis in conjunction with measured velocity and static pressure profiles may be adequate to describe the phenomena, this procedure is incapable in general of predicting deflection angle in terms of the input variables. This difficulty is to be expected since the interaction process in general depends

upon the complex flow field established upon the meeting of these jets, which is highly dependent on interaction region geometry.

Experimental studies of the interaction zone indicate that the velocity profiles for a single power jet are distorted with the addition of the control jets. Firstly, the power jet is not fully expanded at the exit of its nozzle due to control-nozzle static pressure. A positive pressure gradient exists in the interaction region and extends outside this region to a distance depending on control-nozzle width and control pressure level. Secondly, the addition of control momentum tends to pinch the power jet resulting in its further acceleration after leaving the interaction zone. This pinching of the power jet has the effect of distorting the combined jets velocity profile as well as lengthening the zone of flow establishment in the jet. However, downstream of the interaction region the jet will become established, appearing like a free jet [26].

The preceding discussion has indicated the interaction process is one that offers formidable difficulties in its analysis. However, for the special case where pressure forces dominate the interaction process, a simple analysis can be made which has been proven to be in good agreement with experimental data. A summary of the analysis of the pressure controlled interaction process according to Simson [27] follows.

Analysis of Pressure Controlled Interaction Process

Simson in his analysis of the pressure controlled interaction process considered both single and dual control port mixing geometries.

In this review results will be presented only for the case of interest, that is a single control port interacting with a supply jet. The basic mixing region geometry is shown in Figure 27. In order to analyze its operation completely would necessitate the consideration of a number of nonlinear effects. These include the variations in the supply jet profile resulting from jet curvature, pressure differences and nonlinear flow and geometry effects. However, by restricting the operation to small deflection angles it is possible to simplify the analysis. The nonlinear mathematical relationships for the control section will be developed and, subsequently, linearized for the case of small deflection angles.

Equations of Motion in the Interaction Region. It will be assumed that a constant positive pressure P_1 in the control port acts upon the supply jet which results in the jet curvature shown in Figure 27. After the jet leaves the interaction region the ambient pressure on either side of the supply jet is constant and thus the jet follows a straight line.

In the interaction region, Euler's equation of motion in streamline coordinates may be employed to describe the jet's curvature

$$\frac{\partial p}{\partial r} = \frac{\rho v_s^2}{R} \tag{105}$$

R in the previous expression represents the radius of curvature of the jet. v_s and r are the velocity along the streamline and the coordinate normal to the streamline, respectively. Expression (105) may be integrated across the jet if it is assumed that the change in R is small

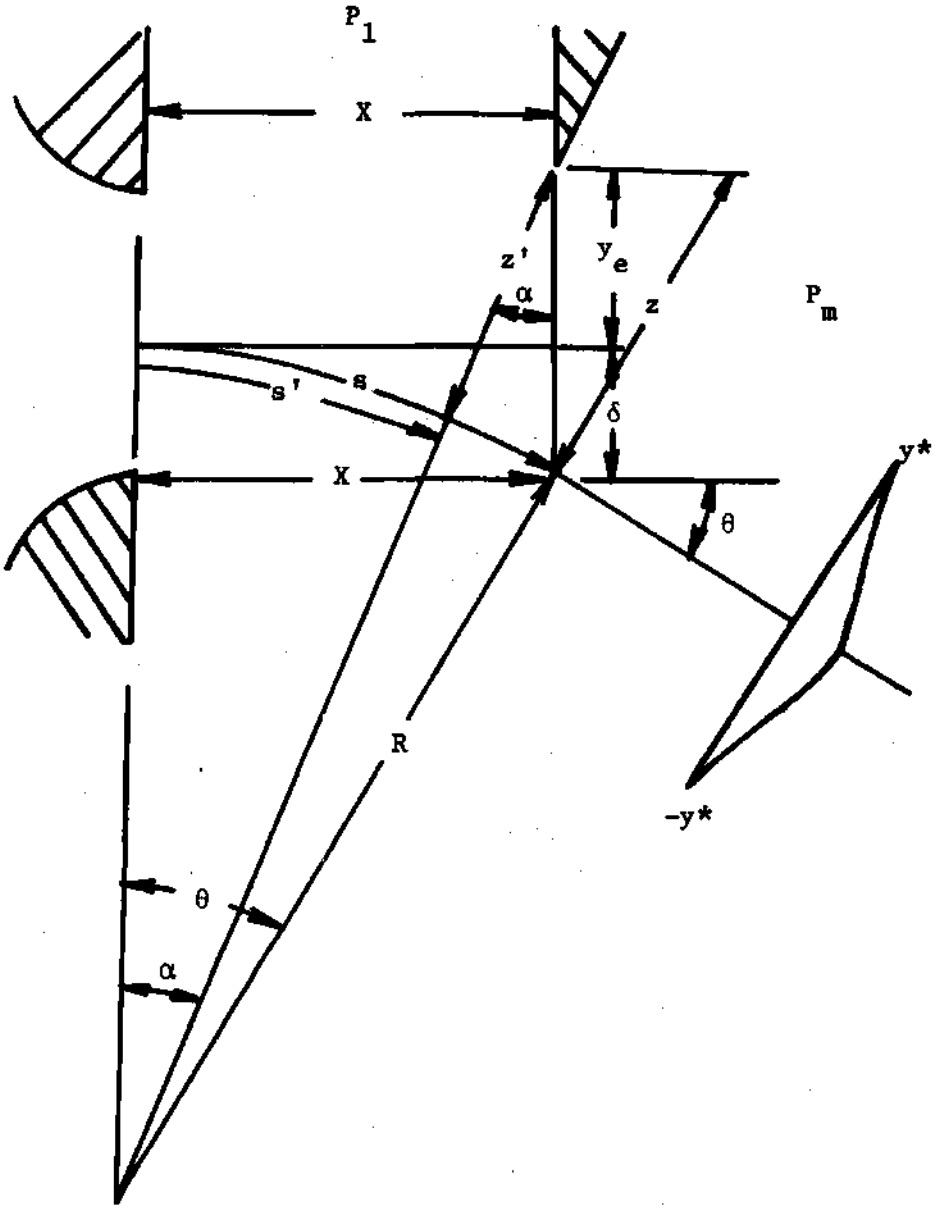

Figure 27. Sketch of Control Port Geometry

compared to R and that the power jet momentum is constant regardless of jet curvature.

$$\int_{R-y^*}^{R+y^*} dp = \frac{1}{R} \int_{R-y^*}^{R+y^*} \rho v_s^2 \, dr \tag{106}$$

y^* in the previous expression is the distance from the centerline to the edge of the jet. Evaluating (106) gives

$$R = \frac{J_\infty}{P_1 - P_m} \tag{107}$$

where J_∞ is the free jet momentum per unit height.

Geometrical Relationships in the Interaction Region. The radius of jet curvature in expression (107) is defined in terms of the free jet momentum and the control port pressure. However, in order to determine the deflection angle of the jet as it leaves the interaction zone, the geometry of the control port must be considered in detail. Employing the control port geometry shown in Figure 27, the following relationships may be found:

$$\delta = R(1-\cos\theta) \tag{108}$$

$$z' = (y_e+\delta)\cos\alpha \tag{109}$$

$$\theta = s/R \tag{110}$$

$$\alpha = s'/R \tag{111}$$

$$\tan\theta = X/(R-\delta) \tag{112}$$

$$\tan \alpha = X/(y_e+R) \tag{113}$$

These relationships are valid for both large and small deflection angles assuming the power jet momentum does not vary with radius of curvature.

If the assumption of small deflection angles is made, the preceding expressions may be simplified. In the text that follows the jet's deflection angle will be restricted to $\theta \leq 10°$.

Using expressions (108), (110) and (112), it can be shown that

$$X \simeq s \quad ; \quad \text{within} \quad 0.3\% \quad \text{for} \quad \theta \leq 10° \tag{114}$$

Substituting the simplification X = s into expression (110) and then substituting R from expression (107), yields

$$\theta = \frac{X(P_1-P_m)}{J_\infty} \tag{115}$$

The relationship for the jet deflection angle, θ, as it leaves the interaction region is completely defined in terms of the power jet momentum, J_∞, the control port width, X, and pressure, P_1.

At this point in the analysis the expressions for z' and s', equations (109) and (111), respectively, will be evaluated for the case of small deflection angles. These two geometric parameters will be required later in the description of the control port flow rate. Inserting expressions (108) and (110) into equation (109) and introducing a trigonometric substitution, simplifies z' to

$$z' \simeq y_e + \frac{X}{2} \tan \theta \quad ; \quad \text{within} \quad 1\% \quad \text{for} \quad \theta \leq 10° \tag{116}$$

Using equations (111) and (113), s' may be simplified for the case of small deflection angles to

$$s' \simeq \frac{R}{y_e + R} X \quad ; \text{within} \quad 1\% \quad \text{for} \quad \theta \leq 10^\circ \tag{117}$$

It is interesting to note that Simson's interaction model when simplified for small deflection angles is identical to that attained by considering a control volume around the interaction region. The inputs to this control volume are the power jet momentum and the control port pressure, while the emerging jet emanates at a prescribed angle from the intersection of the centerlines of the two ports.

Calculation of the Control Port Flow

In attempting to understand the control flow characteristics, it is necessary first to simplify the problem by considering the various components which make up the control flow. Simson has suggested based on water table experiments that the control flow is made up of the proper summation of the entrained flow to the jet, the return flow deflected from the jet by the edge of the control port, and the atmospheric flow to the environment from the control port. These flow components are shown in Figure 28. From this sketch, it is apparent that the continuity equation for the control volume shown may be written as

$$\dot{m}_c = \dot{m}_e - \dot{m}_{re} + \dot{m}_a \tag{118}$$

Each of the components making up the control flow will be considered separately. Mathematical relationships will be developed

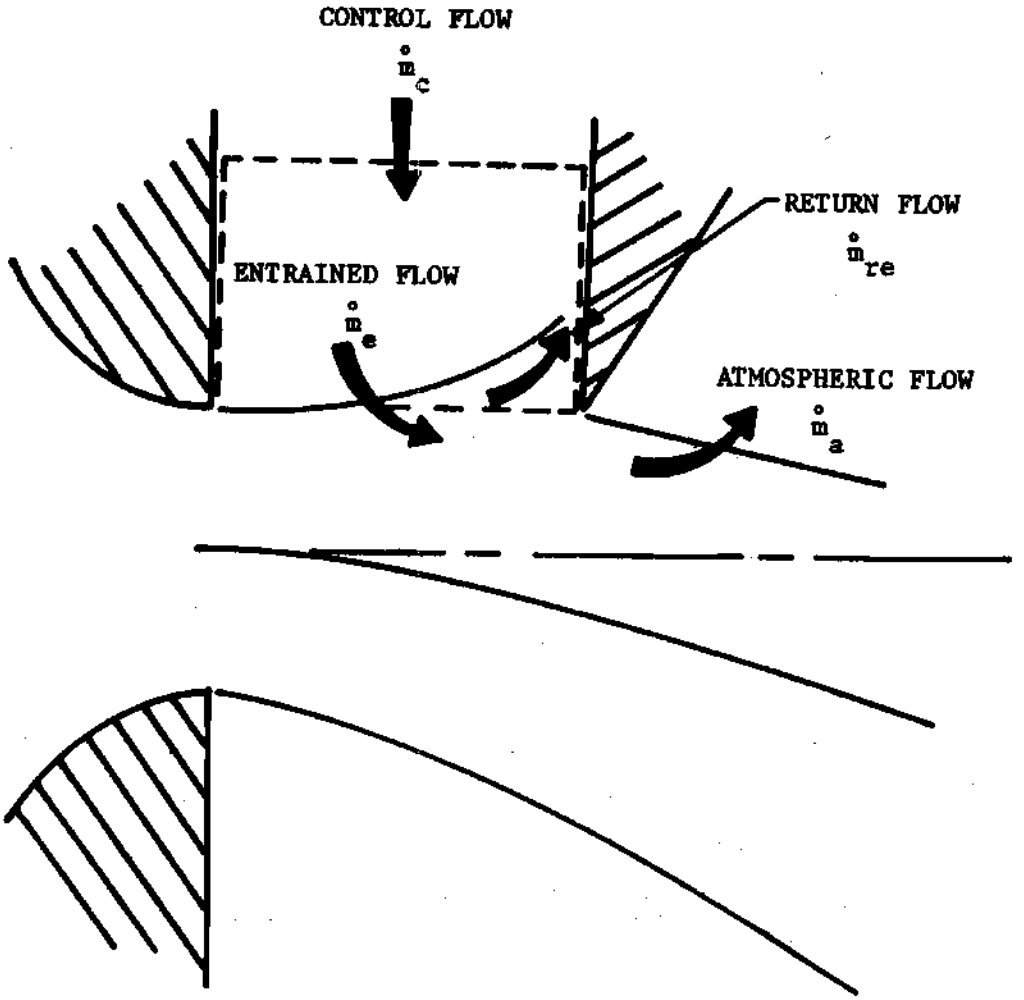

Figure 28. Schematic Representation of Control Flow Components

for each component and then combined to form a relationship for the control flow rate.

Entrained Flow. In determining the entrained component of flow it is assumed that conditions on one side of the supply jet are effectively isolated from conditions on the other side. Thus flow across the jet's centerline does not occur. Under this assumption, the entrained flow component at any downstream position is the difference between the power jet flow from its edge nearest the control port to its centerline and the power jet flow at its exit plane from the edge nearest the control port to its centerline. This may be written as

$$\dot{m}_e = \frac{1}{2} (\dot{m}_d - \dot{m}_i) \tag{119}$$

For large deflection angles, Simson considered the approximate effect of the control pressure on the jet's entrainment characteristics. However, if only small deflection angles are considered the velocity profile of the supply jet may be assumed to be that of a free jet. The mass flow rate of the power jet from its centerline to edge at any downstream station may be written as

$$\frac{1}{2} \dot{m}_d = h \int_0^\infty \rho u \, dy \tag{120}$$

h in the previous expression represents the jet height. Substituting equation (120) into (119) yields the following expression for the entrained flow at any downstream station:

$$\dot{m}_e = h \int_0^\infty \rho u \, dy - \dot{m}_i/2 \tag{121}$$

Returned Flow. In determining the return flow, it is necessary to consider the position of the control port knife edge as the power jet passes. As may be seen from Figure 27, the distance from the jet's centerline to the knife edge is z'. The returned flow may be represented by the integral of the jets velocity profile from z' to ∞ at a location s' downstream of the exit plane. The returned flow may be represented as

$$\dot{m}_{re} = h \int_{z'}^{\infty} \rho u \, dy \tag{122}$$

If small deflection angles of the power jet are considered, expression (116) may be substituted for z' and thus the previous expression becomes

$$\dot{m}_{re} = h \int_{(y_e + \frac{X}{2} \tan \theta)}^{\infty} \rho u \, dy \tag{123}$$

Atmospheric Flow. In Simson's thesis a general procedure was developed to calculate the atmospheric flow, however, this method was inconvenient and generally required a separate graphical solution for each case being considered. In order to overcome this drawback, and still obtain useful information, the analysis was simplified for small deflection angles and small knife edge setbacks. As an aid to understanding the final linearized relationships for the atmospheric flow, the more general nonlinear case for the flow inside the jet boundary will be reviewed briefly. Upon the conclusion of this summary the simplified model will be presented.

In order to calculate the atmospheric flow component, Simson assumed that the half jet flow nearest the control port is initially expanded from the nozzle pressure to the pressure in the control port. Then as the flow nears the control port edge it is expanded from the control port pressure, P_1, to the ambient pressure, P_m. In the accelerated flow at the port edge, it is possible to apply the momentum equation across individual elements of the jet. This implies that it is acceptable to assume that the final turbulent shear stresses across any element cancel out, so that momentum and pressure produce the only net forces on an element. For an individual element the momentum expression which describes the increase in velocity as the jet is expanded across the control port edge may be written as

$$(P_1 - P_m)\ \Delta y = \rho\ |u_x|\ u_x\ \Delta y \qquad (124)$$

In determining the atmospheric flow, Simson firstly calculated the power jets reduced momentum profile based on the expansion from the nozzle pressure to the control port pressure. In this calculation it was assumed that the control ports positive pressure diminished linearly across the power jets profile. Secondly, the increase in velocity resulting from the expansion across the knife edge was calculated. Thirdly, the velocity squared profile of the power jet before the knife edge was added to the velocity squared profile resulting across the knife edge. Taking the square root of this summation produced the final velocity profile out of the control port. The atmospheric flow component is defined as the difference between the

final velocity profile out of the control port and the normally expected velocity profile. The normally expected profile would occur at the control port knife edge if the control port was removed.

In order to simplify the analysis, Simson restricted the derivation to both small deflection angles and small control port setbacks. The control port pressure for these conditions is small in comparison to the supply pressure, thus it may be assumed that the velocity profile in the control port is that of the power jet when expanded from the nozzle pressure to the ambient pressure. It may also be assumed that very little additional atmospheric flow is associated with the small increase in velocity through the potential core as the jet passes the knife edge. Thus this flow may be neglected. The increase in flow outside of the potential core as the jet passes the knife edge, that is the atmospheric flow, may be approximated by a triangular profile whose width is the distance from the edge of the core to the edge of the jet and whose maximum magnitude, which occurs at the edge of the jet, is given by expression (124). Based on these assumptions the atmospheric flow velocity as a function of distance from the core is

$$u_a = \sqrt{\frac{P_1 - P_m}{\rho}} \left(\frac{y - y_c}{y^* - y_c} \right) \tag{125}$$

y_c is the distance from the jet's centerline to the edge of the core. The total atmospheric flow component may be determined by integrating expression (125) from the edge of the core, y_c, to the edge of the control port, z'; see Figure 27.

$$\dot{m}_a = h \int_{y_c}^{(y_e + \frac{X}{2} \tan \theta)} \rho u_a \, dy \tag{126}$$

Since small deflection angles are being considered, expression (116) has been substituted for z'. By inserting the expression for u_a found in (125), the atmospheric flow becomes

$$\dot{m}_a = h \int_{y_c}^{(y_e + \frac{X}{2} \tan \theta)} \sqrt{\rho(P_1 - P_m)} \left(\frac{y - y_c}{y^* - y_c} \right) dy \tag{127}$$

Integrating the previous expression produces

$$\dot{m}_a = \frac{h \sqrt{\rho(P_1 - P_m)}}{2} \frac{(y_e + \frac{X}{2} \tan \theta - y_c)^2}{y^* - y_c} \tag{128}$$

Combined Control Flow Rate. It is now possible to combine the previously calculated individual components of the control flow. Inserting expressions (121), (123) and (128) into (118) and simplifying, yields the relationship

$$\dot{m}_c = h \int_0^{(y_e + \frac{X}{2} \tan \theta)} \rho u \, dy + \frac{h \sqrt{\rho(P_1 - P_m)}}{2} \frac{(y_e + \frac{X}{2} \tan \theta - y_c)^2}{y^* - y_c} - \frac{\dot{m}_i}{2} \tag{129}$$

Since θ is approximately equal to $\tan \theta$ for small angles, the previous expression may be simplified by substituting expression (115) for the $\tan \theta$. Thus the final expression for the control port flow rate is

$$\dot{m}_c = h \int_0^{\left[y_e + \frac{X^2(P_1-P_m)}{2J_\infty}\right]} \rho u \, dy + \frac{h\sqrt{\rho(P_1-P_m)}}{2} \frac{\left[y_e + \frac{X^2(P_1-P_m)}{2J_\infty} - y_c\right]^2}{y^* - y_c} - \frac{\dot{m}_i}{2} \tag{130}$$

It should be noted that the control flow rate is defined completely in terms of the control port differential pressure, the control port geometry and the power jet description. The integral relationship in expression (130) as well as the jet characteristics are evaluated at s', that is the distance downstream of the exit plane where the jet passes the knife edge; see Figure 27. By combining equations (107) and (117), s' may be expressed for the case of small deflection angles as

$$s' = \frac{J_\infty X}{y_e(P_1-P_m) + J_\infty} \tag{131}$$

Simson's Power Jet Description. In calculating the interaction characteristics, Simson made use of a power law velocity distribution. This profile describes the x-component of velocity for two-dimensional incompressible turbulent jet flow. Simson's velocity profile is

$$\frac{u}{u_c} = \left[1 - \left(\frac{y - y_c}{K_1 x}\right)^{7/4}\right]^2 \quad ; \quad \text{for} \quad 0 \leq \frac{y - y_c}{K_1 x} \leq 1 \tag{132}$$

It should be noted that the core region for this model fills the entire nozzle at the exit plane of the jet. The distance to the edge of the jet from the centerline may be calculated from (132) and is

$$y^* = y_c + K_1 x \tag{133}$$

Assuming that the jet momentum is conserved, the value of K_1 is found to be

$$K_1 = 1.378\ b/x_c \tag{134}$$

Simson assumed that the power jet could be broken up into two separate flow regimes, that is a transition region where a potential core existed and an established flow region. The core length, x_c, for the range of Reynolds numbers from 10,000 to 100,000 was considered to be

$$x_c = 5.2\ b \tag{135}$$

The potential core width y_c varied linearly with x and can be written as

$$y_c = \left(1 - \frac{x}{x_c}\right) \frac{b}{2} \tag{136}$$

In the zone of fully established flow the centerline velocity decay was assumed to vary with the -1/2 power of x.

Jet Impingement Upon a Receiver

Literature pertinent to the interaction of a jet flow with a receiver will be considered in this section. It should be noted that this topic has been of recent interest due to its relevance in the design of fluidic devices.

In a number of fluidic elements; such as the proportional fluid amplifier shown in Figure 26, the deflected power jet ultimately impinges

upon a receiver section. In this portion of the amplifier the jet's velocity profile is converted to an output flow rate and pressure. It is thus of interest to determine the flow and pressure characteristics resulting from this impingement. The solution to this problem represents a formidable analytic task, since as the jet profile nears the receiver it is distorted by the existence of this obstacle. The unknown flow field at the inlet to the receiver is a function of the undisturbed power jet profile upstream of the receiver section, the receiver's geometry and its loading conditions. Serving as a further complication to this analysis is the lack of receiver-diffuser performance data for the skewed inlet velocity profiles associated with jet flows [28].

Because of the complexity of this problem, a general solution has not been achieved to the pressure and flow recovery resulting from the impact of a jet upon a receiver section. However, analyses have been made for several limiting cases. These analyses will be reviewed in the following sections.

Analysis of Receiver Performance Under Open Load and Blocked Load Conditions

As an aid to understanding the two limiting cases of the pressure and flow emerging from the receiver section, consider the sketch shown in Figure 29. In this sketch a deflected power jet is impinging upon a stationary receiver. The pressure and flow recovery from the receiver are dependent upon the jet's characteristics upstream of the receiver, the receiver's geometry and loading conditions. If the receiver's load is varied from fully open to fully blocked, with all other parameters held fixed, a relationship between flow and pressure recovery is

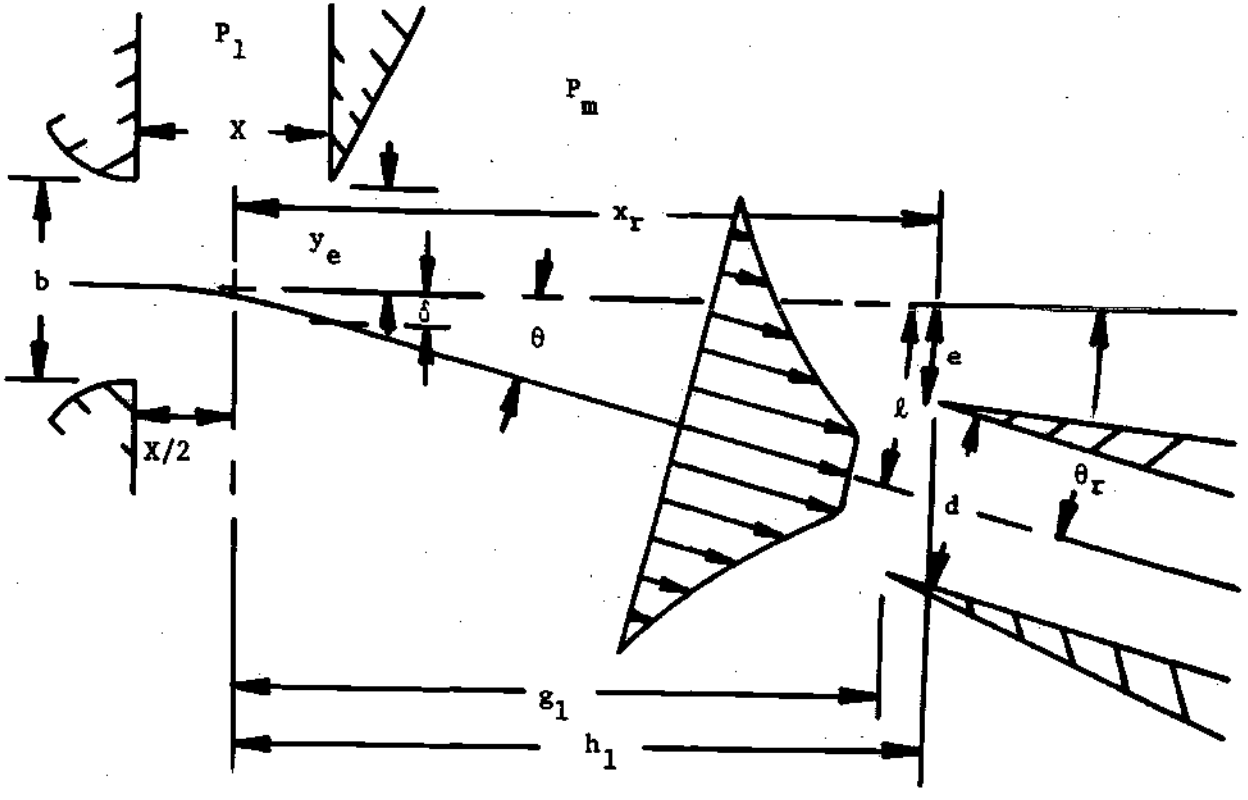

Figure 29. Nonlinear Jet Receiver Interaction Geometry

established. The limiting points to this relationship are referred to as the blocked load and open load conditions, respectively.

Analysis of Open Load Conditions. In determining the open load condition, that is the condition where the receiver's flow rate is a maximum and there is no pressure recovery, Simson [27] assumed that:

1. The presence of the receiver does not affect the power jet velocity profile impinging on the receiver opening.
2. The receiver operates under no-load conditions.
3. There is no back flow out of the receiver.
4. The power jet profile at the receiver is that of a free jet.

Simson assumed the mass flow rate through the receiver is equal to the mass flow rate of the power jet intersecting the receiver entrance. This can be expressed as

$$\dot{m}_r = h \int_{A_r} \rho u \, dy \tag{137}$$

where h and A_r represent the receiver's height and normal area to the jet, respectively.

In order to evaluate expression (137), geometrical relationships must be developed between the jet profile and the receiver; see Figure 29. It will be assumed that the receiver's centerline is located on a radius of length x_r whose origin is the intersection of the centerlines of the control and supply ports. It should be noted that the deflected power jet also appears to originate from this point for the case of small deflection angles.

The arc length, ℓ, through which the supply jet is deflected at the radical position x_r is a function of jet deflection angle, θ, and may be expressed as

$$\ell = x_r \theta \tag{138}$$

Although expression (138) defines the deflection of the power jet profile at the radical location of the receiver, x_r, it is obvious that the receiver's knife edges in general intersect the power jet profile at locations different than x_r. For example, in Figure 29 it may be seen for a jet deflection angle of $\theta = 0°$ the lower knife edge will intersect the power jet profile a distance g_1 downstream of the origin, while the upper knife edge intersects the profile at a position h_1 downstream of the origin. It also may be noted that a reduced projected area of the receiver is seen by the power jet profile under this condition. Expressions for g_1 and h_1, the distances of the receiver's lower and upper knife edges, respectively, from the origin of the jet, may be determined as

$$g_1 = \frac{x_r}{\cos(\theta_r - \theta)} - (d+e) \sin(\theta_r - \theta) \tag{139}$$

$$h_1 = \frac{x_r}{\cos(\theta_r - \theta)} - e \sin(\theta_r - \theta)$$

The reduced projected area of the jet profile on the receiver may be expressed as

$$A_r = d\, h \cos(\theta_r - \theta) \tag{140}$$

Eliminating the height of the receiver from (140) gives the following equation for the reduced frontal length of the receiver:

$$d_r = d \cos (\theta_r - \theta) \tag{141}$$

It is obvious that the evaluation of expression (137) using the previous expressions for g_1, h_1 and d_r would be very tedious. Thus in order to simplify the problem, Simson restricted the motion of the jet to small deflection angles. He also assumed small receiver offset angles and a small receiver inlet area in comparison to the power jet exit area. Under these assumptions

$$g_1 \simeq x_r \tag{142}$$

$$h_1 \simeq x_r$$

$$d_r \simeq d$$

The linearized model of jet and receiver interaction is shown in Figure 30. From this sketch it is apparent that the mass flow integral given in equation (137) is

$$\mathring{m}_r = h \int_{e-\ell}^{e+d-\ell} \rho u \, dy \tag{143}$$

It should be noted that the centerline of the jet represents the origin of the coordinate system in the previous integration. The velocity profile of the power jet used in expression (143) is evaluated at a position $(x_r+X/2)$ downstream of the supply jet's exit plane.

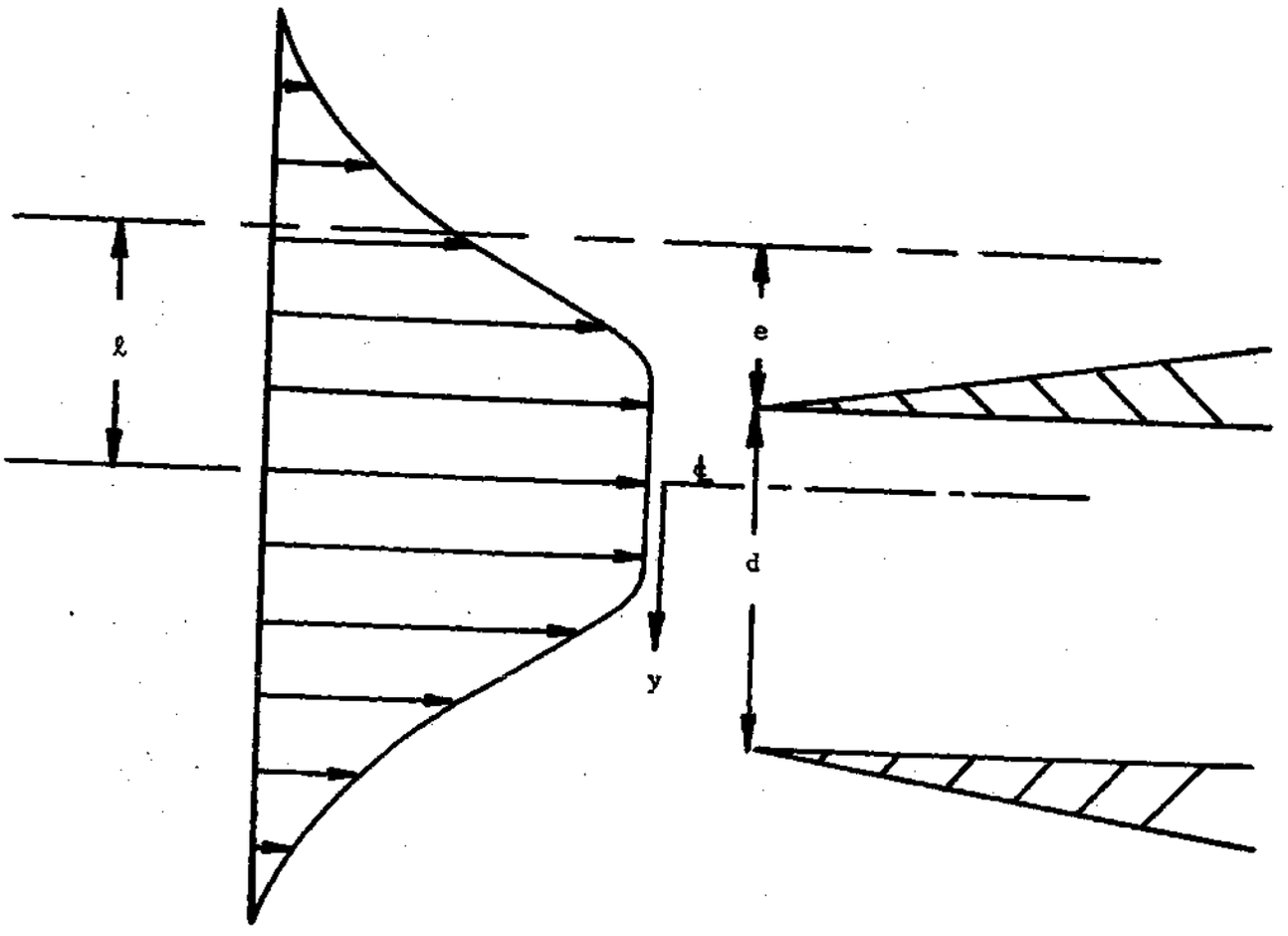

Figure 30. Linearized Jet-Receiver Interaction Geometry

For the case of small deflection angles, ℓ may be simplified by introducing expression (115) for θ

$$\ell = \frac{x_r X (P_1 - P_m)}{J_\infty} \tag{144}$$

Analysis of Blocked Load Conditions. In determining the blocked load condition, that is the case where the receiver pressure is a maximum and there is no flow through the device, Simson also assumed that the power jet profile at the receiver entrance is that of a free jet. It was further assumed that the gauge pressure at the blocked load condition is the average of the total pressure of the power jet over the entrance area of the receiver. For incompressible flow this may be expressed as

$$P_B - P_m = \frac{h}{A_r} \int_{A_r} \frac{\rho u^2}{2} \, dy \tag{145}$$

If as in the previous case the motion of the power jet is restricted to small deflection angles and the receiver offset angle and inlet area are small, then expression (145) may be reduced to

$$P_B - P_m = \frac{1}{d} \int_{e-\ell}^{e+d-\ell} \frac{\rho u^2}{2} \, dy \tag{146}$$

Experimental Investigations of the Impingement of an Axisymmetric Jet Upon a Receiver-Diffuser

Reid [29] made a comprehensive investigation of the flow and pressure characteristics resulting from the impingement of an

axisymmetric jet upon a circular receiver. The centerlines of the receiver and supply nozzle were held coincident in this investigation. The objectives of this research were firstly to study the flow phenomena involved when the nonuniform velocity profile of a free jet intersected a receiver section, and secondly to predict the output flow and pressure as a function of the jet and receiver parameters.

As a result of this research, Reid made several suggestions as to the design of a receiver in order to obtain optimum pressure recovery. It was suggested that a short constant diameter entry section be provided upstream of the diffuser section in order to smooth the nonuniform jet velocity profile. The addition of this section was shown to prevent premature separation in the diffuser and thus improve overall pressure recovery. The best overall included angle for the conical diffuser was suggested to be from 5° to 8°.

Measurements were made of the overall static performance of a jet impacting upon a receiver. Shown in Figure 31 is a typical relationship between receiver pressure and flow rate as the downstream load conditions are varied. The receiver's volumetric flow rate and recovery gauge pressure, Q and P_e, respectively, have been nondimensionalized by the volumetric flow rate of the power nozzle, Q_0, and the power jet's excess pressure above ambient, P_0. For the experimental data obtained in Figure 31, the power jet's nozzle diameter was 1.94 inches while the receiver's entrance diameter was 3.0 inches. The decrease in blocked load pressure recovery, shown in Figure 31 as the nozzle-to-receiver spacing is increased, is due primarily to the spreading of the jet and the resulting decrease in centerline total pressure. The corresponding

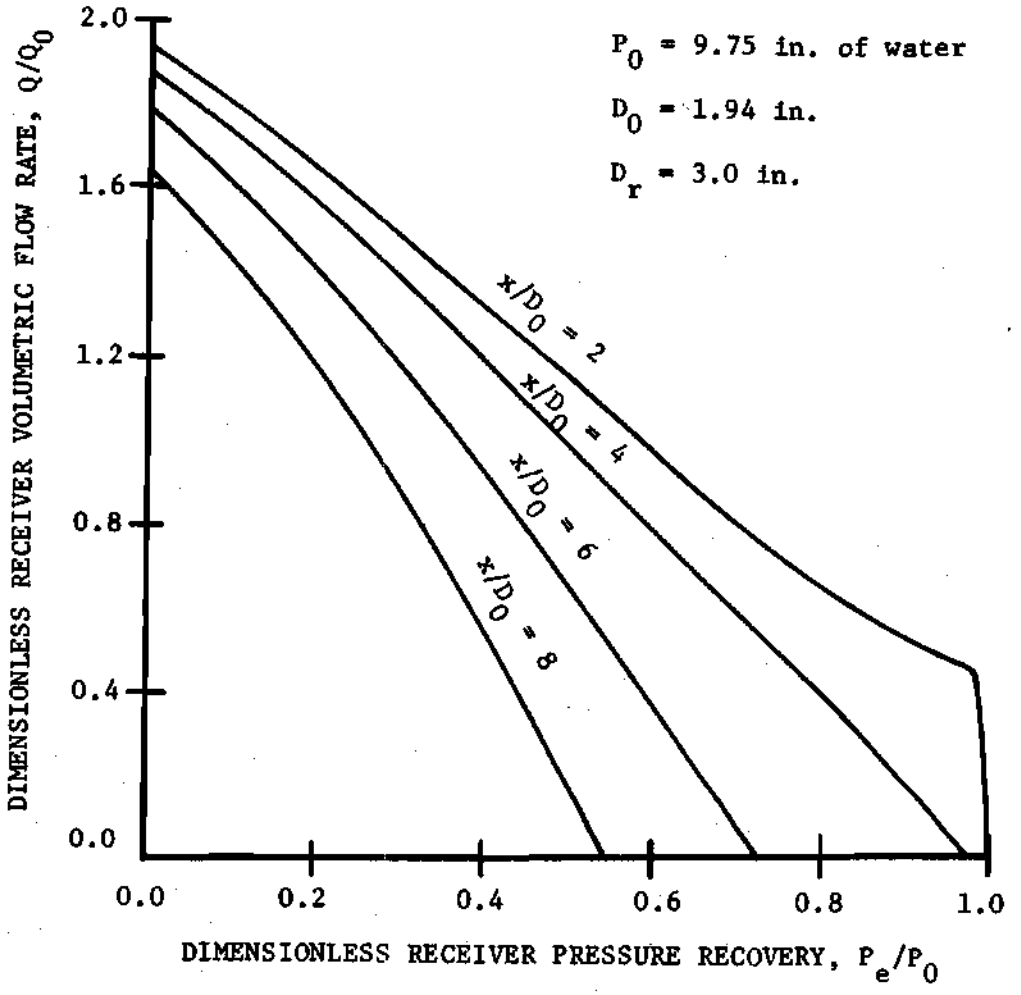

Figure 31. Pressure-Flow Characteristics for a Circular Jet Impinging on a Receiver from Reference [29]

decrease in open load flow recovery is also due to the diffusion of the free jet.

Using the analytical techniques proposed by Simson, described in the previous sections, Reid calculated the blocked load pressure and the open load flow rate for the case found in Figure 31. A comparison of the calculated characteristics and the experimental data is found in Table 1. This information indicates a significant error associated with this analytical technique. The disparity is especially severe at locations near the nozzle's exit plane.

The calculated blocked load pressure is in poor agreement with the experimental data. As a result of this disparity Reid suggested a better approximation of the blocked load pressure was the total pressure of the jet's centerline at the downstream position of the receiver. Reid indicated that this approximation fit the experimental data within a maximum error of six percent.

The calculated values of the open load flow rate were found to be significantly lower than those found experimentally. This effect was again more pronounced for locations nearer the supply jet. Reid attributed this phenomena to the induction of additional ambient air into the receiver.

Reid concluded that for the range of geometrical and operating conditions considered, free jet integrations are inadequate in describing limiting points on the pressure-flow curve. It should be pointed out, however, that the receiver diameter in Reid's study was large compared to the nozzle diameter. As the jet was allowed to spread and

Table 1. Comparison of Measured and Computed Maximum Pressure and Flow Recoveries

$\frac{X}{D_0}$	$\left(\frac{Q}{Q_0}\right)_c$	$\left(\frac{Q}{Q_0}\right)_e$	$\left(\frac{P_B}{P_0}\right)_c$	$\left(\frac{P_B}{P_0}\right)_e$
1	1.130	--	0.409	1.0
2	1.297	1.94	0.413	1.0
3	1.375	--	0.405	1.0
4	1.395	1.89	0.387	0.969
6	1.344	1.81	0.339	0.728
8	1.248	1.65	0.282	0.538
10	1.116	--	0.221	0.390
12	1.017	--	0.182	0.292

Subscripts:

c - Computed by integrating measured free jet (receiver removed) characteristics over area equal to receiver entrance area

e - Experimentally measured with receiver in place

obtain a larger size in relationship to the receiver, the technique described by Simson more nearly matches the experimental data.

Analytical Techniques for Jet-Receiver-Diffuser System Static Performance Prediction. Reid presented four simplified analyses in his thesis to describe the performance of an axisymmetric jet impinging upon a circular receiver section. Only cases where the jet and receiver centerlines were coincident were considered. In the first two of these analyses it is assumed that no jet mixing with the surrounding fluid occurs. This assumption limits the application of these analyses to positions very near the power nozzle's exit plane.

The third and fourth of Reid's analyses are based on the rather unique concept of a "cowl" or "dividing" streamline. It is assumed that a "dividing" streamline exists at the receiver inlet which separates the flow passing through the receiver and all remaining flow which is spilled over. Typical streamlines are sketched in Figure 32 as they are supposed to occur. Experimental data (radical pressure gradient measurements) indicate that streamline curvature changes from concave inwards to concave outwards as receiver back pressure is lowered. The use of this "dividing" streamline concept offers the advantage of eliminating the need to consider the details of the flow patterns at the receiver entrance plane.

In brief, Reid's analysis of jet receiver interaction using the "cowl" streamlines technique would proceed as follows. Firstly, the forces and momentum flux in the x-direction can be written on the control volume between a section in the undisturbed free jet h_0 and the

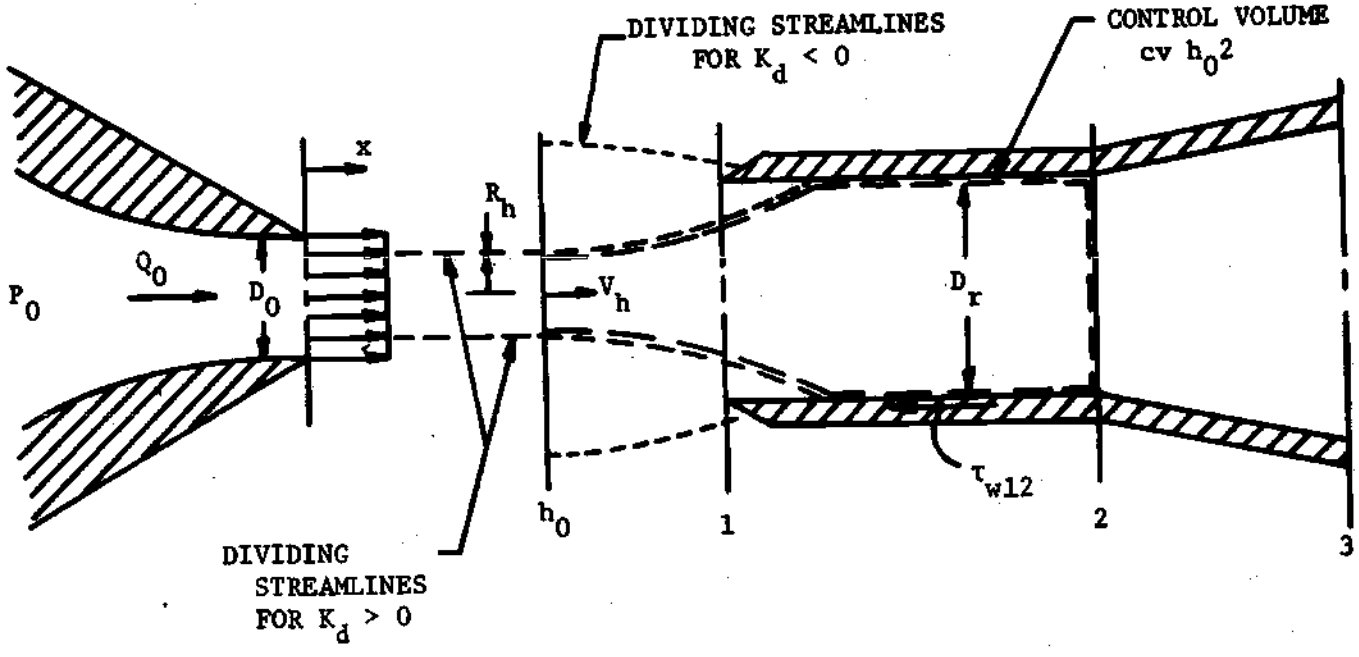

Figure 32. Physical Model for the "Cowl" Streamline Concept

end of mixing section 2. (It should be noted that since this control volume follows the free streamline that no flow passes through the control volume except at sections h_0 and 2.) Secondly, an expression for the pressure recovery across the area change diffuser section, that is section 2 to 3, is determined. Knowing the free jet characteristics, the location of h_0, the pressure forces on the free streamlines and the diffuser characteristics, an expression for flow rate through the diffuser as a function of recovery pressure can be determined. The drawback of this analysis is determining the position of section h_0 in the free jet and then evaluating the pressure forces exerted on the "cowl" streamlines. Unfortunately, no direct method is available for determining this information. Reid attempted to establish a data correlation to evaluate the location of section h_0 and the pressure forces in the x-direction on the "cowl" streamlines. Although this correlation appeared successful for several cases he concluded that insufficient experimental evidence existed for its general application.

CHAPTER II

EQUIPMENT AND INSTRUMENTATION

Experimental Model

Figure 33 is a sketch of the experimental model with important dimensions and features labeled. Included in this sketch is the supply port, control port and receiver-diffuser. It should be noted that during portions of the experimental program the control port and receiver-diffuser were removed. This was to allow for the investigation of free and interacting jet flows.

Air enters the experimental model's supply port and control port through a two inch and one inch diameter pipe, respectively. The air then flows through the supply and control port nozzle blocks into the model chamber. A four inch diameter pipe allows expulsion of exhaust air from the downstream end of the model. The one inch square steel bars which make up the sides of the experimental model are bolted to the 5/8 inch thick aluminum base plate. The supply port and control port chambers are similarly bolted to the base plate. A two inch thick plexiglass plate which covers the entire surface of the model is held tightly against the model's sides with "C" clamps distributed along the edges. With the plexiglass cover plate installed, the supply port and control port chambers rest against the cover plate and the entire one inch thick flow model is sealed from the ambient air.

A complete two-dimensional traverse of the flow field was obtained through the use of a sliding brass bar at the downstream end of

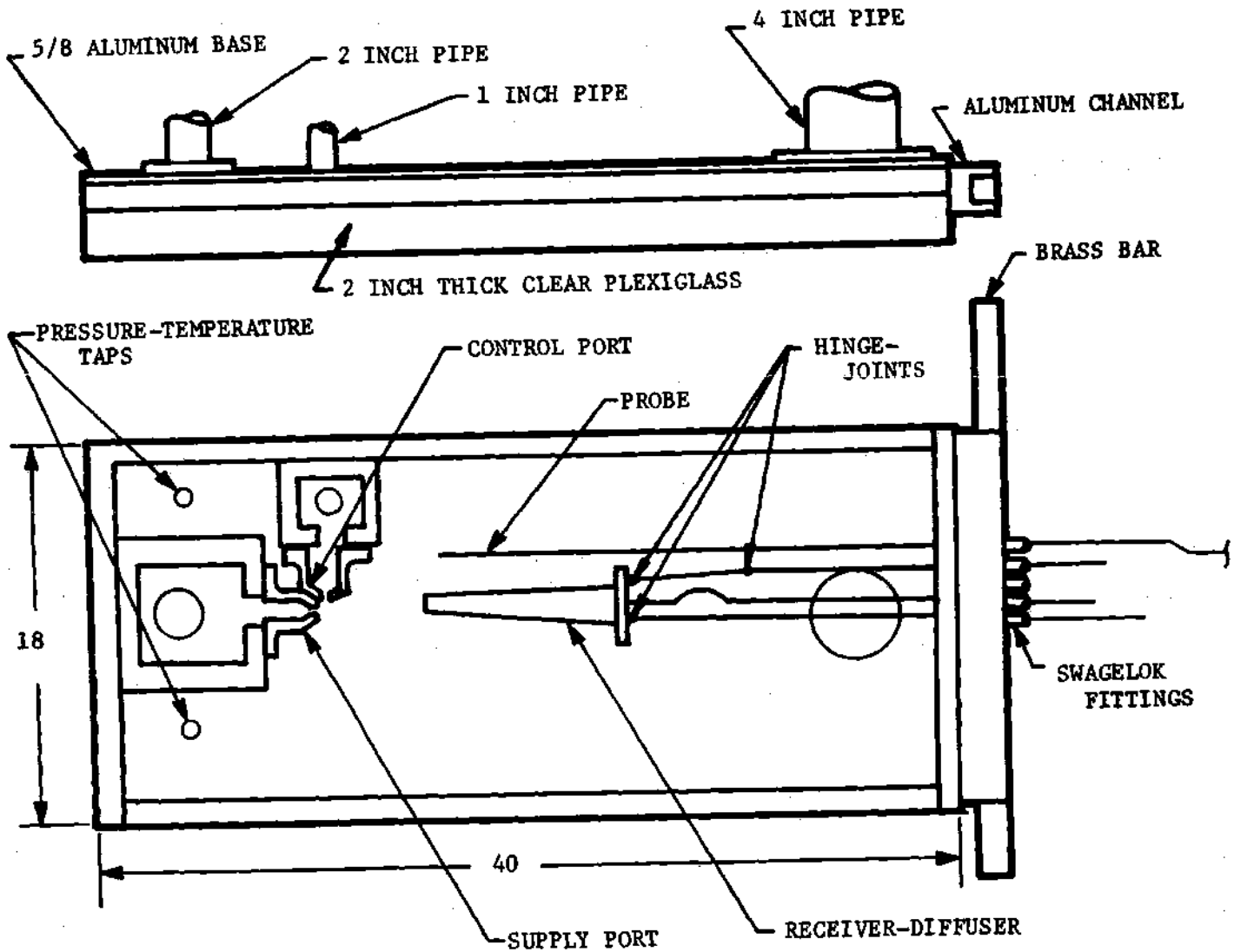

Figure 33. Experimental Model Sketch

the model. The brass bar slides in an aluminum channel which is bolted to the edge of the experimental model. The bar was positioned via a crank and gear arrangement. Probe access and connections to the model from the ambient are achieved through airtight Swagelok fittings in the bar and slotted holes through the channel and edge of the model. Longitudinal probe traverses were achieved by sliding the probes in and out of the model through the Swagelok fittings. Lateral probe traverses were accomplished by moving the bar in the channel.

Positioning of the receiver was accomplished in a similar fashion. The two rods which held the receiver were moved in and out giving longitudinal movement. Lateral motion was accomplished by moving the bar in the channel. The angle of the receiver's inlet in relation to the supply port's exit was also variable. This was accomplished with three hinge-joints. Two hinge-joints were inserted between the receiver base plate and the positioning rods. A third hinge-joint was inserted in the middle of the upper positioning rod. By moving the positioning rods relative to each other, the receiver angle could be varied.

The nozzle blocks used for the supply and control ports were identical in design. A representative sketch with pertinent dimensions is found in Figure 34. These blocks provide rectangular supply and control ports of 0.2 inch width and one inch height or a nozzle aspect ratio of five. The throats of these nozzles were in the form of a cylinder with a 0.75 inch radius. This design was easily fabricated and resulted in a short nozzle flow length, hence, a reduced jet boundary layer thickness at the nozzle's exit plane. The back of the nozzle

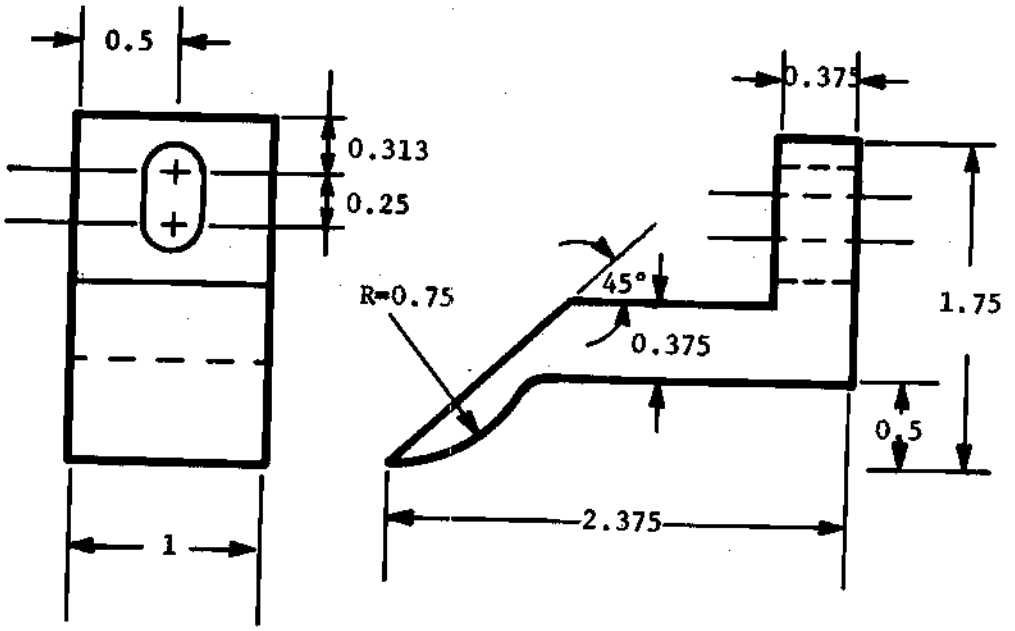

Figure 34. Nozzle Block Sketch

blocks was cut at an angle of 45°, thus allowing the supply and control port centerlines to be positioned at an angle of 90° without producing a dead air space between them.

Figure 35 is a schematic of the receiver-diffuser employed in this research with important dimensions and features labeled. This device is of a rectangular geometry with the receiver's side and back plates constructed of 7/8 inch thick aluminum. Attached to the side and back plates are top and bottom plates of 0.015 inch thick steel shim stock. The addition of the top and bottom plates prevents air from entering or leaving the receiver except at the devices entrance section or exhaust orifice. The receiver was constructed such that the top and bottom plates rested against the model's base plate and plexiglass cover plate, respectively, at the receiver's entrance. The devices flow thickness, however, was reduced gradually through the constant width entrance section to the 7/8 inch of internal flow thickness found in the diffuser section. The region in which the thickness is reduced is illustrated in Figure 35 as section A-A.

A short constant width entrance section was provided upstream of the area change diffuser in order to improve receiver performance as was suggested by Reid [29]. The included angle of the diffuser was 6°. This value is in accordance with suggestions for optimum diffuser performance by Kline [28].

A variable load was imposed upon the diffuser by modulating the distance separating a 3/4 inch circular disk and a 21/32 inch diameter hole in the back plate. The separation between the disk and the hole

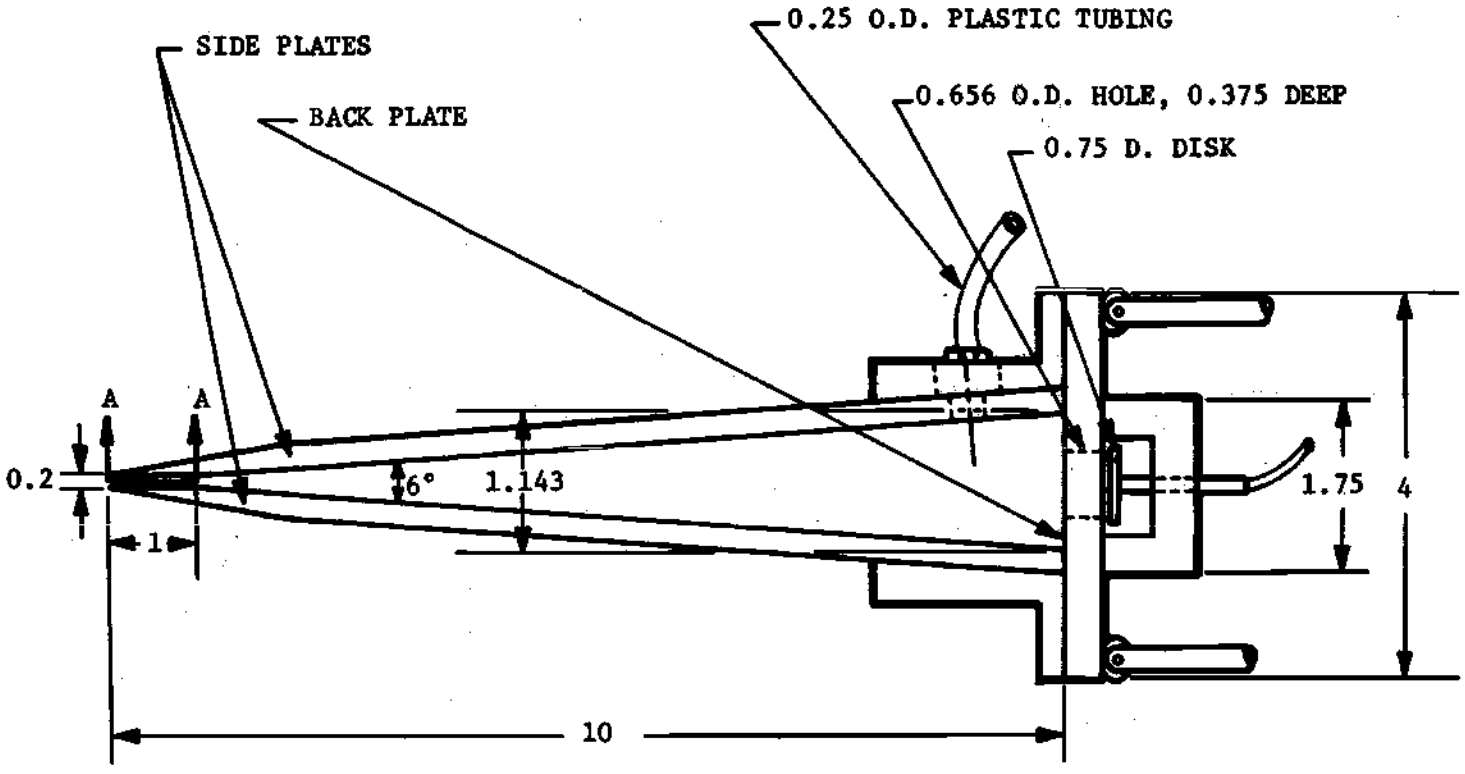

Figure 35. Receiver-Diffuser Sketch

was controlled by turning a rod which was inserted through an airtight fitting on the traversing mechanism. This rod drove through a flexible shaft to a 6-32 screw which was attached to the disk.

Static pressure at the receiver exit was measured by a wall tap in the device's side plate. Inserted into the tap is a Swagelok fitting and a flexible tube. This tube emerges from the experimental model into the ambient through a fitting on the traversing mechanism.

Figure 36 shows a photograph of the assembled experimental model. The plexiglass cover plate which seals the device during testing has been removed in order to show the model details more clearly.

Vacuum Pump

A very high volumetric displacement vacuum pump was required to pull the air through the experimental model at the desired ambient pressure. The pump used was a Beach Russ rotary piston vacuum pump capable of exhausting 1050 cubic feet of air per minute with atmospheric pressure at the pump inlet. The pump was mounted on a metal frame which was bolted to a wooden base composed of four inch by six inch timbers. A cylinder five feet long constructed of eight inch diameter pipe was connected to the pump's input manifold for use as a damper of any suction surges caused by the pump. Two short lengths of three inch diameter pipe were welded to the cylinder to provide for the model's exhaust flow into the pump. The vacuum pump exhaust flow was carried outside the building which housed the experimental equipment by a line composed of eight inch diameter pipe and sheet metal ducting.

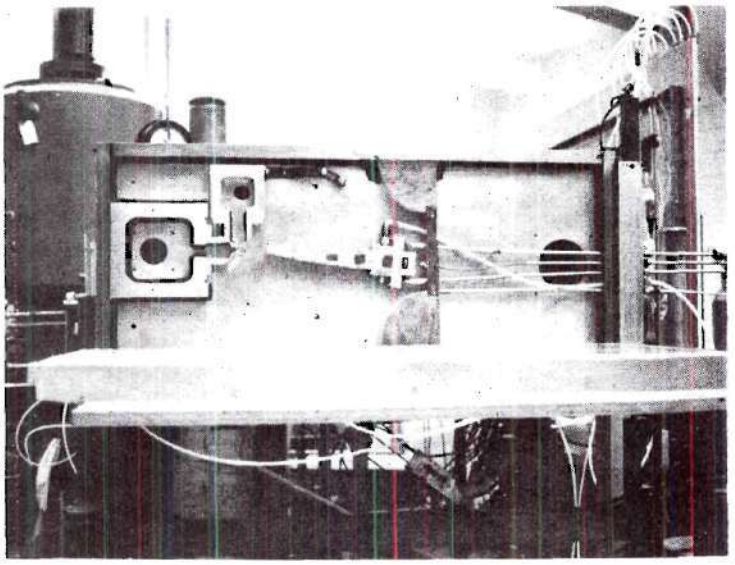

Figure 36. Photograph of Experimental Model

Support Equipment

Figure 37 is a schematic of the entire experimental apparatus with the major parts labeled. The air entering the apparatus from the atmosphere is first filtered and dried in a 30 inch thick bed of silica gel found within the desiccator. It is then filtered a second time to eliminate any silica gel dust that is swept up from the bed. After the second filtering the air flow splits. One portion goes to the supply reservoir and the other to the control reservoir. The mass flow rate of each flow is carefully measured by rotameters. These rotameters were calibrated using a water displacement procedure and then the calibration was checked to insure repeatibility. After leaving the respective rotameters the flows passed through banks of metering valves into the control and supply reservoir chambers. The supply reservoir was constructed of two 34 inch lengths of 10 inch diameter steel pipe. Baffles were arranged in the supply reservoir in such a manner that the supply air required four passes along the length of the pipe to flow through the device. The control reservoir was constructed from a 24 inch length of eight inch diameter steel pipe.

The air flowed from the control and supply reservoirs through the appropriate nozzles into the experimental model. This air was then discharged from the model through a four inch diameter pipe into the downstream tank. This tank is similar in shape to a standard cylindrical propane tank with domed ends; it's volume is approximately 18 cubic feet. The purpose of the tank is to provide a reservoir for the experimental model of sufficient volume to permit manual adjustment of the

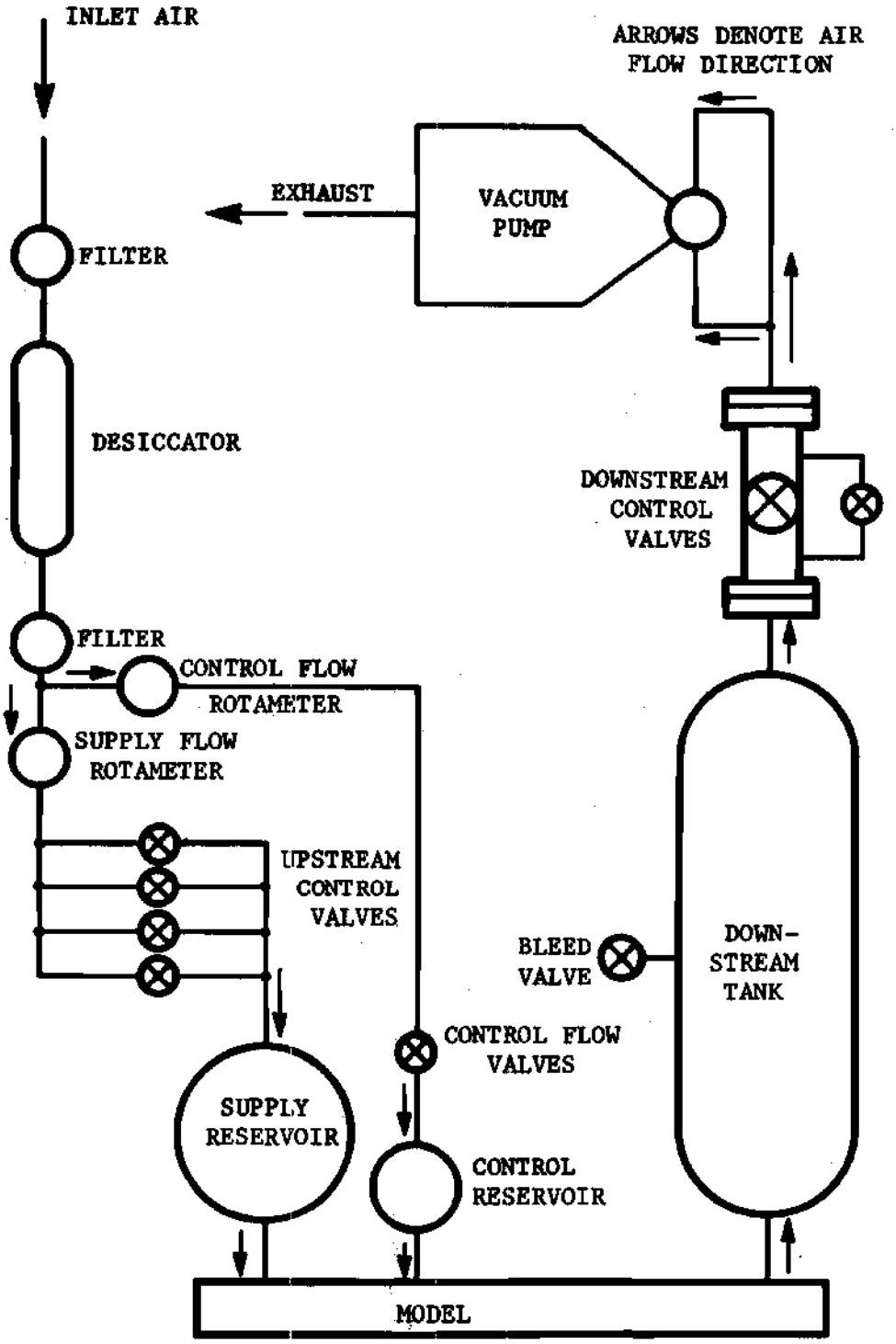

Figure 37. Experimental Apparatus Diagram

ambient pressure within the model. Located in the side of the downstream tank was a large bleed valve. This valve allowed injection of atmospheric air into the system downstream of the model.

Following the tank was the downstream control valves. These valves consisted of a one inch diameter bellows type vacuum valve connected in parallel with a four inch diameter butterfly valve. These two valves restrict the flow into the vacuum pump by reducing the effective flow area between the model and the pump.

Instrumentation

Probes and Sensors

Found in Figure 38 is a sketch of the probe used to measure the static pressure in the experimental model. The design of this device was based on a similar probe employed by Miller and Comings [8]. The static pressure probe was designed to minimize disturbances in the flow model. The probe's head was in the form of a 1/4 inch diameter brass disk. This disk was flat on top and receded from the sharp leading edge at an angle of 15°. In the center of the disk was a 0.021 inch diameter pressure sensing hole. The entire probe head was polished in order to reduce flow disturbances. The probe head was soldered to a 1/16 inch outside diameter, 1/64 inch wall thickness brass tube. This small brass tube was soldered to a 1/4 inch diameter brass tube a distance two inches downstream of the probe head. The 1/4 inch diameter tube slipped through a Swagelok fitting on the brass bar of the model's traversing mechanism and was connected to one leg of a "U" tube manometer with flexible tubing. The sensing hole in the probe head was

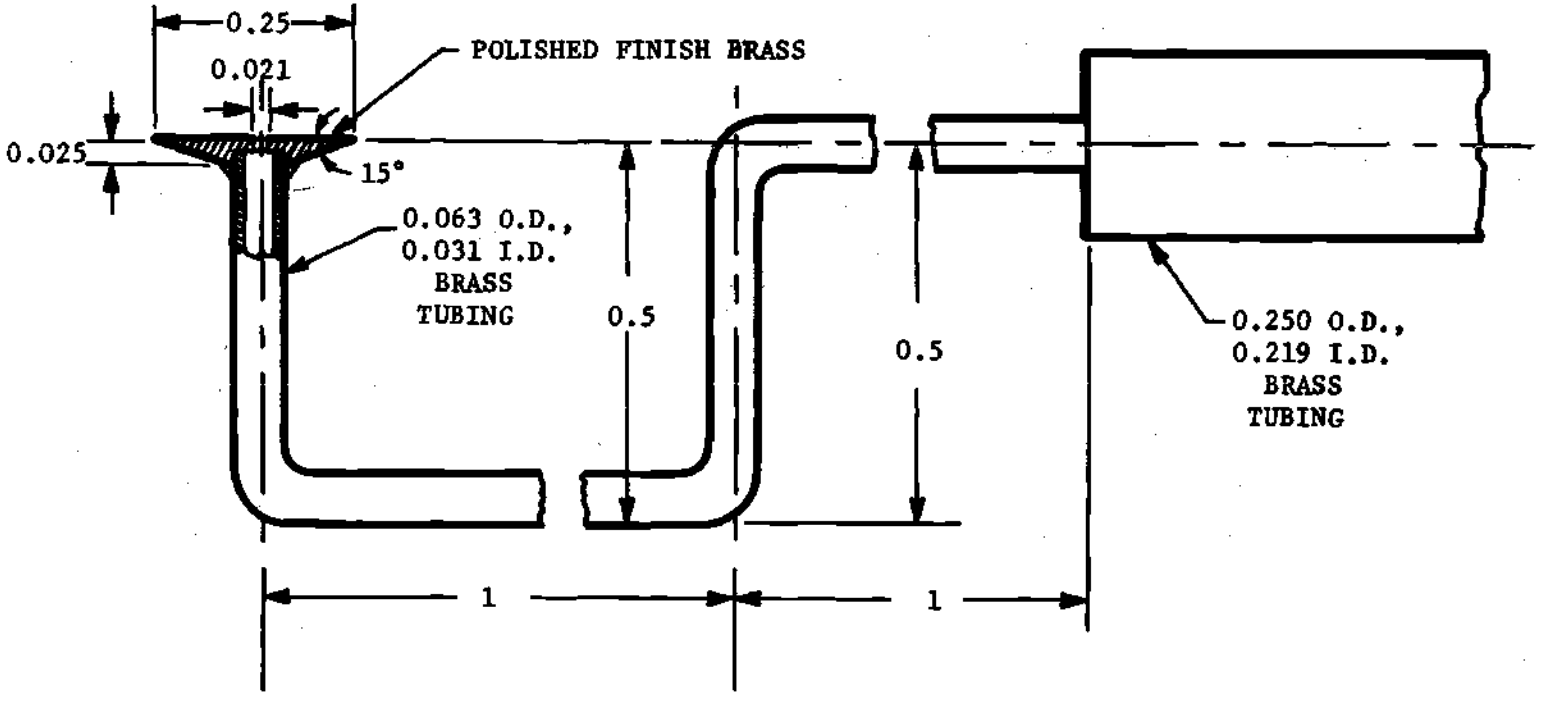

Figure 38. Sketch of Static Pressure Probe

maintained at a position 0.5 inches from the aluminum base plate and thus measured static pressure at the centerplane of the experimental model.

Static pressure was sensed in the supply reservoir, control reservoir and the experimental model by means of wall taps. The taps were constructed by inserting Swagelok fittings into drilled and tapped holes. Flexible tubing was employed to connect these pressures to "U" tube manometers.

Shown in Figure 39 is the velocity direction sensor employed in this research. The sensor is formed from a 0.1 inch long piece of flattened black sewing thread which was tied about a 0.03 inch diameter copper wire. The thread was tied such that it could move freely about the wire, however, would not slip off. It was maintained at a distance between 0.45 inch and 0.55 inch from the experimental model's base plate, and thus measured the direction of the velocity vector near the centerplane of the model. Soldered to the 0.03 inch copper wire was 1/16 inch diameter brass tubing. This tubing extended 5.5 inches downstream where it attached to 1/4 inch diameter brass tubing. The larger tubing, which was solder plugged, slipped through a fitting in the traversing mechanism.

The impact probe which was used to obtain total pressure is shown in Figure 40. The device is constructed of five inches of 1/8 inch outside diameter, 1/64 inch wall thickness brass tubing which is soldered to 1/4 inch outside diameter, 1/64 inch wall thickness brass tubing. The tip of the device is shaped to provide a sharp edge with

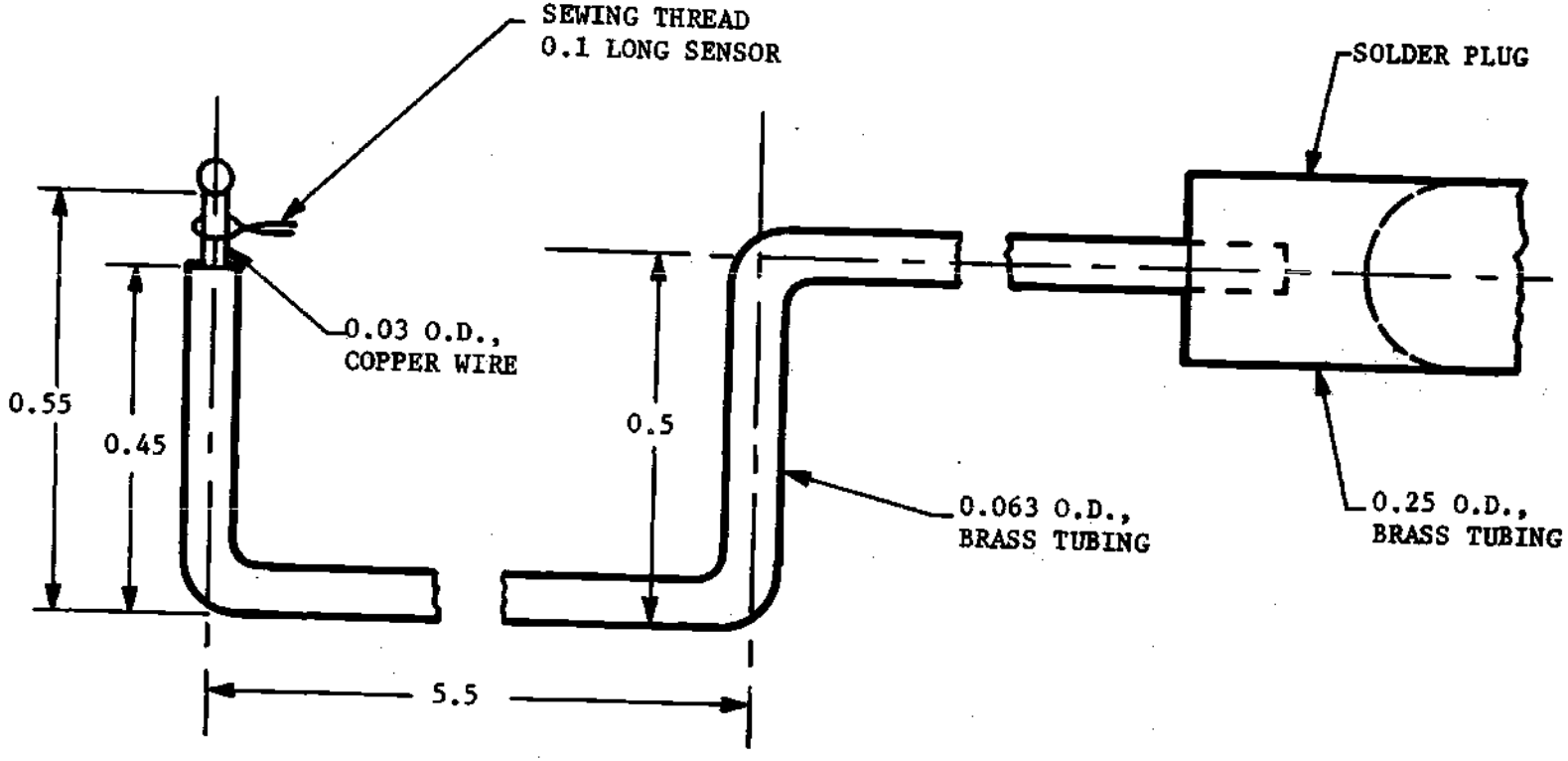

Figure 39. Velocity Direction Sensor

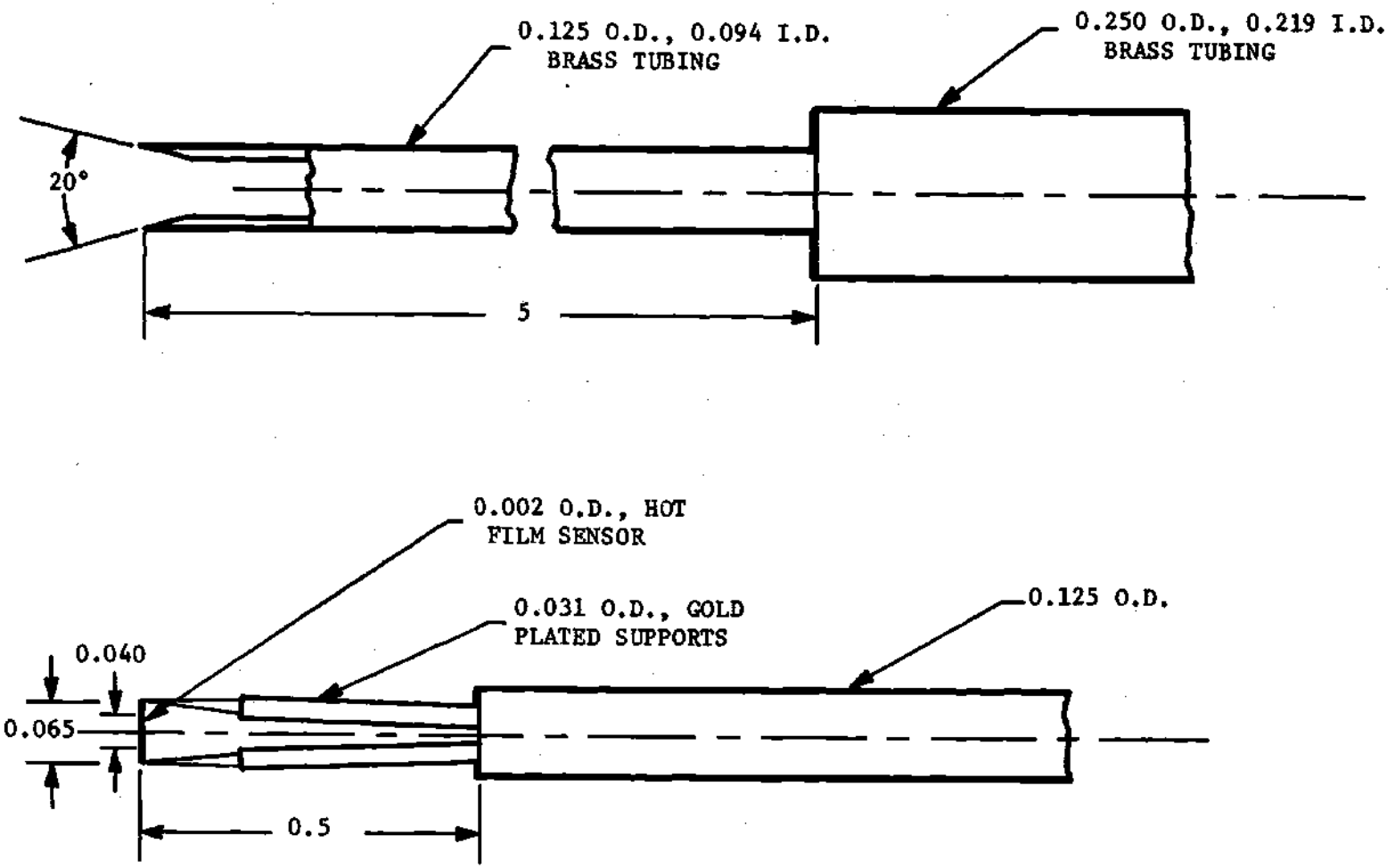

Figure 40. Velocity Sensors

a 20° included angle. This shape is recommended by Sherman [30] to provide the most accurate pressure measurements at low Reynolds number conditions. The 1/4 inch diameter tubing slipped through a fitting on the traversing mechanism and was connected to one leg of a "U" tube manometer by flexible tubing.

A sketch of the hot film anemometer sensor is shown in Figure 40. This device was used to measure both steady state and fluctuating components of velocity in the experimental study. The tip was a Thermal Systems Incorporated Model 20 sensor. It was in the form of a cylindrical glass rod 0.065 inch long with a diameter of 0.002 inch. The sensing material was a film of platinum which extended a distance of 0.040 inch on the sensor. The cylindrical sensor was held in place by two gold plated supports of 1/32 inch diameter which extended back 1/2 inch to the electrical connector. The electrical connector slipped through an airtight fitting on the traversing mechanism. It was anticipated that the small size of the anemometer sensor would produce a minimum flow disturbance. This element was supported 1/2 inch from the aluminum base plate and thus measured the flow field at the centerplane of the model.

Static temperature was sensed in the supply reservoir, control reservoir and in the experimental model by the thermocouple probe shown in Figure 41. These copper-constantan thermocouples were cast in epoxy inside 1/4 inch diameter brass tubing. They were inserted into the appropriate locations through Swagelok fittings which provided an airtight seal.

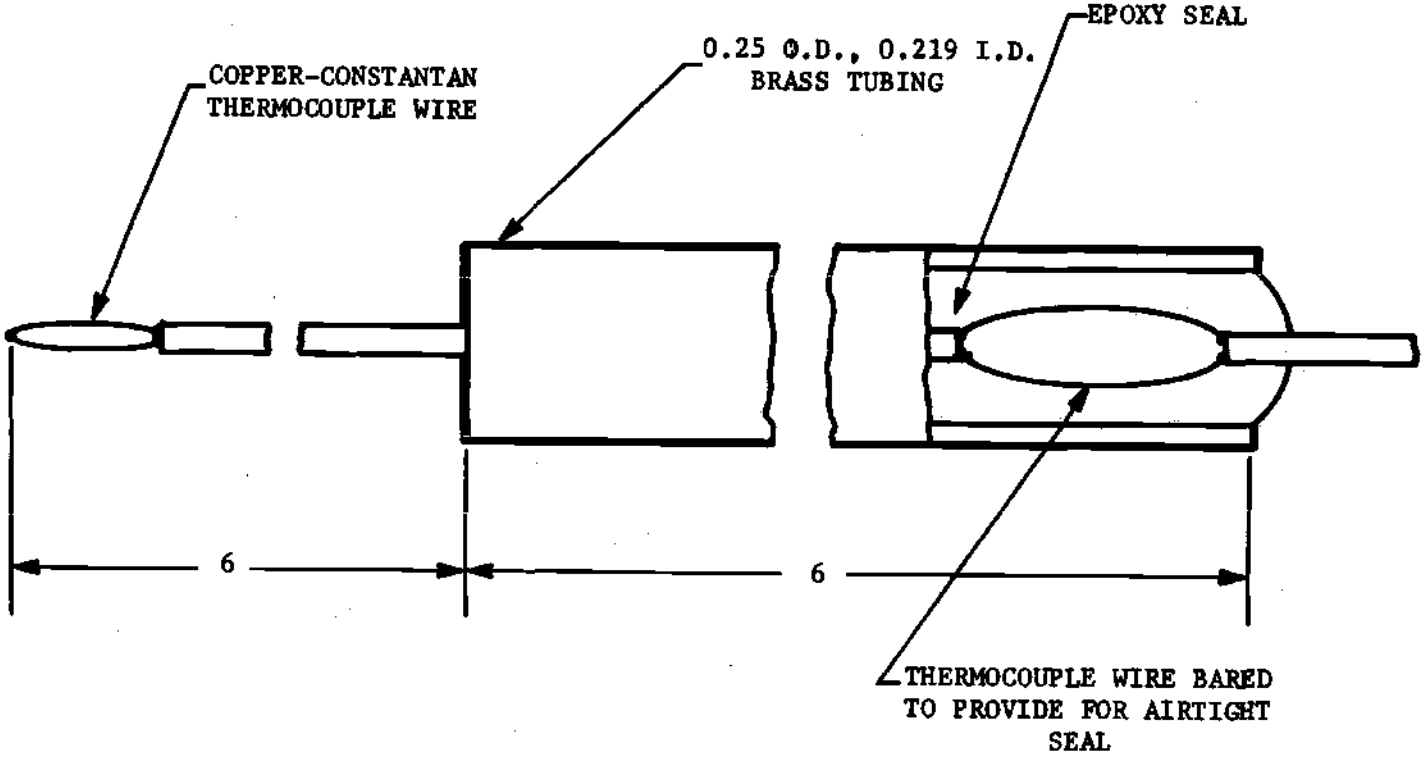

Figure 41. Thermocouple Probe

Static Pressure Measurements

"U" tube manometers were employed to measure the static pressure in the supply reservoir, control reservoir and in several pressure probes. The manometer indicating fluid is red Meriam manometer oil which has a specific gravity of 1.04. It is a very low vapor pressure indicating fluid and thus is suitable in high vacuum applications. One leg of each manometer was connected to the appropriate location on the experimental apparatus while the other leg was connected to the model. This established the static pressure in the experimental model as the reference for these differential pressure measurements. The static pressure in the model was determined by two methods, depending upon its magnitude. A calibrated McLeod gauge was employed to measure the model's absolute pressure for values of less than one mm. hg., while an absolute "U" tube manometer was used for pressures above one mm. hg. One leg of this absolute manometer was connected to the experimental model and the other to a low pressure reservoir. A small vacuum pump was utilized to maintain this reservoir at approximately 0.05 mm. hg.

Several safety features were incorporated into the pressure measuring system to prevent the discharge of manometer oil into the experimental apparatus as a result of mechanical failure or improper procedure. Traps were inserted into the flexible tubing which ran from the manometers to the experimental apparatus. These devices were designed to prevent manometer oil from being discharged into the system. Valving was provided on the absolute "U" tube manometer which vented across the manometer legs and disconnected the small vacuum pump from

the circuit during experimental apparatus start up and shut down transients.

A cathetometer was used to measure the differential height in the oil columns of the "U" tube manometers. This device was located on a table in front of and approximately three feet away from the manometer board. A lighting system was provided upon the manometer board to establish proper illumination for these optical measurements. A photograph of the static pressure measurement equipment is found in Figure 42.

Anemometer Support Equipment

Electronic support equipment for the hot film anemometer included a Thermal Systems Incorporated Model 1050 constant temperature anemometer module. This module included the electrical bridge, variable control resistor, voltage readout and output voltage signal conditioner. A Thermal Systems Incorporated Model 1060 true rms voltmeter was used in connection with the basic module for measurements of turbulent fluctuations. An oscilloscope was employed along with a 50 Hertz low pass filter and a voltage potentiometer to measure the steady state component of velocity at low density levels. A photograph of the anemometer support equipment used in this research is found in Figure 42.

Static Temperature Measurements

Static temperature measurements were made via copper-constantan thermocouples. The output voltages from these devices were connected through a thermocouple switch to a potentiometer circuit. The cold

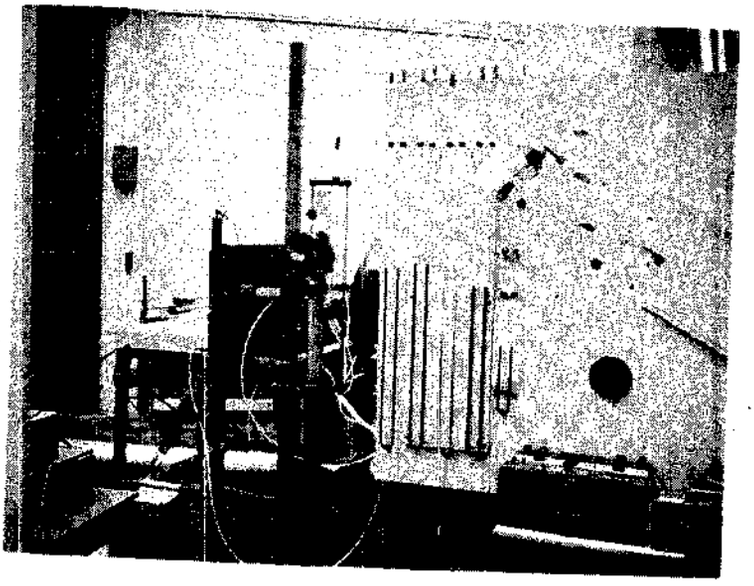

Static Pressure Measurement Equipment

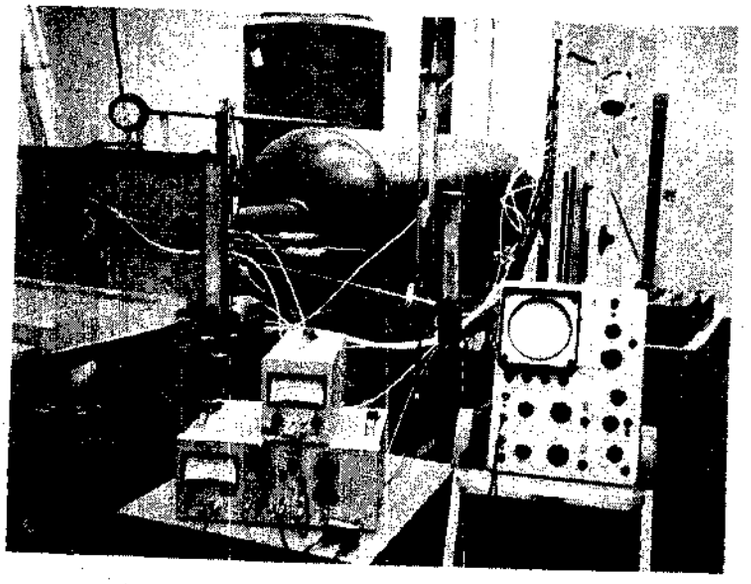

Anemometer Support Equipment

Figure 42. Instrumentation Photographs

junction of this circuit was maintained at 32°F in an ice bath. Temperatures were computed with standard thermocouple tables.

CHAPTER III

PROCEDURE

Preliminary Considerations

The experimental investigation was divided into three segments which consisted of free jet studies, jet interaction studies and studies of the interaction of a jet upon a receiver-diffuser. Before these investigations were conducted, however, extensive checks and calibrations were performed on the experimental apparatus. The first step of these checkout examinations consisted of testing for leakage under positive pressure. This was accomplished by sealing the system from the supply and control rotameter inlets to the downstream control valves and then pressurizing the apparatus. A solution of soap and water was applied to all joints and seals of the experimental equipment. The formation of bubbles indicated leaks which were subsequently repaired with either Glystol or Apiezon Q sealant.

After all detectable leaks in the experimental equipment were eliminated in the previously described fashion, tests were performed to determine the magnitude of the leakage remaining. This was accomplished by evacuating individual elements through a line containing an airtight valve. After sufficient outgassing time the line was sealed and the rise in pressure as a function of time was determined by a mercury filled "U" tube manometer. From the calculated volume of the element and the observed rise in pressure with time, the maximum leakage

of important portions of the experimental apparatus was determined. The leakages in the control and supply reservoirs from the respective rotameters to the model were determined to be 1.08×10^{-8} lbm./min. and 1.49×10^{-6} lbm./min., respectively. These flow rates represent approximately 0.01 percent of the minimum flow rates which passed through these reservoirs in the experimental study. The leakage rate in the experimental equipment from the inlet of the control and supply rotameters to the downstream control valves was determined to be 2.79×10^{-4} lbm./min. This represents 2.2 percent of the minimum flow rate through the supply port in this investigation. It should be noted that the majority of this flow was located within the traversing mechanism at the downstream end of the model. This fact was ascertained by temporarily sealing the traversing mechanism and then observing the reduced leakage rate. The leakage in the traversing mechanism was considered acceptable in this research since its magnitude was small and it was located well downstream of the supply port.

Preliminary investigations were made to insure the accuracy of the various manometers and the McLeod gauge. The first step of this procedure was to check the glass portions of these devices for leaks while under a vacuum with an electrical discharge detector. The instruments were then checked for leaks by pressurizing and applying a soap and water solution to all connections. Upon the successful completion of this procedure, both legs of the "U" tube manometers were connected to a common pressure point and then evacuated to a low pressure. The cathetometer was then employed to insure that no differential oil column

existed. This was achieved for each manometer to within the accuracy of the cathetometer which is 0.05 mm. of indicating fluid. The McLeod gauge, which was previously calibrated, was checked against the absolute "U" tube manometer to insure its calibration.

The temperature and pressure probes were checked before the experimental investigations were conducted. The temperature probes were calibrated at room temperature and at the boiling temperature of water to insure their accuracy. The three probes were found to indicate the same temperature to within 0.5°F under these conditions. The static pressure and the impact pressure probes were checked for leakage by pressurizing these devices while immersed in a liquid bath.

Calibration of the Anemometer and Associated Instrumentation

Two devices were considered before a hot film anemometer was chosen to measure the flow field in this research. A corna discharge probe which operates on the principle of varying drift speeds of ionized gas between charged electrodes was considered. This device was not employed because it had been previously demonstrated to have an unpredictable useful life. Standard impact and static pressure probes were initially considered since they are easy to construct and normally required no calibration. In this research, however, several disadvantages were associated with this method of measuring velocity. Firstly, this method only provides information on the steady state components of velocity in the flow field. Secondly, under the low Reynolds number conditions of this research the probe would have to be calibrated to

provide accurate steady state velocity measurements. In order to measure the velocity at a point in the flow field of the jet, the impact probe must be necessarily small in comparison to the jet. A small probe operating at the conditions encountered in this research would be at a very low Reynolds number. Sherman [30] has shown that calculation of velocity from inviscid perfect gas relationships for the probe shown in Figure 40 are in error for Reynolds numbers less than approximately 70 based on free stream conditions and probe diameter.

The hot film anemometer was ultimately chosen due to its small size and consequently minimum flow restriction, its ability to be used in the continuum through free molecular flow regime, and its capability to measure both steady state and fluctuating components of velocity. A hot film sensor was chosen over a hot wire sensor element due to its demonstrated strength, stability and life which outweighed its reduced sensitivity. The disadvantage of the anemometer system is the necessity for accurate calibration.

The calibration of the anemometer is necessary since the device measures the heat transfer from a sensing element which is suspended in the flow field. The heat transfer from the sensor is in general a function of a number of variables, however, for the case of a fixed sensor geometry, sensor temperature, air stagnation temperature and ambient pressure the heat transfer is only a function of velocity for a single gas. In the calibration and subsequent research a single anemometer sensor which was maintained at a constant temperature was employed. The measured value of the total temperature in the gas was found to be

essentially constant for an experimental run. However, over a period of several months the total temperature was found to vary less than 5°F about the value 72°F. The device was subsequently calibrated with respect to the previous constraints to provide a voltage signal which is a function of velocity at a fixed ambient pressure. Calibration data were taken for model pressures of approximately 0.51 mm. hg., 1.0 mm. hg., 2 mm. hg., 5 mm. hg., 10 mm. hg. and 20 mm. hg. These pressures were maintained constant during the calibration studies and subsequent research to a maximum pressure variation of ±0.0115 mm. hg.

Calibration of the device consisted of determining the voltage drop across the sensor as a function of a known velocity for the previously mentioned conditions of a fixed gas, sensor, stagnation temperature and model pressure. The velocity field used for the calibration was the undisturbed jet flow issued from the model's supply port. The anemometer was inserted into this flow at a position of known velocity and the voltage from the device measured. Two different methods were employed to determine the velocity of points in the field for the calibration procedure. The first method used the impact tube shown in Figure 40. The second consisted of determining the velocity of the core region from the pressure ratio and stagnation temperature by using inviscid perfect gas relationships.

At several intervals in the research the anemometer calibrations were checked. No detectable shift in the calibrations was detected by this procedure. A complete description of information pertinent to the anemometer calibration is given in Appendix A.

Experimental Procedure

Prior to each experiment the brass bar and the aluminum channel of the traversing mechanism were covered with a thin layer of vacuum grease. If the plexiglass cover plate had been removed between experiments, it was resealed. This was accomplished by first cleaning and then coating with a thin layer of vacuum grease the plexiglass plate and one inch ridge upon which it rested. The cover plate was then attached firmly to the model with "C" clamps.

The initial step of each experimental run was to evacuate the apparatus to a low absolute pressure. This was required to eliminate accumulated moisture and contamination from the apparatus. During this procedure no air was allowed to flow through the control valves and thus the system was at a common pressure. The "U" tube manometers were checked with the cathetometer during this period to insure that no differential oil columns were present. The seal between the plexiglass cover plate and the model was also checked visually to insure no leakage paths into the apparatus had developed.

Upon the completion of an outgassing period of sufficient length to obtain a low system pressure, the experimental flow was established. The first step of this procedure was to allow a large quantity of flow through the bleed valve (in comparison to the flow through the supply and control ports) into the downstream tank. The downstream control valves were then adjusted until the proper model ambient pressure was obtained. The upstream valves were subsequently opened and the proper conditions were established across the supply and control ports. The

introduction of flow through the supply and control valves slightly upset the model pressure and thus readjustment of the model pressure with the downstream control valves was required. Upon the establishment of the proper flow conditions, the pressures in the apparatus were monitored for approximately one hour to insure steady state had been achieved.

Free Jet Investigations

The absolute pressure in the experimental model and the differential pressure across the supply nozzle were used in this investigation to establish the flow conditions of the free jet. The model pressure was monitored during the course of an experiment and maintained constant by manually adjusting the system's downstream control valves to within a maximum pressure error of ±0.0115 mm. hg. The differential pressure across the supply port was maintained constant during an experimental run to within ±0.0038 mm. hg. by manually adjusting the flow rate through the upstream control valves.

Static Pressure Measurements in the Free Jet. Measurements were made of the static pressure in the experimental jet flow with the probe shown in Figure 38. The validity of the probe's readings was checked by utilizing three 3/32 inch wall pressure taps in the aluminum base plate. The differential pressure between the jet and the model was obtained with an oil filled "U" tube manometer. A cathetometer with an accuracy of approximately 0.05 mm. of oil was utilized to measure the differential oil column height. A second cathetometer was used to measure the lateral position of the probe's sensing hole in relation to the supply

jet's nozzle blocks. Longitudinal position of the probe was controlled by markings on the aluminum base plate. The lateral position measurements of the probe are accurate to within an estimated accuracy of 0.05 mm.

Velocity Direction Measurements in the Free Jet. Measurements were made of the direction of the velocity vector with the probe shown in Figure 39. The angular deflection of the probe's sensor was determined optically with a projector and a cathetometer. The projector was attached to the experimental model's cover plate. The cathetometer was used first to measure the lateral position of the probe with respect to the nozzle blocks, and then the hairline on the instrument was aligned with the probe's sensor. The hairline image was transferred to the projector where the differential angle from normal was measured. The estimated error associated with this procedure is approximately 1/2° of angle. The estimated error in the lateral position measurement of the sensor is approximately 0.05 mm.

Fluctuating and Steady State Velocity Measurements. The steady state and fluctuating components of velocity in this study were measured with the anemometer sensor shown in Figure 40 and associated electronic instrumentation. The lateral position of the sensing element was obtained with a cathetometer to within an expected accuracy of 0.05 mm. The longitudinal position of the probe was controlled optically with reference to marks on the aluminum base plate. The calculation of steady state and fluctuating components of velocity from anemometer data and an analysis of the uncertainty associated with these measurements is

described in Appendix B. The uncertainty analysis indicated the maximum uncertainty in the measurement of the mean velocity is 22.31 ft./sec. This uncertainty represents approximately three percent of the maximum velocity measured at that pressure level. The maximum percentage uncertainty in the fluctuating component of velocity which is reported in this investigation was computed to be 8.18 percent.

Jet Interaction Investigation

The absolute pressure in the experimental model and the differential pressures across the supply and control port nozzles were used in this study to establish the flow condition. The absolute pressure in the experimental model was monitored and maintained constant during an experimental run to within a maximum pressure error of ±0.0115 mm. hg. The differential pressures across the supply port and control port were maintained constant by manual adjustment of the respective flow rates to within ±0.0038 mm. hg.

Studies were made of the velocity profiles, direction of the velocity and the static pressure distribution in the jet which resulted from the interaction of the supply and control port flows. These measurements were made using the same procedures discussed in the free jet investigation.

Jet Interaction with a Receiver-Diffuser

The experimental equipment in this portion of the research was identical to that in the jet interaction investigation except for the addition of the receiver-diffuser shown in Figure 35. The flow condition in the model was established based on the model's absolute pressure

and the differential pressure across the control and supply ports. The receiver's downstream position and angular offset from the centerline of the supply port were determined optically with relation to marks scribed on the model's base plate. The uncertainties in these linear and angular positions are estimated to be 0.01 inch and 0.5 degrees of angle, respectively.

Measurements were made of the static pressure in the receiver by a wall tap which was connected to an oil filled "U" tube manometer. These measurements were obtained for various combinations of diffuser loadings, deflected jet conditions, receiver setbacks and receiver offset angles at prescribed values of absolute model pressure. The loading conditions on the receiver were obtained by modulating a flat disk on a hole. The load was varied in discrete turns of the disk and was precisely determined by alignment marks on the disk and receiver.

CHAPTER IV

FREE JET EXPERIMENTS

Experimental Data

A complete collection of the experimental data which describes the structure of a free jet in the low Reynolds number compressible flow regime is presented in Appendix C. These data include time-average and fluctuating velocity measurements for 15 flow cases as well as static pressure and velocity vector measurements for several conditions. Reynolds number and Mach number based on the measured state at the centerline of the nozzle's exit plane and nozzle width are employed to describe the flow conditions in this research. The expressions used to calculate these nondimensional parameters along with a sample calculation are presented in Appendix C.

Free Jet Structure

The Reynolds and Mach number range of the present investigation is compared to those of previous studies of two-dimensional free jet flows in Figure 43. The flow regime considered in this research is bordered by both the high Reynolds number turbulent jet studies of Miller and Comings [8] and Olson and Miller [13] as well as the low Reynolds number laminar jet investigations of Chanaud and Powell [18]. It is interesting to note that the impact pressure studies of Anderson [21] overlap a portion of the present experimental regime. In the next section a qualitative description will be made of the jet's flow

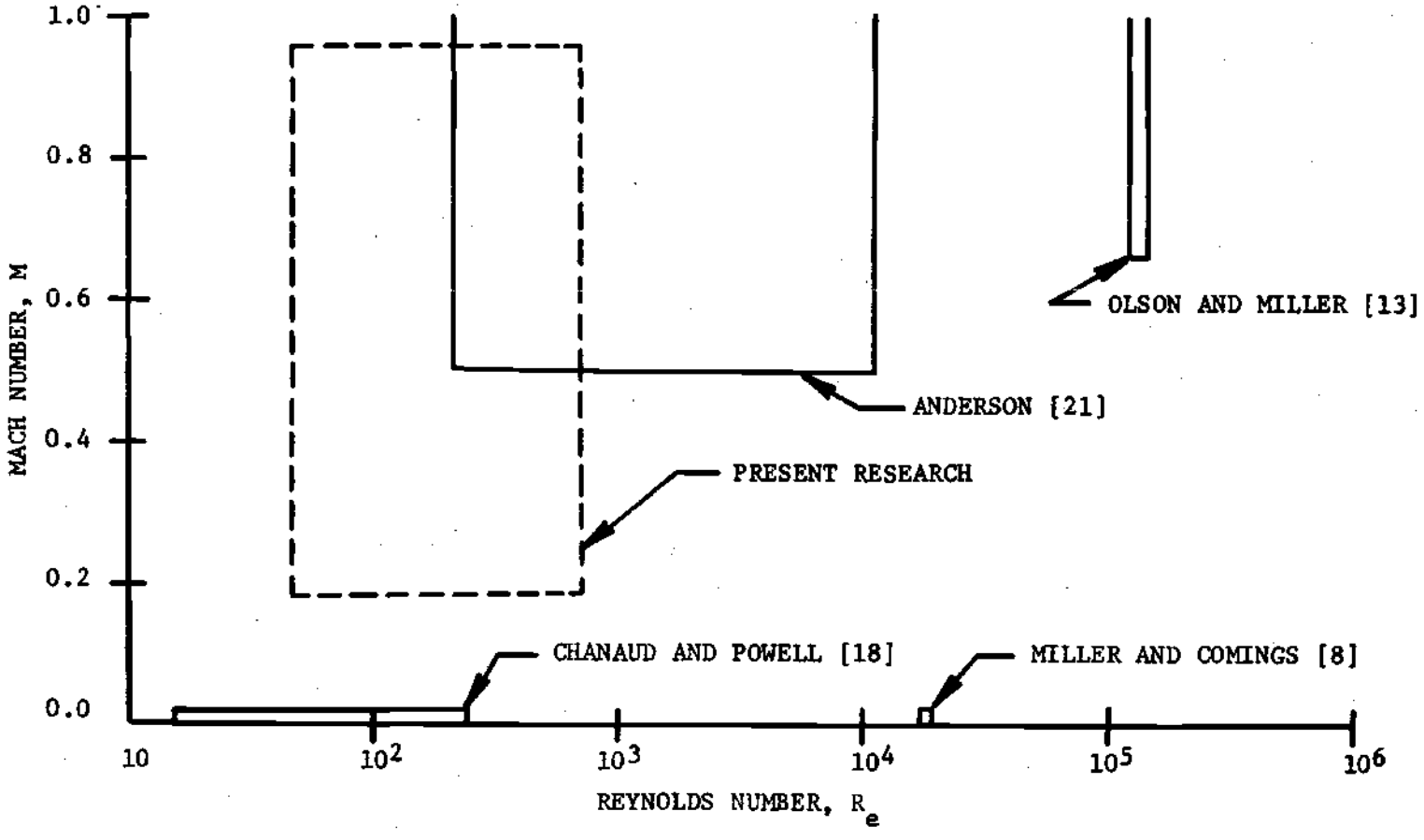

Figure 43. Comparison of Present Flow Regime to Previous Investigations

structure in the low Reynolds number compressible flow regime. Upon the completion of this description, data from this regime will be compared to data from previous investigations as well as analytical expressions for the limiting cases of laminar and turbulent plane jet flow.

A general description of the jet's flow structure in this regime may be made by considering the experimental data presented in Figures 44 through 48. In Figure 44 a plot of jet centerline velocity as a function of downstream position is presented for four flow cases. Profiles of the time-average and fluctuating components of velocity for several downstream stations for these same conditions are presented in Figures 45 through 48. These data illustrate the change of the flow structure as lower Reynolds number conditions are approached.

The data from this investigation demonstrate the importance of the turbulent mechanism on the structure of a free jet in this flow regime. This effect may be illustrated by examining the centerline velocity decay and profile spread rate for several flow conditions as a function of the growth and intensity of the turbulent shear layer. Figures 44 and 45 show the characteristics of a flow with a Reynolds number of 546 and a Mach number of 0.183. Two separate and symmetric turbulent shear layers are found near the nozzle exit plane in Figure 45 for this flow condition. The root mean square velocity measurements indicate these shear layers are rather narrow and of low turbulent intensity. The shear layers are shown to spread in the downstream direction while the turbulent intensity remains low until the layers intersect. After

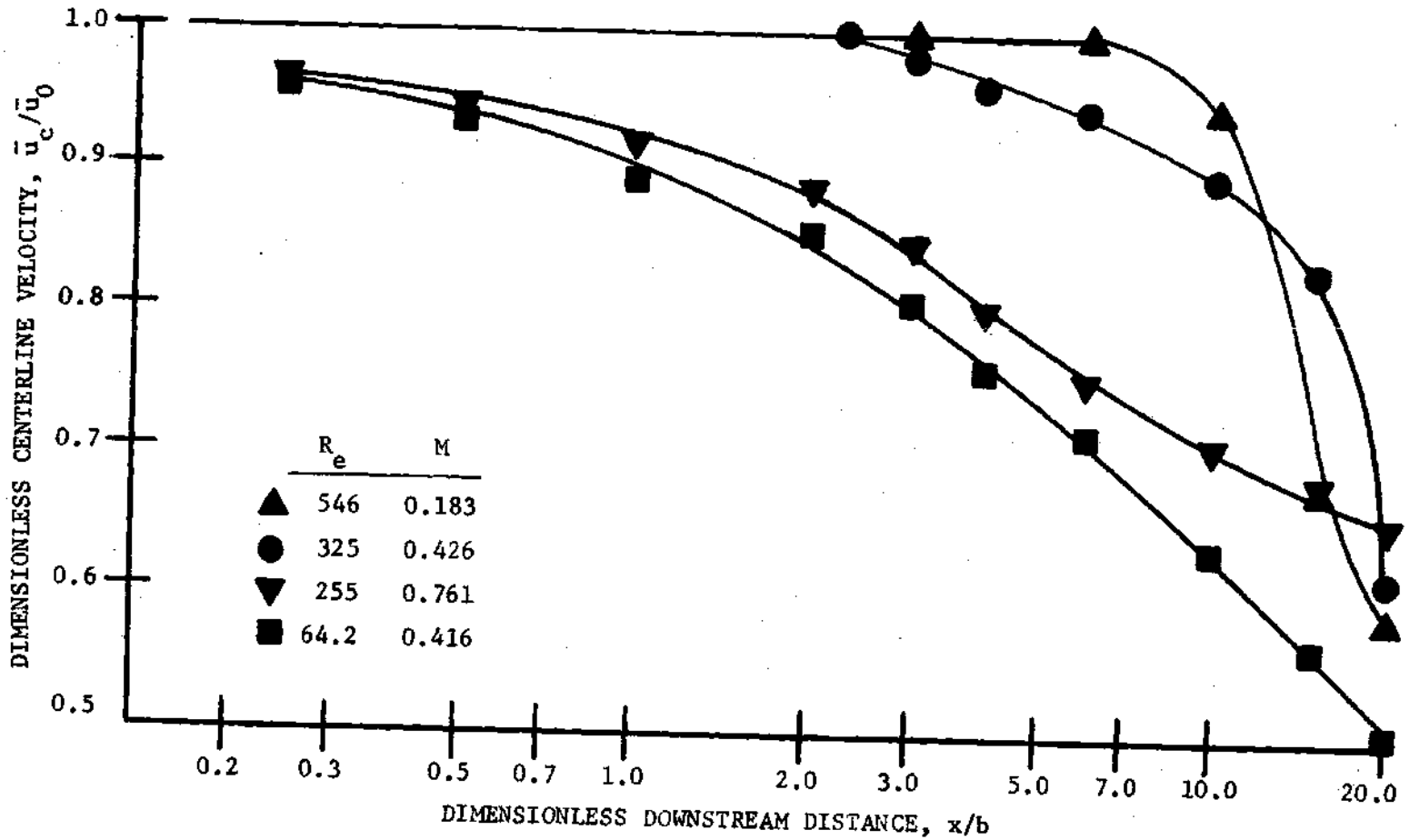

Figure 44. Centerline Velocity Decay Rate Data

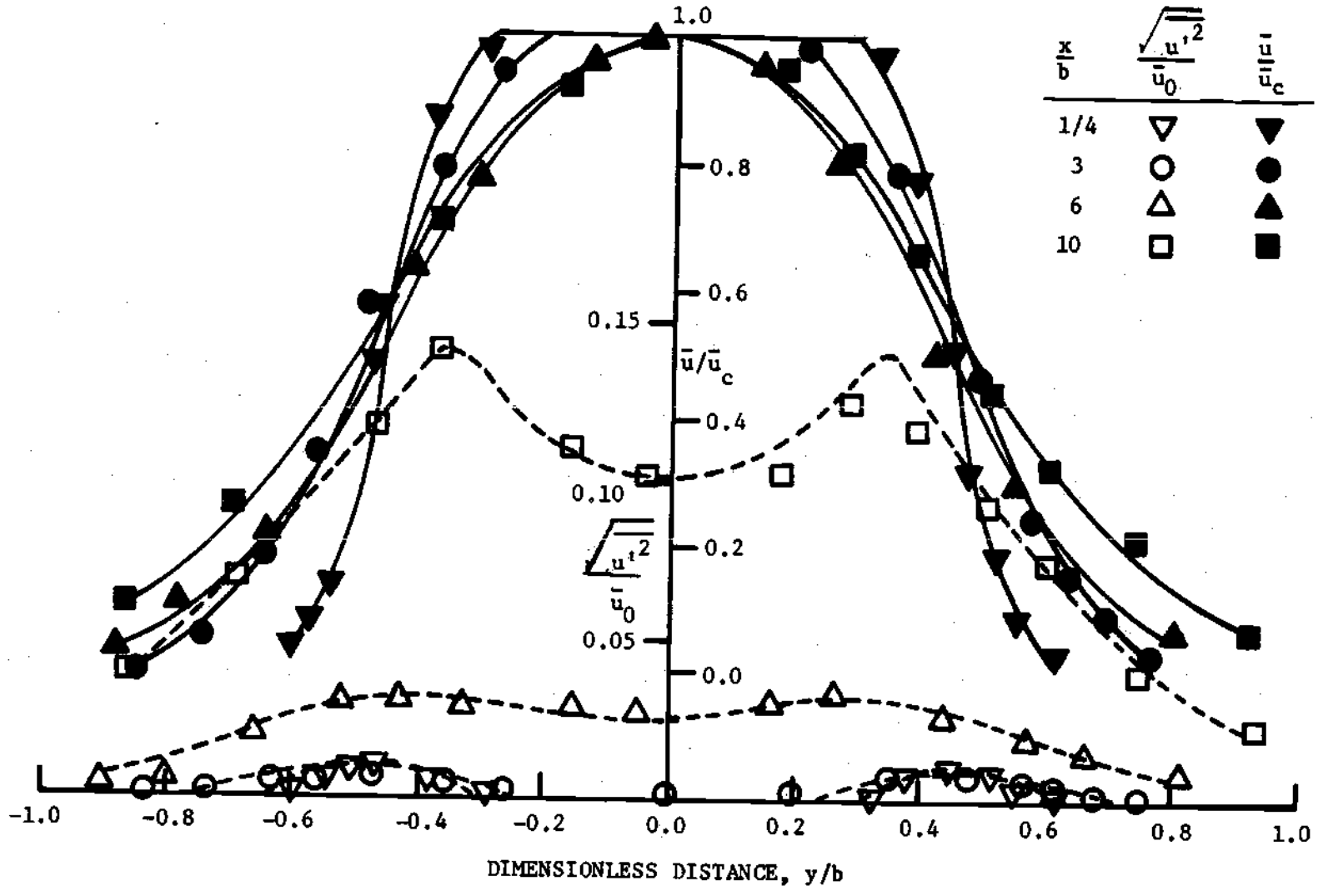

Figure 45. Time-Average and Fluctuating Velocity Data for R_e = 546, M = 0.183

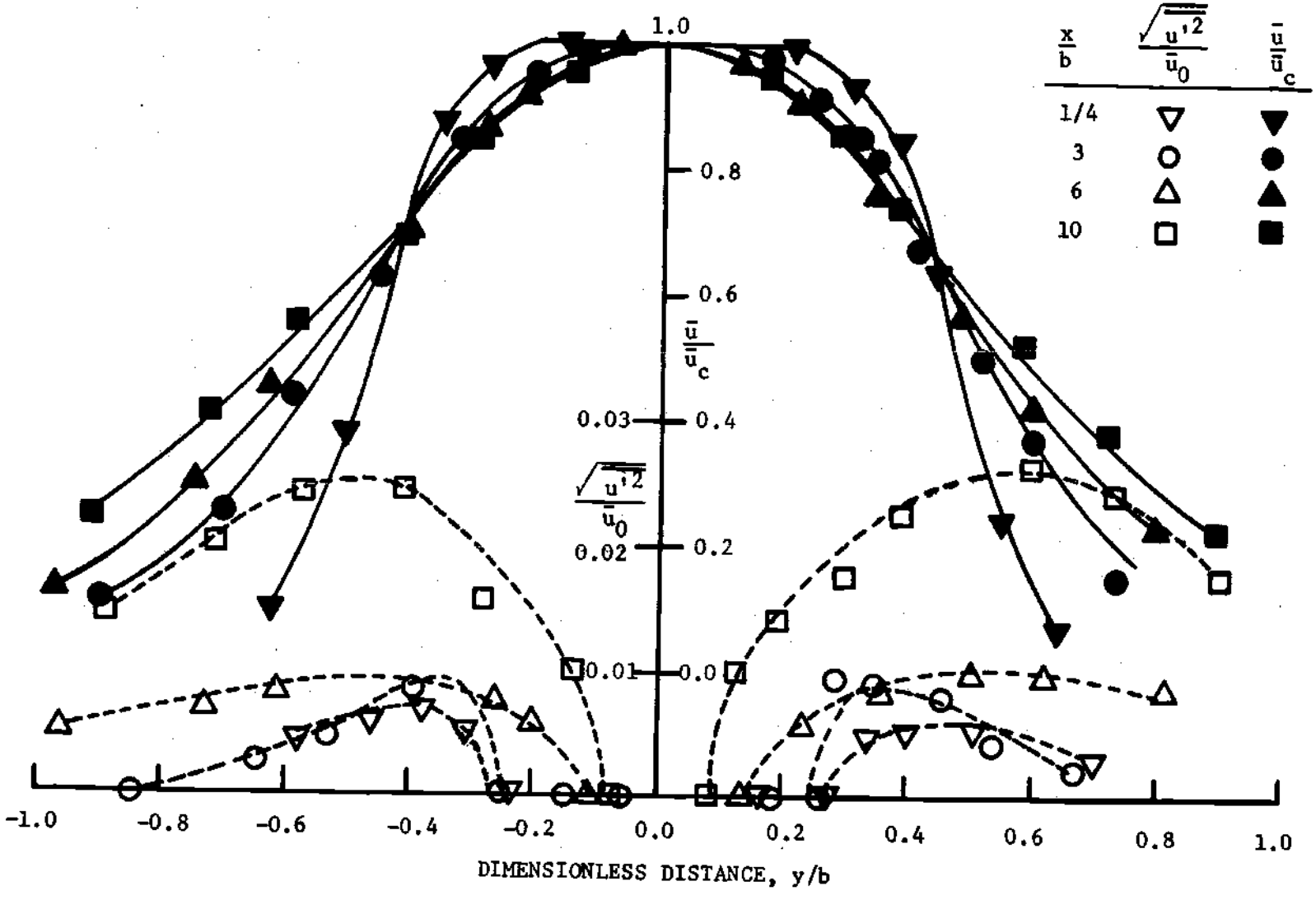

Figure 46. Time-Average and Fluctuating Velocity Data for R_e = 325, M = 0.426

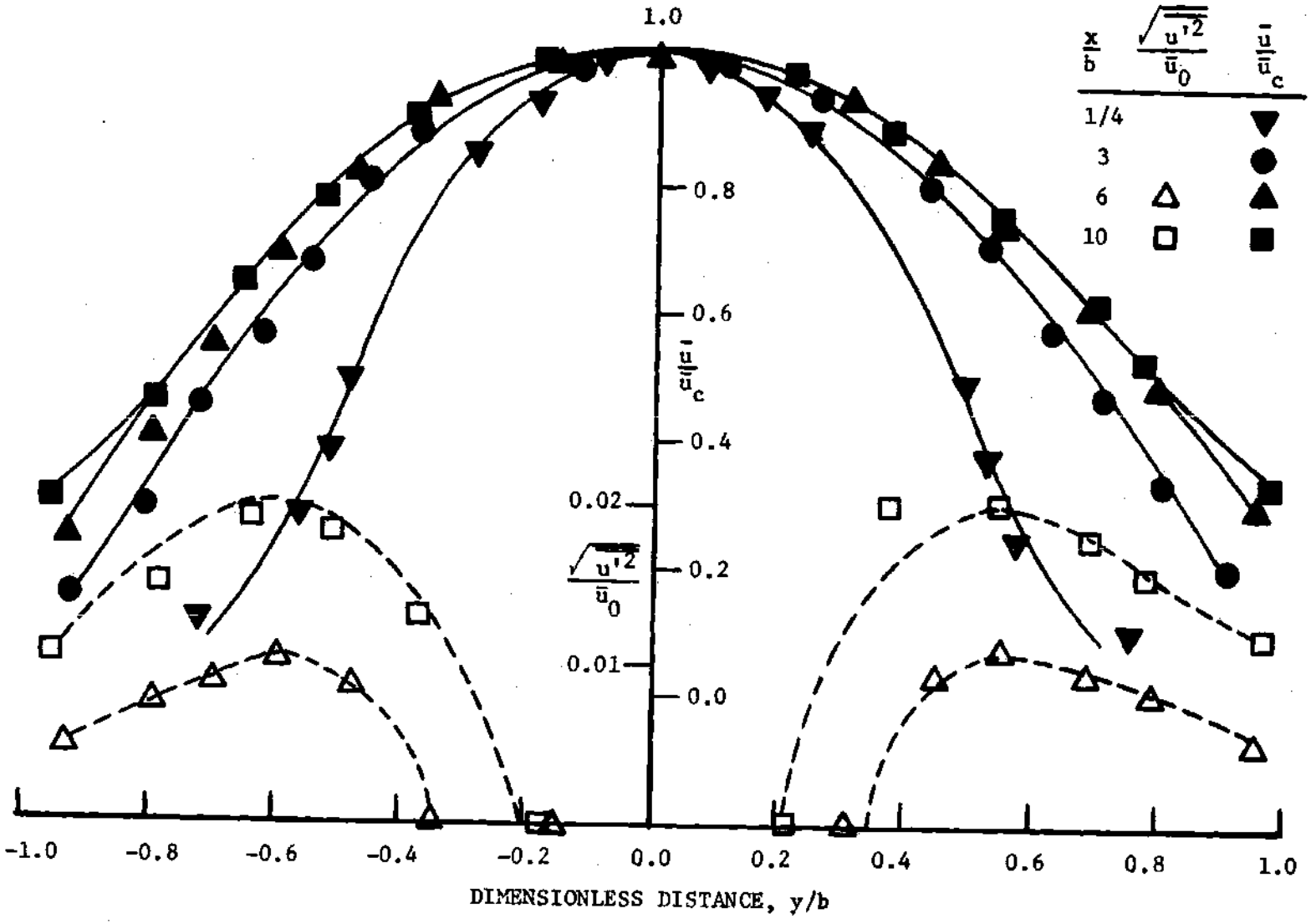

Figure 47. Time-Average and Fluctuating Velocity Data for R_e = 255, M = 0.761

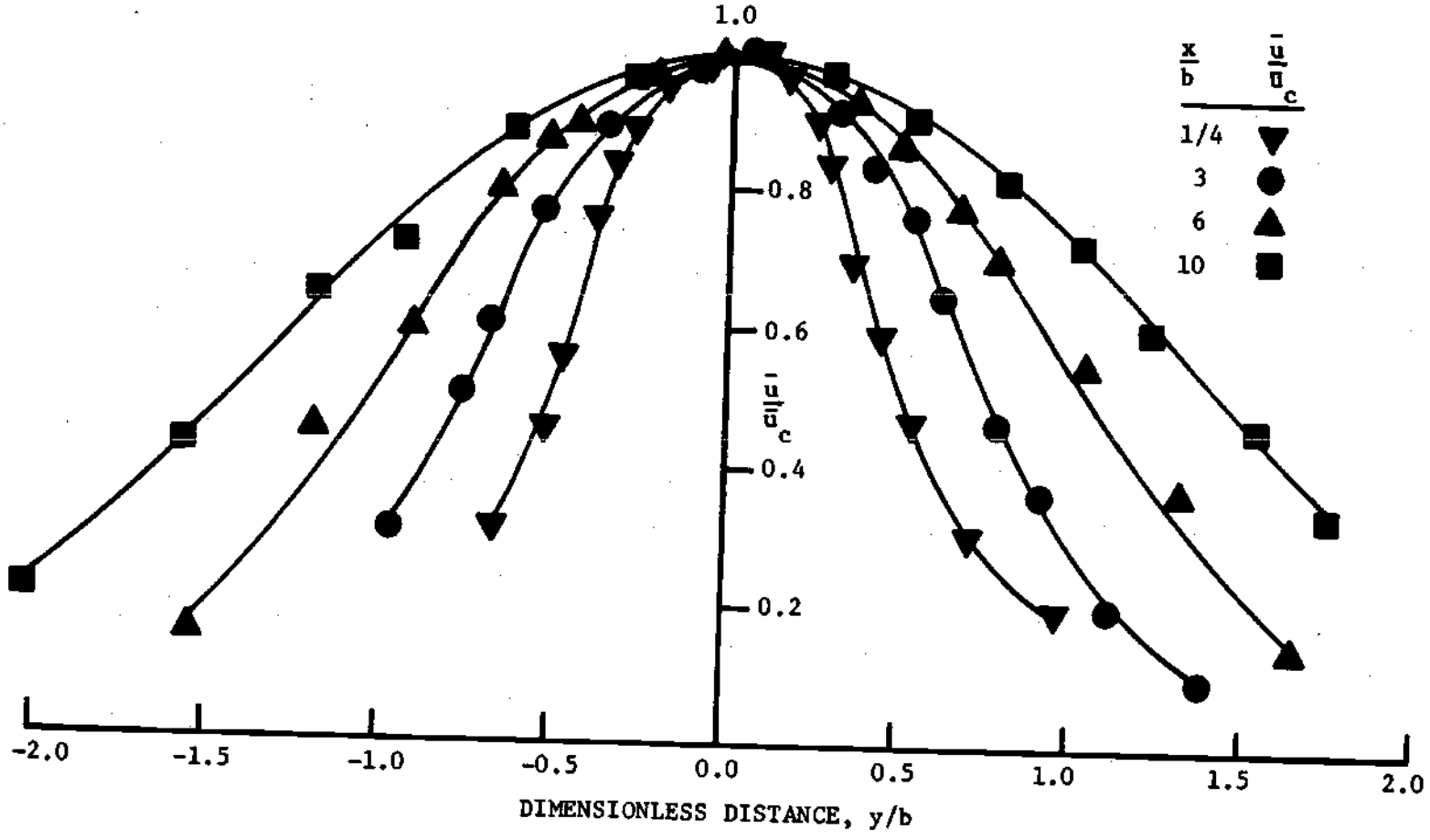

Figure 48. Time-Average Velocity Data for R_e = 64.2, M = 0.416

intersection the intensity of the turbulent fluctuations grows rapidly. The effect of this rapid growth is observed in the increased decay rate of the centerline velocity and the increase in the width of the velocity profile. The centerline velocity decay characteristics of this flow condition are similar to that of a turbulent jet; that is a long core region followed by a sharp transition to rapid centerline velocity decay. It is interesting to note that the turbulent shear layers have met upstream of the vertex of the potential core which is located approximately six nozzle widths downstream of the exit plane. Relatively thick boundary layers are found on the nozzle walls for this condition and make up approximately 15 percent of the flow area at the exit plane.

The characteristics of a flow condition where the Reynolds number is 325 and the Mach number is 0.426 are presented in Figures 44 and 46. It can be observed in Figure 46 that the spread and increase in intensity of the turbulent shear layers is much slower for this condition in comparison to the previous case. For this lower Reynolds number condition the boundary layers at the nozzle exit are thicker and consequently the core length is shorter. Beyond this short core regime is a region of low turbulence, and consequently a region of gradual centerline velocity decay and slow velocity profile spread rate. The turbulent shear layers are found to meet a short distance beyond 10 nozzle widths downstream and grow rather rapidly in intensity following this point. This rapid shear layer growth resulted in a much higher rate of centerline velocity decay in this region. Although this free jet possesses turbulent shear layers, the centerline velocity characteristics are

quite different from that of a turbulent jet flow at high Reynolds number as described by Miller and Comings [8]. That is the core region is much shorter and is followed by a long transition regime before rapid centerline velocity decay rate is attained.

The characteristics of a still lower Reynolds number condition are presented in Figures 44 and 47. Figure 47 illustrates that no turbulence was discovered at the nozzle exit plane. Hot film surveys indicated that turbulence developed to a detectable intensity at a point downstream between three and six nozzle widths. The turbulent shear layers were found not to intersect within 20 nozzle widths of the exit plane and were found to be of low intensity and slow growing. The low turbulent intensity level in this jet results in both a rather gradual centerline velocity decay rate and a slow profile diffusion rate. It is interesting to note that a pronounced change of centerline velocity slope does not occur within 20 nozzle widths of the exit plane. This pronounced slope change was associated with the formation of highly turbulent shear layers in the prior flow cases. For this condition the boundary layers were found to have met at the nozzle exit plane and thus no potential core existed. The free jet's centerline velocity decay rate is not characteristic of either a laminar or a turbulent jet. Although turbulence exists in this jet, it is not of sufficient intensity to produce the high centerline velocity decay rates associated with the previous cases.

The characteristics of a very low Reynolds number condition are presented in Figures 44 and 48. No turbulence was detected in this jet

flow within 20 nozzle widths of the exit plane. The steady state velocity profiles indicate the boundary layers have met in the nozzle and thus no potential core exists. The slowly decreasing value of centerline velocity is somewhat similar to that observed in the previous case, however, the rate is larger. The flow structure encountered at this condition is laminar and appears very similar to that reported by Chanaud and Powell [18]. The centerline velocity decay rate appears to be approaching asymptotically that predicted for a laminar incompressible plane jet.

Comparison of Experimental Data to Previous Studies

In the following section a comparison is made of the jet's flow structure in the presently investigated regime to analytical theories and data from previously investigated flow regimes. This comparison is divided into considerations of both time-average and fluctuating jet parameters.

Characteristics of the Steady State Velocity Profiles

Centerline velocity decay data from the present research are presented in Figure 49. These data represent the approximate limiting states in terms of Reynolds number which were investigated. Shown for comparison are data from the turbulent incompressible flow regime by Miller and Comings [8] and the laminar incompressible flow regime by Chanaud and Powell [18].

A comparison of the high Reynolds number case from the present research to data from Miller's investigation indicates the characteristics

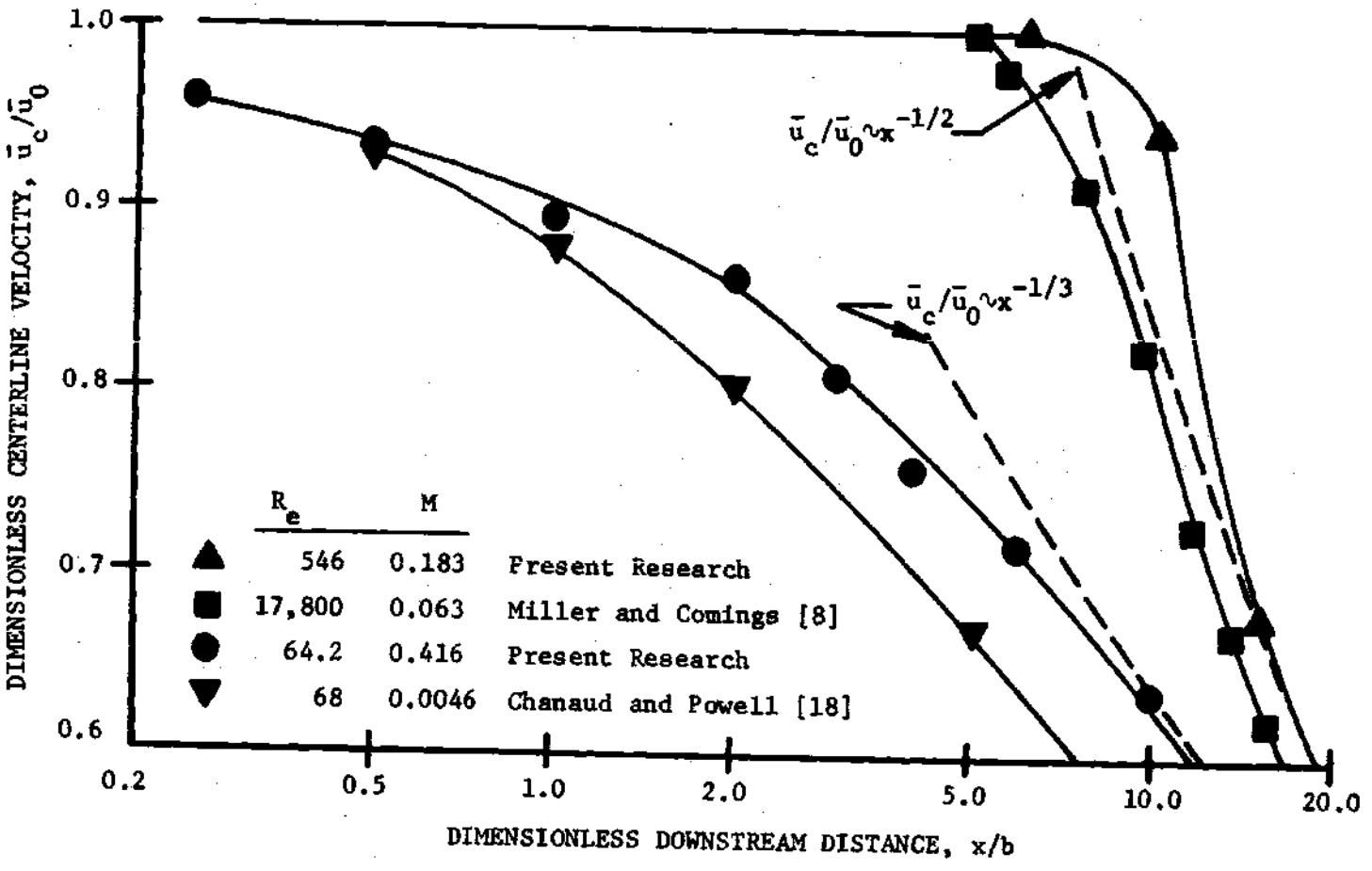

Figure 49. Comparison of Centerline Velocity Decay Data from the Present Investigation to Data from other Flow Regimes

are rather similar. That is both exhibit a long core region followed by a regime of rapid centerline velocity decay. The case from the present research, however, exhibits both a slightly longer core region and a longer transition region to fully developed turbulent flow. A comparison is made in Figure 49 of the present high Reynolds number flow case to the centerline decay rate predicted for a turbulent incompressible plane jet; see expression (45). This comparison demonstrates the present data approaches the predicted decay rate, proportional to $x^{-1/2}$, approximately 15 nozzle widths downstream. An unexpected steep decay rate is observed for this flow case between approximately 10 and 15 nozzle widths downstream of the exit plane. The data of Miller does not exhibit this phenomena. A possible explanation for this pronounced decay rate is the loss of two-dimensional flow in the experimental jet. A check of the velocity profiles in this region with the anemometer indicated the boundary layers from the top and bottom plates of the apparatus were relatively thick. The velocity profile data also suggested a slight loss of momentum in the direction of flow for this region which again indicated the flow was becoming three-dimensional.

A comparison is made in Figure 49 of a low Reynolds number case from the present research to a set of data with approximately the same Reynolds number from the research of Chanaud and Powell [18]. These centerline velocity data are again rather similar. It should be noted that the reported Reynolds number of 68 for Chanaud's data is based on flow rate and thus the Reynolds number based on centerline velocity at the nozzle exit would be somewhat larger. The centerline velocity decay

rate for both the present case and that of Chanaud would appear to approach asymptotically that predicted for a laminar incompressible jet; see equation (84). The general trend exhibited by low turbulence level cases from the present research, that is the centerline velocity decay rate decreased with higher Reynolds number conditions, was also in qualitative agreement with Chanaud's results.

Centerline velocity decay and jet width data from the research of Anderson [21] are compared in Figure 50 to data from the present investigation. A good quantitative comparison is difficult to make between these two studies since only two conditions considered by Anderson are within the range of the present experimentation. As may be seen from Figure 50, the centerline velocity decay characteristics for these two studies at approximately the same Reynolds and Mach number conditions are quantitatively different. A qualitative comparison of the data from the two studies, however, demonstrates many similar trends. Firstly, the core length is shown to obtain a maximum value at an approximate Reynolds number based on centerline conditions of 700. For lower Reynolds number conditions the core length decreases rapidly. The present data also indicate the core length decreases with Mach number. This effect was not indicated by Anderson's data, however, it was demonstrated for the studies of compressible turbulent jets by Olson and Miller [13]. Secondly, lower Reynolds and higher Mach number flow conditions decrease the centerline velocity decay rate for positions beyond the potential core. The present investigation demonstrates this effect is the result of such conditions retarding the growth of the turbulent

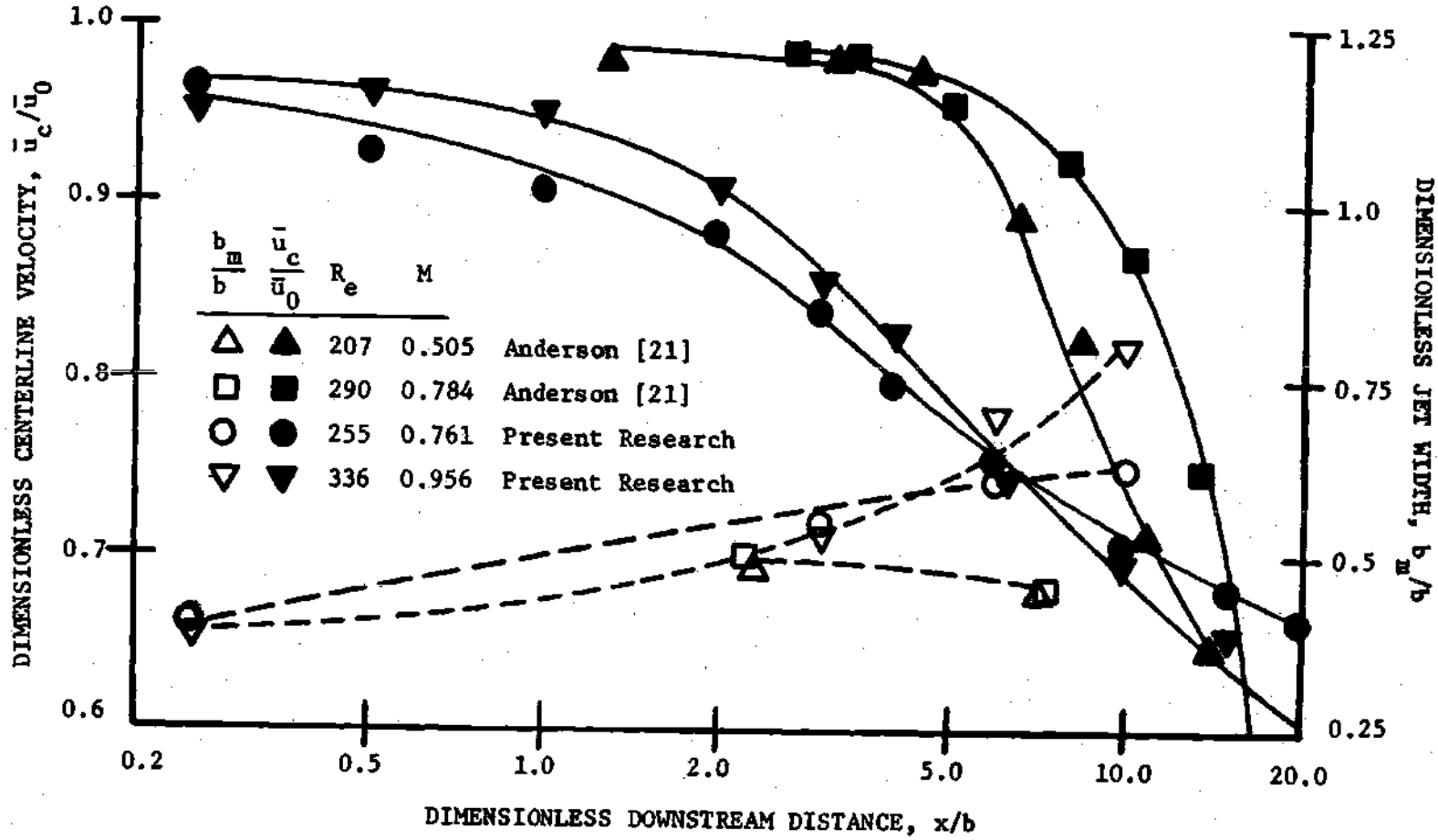

Figure 50. Comparison of Time-Average Characteristics from the Present Research to Data from Reference [21]

shear layers in the jet. For very low Reynolds number conditions, however, this trend is reversed. In such cases the flow is laminar and consequently the higher momentum of the larger Reynolds number jet produces a reduced centerline velocity decay rate near the nozzle exit.

Jet width data which again represent the approximate limiting conditions for the present research are presented in Figure 51. Also shown for comparison are data from the research of Miller and Comings [8] and Chanaud and Powell [18]. The jet width, b_m, represents the lateral distance from the centerline to the position where the dimensionless velocity $\bar{u}/\bar{u}_c$ is equal to 0.67.

A comparison may be made by referring to Figure 51 between a high Reynolds case from this research to data from Miller and Coming's study. These data demonstrate the essential absence of jet spread for the present case up to 10 nozzle widths downstream. This is in qualitative agreement with Figure 49 which indicates the centerline decay rate is much lower in comparison to Miller's data up to this position. The narrower jet width for the present case near the nozzle exit is an indication of the thick nozzle boundary layers.

The comparison of a low Reynolds number case from the present study and data from the research of Chanaud and Powell again indicates rather similar characteristics. It is interesting to note that the case from the present research has both a higher nondimensional centerline velocity and a wider nondimensional profile width at a common distance downstream of the exit plane. A plausible explanation for this observation is that Chanaud's jet emerged from a long channel while

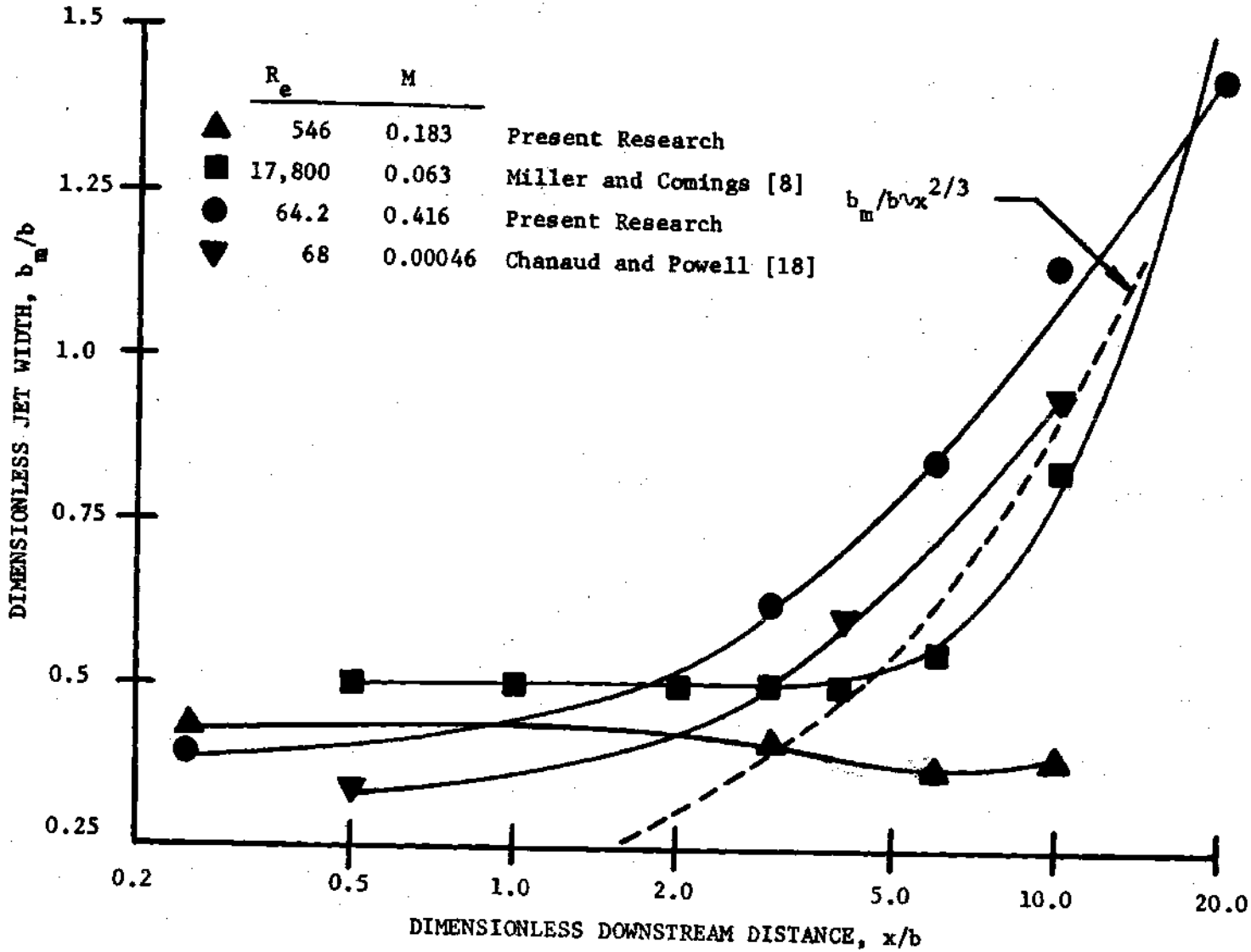

Figure 51. Comparison of Jet Width Data from the Present Research to Data from other Flow Regimes

the present study employed a nozzle. The jet flow emerging from a nozzle could be expected to have a greater portion of the profile at a higher velocity due to the decreased drag effect of the nozzle. It thus could have a wider nondimensional jet width and still be expected to have a slower centerline decay rate as a result of its higher momentum. A comparison of the jet's spread rate to that predicted for laminar incompressible flow, that is spread rate proportional to $x^{2/3}$, demonstrates the low Reynolds number case from the present research appears to be approaching but has not attained this relationship at a distance 20 nozzle widths downstream.

Jet width data from the present research and that of Anderson [21] are presented in Figure 50. These data again exhibit quite different characteristics. Anderson's data demonstrate essentially no spread rate in the region from two to seven nozzle widths downstream of the exit plane while data from the present investigation reveal a large spread rate in the same regime. The centerline velocity decay and spread rate parameters of Anderson's jet exhibit the same general characteristics found in higher Reynolds number cases in the present research. This may be observed by comparing the data from a case where the Reynolds number is 546 and the Mach number is 0.183 to that of Anderson; see Figures 49 and 51. A possible explanation of the dissimilar jet characteristics shown in Figure 50 at approximately the same flow conditions could be the nozzle geometries used in these two investigations. Anderson's experimental nozzle had a width of 0.2 inch with an aspect ratio of five as was the case in the present research. The

converging section of his nozzle was formed by two 0.25 inch radial sections while the nozzle from this research was formed by two 0.75 inch radial sections. The longer converging flow sections for the present research could be producing thicker boundary layers at the nozzle exit plane. These thicker boundary layers could explain the characteristics exhibited by Anderson's jet in Figure 50 which are similar to characteristics of higher Reynolds number cases in the present research.

Measurements of the time-average component of velocity in the x-direction demonstrated two distinct flow conditions existed in the low Reynolds number compressible flow regime. The jet was found to possess a potential core for relatively high Reynolds number conditions while in low Reynolds number cases the boundary layers had met in the nozzle and no core existed. In either of these situations the time-average velocity profiles outside of the core, if it existed, could be fitted to a Gaussian distribution. This profile was found to fit the experimental data as near as 0.25 nozzle widths from the exit plane. Shown in Figure 52 is a typical set of time-average velocity data fitted to a Gaussian profile. The investigations of Miller and Comings [8], Chanaud and Powell [18] and Anderson [21] also indicated the steady state velocity profiles could be fitted to a Gaussian distribution.

In the regime where a core existed, its width was found to decrease in proportion to the distance from the nozzle exit plane. This is in agreement with the analytical result for a two-dimensional incompressible turbulent free jet boundary; see equation (42). The decay of the potential core in proportion to x rather than $x^{1/2}$, as is predicted

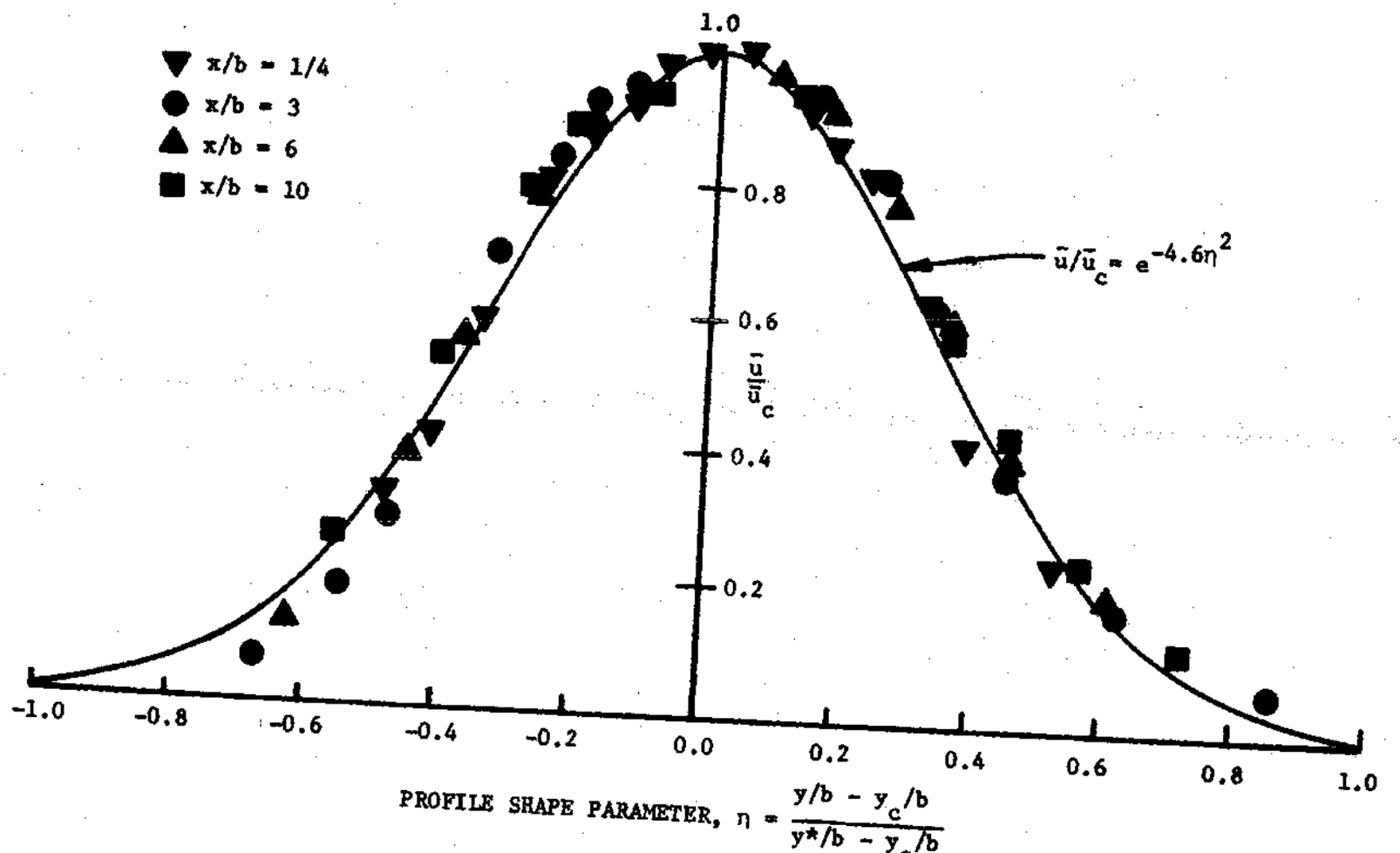

Figure 52. Comparison of Gaussian Distribution to Time-Average Velocity Profiles for R_e = 109, M = 0.67

for a two-dimensional incompressible laminar free jet boundary; see equation (82), may be explained by the observation that in any case where a core was detected there also existed turbulence in the mixing zone near the exit plane. In flow cases where the jet was laminar near its exit plane, the boundary layers had met in the nozzle and no core existed.

Characteristics of Fluctuating Velocity Profiles

A comparison is presented in Figures 53 and 54 of fluctuating velocity profiles from the present research to similar data reported for a plane turbulent incompressible jet by Miller and Comings [8]. These data again illustrate the effect of the lower Reynolds number conditions which were encountered in this research upon the formation and growth of the turbulent shear layers. Presented in Figure 53 are fluctuating velocity profiles for several positions within the potential core. These parameters are nondimensionalized by the velocity at the centerline of the nozzle exit plane, $\bar{u}_0$, and the nozzle width, b, respectively. A comparison of these data demonstrates a more rapid growth of the turbulent shear layers in the high Reynolds number flow case investigated by Miller. The position at which the turbulent intensity is a maximum lies closer to the jet centerline for the present research. This is an indication of the thick boundary layers occurring for the present flow cases.

Data illustrating the growth of the turbulent shear layers in the regime of flow beyond the potential core are presented in Figure 54. The fluctuating velocity component and distance from the centerline

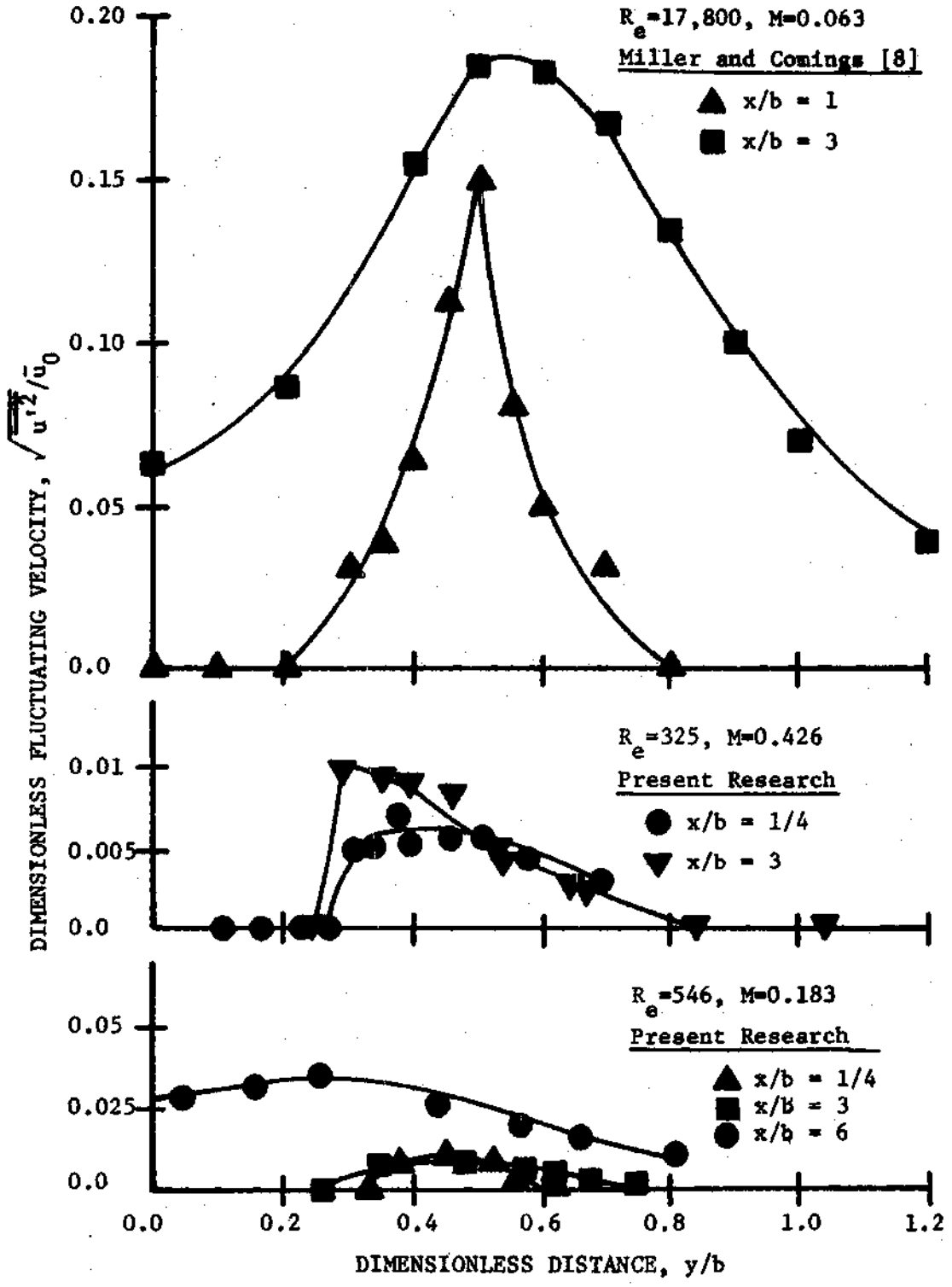

Figure 53. Comparison of Core Region Fluctuating Velocity Profiles from the Present Research to Data of Reference [8]

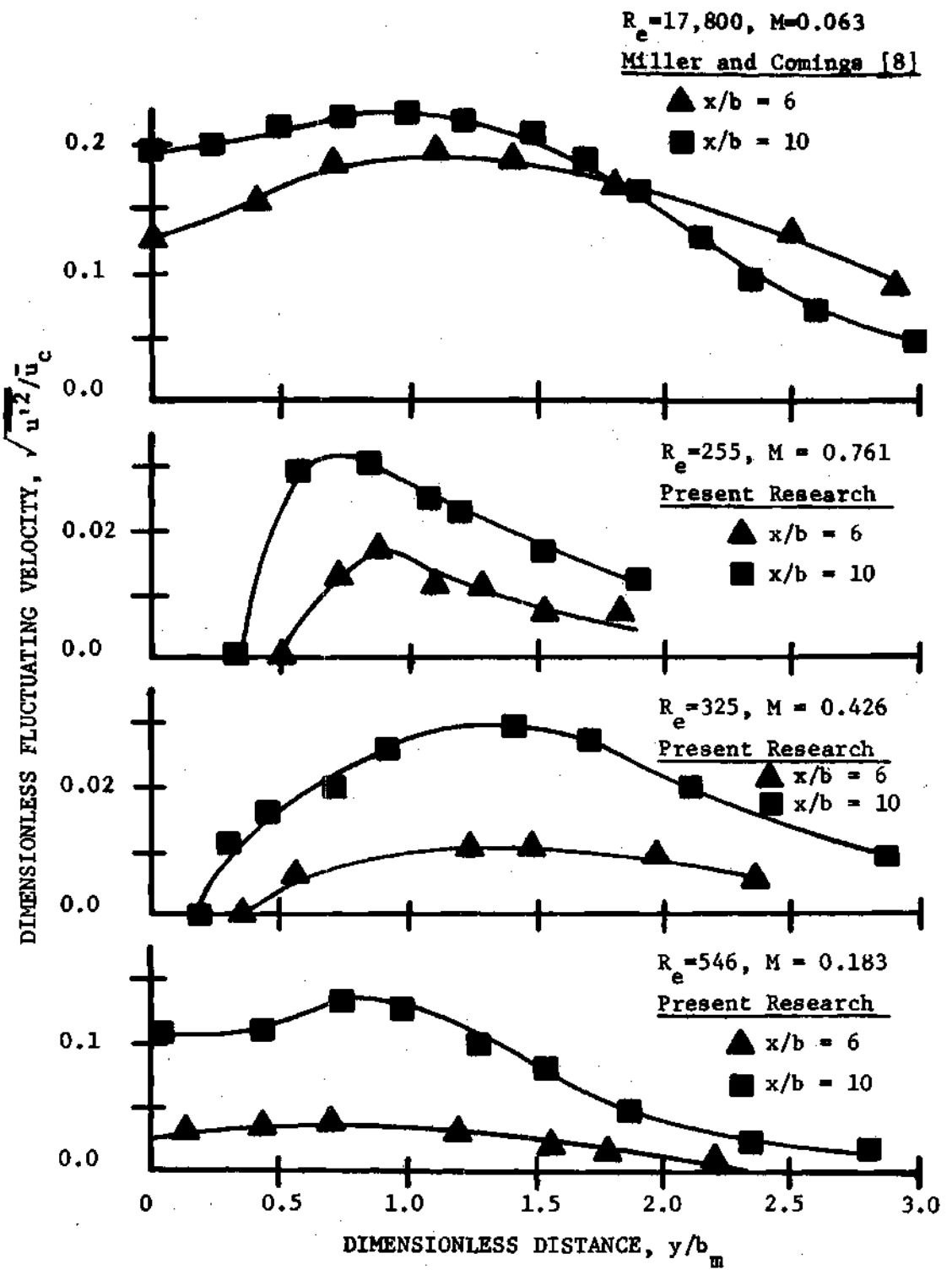

Figure 54. Comparison of Developed Region Fluctuating Velocity Profiles from the Present Research to Data of Reference [8]

in this figure are nondimensionalized by the appropriate centerline velocity, $\bar{u}_c$, and the jet width parameter, b_m, respectively. These data demonstrate the lower Reynolds number conditions considered in the present research retard the growth of the turbulent shear layers. Figure 54 indicates for a flow condition where the Reynolds number is 255 and the Mach number is 0.761 the turbulent shear layers have not met within 10 nozzle widths of the exit plane and are of low intensity. As the Reynolds number is increased to 325 at a Mach number of 0.426 the turbulent shear layers appear to have spread, however, the intensity of the fluctuations is still small. At a still higher Reynolds number condition of 546 and at a Mach number of 0.183 the turbulent shear layers have met at six nozzle widths downstream. The fluctuating velocity profiles for this condition are very similar in shape to those reported by Miller, however, the intensity of the turbulent fluctuations is of a lower magnitude.

The research of Miller indicates the position of maximum intensity in the fluctuating velocity profile is approximately at y/b_m equal to one. That is the point in the steady state velocity profile where the velocity is 67 percent of its centerline value. This point corresponds approximately to the inflection point in the time-average velocity profile. Data from the present research agree with this conclusion within experimental uncertainty.

Transition to Turbulent Flow

Turbulent transition data from the present research and the investigations of Andrade [17] are presented in Figure 55. This figure

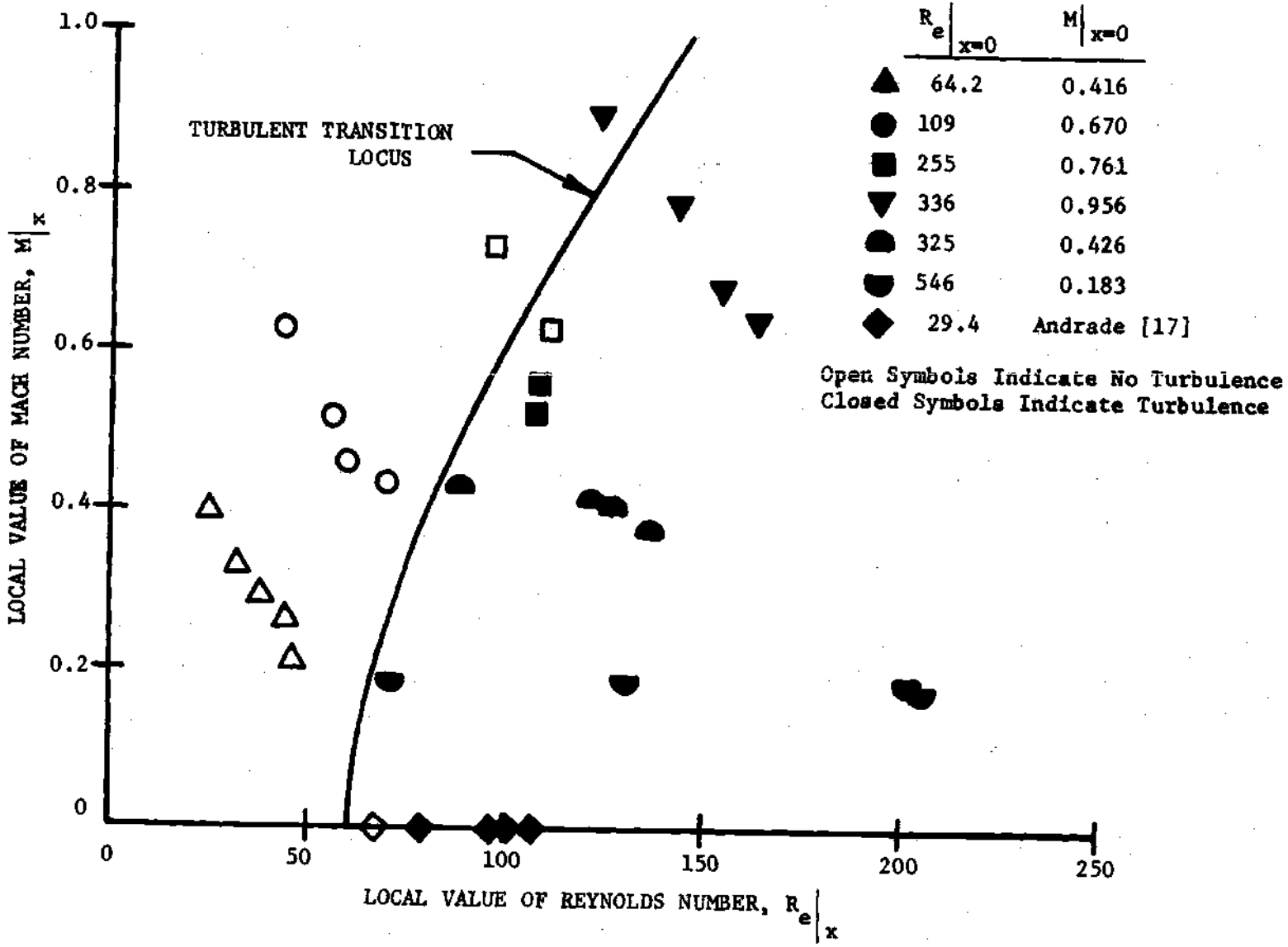

Figure 55. Transition Conditions from Laminar to Turbulent Flow

presents for several flow cases the locus of local Reynolds and Mach number conditions as the plane jet passes through a fluid at rest. The local Reynolds and Mach numbers are defined as

$$R_e = \frac{\rho \bar{u}_c b_w}{\mu} \quad ; \quad M = \bar{u}_c / c \tag{147}$$

b_w in the previous expression is the distance from the edge of the jet's core to the point where $\bar{u}/\bar{u}_c = 0.67$. In the cases where no core exists b_w is measured from the jet's centerline. The calculation of ρ, μ and c is based upon conditions at the jet's centerline.

Experimental data points in Figure 55 which are open indicate states at which no turbulence has been detected in the jet as opposed to darkened data points which indicate the presence of turbulence. The existence of turbulence was ascertained in the present research by hot film anemometer measurements. In the research of Andrade turbulence was detected by injecting dye into the experimental water jet and observing the resulting flow patterns. The point at which the dye pattern began to break up is interpreted as the state at which turbulence existed in the jet.

A correlation between the growth of the turbulent shear layers and the locus of local Reynolds and Mach number conditions can be made with reference to Figures 53 through 55. These data demonstrate that turbulent flow conditions in which the local Reynolds number increases slowly exhibits a comparable slow growth of the turbulent shear layers. This may be illustrated by considering the states shown in Figures 54 and 55 where the Reynolds numbers are 255 and 546 and the Mach numbers

are 0.761 and 0.183, respectively. This trend agrees qualitatively with Curle's [23] analysis of the stability of a plane incompressible jet, that is higher local Reynolds number flows are more unstable to disturbances.

The approximate locus of states separating the completely laminar region of flow from the conditions which exhibit turbulent fluctuations is presented in Figure 55. These data indicate the transition point for a laminar incompressible plane jet occurs at a local Reynolds number of approximately 60. This condition is approximately and order of magnitude higher than reported by Curle for complete insensitivity to disturbances of any wave length. The locus of transition Reynolds numbers presented in Figure 55 is found to increase with Mach number. This trend agrees with the analysis of Pai [24]. Pai's analysis indicated for a local Mach number exceeding 2.5 the flow is stable to all disturbances. This hypothesis could not be checked since only subsonic flows were investigated. The shape of the transition locus, however, did not exclude such a phenomena.

Static Pressure and Velocity Vector Distributions

Representative static pressure profiles from the present investigation are compared in Figure 56 to results from the research of Miller and Comings [8]. The parameter $(P-P_m)$ in this figure represents the variation from the static pressure at rest in the experimental model. Surveys of positions nearer than three nozzle widths of the jet's exit plane were not possible in the present research. This was due to the relatively large static pressure probe which tended to block the nozzle

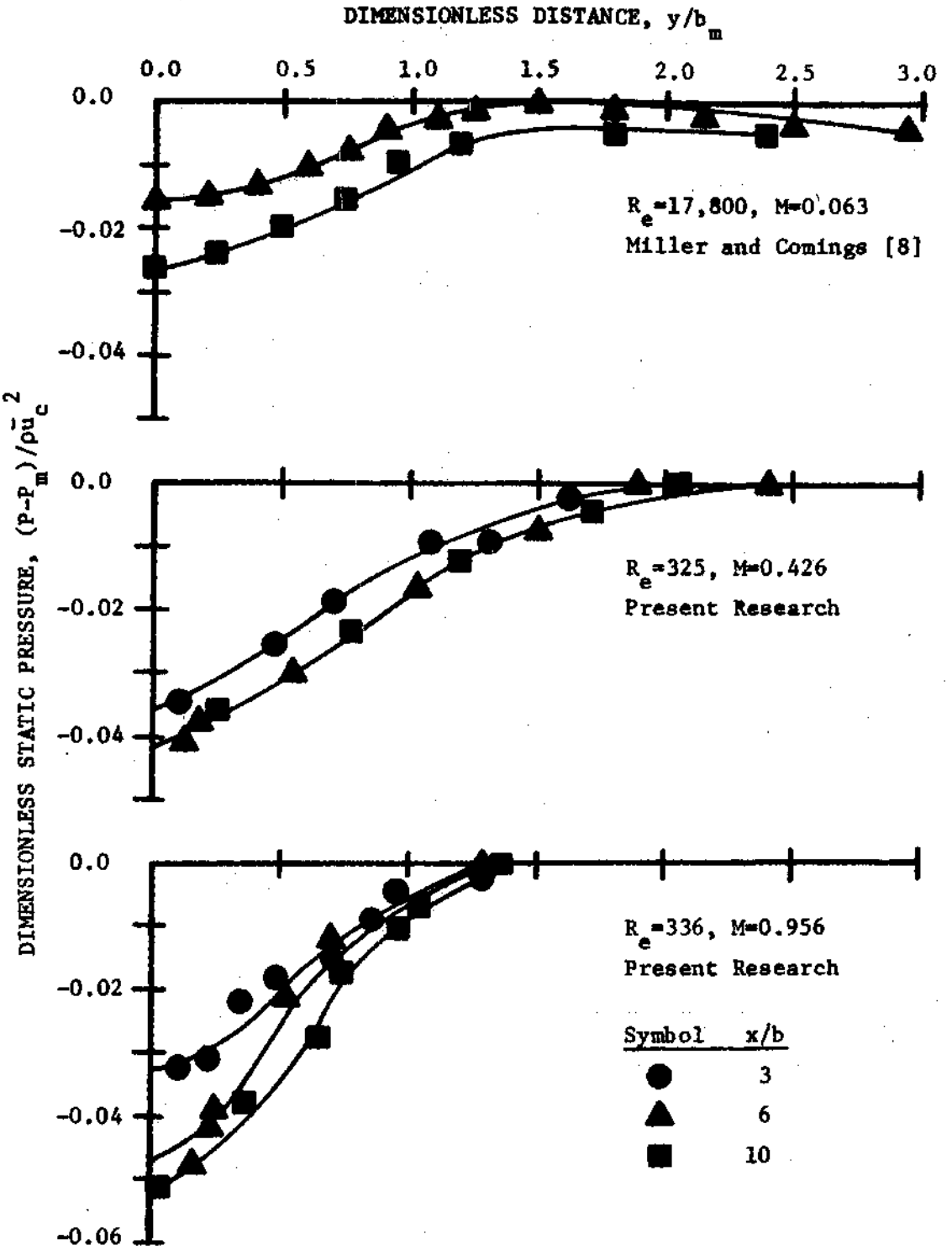

Figure 56. Comparison of Free Jet Static Pressure Distributions from the Present Research to Data from Reference [8]

when near. Positive static pressures reported by Miller for positions near the nozzle exit were not detected at the nearest plane of investigation in the present research. Figure 56 demonstrates the static pressure distributions reported by Miller in the developed regime of flow are very similar in shape to the profiles obtained in the present research. The pressure distributions from this investigation, however, are of a larger nondimensional magnitude at a common downstream distance.

The experimental data in Figure 56 demonstrate the jet's longitudinal momentum is much larger than the jet's unbalanced static pressure force. By integrating the quantities $\rho\bar{u}^2$ and $(P-P_m)$ over their respective profiles it is determined that the maximum unbalanced static pressure force shown in this figure is approximately 3.54 percent of the respective longitudinal momentum force. The assumption of conservation of momentum in the longitudinal direction would thus appear to be a valid approximation.

Investigations of the low Reynolds number compressible flow regime demonstrated the jet's velocity vector is essentially in the longitudinal or x-direction except near the outer extremities of the jet. For the flow conditions investigated, the absolute value of velocity may be approximated to within one percent by the longitudinal component of velocity for positions in the profile up to $\bar{u}/\bar{u}_c = 0.18$. The absolute difference between the velocity and its longitudinal component is less than one percent of the centerline value of velocity.

Free Jet Data Correlations

In the following section a data correlation will be presented which describes the time-average longitudinal velocity field of a free jet in the low Reynolds number compressible flow regime. This empirical correlation is based upon determining the longitudinal component of momentum in the jet and assuming it is conserved. With a known momentum and an assumed velocity distribution, the longitudinal velocity field is prescribed if, respectively, the core configuration and centerline velocity beyond the core regime are known.

Evaluation of Free Jet Momentum

The experimental data demonstrated the jet's longitudinal velocity profile could be described by a simple Gaussian distribution. The form of the assumed time-averaged longitudinal velocity distribution is

$$\bar{u}/\bar{u}_c = e^{-4.6\eta^2} \quad \text{for} \quad -y_c \geq y \geq -\infty \qquad (148)$$

$$y_c \leq y \leq \infty$$

$$\bar{u}/\bar{u}_c = 1 \quad \text{for} \quad -y_c \leq y \leq y_c$$

where the profile shape parameter, η, is defined as

$$\eta = \frac{y/b - y_c/b}{y^*/b - y_c/b} \qquad (149)$$

The variables y_c/b and y^*/b represent the nondimensional distances from the jet's centerline to the edge of the core and from the centerline to the point where the velocity diminishes to one percent of the centerline value, respectively. A sketch of the assumed time-averaged

velocity profile is shown in Figure 57.

The longitudinal momentum per unit height of the jet may be written as

$$J_\infty = \int_{-\infty}^{\infty} \rho \bar{u}^2 \, dy \tag{150}$$

For the isoenergetic flow of an ideal gas with constant specific heats, the density may be written as

$$\rho = \frac{\rho_T \, (P/P_T)}{\left[1 - \frac{k-1}{2} \left(\frac{\bar{u}_c}{c_T}\right)^2 \left(\frac{\bar{u}}{\bar{u}_c}\right)^2\right]} \tag{151}$$

where the subscript T refers to conditions in the stagnation tank, k is the ratio of specific heats, and c_T is the stagnation sonic velocity. Introducing the expression for density into equation (150) with the assumption of constant momentum per unit height, one obtains

$$J_\infty = \rho_T (P/P_T) \, \bar{u}_c^2 \int_{-\infty}^{\infty} \frac{(\bar{u}/\bar{u}_c)^2 \, dy}{\left[1 - \frac{k-1}{2} \left(\frac{\bar{u}_c}{c_T}\right)^2 \left(\frac{\bar{u}}{\bar{u}_c}\right)^2\right]} \tag{152}$$

Substituting the velocity profile given in equation (148) into the previous expression, yields after evaluation

$$J_\infty = 2b\left(\frac{2k}{k-1} P_m B\right) \left[\frac{\bar{y}_c/b}{1-B} + 0.292 \, (y^*/b - y_c/b) \sum_{m=0}^{\infty} \frac{B^m}{\sqrt{m+1}}\right] \tag{153}$$

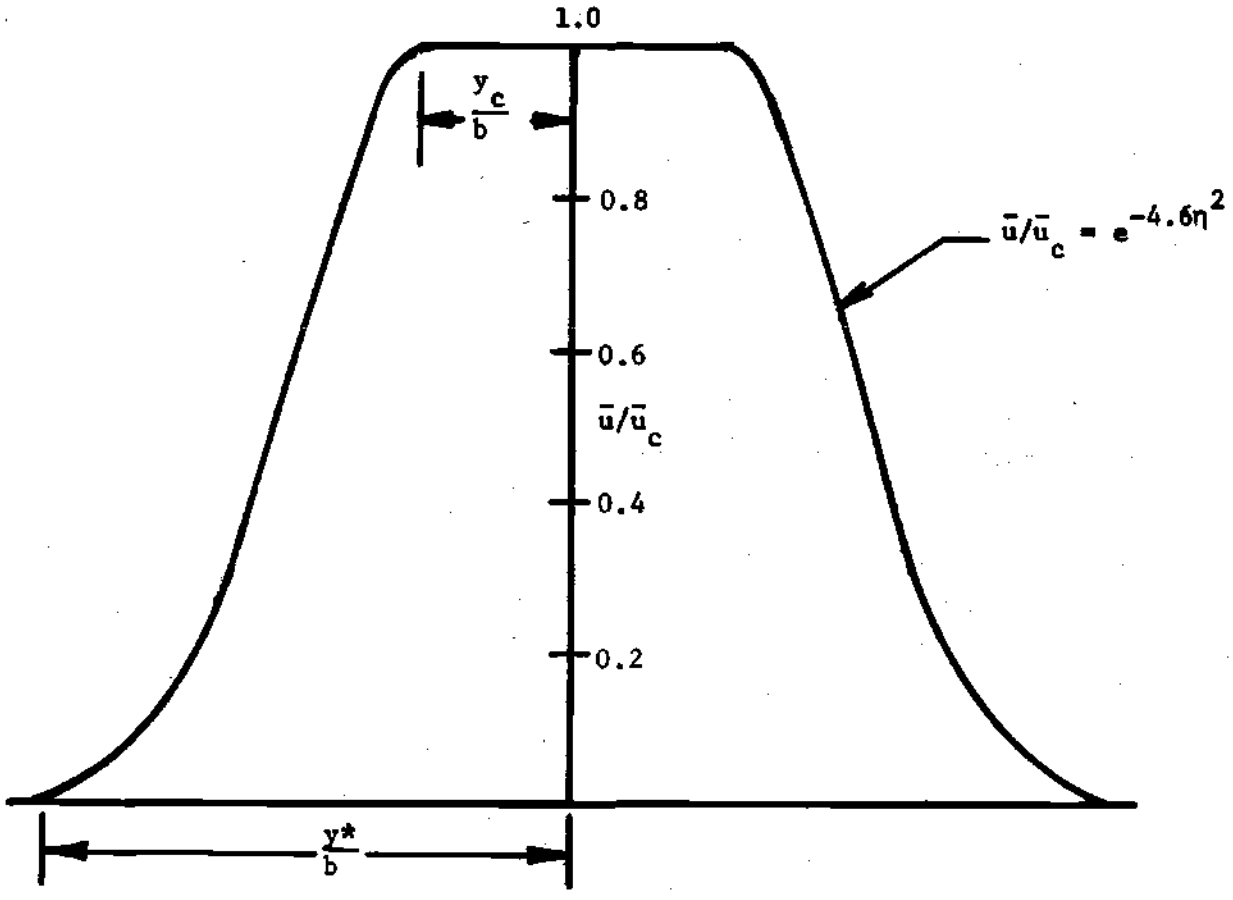

Figure 57. Free Jet Longitudinal Time-Average Velocity Distribution

where P_m is the constant static pressure in the experimental jet. The centerline velocity function, B, is defined as

$$B = \frac{k-1}{2} (\bar{u}_c/c_T)^2 \tag{154}$$

A detailed description of the evaluation of equation (152) is presented in Appendix D.

The momentum per unit height of the free jet is defined in equation (153) in terms of the unknown variables y*/b, y_c/b and $\bar{u}_c$

$$J_\infty = J_\infty (y^*/b, y_c/b, \bar{u}_c) \tag{155}$$

In the potential core regime of the jet $\bar{u}_c$ is known and consequently the jet's momentum is a function of y*/b and y_c/b. Since the jet's momentum is conserved, expression (153) may be used to determine y*/b in terms of y_c/b. Similarly, in the flow field beyond the core the momentum of the jet is only a function of y*/b and $\bar{u}_c$, thus expression (153) may be used to determine y*/b in terms of $\bar{u}_c$.

In the following sections analytical expressions will be presented for y_c/b and $\bar{u}_c$. These analytical expressions are provided by a correlation of the experimental data. It can be shown from the equations of motion that equality of Reynolds and Mach number, based on the centerline velocity at the exit plane, insure dynamic similarity. Assuming similar geometries for model and prototype then a set of similarity parameters are Reynolds number, Mach number and distances in the x and y-direction nondimensionalized by power nozzle width, b.

Evaluation of Centerline Velocity

Centerline velocity decay data from the present research suggested the flow can be divided into the four regimes which follow:

1. Core regime. The regime in which the centerline velocity can be calculated from the pressure ratio across the nozzle and the upstream conditions.
2. Laminar transition regime. The regime in which the centerline velocity is less than the potential core velocity, however, the effect of turbulence is negligible.
3. Turbulent transition regime. The flow regime in which the turbulent shear layers have met and the flow is approaching a fully turbulent jet.
4. Fully turbulent regime. The regime in which the flow is dominated by the turbulent shear layers and the centerline velocity may be expressed by a power law distribution.

As a practical consideration it is rather difficult to differentiate between the laminar and turbulent transition regimes. Thus in order to simplify the data correlation, both will be lumped together and referred to as the transition regime. A sketch of the free jet representation employed in the data correlation is shown in Figure 58.

Core Regime. The velocity in the potential core is prescribed in terms of the pressure ratio across the nozzle and stagnation conditions in the upstream reservoir. This region's nondimensional length

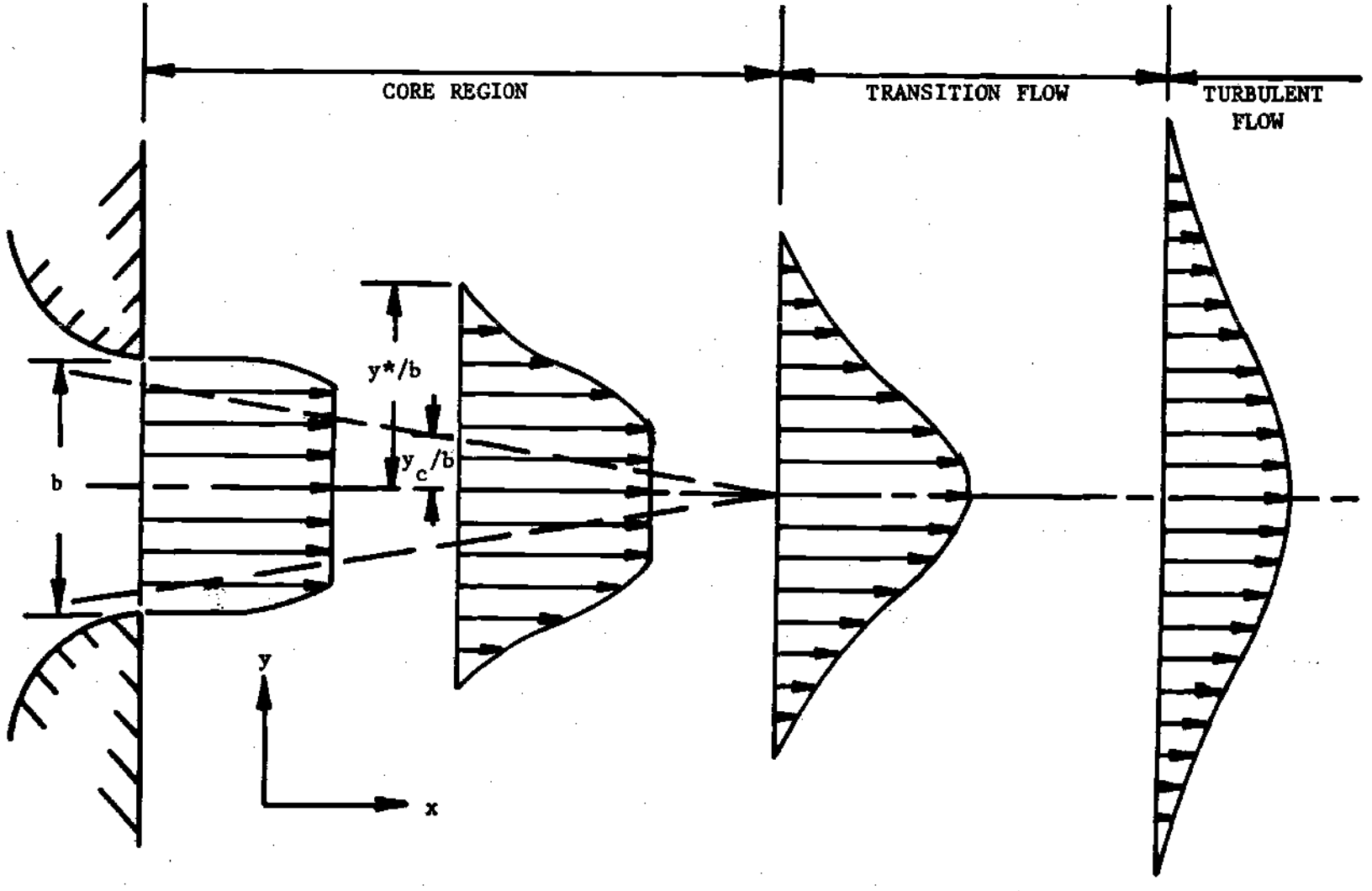

Figure 58. Free Jet Representation

may be expressed as

$$x_c/b = \frac{R_e^{3/4}}{10.3\ (1+M^2)} - 3.95 \tag{156}$$

The experimental data demonstrated the width of the potential core decreased linearly from the thickened nozzle boundary layers. The non-dimensional core width is expressed as a function of downstream distance by

$$y_c/b = \frac{1}{2}\left\{\left(\frac{x_c}{b} - \frac{x}{b}\right)\left[\frac{10.3\ (1+M^2)}{R_e^{3/4}}\right]\right\} \tag{157}$$

It should be noted that an evaluation of equation (156) which results in a zero or a negative number indicates the core terminates at the nozzle exit or ends within the nozzle, respectively. In the latter situation the pressure ratio and upstream stagnation conditions are insufficient to determine the exit plane velocity. To alleviate this difficulty a velocity coefficient is defined in terms of the calculated isentropic velocity

$$c_v = \bar{u}_0/\bar{u}_i \tag{158}$$

The correlation expression for the velocity coefficient in terms of the Reynolds and Mach number based on isentropic flow is

$$c_v = 0.845 + 0.00382\ R_e^{0.75}/(1+M^2) \tag{159}$$

The value of c_v is matched to the core length expression; that is conditions which produce a zero core length also produce a velocity

coefficient of one. In summary, when an evaluation of the core length produces a negative number then the actual velocity at the nozzle exit plane must be recalculated from expressions (158) and (159). The Reynolds and Mach numbers then must be recomputed based on the true velocity before the correlation can proceed.

Flow parameters for the core regime are presented graphically in Figure 59. Expressions (156), (157) and (159) are presented in this nomograph. In the plot to the right of this figure, the core length, x_c/b, and the velocity coefficient, c_v, are shown as a function of the potential Reynolds and Mach number. In the plot to the left, the core width, y_c/b, is presented as a function of downstream distance, x/b, for constant values of core length.

Transition Regime. The centerline velocity in the transition regime may be expressed as

$$\frac{\bar{u}_c}{\bar{u}_0} = e^{\left[1 - \left(\frac{x/b + x_0/b}{x_c/b + x_0/b}\right)^{0.45}\right] / 9} \tag{160}$$

where $\bar{u}_0$ represents the velocity at the centerline of the nozzle's exit plane. Expression (160) is valid for the regime

$$\frac{x/b + x_0/b}{x_c/b + x_0/b} \geq 1 \tag{161}$$

the transition regime stretches from the end of the core region, or in the case of no core, from the nozzle exit plane. This regime terminates in either a fully laminar or fully turbulent jet. In the present

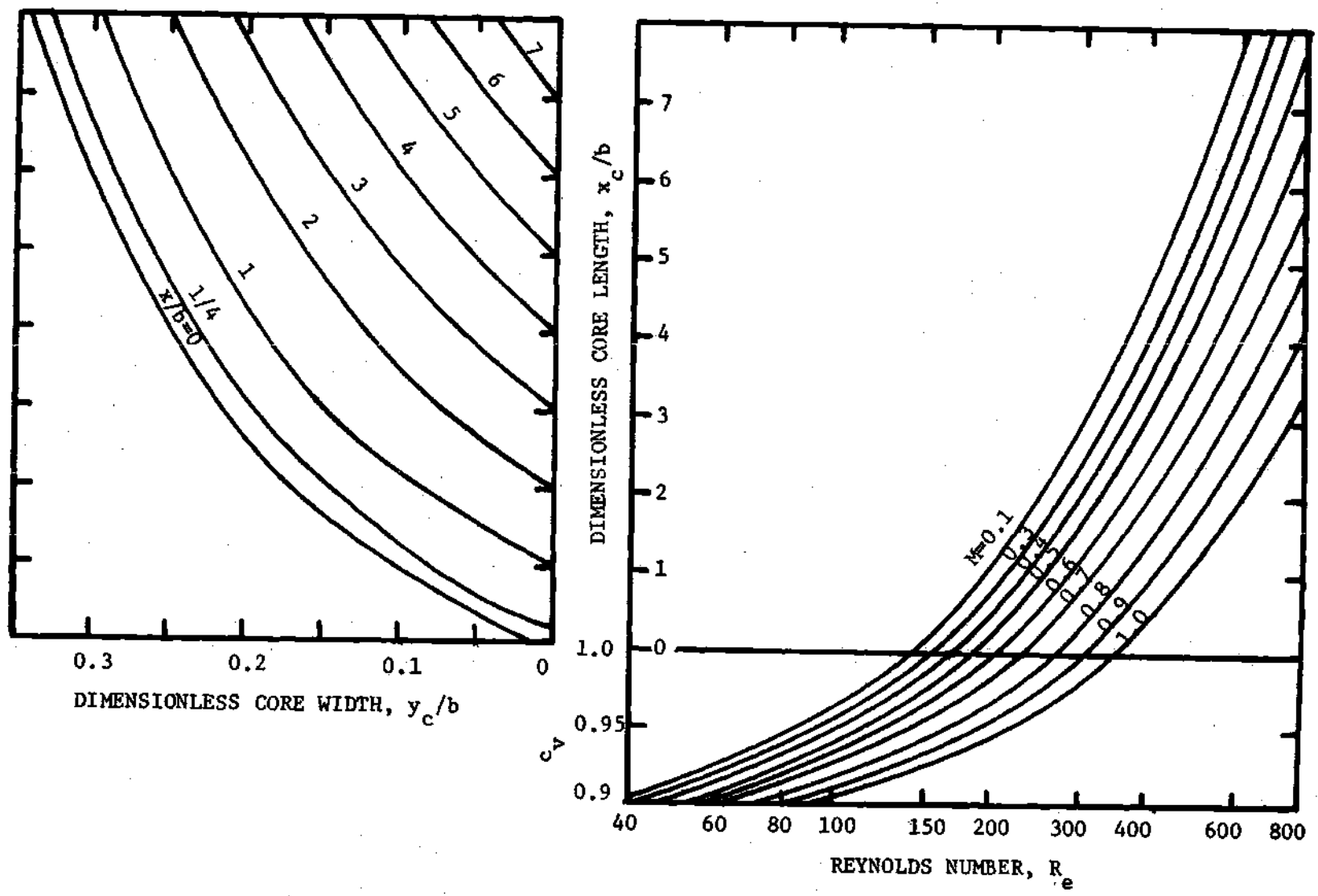

Figure 59. Graphical Presentation of Expressions for x_c/b, y_c/b and c_v

investigation it was found to only terminate in a turbulent jet. It is anticipated a fully laminar jet would have occurred at the lower Reynolds number conditions for large downstream distances. The value of x_0/b is given by

$$x_0/b = 0.0036\ R_e/(1 + 1.25\ M^4) \tag{162}$$

Equations (160) and (162) which describe the centerline velocity in the transition region are presented in Figures 60 and 61. In Figure 60 the transition parameter, x_0/b, is presented as a function of the Reynolds and Mach number of the flow. In Figure 61 the nondimensional centerline velocity in this regime is plotted in terms of x_0/b, x_c/b and x/b. In the plot to the right of this nomograph the transition function, $\left(\frac{x_0/b}{x_c/b + x_0/b}\right)$, is evaluated from the values of x_0/b and x_c/b. The nondimensional centerline velocity is then calculated on the plot to the left as a function of $\left(\frac{x/b}{x_o/b}\right)$ with the parameter $\left(\frac{x_0/b}{x_c/b + x_0/b}\right)$ held fixed.

Turbulent Regime. The centerline velocity in the turbulent region was found to fit the expression

$$\bar{u}_c/\bar{u}_s = \left(\frac{x/b}{x_s/b}\right)^{-1/2} \tag{163}$$

where x_s represents the point separating the transition and turbulent regimes and $\bar{u}_s$ is the centerline velocity at the end of the transition region which may be calculated from equation (160). The boundary point, x_s, may be expressed as

$$x_s/b = 545\ (1 + 0.6\ M^4)/R_e^{0.65} \tag{164}$$

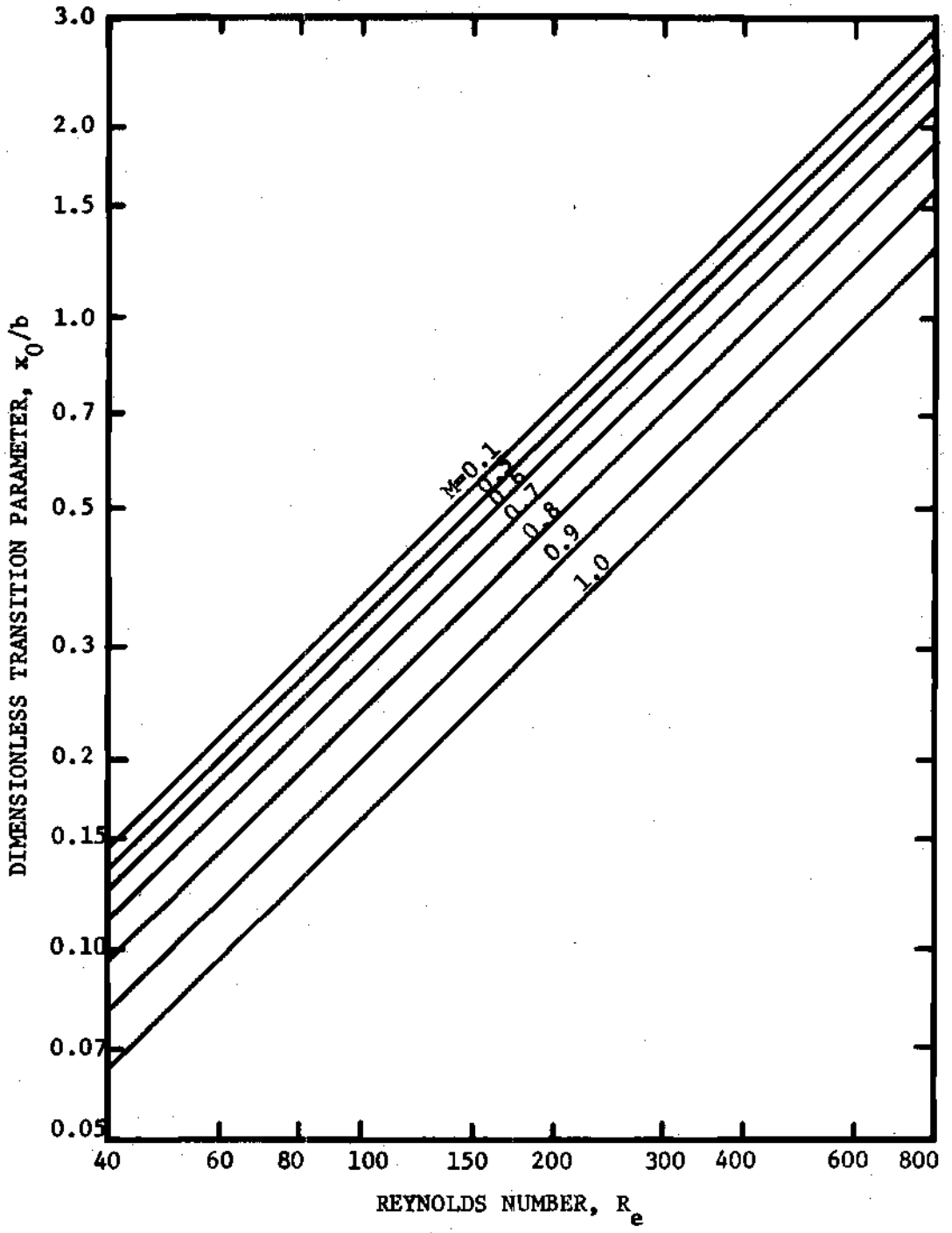

Figure 60. Graphical Presentation of Expression for x_0/b

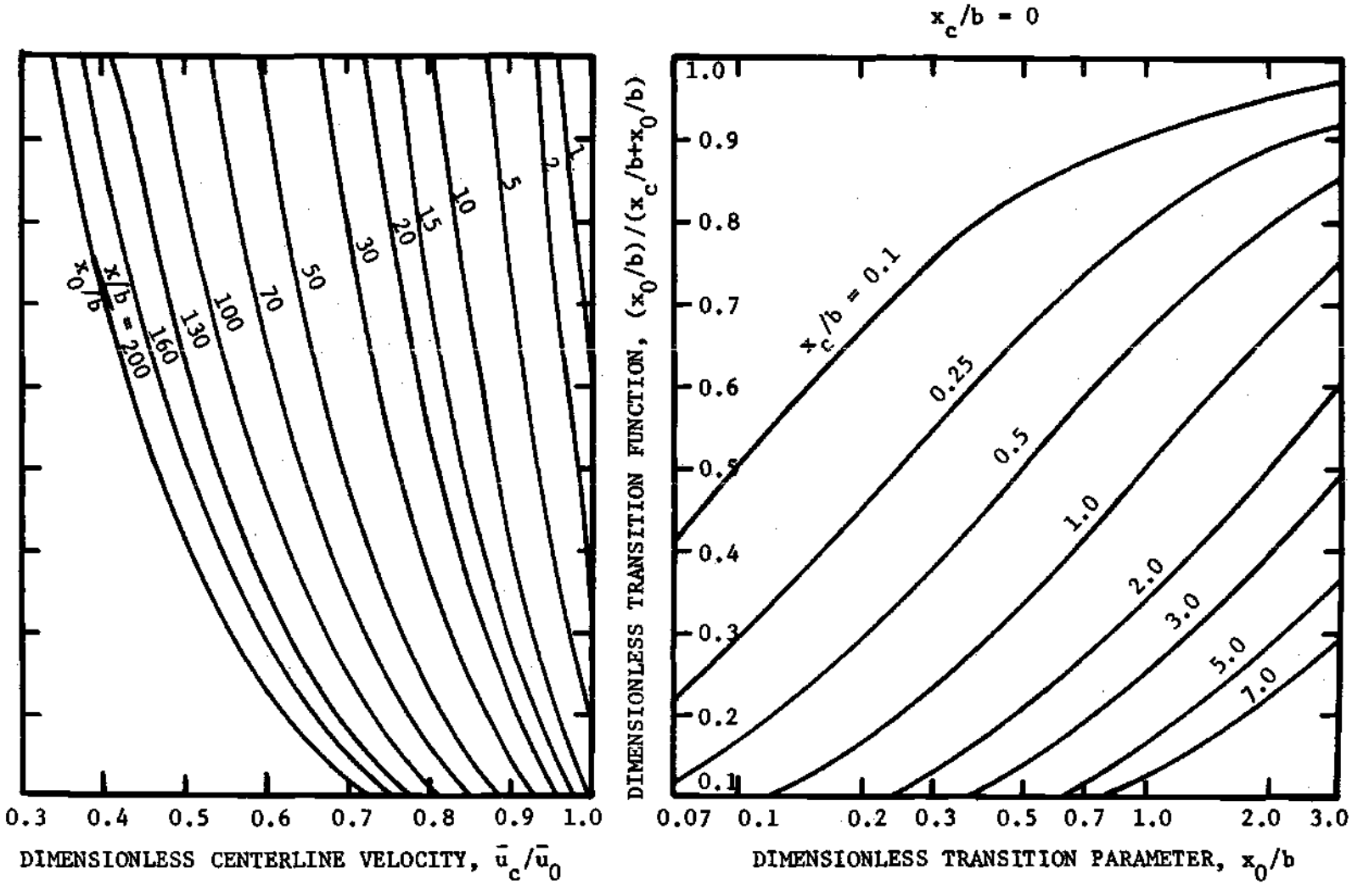

Figure 61. Graphical Presentation of Centerline Velocity in the Transition Region

Expressions (163) and (164) are presented in Figure 62. On the right side of this nomograph the nondimensional boundary point between the transition and turbulent regimes is plotted as a function of Reynolds and Mach number. The nondimensional centerline velocity is then calculated on the plot to the left as a function of x/b for a constant value of x_s/b.

Evaluation of y*/b

In previous investigations of high Reynolds number turbulent jets, the momentum of the jet was easily calculated at the nozzle exit plane. At this position the pressure drop across the nozzle could be used to compute the potential velocity which essentially filled the entire exit plane. In the low Reynolds number compressible flow regime, however, very thick boundary layers were always found at the exit plane. At low Reynolds number conditions the boundary layers met in the nozzle and the core was entirely absent. Rather than base the momentum of the jet on the exit condition at which the velocity profile was unknown, the momentum in this correlation is calculated at the station one fourth nozzle width downstream. Experimental data demonstrated the velocity profiles at this position were Gaussian and consequently equation (153) could be used to calculate J_∞. The correlation expression for the jet width parameter, y*/b, at this position is

$$y^*/b\Big|_{x/b=1/4} = \left(\frac{6.73}{R_e^{0.45}} - 0.128\right)(1+2.3\ M^2)(0.25)^{0.00808\sqrt{R_e}+0.185} + 0.5 \tag{165}$$

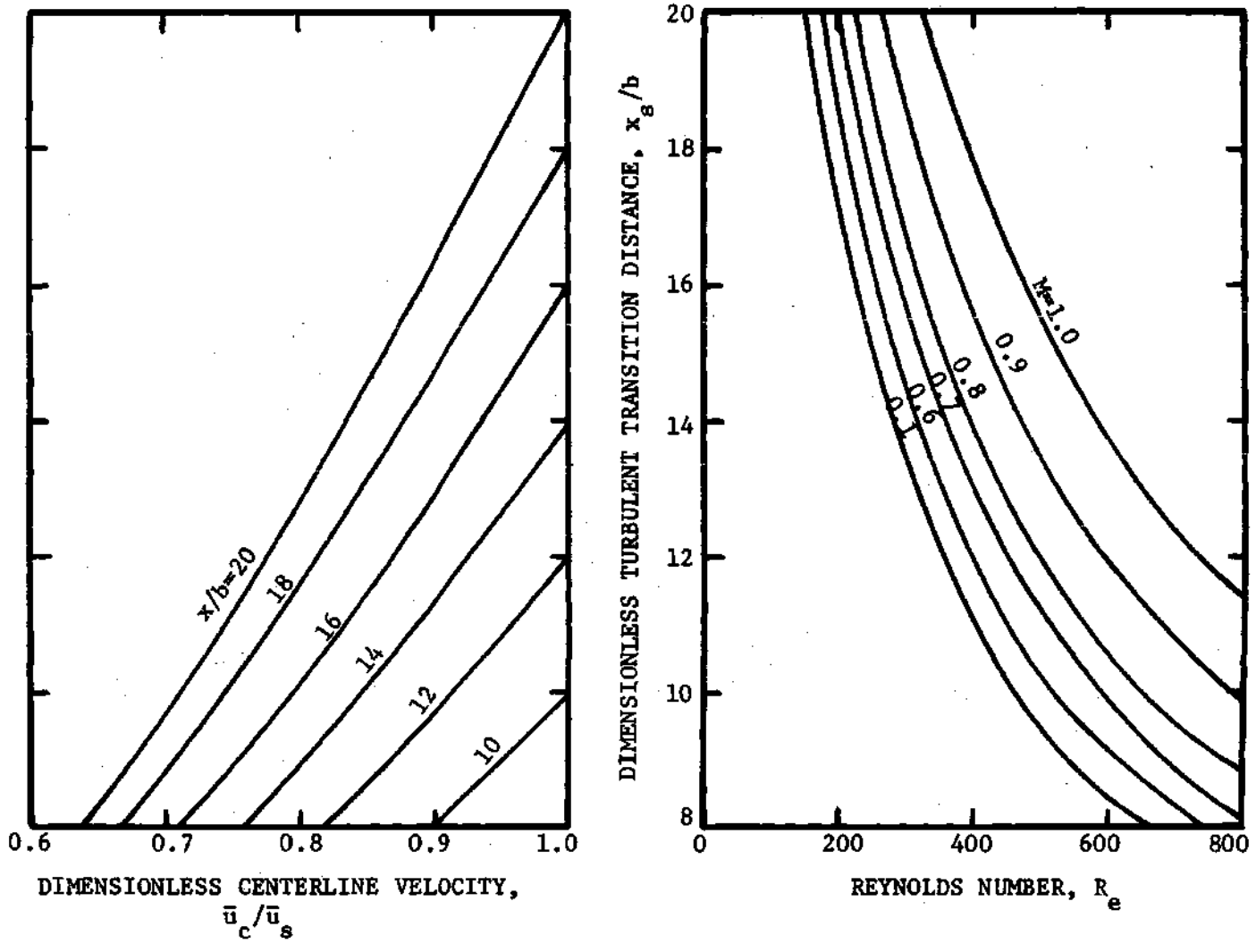

Figure 62. Graphical Presentation of Centerline Velocity in the Turbulent Regime

Expression (165) is presented as a function of Reynolds and Mach number in Figure 63.

Since the longitudinal momentum is conserved, the momentum at any arbitrary position can be equated to that at x/b = 0.25

$$J_\infty\Big|_x = J_\infty\Big|_{x/b=1/4} \tag{166}$$

Substituting equation (153) into the previous expression and solving for y*/b, yields

$$\frac{y^*}{b}\Big|_x = \frac{y_c}{b}\Big|_x + \frac{B\left[\frac{y_c/b}{1-B} + 0.292(y^*/b - y_c/b)\sum_{m=0}^{\infty}\frac{B^m}{\sqrt{m+1}}\right]\Big|_{\frac{x}{b}=\frac{1}{4}} - \frac{y_c}{b}\left(\frac{B}{1-B}\right)\Big|_x}{0.292\ B\sum_{m=0}^{\infty}\frac{B^m}{\sqrt{m+1}}\Big|_x} \tag{167}$$

The value of the power series $\sum_{m=0}^{\infty}\frac{B^m}{\sqrt{m+1}}$ is presented in Figure 64 as a function of B.

Examples of Data Correlation

In order to illustrate the application of Figures 59 through 64, two sets of experimental data will be compared to the predictions of the data correlation. In the first set of data the boundary layers have met within the nozzle and thus no potential core exists. In the second set of data the core persists some distance beyond the exit of the nozzle.

In the first example the pressure and temperature in the stagnation tank upstream of the nozzle are 1.149 mm. hg. and 532°R, respectively. The pressure in the experimental model is 1 mm. hg. The pressure ratio

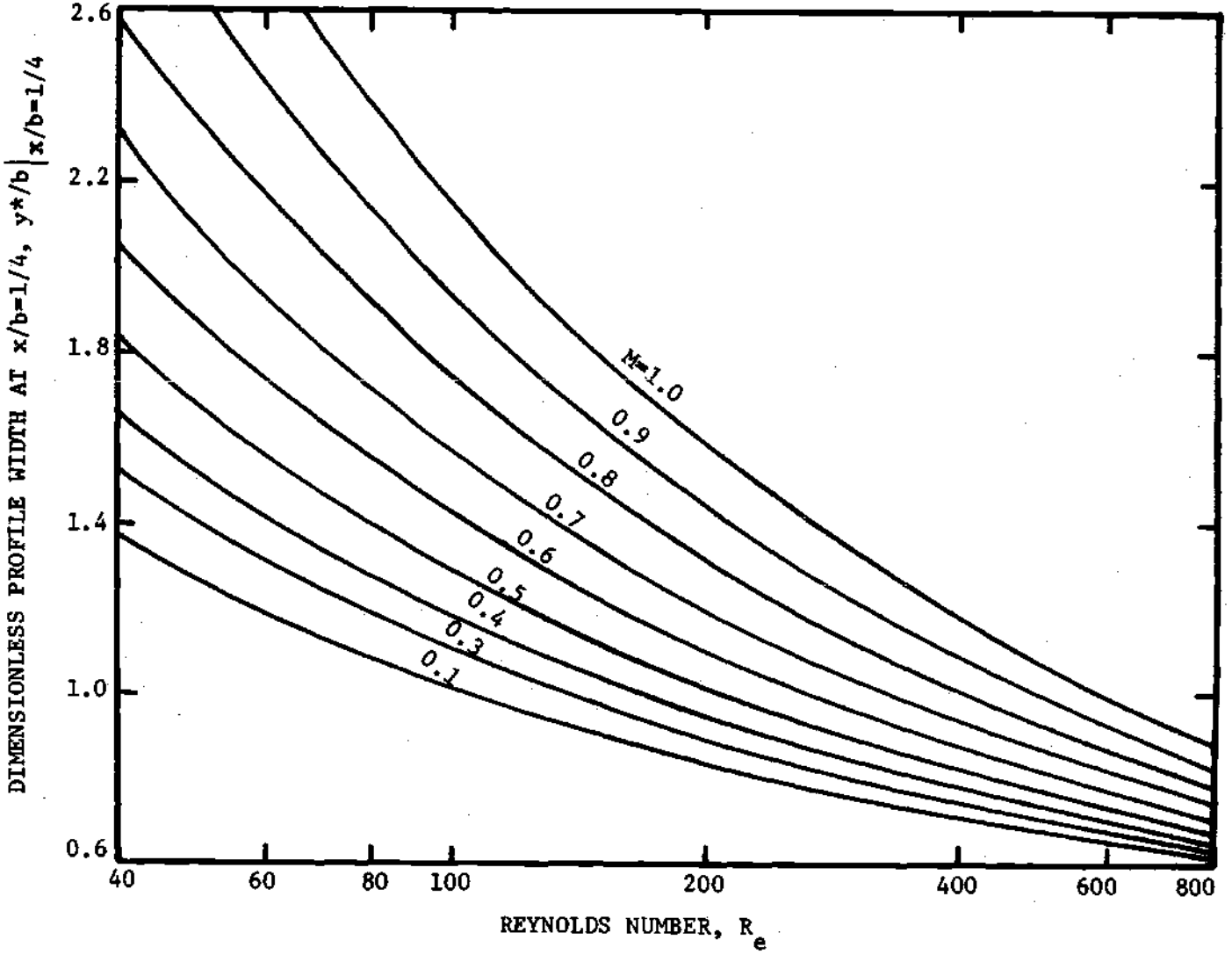

Figure 63. Graphical Presentation of Dimensionless Profile Width at x/b = 1/4

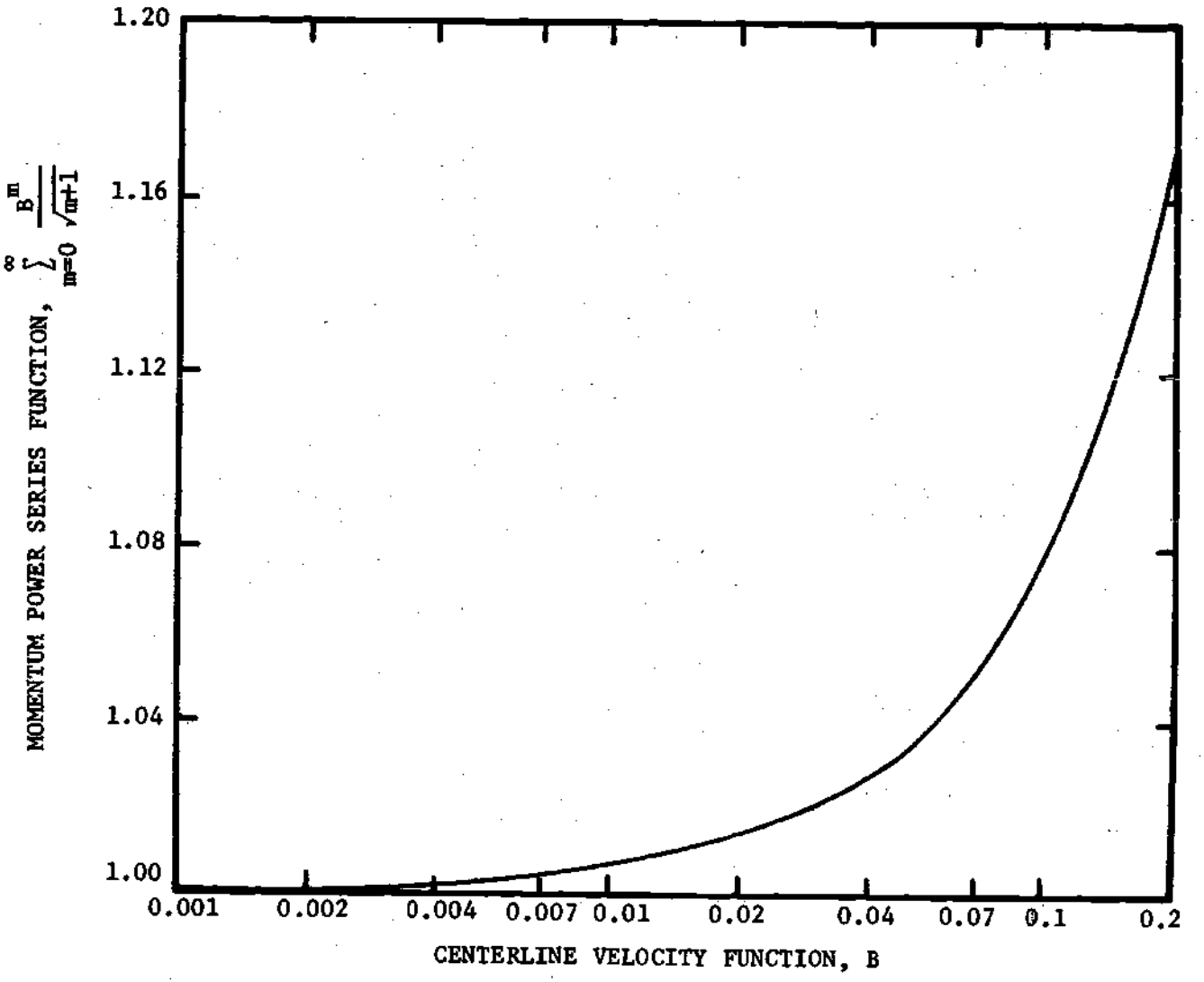

Figure 64. Graphical Presentation of Momentum Power Series Function

across the nozzle is

$$P_m/P_T = \frac{1.00 \text{ mm. hg.}}{1.149 \text{ mm. hg.}} = 0.8703 \tag{168}$$

The Mach number and ratio of static to total temperature at the nozzle exit are calculated from one-dimensional perfect gas relationships to be

$$M = 0.45 \quad ; \quad T/T_T = 0.9611 \tag{169}$$

The static temperature at the nozzle exit is calculated to be 512°R. The sonic velocity of the flow is defined as

$$c = \sqrt{k \bar{R} T g_c} \tag{170}$$

The velocity at the centerline of the nozzle exit plane is

$$\bar{u}_0 = M c \tag{171}$$

The sonic velocity and the velocity at the centerline of the nozzle exit plane are computed from the previous definitions to be 1108 ft./sec. and 499 ft./sec., respectively.

The Reynolds number at the centerline of the nozzle exit is defined as

$$R_e = \frac{\rho \bar{u}_0 b}{\mu} \tag{172}$$

If it is assumed the gas is ideal, then the density may be expressed as

$$\rho = P_m/\bar{R} T \tag{173}$$

Assuming the viscosity of the gas is proportional to the square root of temperature, then viscosity may be expressed as

$$\mu = \mu_* \, (T/T_*)^{1/2} \tag{174}$$

where μ_* represents the viscosity at some reference temperature T_*.

The density may be computed from expression (173) and is

$$\rho = (1.0 \text{ mm.hg.})(2.783 \text{ lbf./ft.}^2\text{mm.hg.})/(53.34 \tfrac{\text{ft.lbf.}}{\text{lbm.}^\circ\text{R}})(512^\circ\text{R})$$

$$\rho = 1.02 \times 10^{-4} \text{ lbm./ft.}^3 \tag{175}$$

The viscosity of the gas from expression (174) is

$$\mu = 0.37 \times 10^{-6} \sqrt{\frac{512^\circ\text{R}}{492^\circ\text{R}}} \tag{176}$$

$$\mu = 0.377 \times 10^{-6} \text{ lbf.sec./ft.}^2$$

Introducing the values of density and viscosity into equation (172) where b is equal to 0.0167 feet, yields

$$R_e = (1.02 \times 10^{-4})(499)(0.0167)/(0.377 \times 10^{-6})(32.2) \tag{177}$$

$$R_e = 70.0$$

The Reynolds number and Mach number based on potential flow conditions at the nozzle exit are thus 70 and 0.45, respectively. Entering the plot to the right in Figure 59 with these values, it is determined there is no potential core and the velocity coefficient, c_v, is 0.921. The Reynolds number and Mach number, therefore, must be

recomputed before the correlation can proceed. The velocity at the centerline of the nozzle's exit plane may be calculated from equation (158) and is

$$\bar{u}_0 = c_v \bar{u}_i \tag{178}$$

$$\bar{u}_0 = (0.921)(499 \text{ ft./sec.}) = 460 \text{ ft./sec.}$$

If it is assumed that the flow is isoenergetic, the static temperature, T, at the centerline of the nozzle's exit plane may be expressed as

$$T = T_T - \bar{u}_0^2/2\, g_c\, C_p \tag{179}$$

The value of T is calculated to be 514.4°R. The sonic velocity, c, and the Mach number which are defined in expressions (170) and (171) are recomputed to be 1110 ft./sec. and 0.414, respectively. The Reynolds number is recalculated to be 64 based on the exit plane centerline velocity of 460 ft./sec. and the temperature of 514.4°R.

With the computation of the true values of Reynolds and Mach number the correlation may proceed. Entering the plot to the right in Figure 62 with a Reynolds number of 64 and a Mach number of 0.414, it is determined that turbulent transition does not occur within 20 nozzle widths of the exit plane. The centerline velocity is described by the transition regime from the exit plane to 20 nozzle widths downstream. From Figure 60 the transition parameter, x_0/b, is determined to be 0.214. Entering the plot to the right of Figure 61 with the values of x_0/b =

0.214 and $x_c/b = 0$, the parameter $\left(\frac{x_0/b}{x_c/b + x_0/b}\right)$ is determined to be one. The centerline velocity may be evaluated from the plot on the left side of this nomograph. For example, at the position $x/b = x_0/b$ the centerline velocity is 96.2 percent of the value at the exit plane. A comparison is shown in Figure 65 between the predicted centerline velocity and experimental data. Although the experimental data exhibit a slightly higher velocity for large distances from the exit plane, the correlation provides a reasonable description.

With the centerline velocity known it is possible to calculate the value of the jet width parameter, y*/b, and thus completely describe the flow. From Figure 63 y*/b at x/b = 0.25 is found to be 1.40. Introducing this value into the expression for the jet width parameter, equation (167), and simplifying for the case where $y_c/b = 0$ yields

$$y^*/b\Big|_x = \frac{1.40 \left(B \sum_{m=0}^{\infty} \frac{B^m}{\sqrt{m+1}}\right)\Big|_{x/b=1/4}}{\left(B \sum_{m=0}^{\infty} \frac{B^m}{\sqrt{m+1}}\right)\Big|_x} \qquad (180)$$

A summary of the calculated values of y*/b for several downstream stations is provided in Table 2. The value of B is calculated from equation (154) while the summation $\sum_{m=0}^{\infty} \frac{B^m}{\sqrt{m+1}}$ is determined from Figure 64.

A comparison between time-average velocity profiles and correlation predictions is made in Figure 66. The velocity data have been nondimensionalized at the appropriate downstream position with the

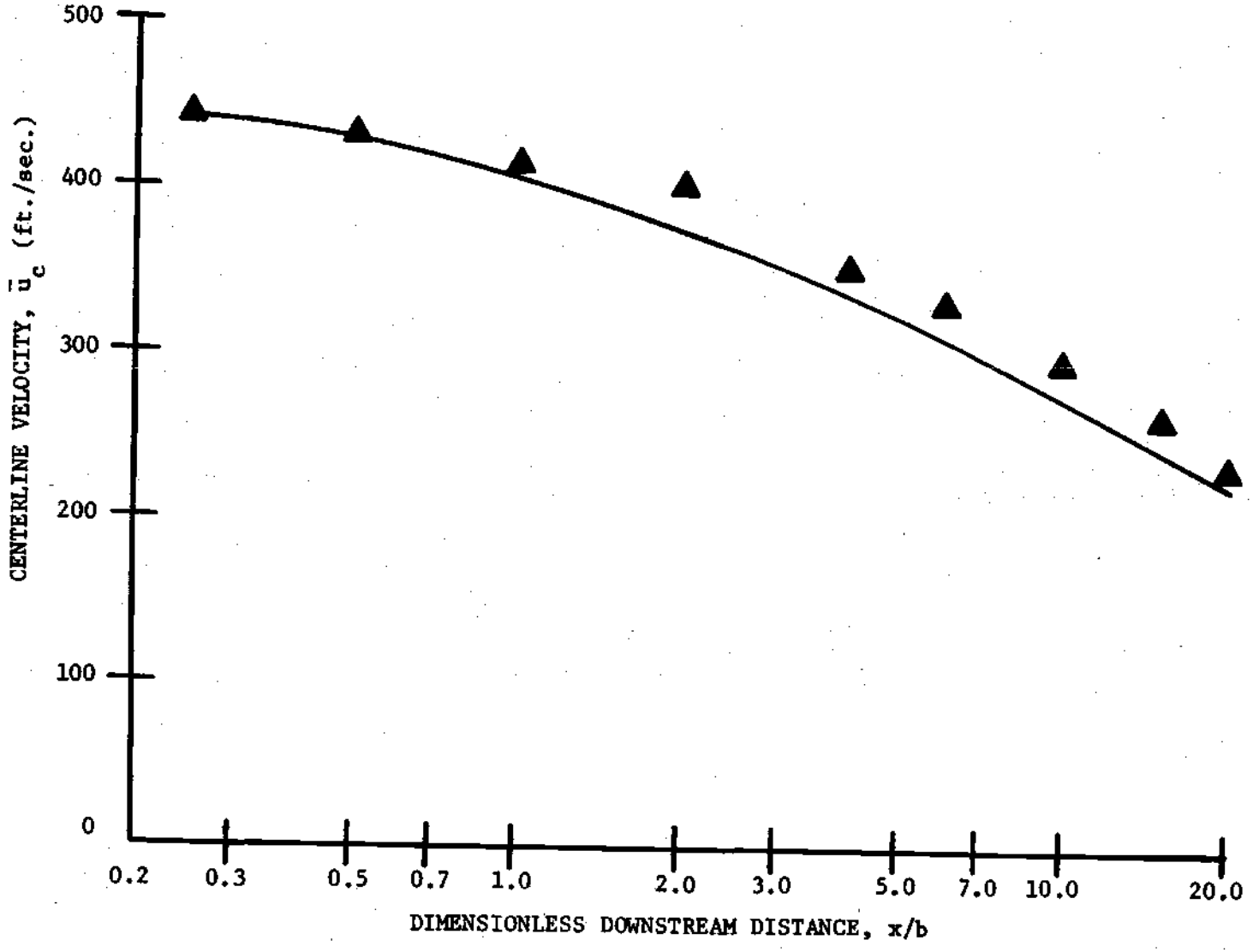

Figure 65. Comparison of Correlation to Centerline Velocity Data for R_e = 64.2, M = 0.416

Table 2. Tabulation of Jet Width Parameters for Example 1

x/b	$\bar{u}_c$ (ft./sec.)	B	$\sum_{m=0}^{\infty} \frac{B^m}{\sqrt{m+1}}$	y*/b	y_c/b
0.25	443	0.03071	1.021	1.40	0.0
3.0	352	0.01939	1.014	2.23	0.0
6.0	310	0.01504	1.011	2.89	0.0
10.0	272	0.01158	1.009	3.76	0.0
20.0	221	0.00764	1.006	5.71	0.0

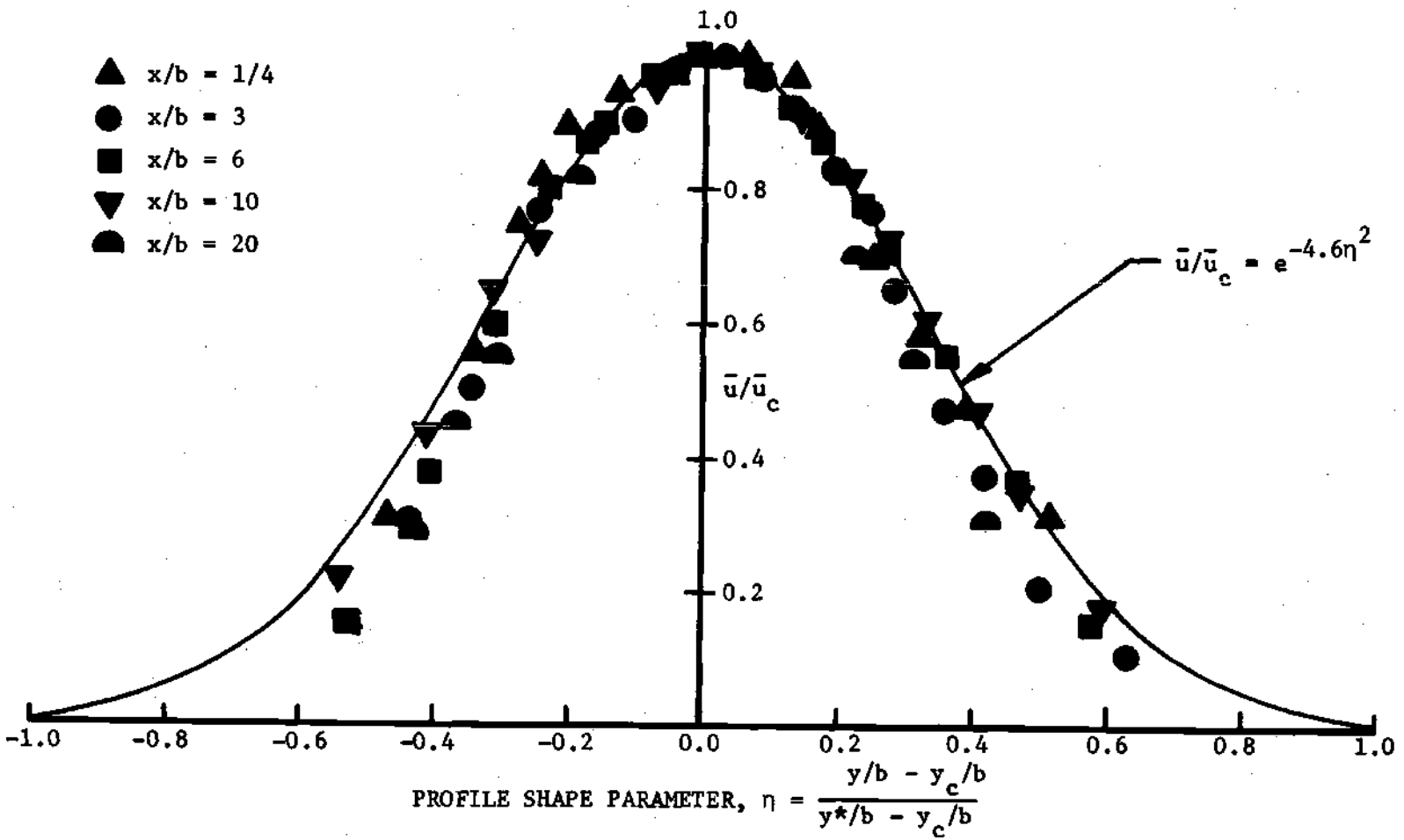

Figure 66. Comparison of Correlation to Time-Average Velocity Profiles for R_e = 64.2 and M = 0.416

parameters in Table 2. Figure 66 illustrates the data correlation provides a reasonable description of the velocity profiles shown. The fit would appear to be more accurate near the jet's centerline in comparison to the edges of the jet.

In the second example the absolute pressure and temperature in the stagnation tank are 5.666 mm. hg. and 532°R, respectively. The pressure in the experimental model is 5.0 mm. hg. The pressure ratio across the nozzle is

$$P_m/P_T = \frac{5.0}{5.666} = 0.8828 \qquad (181)$$

The Mach number and ratio of static to total temperature at the centerline of the nozzle exit are computed from one-dimensional flow tables to be 0.427 and 0.965, respectively. The static temperature at the nozzle exit is calculated to be 513°R. The sonic velocity and the velocity at the centerline of the nozzle's exit plane are calculated from expressions (170) and (171) to be 1110 ft./sec. and 473 ft./sec., respectively.

The density at the centerline of the nozzle exit plane may be calculated from expression (173) and is

$$\rho = (5.0 \text{ mm.hg.})\left(2.783 \frac{\text{lbf.}}{\text{ft.}^2\text{mm.hg.}}\right)/\left(53.34 \frac{\text{ft.lbf.}}{\text{lbm.°R}}\right)(513°\text{R}) \qquad (182)$$

$$\rho = 5.085 \times 10^{-4} \text{ lbm./ft.}^3$$

The viscosity of the gas from expression (174) is

$$\mu = 0.37 \times 10^{-6} \sqrt{\frac{513°R}{492°R}} \qquad (183)$$

$$\mu = 0.378 \times 10^{-6} \text{ lbf.sec./ft.}^2$$

Introducing the values of density, viscosity and velocity into equation (172), yields

$$R_e = (5.085 \times 10^{-4})(473)(0.0167)/(0.378 \times 10^{-6})(32.2) \qquad (184)$$

$$R_e = 330$$

The Reynolds number and Mach number based upon potential flow conditions at the nozzle exit are thus 330 and 0.426, respectively. Entering the plot to the right in Figure 59 with these values, it is determined the core length is $x_c/b = 2.4$. Entering the plot to the left of the nomograph with $x_c/b = 2.4$, the core width may be calculated as a function of downstream distance. For example, at $x/b = 0.25$ the core width is $y_c/b = 0.167$.

The first step in computing the centerline velocity beyond the core region is to determine the point separating the transition and fully turbulent regimes. Using the plot to the right in Figure 62, turbulent transition is found to occur at $x_s/b = 12.9$. The transition parameter, x_0/b, which is required to calculate the centerline velocity in the transition regime, is found from Figure 60 to be 1.12. Entering the plot to the right in Figure 61 with $x_0/b = 1.12$ and

$x_c/b = 2.4$, the parameter $\left(\frac{x_0/b}{x_c/b + x_0/b}\right)$ is found to be 0.318. The centerline velocity in the transition regime may be calculated in the plot to the left of this nomograph as a function of downstream distance. For example, at $x/b = 5$ x_0/b the nondimensional centerline velocity is $\bar{u}_c/\bar{u}_0 = 0.968$. The centerline velocity in the turbulent regime may be calculated from the plot to the left in Figure 62 as a function of downstream distance. For example, the nondimensional centerline velocity at $x/b = 16$ is $\bar{u}_c/\bar{u}_s = 0.9$. A comparison is presented in Figure 67 of the centerline velocity prediction and the experimental data. The correlation gives a good description of the data except at 20 nozzle widths downstream of the exit plane. The high centerline velocity decay rate at this position was assumed to be the result of three-dimensional flow developing in the experimental jet.

With the centerline velocity known, the jet width parameter, y^*/b, may be determined and the flow completely described. The jet width parameter, y^*/b, at $x/b = 0.25$ is found from Figure 63 to be 0.836. The value of y^*/b can consequently be determined for any downstream position from expression (167). A tabulation is provided in Table 3 of the calculated values of y^*/b for several downstream positions.

Table 3. Tabulation of Jet Width Parameters for Example 2

x/b	$\bar{u}_c$ (ft./sec.)	B	$\sum_{m=0}^{\infty} \frac{B^m}{\sqrt{m+1}}$	y*/b	y_c/b
0.25	473	0.03501	1.024	0.836	0.167
3.0	471	0.03471	1.024	1.259	0.0
6.0	458	0.03282	1.0225	1.333	0.0
10.0	439	0.03015	1.021	1.453	0.0

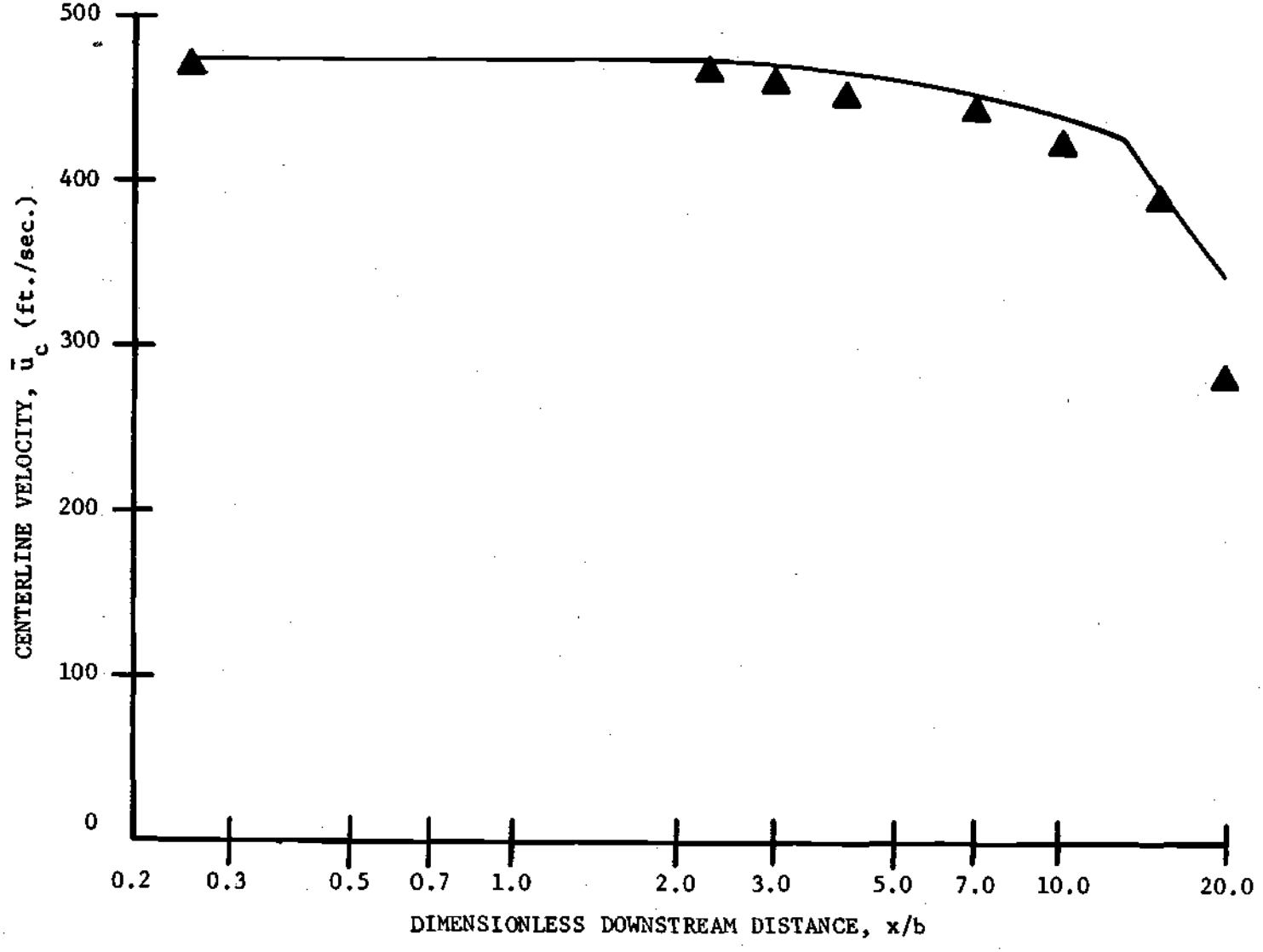

Figure 67. Comparison of Correlation to Centerline Velocity Data for R_e = 325 and M = 0.426

A comparison is made in Figure 68 between predicted and actual time-average velocity profiles. The velocity data are nondimensionalized with the parameters in Table 3. This figure illustrates the correlation provides a reasonable description of the data. The fit would appear again to be more accurate near the centerline in comparison to the edges of the jet.

Estimated Accuracy of the Data Correlation

In order to indicate the accuracy of the correlation, the experimental data in the free jet investigation were compared to the predicted values of these parameters. A summary of the maximum errors between predicted and actual centerline velocity data is presented in Table 4. In this table the maximum error between data and prediction is presented for the positions from the exit plane to 10 and 20 nozzle widths downstream, respectively. The maximum percentage error is calculated by dividing the velocity error by the measured value of exit plane velocity, $\bar{u}_0$. Table 4 indicates that for positions between the nozzle exit and 10 nozzle widths downstream, the maximum error is 10.1 percent with an expected error of approximately five percent. For positions from 10 to 20 nozzle widths downstream the expected error increases in the higher Reynolds number cases to approximately 10 percent. This was assumed to be the result of three-dimensional flow developing in the experimental jet for these conditions.

The computation of the time-average velocity profiles is dependent on the correlation of y_c/b, y^*/b at $x/b = 0.25$ and $\bar{u}_c$. A comparison of the experimental data and the analytical predictions indicated

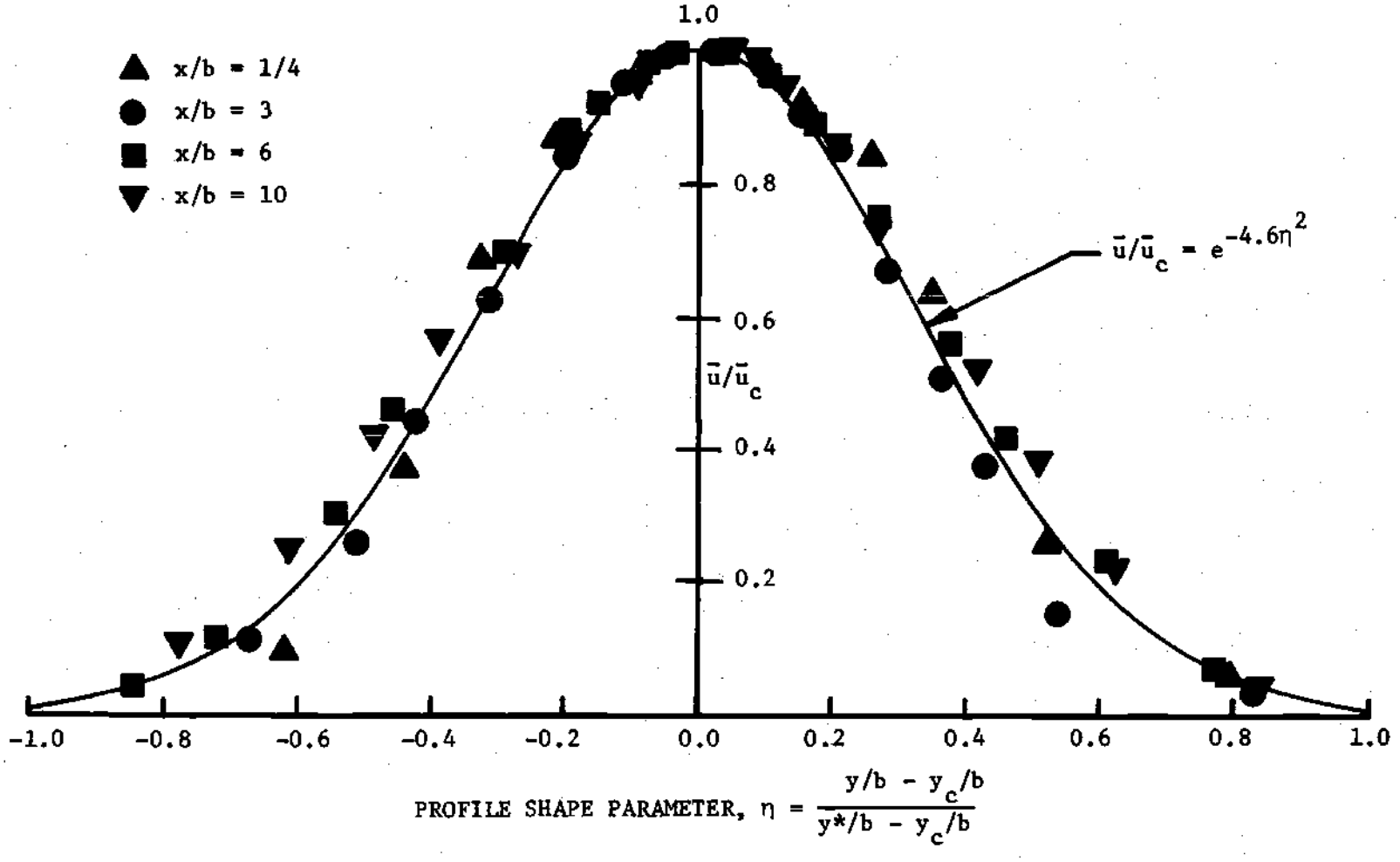

Figure 68. Comparison of Correlation to Time-Average Velocity Profiles for R_e = 325 and M = 0.426

Table 4. Tabulation of Error Between Measured Values of Centerline Velocity and Data Correlation Predictions

Reynolds Number of Flow	Mach Number of Flow	Maximum Percentage Centerline Velocity Error to x/b = 10	Maximum Percentage Centerline Velocity Error to x/b = 20
47.7	0.591	10.10	10.10
64.2	0.416	6.04	6.04
109	0.670	3.03	5.10
152	0.885	4.62	4.62
142	0.457	3.75	3.75
255	0.761	5.50	5.50
336	0.956	5.70	5.70
262	0.347	2.30	6.70
325	0.426	3.85	14.10
515	0.646	1.10	17.80
359	0.240	2.00	11.20
558	0.368	3.70	11.60
705	0.458	1.70	8.90
546	0.183	0.50	9.00
645	0.216	3.10	7.40

the correlation was quite accurate in the estimates of y_c/b and y^*/b at $x/b = 0.25$. The main source of error resulted from the calculation of y^*/b as a function of the correlated value of $\bar{u}_c$. Since y^*/b is proportional to $\bar{u}_c^2$, the expected maximum error in y^*/b and η is approximately double the expected maximum error in $\bar{u}_c$. Thus for positions up to 10 nozzle widths downstream of the exit plane, the expected maximum error in the profile similarity parameter, η, is approximately 10 percent. The expected maximum error for high Reynolds number cases between the positions of 10 to 20 nozzle widths downstream is anticipated to increase to approximately 20 percent.

In summary, the free jet experiments yielded the following conclusions:

1. Lower Reynolds number and higher Mach number flow conditions retard the growth of turbulent free shear layers; this observation is in agreement with the predictions from stability theory by Curle [23] and Pai [24].
2. The power profile solution of Schlichting [15] is not in agreement with the latter up to 20 nozzle widths from the exit plane for the lower Reynolds number jet flows, although it would appear to approach this distribution in the limit.
3. Jet flows in this regime may be composed of a potential core regime, a laminar transition regime where the turbulent shear layers have not met and their effect is small, a turbulent transition region beyond the coalescence of the free turbulent layers and a fully turbulent zone.

4. Not all four regions may be present in a single case. This is apparent since no laminar transition region existed for high Reynolds number conditions. Likewise, no core regions were found for low Reynolds number flows.

A correlation of the time-average component of velocity in the longitudinal direction is presented. This correlation employs only simple calculations along with the graphs shown in Figures 59 through 64 to describe the jet's centerline velocity and profile shape. The predictions of the data correlation up to 10 nozzle widths downstream are expected to be within approximately five percent for the centerline velocity and 10 percent for the jet width parameter, η.

CHAPTER V

JET INTERACTION EXPERIMENTS

Experimental Data

A complete collection of the experimental data is presented in Appendix D which describe the interaction process of two transverse jets in the low Reynolds number compressible flow regime. These data include the deflection angle of the power jet after the interaction process as well as steady state velocity, static pressure and velocity vector profiles. Reynolds and Mach number based upon upstream stagnation conditions and differential pressure across the nozzle are employed to describe the several power jet flow conditions. The differential pressure and mass flow rate through the control port along with the geometry serve to complete the description of the experiments. Sample calculations are presented in Appendix H of the power jet deflection angle as well as the power and control port mass flow rates. These predictions are based upon Simson's [27] model of the interaction process and the free jet correlation from this flow regime.

Jet Deflection Angle

Experimental investigations were performed at a number of flow conditions in the low Reynolds number compressible flow regime. In these studies the power jet flow was subjected to a control pressure from a transversely positioned jet; see Figure 27. This control pressure resulted in the deflection of the power jet away from the control

port. The deflection angle of the power jet was measured downstream of the interaction zone and its value was compared to the prediction of Simson's interaction model [27].

The power jet's momentum which is required for the prediction of jet deflection angle is provided by the free jet data correlation. The first step in determining the momentum consists of computing the Reynolds and Mach number of the power jet from the upstream stagnation conditions and the differential pressure across the supply port. Then after employing Figures 59 through 64 to determine the required jet parameters, the momentum of the power jet is calculated from expression (153). With the power jet momentum known the jet deflection angle may be computed from Simson's interaction model, that is equation (115), in terms of the control port pressure and the interaction geometry. A sample calculation of the power jet deflection angle is presented in Appendix H.

Typical experimental data are compared to predicted values of the power jet deflection angle in Figure 69. The independent variable in these tests was the control pressure which is given in terms of mm. of oil (specific gravity 1.04) above the model's ambient pressure. The deflection angle was determined by taking the best average of the jet's centerline position at several stations downstream of the interaction region; see Figure 70. Figure 69 illustrates Simson's model in conjunction with the free jet correlation provides a good description of the experimental data. Of the 18 deflection angles measured, the maximum error in the prediction was 1.9° while the average error was 1°.

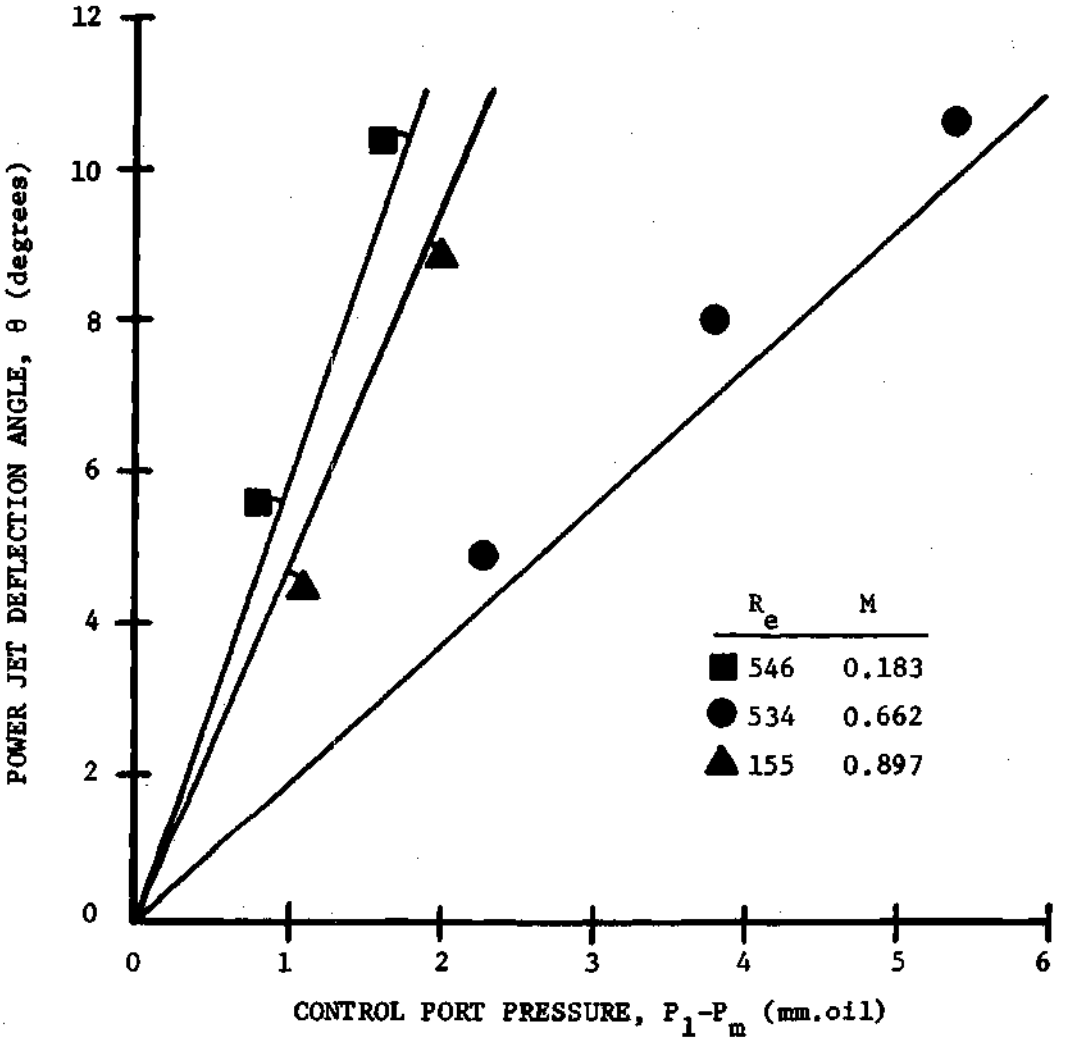

Figure 69. Comparison of Predicted Values of Jet Deflection Angle to Experimental Data

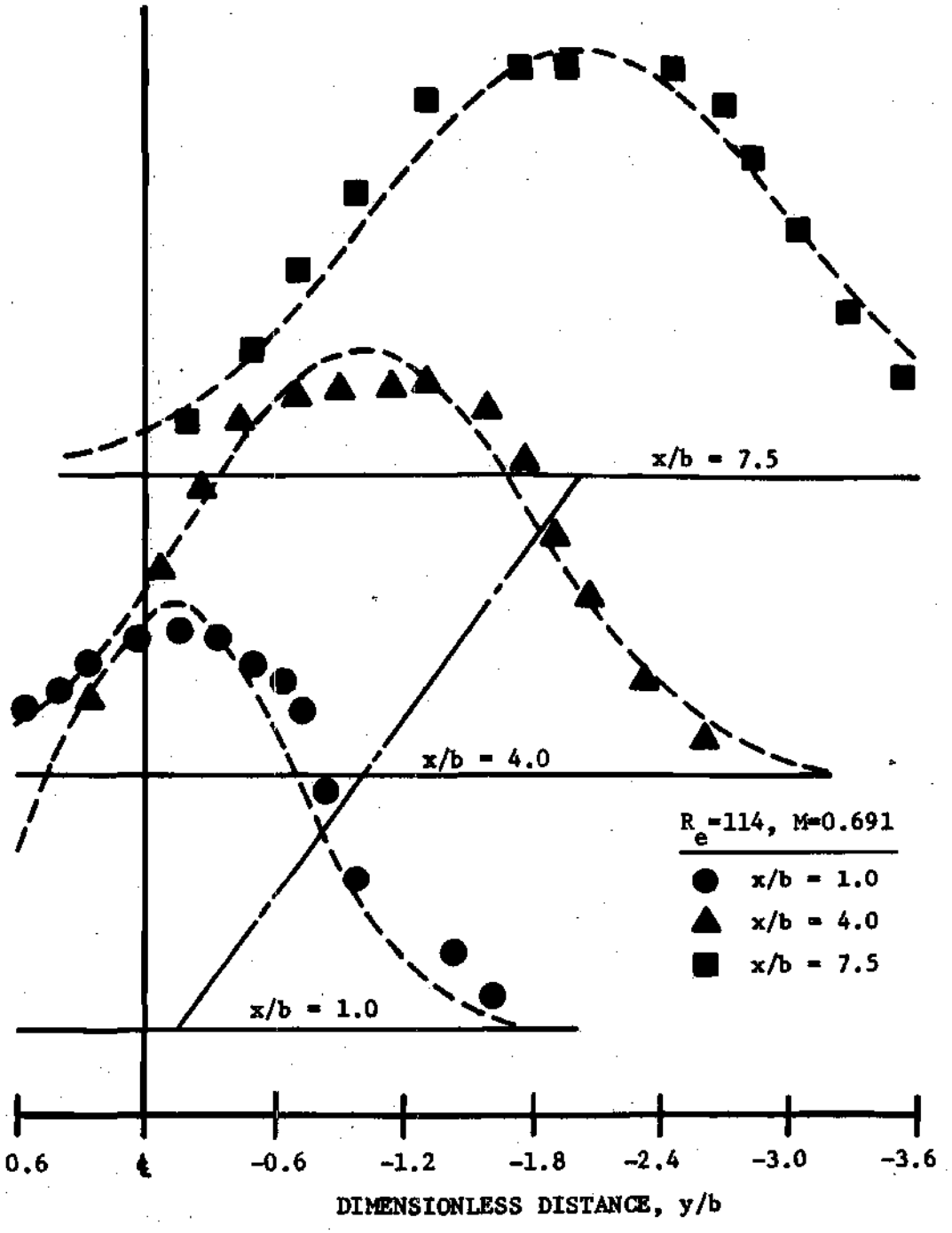

Figure 70. Comparison of Predicted and Measured Time-Average Velocity Profiles in a Deflected Jet

The agreement between the calculated and measured values of jet deflection angle suggests the interaction process is not significantly affected by molecular effects in the regime investigated. That is the regime described by

$$1 \times 10^{-2} \geq K_n \geq 5 \times 10^{-4} \tag{185}$$

where K_n is the Knudsen number based on nozzle width, b.

Typical deflected jet velocity profiles are compared in Figure 70 with the predictions of the data correlation. The time-averaged velocity data in this figure have been nondimensionalized at each longitudinal station by the corresponding prediction of centerline velocity. It should be noted that the correlation was evaluated at the longitudinal position of the corresponding traverse. Variations of axial distance traveled by the jet across the plane of the traverse were found to be small and thus were not considered in the prediction. As is expected, Figure 70 illustrates the velocity profile at the trailing edge of the control port, which is located one nozzle width downstream, is not in agreement with the prediction. Firstly, the velocity near the control port edge is much higher than predicted. This would appear to result from the pressure differential across the control port edge. Secondly, the central portion of the velocity profile appears to be skewed slightly away from the control port as a result of its force. As the jet progresses downstream the asymmetries in the velocity profile are smoothed by diffusion with the fluid at rest. This effect may be observed in the velocity profile four nozzle widths downstream. At

this location the data correlation compromises a reasonable representation of the data. In general, it is observed that beyond a streamwise station about three nozzle widths from the power jet exit plane the correlation is in good agreement.

Studies were made of the static pressure and velocity vector distributions in the deflected power jets. A comparison of these data to profiles obtained in the free jet investigation demonstrated that the pressure and velocity vector profiles were essentially the same for positions greater than three nozzle widths downstream of the exit plane. The comparison was made about the respective centerlines of each jet at a common flow state and downstream position.

Control Port Flow Rate

Simson's model of the pressure controlled interaction process describes the control port mass flow rate in terms of the power jet description, control port differential pressure and interaction region geometry. In the following section Simson's model will be simplified and subsequently evaluated for the present flow regime.

For the isoenergetic flow of an ideal gas with constant specific heats, the expression for density presented in equation (151) may be introduced into Simson's analytical model. The control port flow rate found in equation (130) becomes

$$\dot{m}_c = \rho_T (P_m/P_T)\ \bar{u}_c\ h \int_0^{y_e + \frac{X^2(P_1 - P_m)}{2J_\infty}} \frac{\bar{u}/\bar{u}_c\ dy}{[1 - B(\bar{u}/\bar{u}_c)^2]} \qquad (186)$$

$$+ \frac{h\sqrt{\rho(P_1-P_m)}}{2} \frac{\left[y_e + \frac{X^2(P_1-P_m)}{2J_\infty} - y_c\right]^2}{y^* - y_c} - \frac{\dot{m}_i}{2} \qquad (186)$$

Substituting the Gaussian velocity profile given in equation (148) into the first term of the previous expression and integrating, yields

$$\dot{m}_c = \frac{h\ b\ P_m\ \bar{u}_c}{\bar{R}\ T_T}\left[\frac{\bar{y}_c/b}{1-B} + 0.8264\ (y^*/b - y_c/b)\ \Gamma_2\ (B,\eta_2)\right] \qquad (187)$$

$$+ \frac{h\ b\sqrt{\rho(P_1-P_m)}}{2}\ (y^*/b - y_c/b)\ \eta_2^{\,2} - \frac{\dot{m}_i}{2}$$

where $\bar{R}$ and T_T represent the gas constant and total temperature of the gas, respectively.

The parameter η_2 in equation (187) is defined as

$$\eta_2 = \frac{y_e/b + \frac{(X/b)^2\ (P_1-P_m)}{2J_\infty/b} - y_c/b}{y^*/b - y_c/b} \qquad (188)$$

The function $\Gamma_2(B,\eta_2)$ is

$$\Gamma_2(B,\eta_2) = \sum_{m=0}^{\infty} \frac{B^m}{\sqrt{2m+1}}\ \phi\ (\sqrt{9.2\ (2m+1)}\ \eta_2) \qquad (189)$$

$\phi(x)$ in the previous equation represents the cumulative distribution function which is tabulated in handbooks dealing with probability. The free jet mass flow rate function, $\Gamma_2(B,\eta_2)$, has been evaluated in terms of B and η_2 and the results are presented in Figure 71. A detailed description

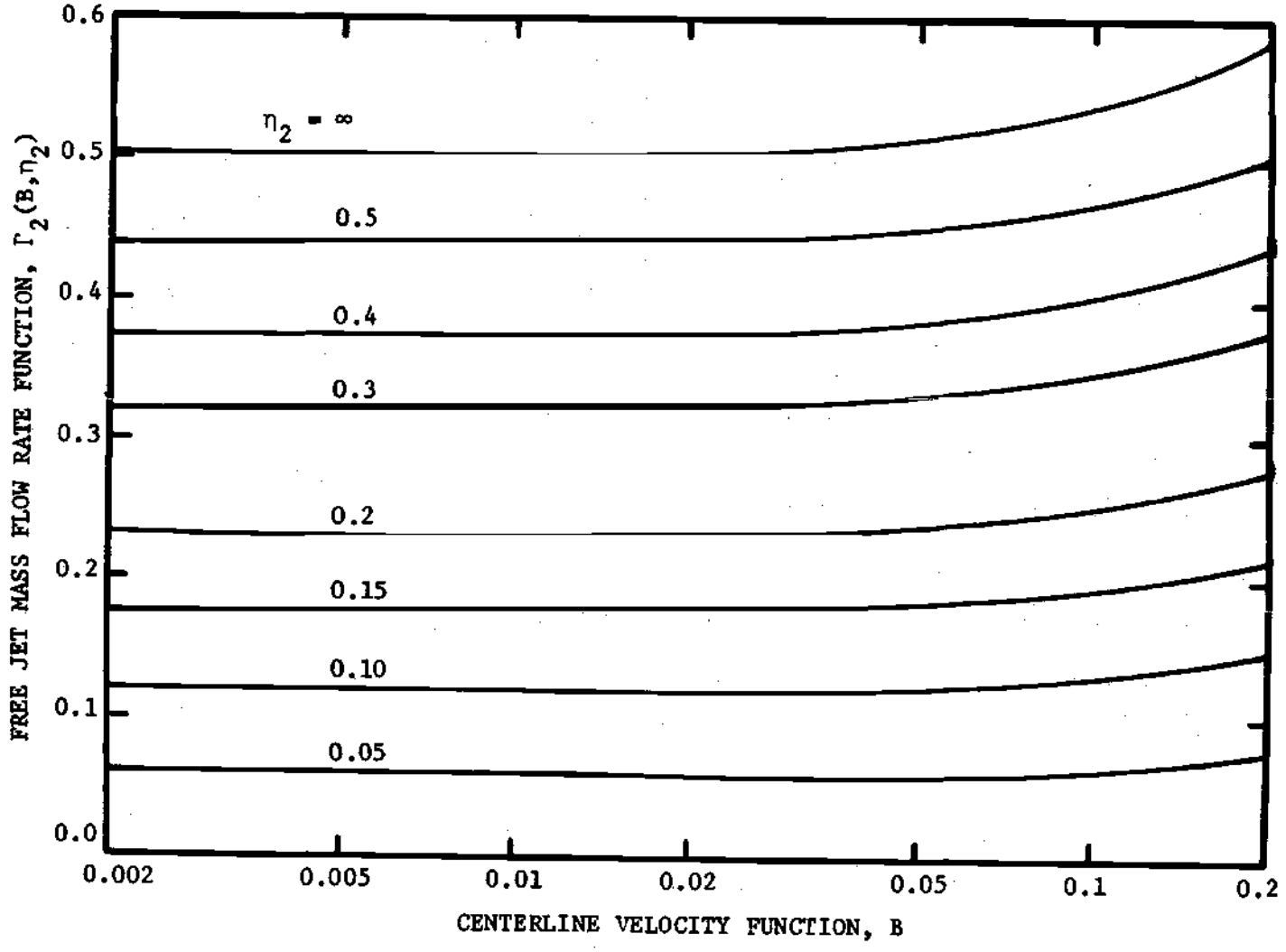

Figure 71. Graphical Presentation of Free Jet Mass Flow Rate Function

of the evaluation of the first term of equation (186) is presented in Appendix F.

The control port mass flow rate which is presented in equation (187) is completely specified in terms of the control port pressure, the interaction region geometry, the free jet characteristics and the supply nozzle flow. The free jet characteristics are evaluated at the downstream position where the power jet passes the knife edge; see Figure 27. This distance nondimensionalized by the supply jet width may be expressed for small deflection angles as

$$s'/b = \frac{(J_\infty/b)(X/b)}{(y_e/b)(P_1-P_m) + J_\infty/b} \tag{190}$$

A comparison of measured and predicted values of the control port mass flow rate is presented in Figure 72 as a function of control port pressure. These data are from several tests at the same flow conditions and demonstrate the results are repetitive. The free jet characteristics employed in the evaluation of expression (186) were determined from the data correlation, however, the mass flow rates from the supply nozzle were determined experimentally. It is noted that Figure 72 illustrates better agreement for lower values of the control port pressure. This is to be expected since the analysis has been restricted to small deflection angles which occur at low control port pressures. For this research the control port mass flow rates which are calculated from equation (187) are in reasonable agreement with experimental data. The maximum error in the prediction is approximately 20 percent of the maximum control port mass flow rate.

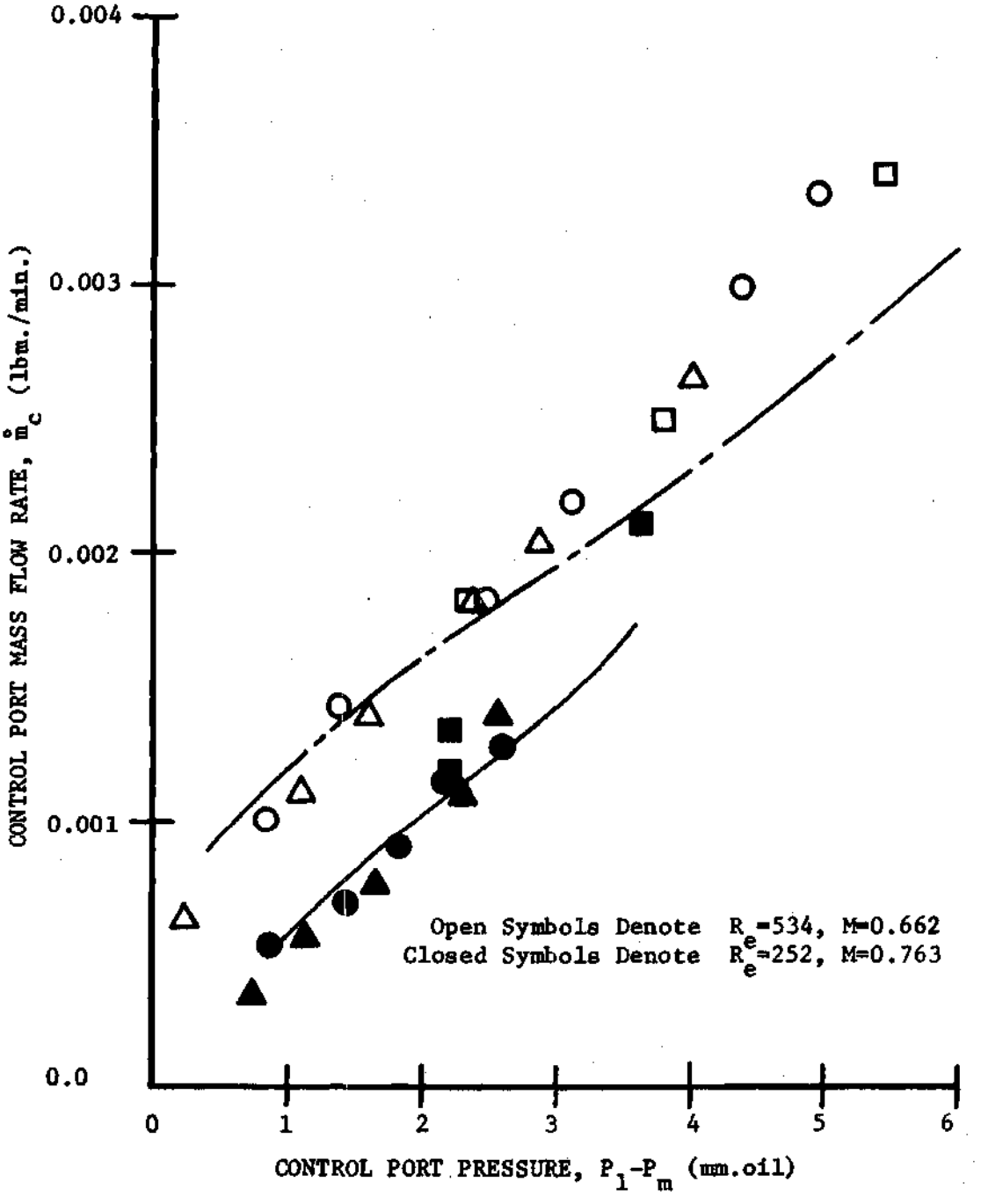

Figure 72. Comparison of Predicted and Measured Values of Control Port Mass Flow Rate

Estimation of the Supply Nozzle Mass Flow Rate

The expression for the control port mass flow rate which was formulated in the preceding section required the value of the power nozzle mass flow rate. In order to make this expression useful for design, the power nozzle flow must be computed from the known values of upstream stagnation condition, the pressure drop across the power nozzle and its geometry. The supply nozzle flow was computed in Simson's investigation of high Reynolds number turbulent jets from these data. In that case the pressure drop across the nozzle was used to calculate the potential velocity which essentially filled the exit plane. In the present flow regime this procedure is not applicable, since very thick boundary layers are present even for the highest Reynolds number cases. In the following section a procedure will be described to estimate the exit plane velocity profiles in the present flow regime. This method is based upon the free jet data correlation and an assumed form of the exit plane profile. The supply nozzle mass flow rate will be subsequently calculated from this profile.

Experimental data indicated the power jet's exit plane velocity profiles could be represented by a power law distribution of the form

$$\bar{u}/\bar{u}_c = 1.0 \qquad \text{for} \quad 0 \leq y \leq y_c \tag{191}$$

$$\bar{u}/\bar{u}_c = 1.0 - \left(\frac{y/b - y_c/b}{1/2 - y_c/b}\right)^n \qquad \text{for} \quad y_c \leq y \leq b/2$$

where n represents a variable profile distribution coefficient.

If it is assumed that the supply jet is not influenced by the control port, the longitudinal momentum per unit height of the supply

jet at the exit plane is

$$J_\infty = 2 \int_0^{b/2} \rho \bar{u}^2 \, dy \tag{192}$$

For the isoenergetic flow of an ideal gas with constant specific heats, the expression for density found in equation (151) may be introduced into the preceding equation. Equation (192) becomes

$$J_\infty = 2 \, \rho_T (P_m/P_T) \, \bar{u}_c^{\,2} \int_0^{b/2} \frac{(\bar{u}/\bar{u}_c)^2}{[1 - B(\bar{u}/\bar{u}_c)^2]} \, dy \tag{193}$$

Substituting the velocity profile given in equation (191) into the previous expression and evaluating, yields

$$J_\infty = 4 \left(\frac{k}{k-1}\right) P_m \, B \, b \left[\frac{y_c/b}{1-B} + (1/2 - y_c/b) \, \phi_1(B,n)\right] \tag{194}$$

$$\phi_1(B,n) = \sum_{m=0}^{\infty} B^m \int_0^1 (1-\tau_1^{\,n})^{2(m+1)} \, d\tau_1$$

The nozzle exit momentum function, $\phi_1(B,n)$, has been evaluated in terms of B and n and the results are presented in Figure 73.

Solving equation (194) for $\phi_1(B,n)$, yields

$$\phi_1(B,n) = \left[\frac{J_\infty/b}{4 \left(\frac{k}{k-1}\right) P_m \, B} - \frac{y_c/b}{1-B}\right] \left(\frac{1}{1/2 - y_c/b}\right) \tag{195}$$

If it is assumed that the longitudinal momentum of the power jet is conserved, then the momentum at the nozzle exit plane in the preceding

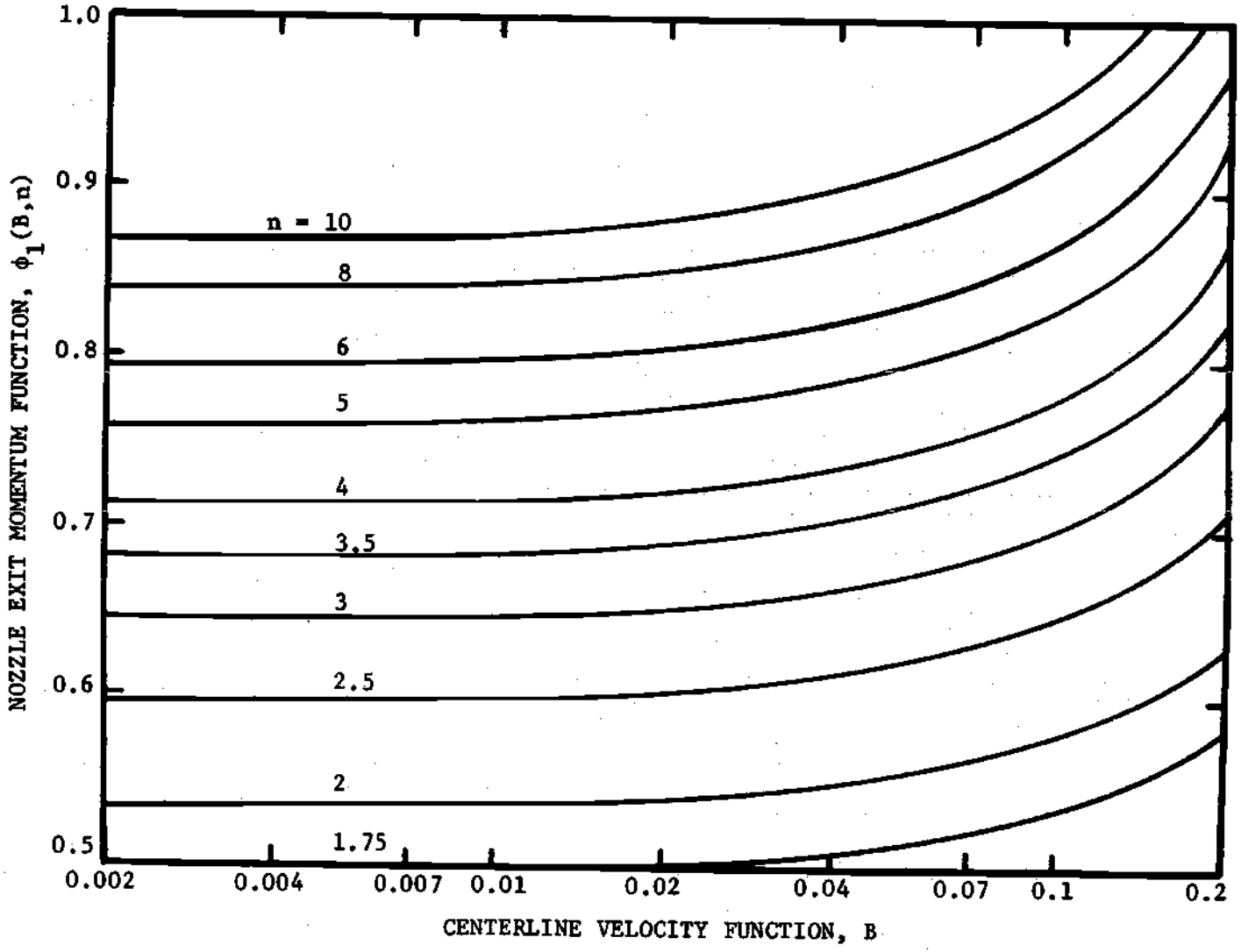

Figure 73. Graphical Presentation of Nozzle Exit Momentum Function

equation may be determined from the free jet data correlation. The core width and centerline velocity at the nozzle exit plane may also be computed from the free jet correlation. The function $\phi_1(B,n)$ is thus known. The value of the profile distribution coefficient, n, may be determined as a function of $\phi_1(B,n)$ and B from Figure 73.

The exit plane velocity profile is completely described by the core width, centerline velocity and the profile distribution coefficient, n, computed above. The mass flow rate from the supply port will be estimated from this description. The mass flow rate per unit height through the supply nozzle may be expressed as

$$\dot{m}_i = 2 \int_0^{b/2} \rho \bar{u} \, dy \tag{196}$$

Introducing into the previous equation the expression for density in an isoenergetic flow process

$$\dot{m}_i = 2 \, \rho_T (P_m/P_T) \, \bar{u}_c \int_0^{b/2} \frac{\bar{u}/\bar{u}_c}{[1 - B(\bar{u}/\bar{u}_c)^2]} \, dy \tag{197}$$

Substituting the assumed velocity profile which is presented in equation (191) into the preceding expression and evaluating, yields the expression for power nozzle mass flow rate

$$\dot{m}_i = \frac{2 \, P_m \, \bar{u}_c \, bh}{\bar{R} \, T_T} \left[\frac{y_c/b}{1-B} + (1/2 - y_c/b) \, \phi_2(B,n) \right] \tag{198}$$

$$\phi_2(B,n) = \sum_{m=0}^{\infty} B^m \int_0^1 (1-\tau_1^n)^{2m+1} \, d\tau_1$$

The nozzle exit mass flow rate function, $\phi_2(B,n)$, has been evaluated in terms of B and n and the results are presented in Figure 74. It should be noted that the free jet characteristics in equations (194) and (198) are evaluated at the nozzle exit plane.

In summary, the method for calculating the mass flow rate through the supply nozzle consists of three steps. Firstly, the free jet data correlation is employed to calculate the jet momentum, the core width and centerline velocity at the nozzle exit plane. Secondly, after solving equation (195) for $\phi_1(B,n)$ the profile distribution function, n, is determined from Figure 73. Thirdly, using Figure 74 the mass flow rate through the supply port nozzle is calculated from equation (198). A complete description is presented in Appendix G of the evaluation of the momentum and mass flow rate expressions at the nozzle exit plane.

A comparison is presented in Table 5 of calculated and measured values of power nozzle mass flow rate. This information indicates a maximum and average error in the prediction technique of approximately 10 percent and 4.6 percent, respectively. The computed and measured values of power nozzle flow are in good agreement for both low Reynolds number and high Reynolds number cases. In the former the boundary layers meet well upstream of the nozzle exit, while in the latter a substantial core exists at the exit plane. For intermediate Reynolds number cases, at which the core terminates near the exit plane, the prediction is in the greatest error. This would suggest the assumed power law distribution is somewhat in error for these exit plane profiles.

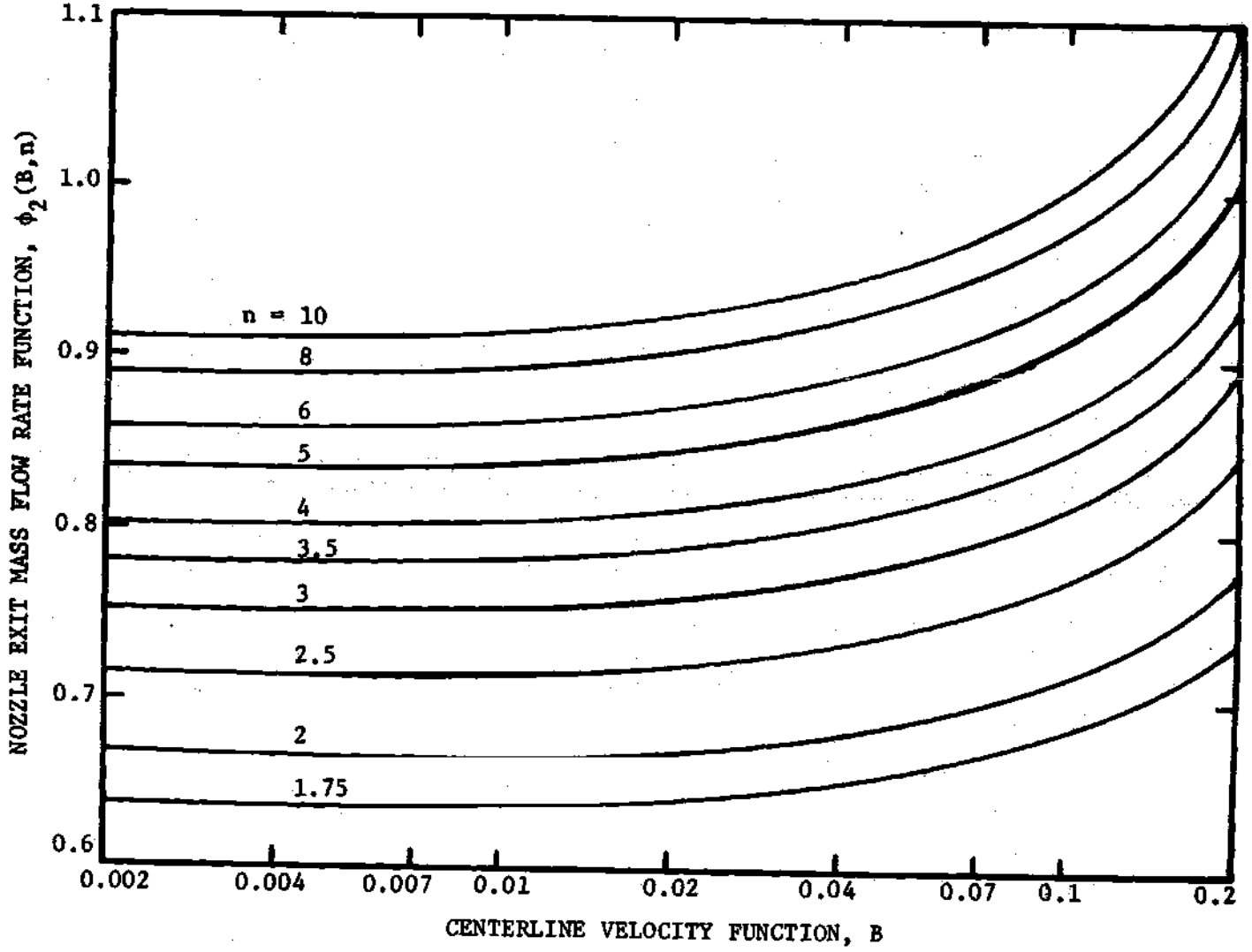

Figure 74. Graphical Presentation of Nozzle Exit Mass Flow Rate Function

Table 5. Comparison of Measured and Computed Power Nozzle Mass Flow Rates

Reynolds Number	Mach Number	$\dot{m}_i\|_c$ (lbm./min.)	$\dot{m}_i\|_e$ (lbm./min.)
114	0.691	0.005662	0.00544
155	0.892	0.00774	0.00796
252	0.763	0.01079	0.0120
341	0.970	0.0144	0.01586
326	0.434	0.01574	0.0164
534	0.662	0.02668	0.02796
546	0.183	0.02917	0.0292
700	0.222	0.03809	0.0388

Subscripts:

c - Computed from power law profile and free jet data correlation

e - Experimentally measured

In summary, the calculated values of jet deflection angle, using Simson's interaction model in conjunction with the free jet correlation, are reasonably accurate. The maximum and average errors in the jet deflection angles were found to be 1.9° and 1°, respectively. This good agreement suggests the interaction process is not significantly affected by molecular effects in the regime

$$1 \times 10^{-2} \geq K_n \geq 5 \times 10^{-4} \tag{199}$$

where K_n is the Knudsen number based on nozzle width.

Considering the simplicity of Simson's interaction model, the prediction of the control port mass flow rate using the measured value of power nozzle flow is reasonably accurate. The maximum error in the control port mass flow rate is approximately 20 percent of the maximum control port flow. If the predicted values of power nozzle flow are employed in the calculations, the maximum error in the control port mass flow rate increases to approximately 26 percent of the maximum control port flow. Better agreement between measured and predicted control port mass flow rates is found for low control port pressures. This is to be expected since the mathematical model is restricted to small deflection angles.

A technique is presented for predicting the power nozzle mass flow rate and thus making the expression for control port flow useful for design. This procedure is based on the free jet data correlation and an assumed velocity profile at the nozzle exit plane. The maximum and average error in this prediction is approximately 10 percent and 4.6 percent, respectively.

The deflected power jet's velocity profiles are found to be distorted by the control port for positions near the interaction region. However, through diffusion with the fluid at rest the velocity profiles smoothed rapidly and were in good agreement with the data correlation beyond a streamwise station three nozzle widths from the exit plane.

CHAPTER VI

JET RECEIVER IMPINGEMENT EXPERIMENTS

Experimental Data

A complete collection is presented in Appendix E of the experimental data which describe the impingement process of a free jet upon a receiver in the low Reynolds number compressible flow regime. These data include the receiver's output flow rate and pressure recovery as a function of the power jet flow condition, the position of the jet with respect to the receiver inlet and the receiver loading. Reynolds and Mach number based upon upstream stagnation conditions and differential pressure across the nozzle are employed to describe the several power jet flow conditions investigated. The control port's differential pressure and mass flow rate along with the geometry serve to identify the jet's location with respect to the receiver inlet. Receiver loading was established by modulating the distance separating the circular disk and the hole in the back plate of the receiver-diffuser. In this manner the exhaust area from the receiver was varied. Sample calculations are presented in Appendix H of the open load flow rate and the blocked load pressure. These predictions are based upon the jet receiver impingement models of Simson [27] and Reid [29] in conjunction with the free jet data correlation from the present research.

Computation of the Open Load Flow Rate

The open load flow rate for small deflection angles was presented in equation (143) for Simson's model of jet receiver interaction. Rewriting this expression

$$\dot{m}_r = h \int_{e-\ell}^{e+d-\ell} \rho \bar{u}\, dy \tag{200}$$

Since the power jet appears to emanate from the intersection of the supply and control port centerlines, the deflection distance, ℓ, may be expressed as

$$\ell = \frac{x_r \, X \, (P_1 - P_m)}{J_\infty} \tag{201}$$

The open load flow rate may be evaluated for the low Reynolds number compressible flow regime in the same manner as the generalized mass flow rate function which is presented in Appendix F. Introducing the expression for density within an isoenergetic flow process into expression (200) and simplifying, yields

$$\dot{m}_r = h \, \rho_T \, (P_m/P_T) \, \bar{u}_c \int_{e-\ell}^{e+d-\ell} \frac{\bar{u}/\bar{u}_c}{[1 - B(\bar{u}/\bar{u}_c)^2]} \, dy \tag{202}$$

The assumed Gaussian velocity distribution of a free jet may be introduced into the previous expression and the result integrated. Before preceding with this integration, the possible velocity profiles which can intersect the receiver inlet will be considered. A sketch is presented in Figure 30 of the impingement of the deflected power jet

upon the receiver inlet. In this sketch the receiver intersects only the lower developed portion of the jet. The integrand in expression (202) would thus consider only the velocity distribution outside the potential core. For larger values of the deflection distance, ℓ, the appropriate mathematical expression for the potential core velocity must be considered. It is apparent that the mathematical description of the velocity profile which intersects the receiver inlet will vary with jet deflection distance.

If it is assumed that the power jet's centerline is only deflected to the receiver's centerline, then four possible mathematical expressions for the velocity distribution are required. The result of evaluating expression (202) for each of these distributions is presented in the following section.

Configuration one is defined by the boundary

$$e - \ell \geq y_c \tag{203}$$

Within this regime the receiver intersects only the developed portion of the free jet's velocity profile. The open load flow rate within this region may be expressed as

$$\dot{m}_r = \frac{hb\ P_m\ \bar{u}_c}{\bar{R}\ T_T} \{0.8264\ (y^*/b - y_c/b)\ [\Gamma_2(B,\eta_3) - \Gamma_2(B,\eta_4)]\} \tag{204}$$

where $\Gamma_2(B,\eta)$ is defined in expression (189) and

$$\eta_3 = \frac{(e+d-\ell)/b - y_c/b}{y^*/b - y_c/b} \tag{205}$$

$$\eta_4 = \frac{(e-\ell)/b - y_c/b}{y^*/b - y_c/b}$$

Configuration two is defined by the boundaries

$$y_c \geq e-\ell \geq -y_c \tag{206}$$

$$e+d-\ell \geq y_c$$

In this regime the lower edge of the receiver intersects the developed portion of the jet while the upper edge intersects the core region. The open load flow rate for this regime is

$$\dot{m}_r = \frac{hb\ P_m\ \bar{u}_c}{\bar{R}\ T_T}\left[\frac{y_c/b - (e-\ell)/b}{1 - B} + 0.8264\ (y^*/b - y_c/b)\ \Gamma_2(B,\eta_3)\right] \tag{207}$$

where η_3 is defined in (205).

Configuration three is bounded by the region

$$e-\ell \leq -y_c \tag{208}$$

$$e+d-\ell \geq y_c$$

Within this regime the potential core lies between the upper and lower edge of the receiver. The open load flow rate for this condition is

$$\dot{m}_r = \frac{hb\ P_m\ \bar{u}_c}{\bar{R}\ T_T}\left\{\frac{2y_c/b}{1 - B} + 0.8264\ (y^*/b - y_c/b)\left[\Gamma_2(B,\eta_3) + \Gamma_2(B,\eta_4)\right]\right\} \tag{209}$$

where η_3 is again defined in (205), however, η_4 is defined as

$$\eta_4 = \frac{-(e-\ell)/b - y_c/b}{y^*/b - y_c/b} \tag{210}$$

Configuration four is defined by

$$e+d-\ell \leq y_c \tag{211}$$

In this configuration the velocity profile at the receiver inlet is composed completely of potential core. The open load flow rate for this regime is

$$\dot{m}_r = \frac{hd\ P_m\ \bar{u}_c}{\bar{R}\ T_T(1-B)} \tag{212}$$

It should be noted that the free jet characteristics which are found in expressions (204), (207), (209) and (212) are evaluated at the axial distance traversed by the jet to the receiver inlet plane. If no potential core exists at the receiver inlet, configurations one and three are sufficient to compute the open load flow rate.

Computation of Blocked Load Pressure

Simson assumed that the blocked load pressure is equal to the average of the total pressure of the power jet velocity profile which is coincident to the receiver inlet. For compressible flow this may be expressed as

$$P_B = \frac{\int_{A_r} P_m \left[1 + \left(\frac{k-1}{2k\ P_m}\right)\ (\rho\bar{V}^2)\right]^{k/k-1}\ dy}{d} \tag{213}$$

where the integration above is performed over the inlet area of the receiver, A_r. Since the x-component of velocity, $\bar{u}$, is essentially equal in magnitude to the vector component of velocity, $\bar{V}$, expression (213) may be simplified to

$$P_B = \frac{\int_{A_r} P_m \left[1 + \left(\frac{k-1}{2k\ P_m}\right)(\rho \bar{u}^2)\right]^{k/k-1} dy}{d} \qquad (214)$$

Experimental Results

Experimental investigations were performed at a number of flow conditions in the low Reynolds number compressible flow regime. In these studies the power jet flow impinged upon a stationary receiver; see Figure 29. Receiver centerline offset angles of 0° and 10° were considered in this research. At a receiver offset angle of 0° the control port pressure was adjusted to a zero value and consequently the power jet and receiver centerlines were coincident. At a receiver offset angle of 10° the control port pressure was varied in order to position the power jet at various offset angles with respect to the receiver inlet.

Typical experimental receiver mass flow rate and pressure recovery characteristics are presented in Figure 75 for coincident power jet and receiver centerlines. The open load flow rate was determined from these data by extrapolating the respective flow rate pressure recovery characteristics to zero pressure. Comparisons are made in Figures 76 through 78 of experimental and predicted values of open load flow rate and blocked load pressure for the case of coincident

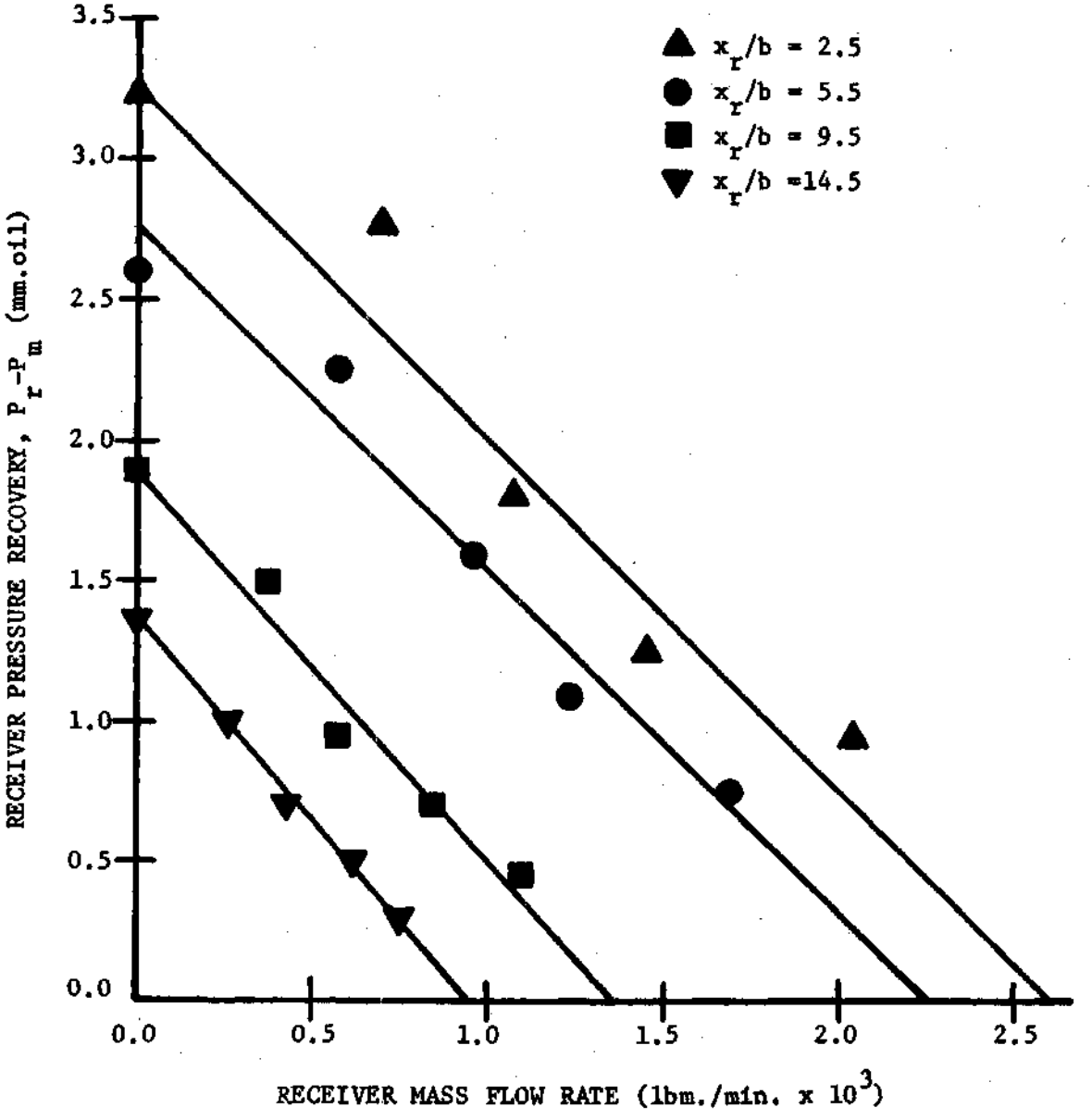

Figure 75. Receiver Mass Flow Rate and Pressure Recovery Characteristics for R_e = 107, M = 0.653 and θ_r = 0°

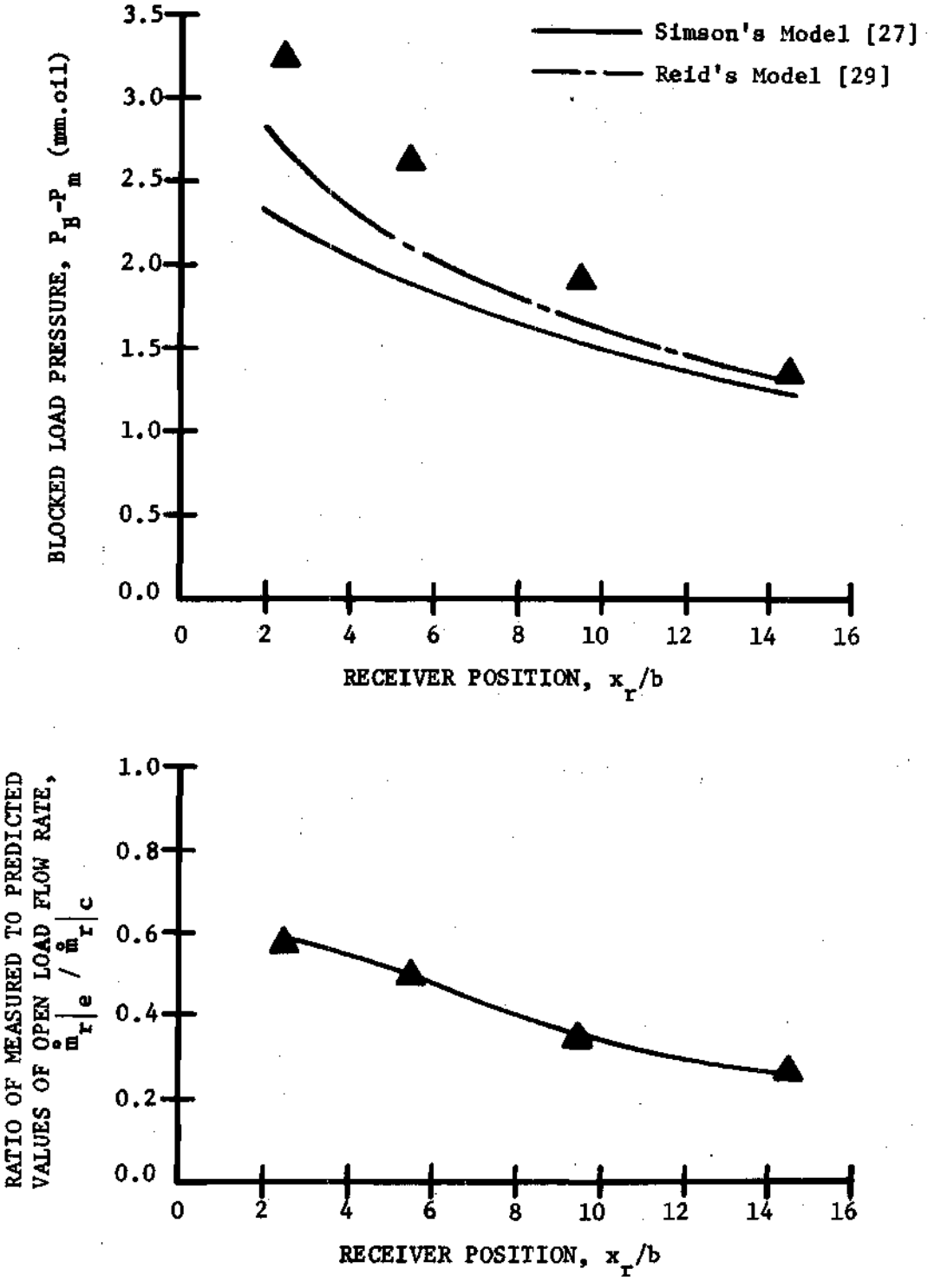

Figure 76. Comparison of Measured and Predicted Values of Receiver Characteristics for R_e = 107, M = 0.653, and θ_r = 0°

centerlines. The computation of these predictions from the models of Simson [27] and Reid [29] was performed with a digital computer program. This program made use of the free jet data correlation, the power jet flow condition, control port pressure, receiver location and geometry to calculate this information. The open load flow rate was computed from the appropriate form of expression (200). The prediction of blocked load pressure based on Simson's model was determined by integrating expression (214) across the inlet plane of the receiver. The estimate of blocked load pressure recovery suggested by Reid was determined from the computed value of the centerline velocity at the entrance plane of the receiver. A description and listing of this computer program is presented in Appendix I.

The jet receiver interaction characteristics are presented in Figure 76 of a power jet flow condition in which the Reynolds number is 107 and the Mach number is 0.653. In the plot at the top of this figure, the blocked load pressure is presented as a function of downstream receiver location, x_r/b. The predicted values of this parameter based on the respective models of Simson and Reid are presented for the purpose of comparison. In the plot at the bottom of this figure, the open load flow rate nondimensionalized by the computed value of this parameter is again plotted against downstream receiver location. It may be observed that for this flow condition both methods of predicting the block load pressure are reasonably accurate. The actual value of open load flow rate, however, is less than 60 percent of that predicted at the nearest receiver location investigated. The experimental values of this parameter

are observed to decrease in comparison to the prediction for larger values of x_r/b.

Presented in Figure 77 are characteristics of a flow condition in which the Reynolds number is 252 and the Mach number is 0.763. The predictions of blocked load pressure from Reid's model are observed to be the more accurate for small values of x_r/b while for larger values of x_r/b the predictions based on Simson's model are the more accurate. The calculated values of open load flow rate for positions near the power nozzle exit plane are observed to be very good. The actual values of open load flow rate are observed to diminish rapidly as x_r/b increases.

The characteristics of a flow condition in which the Reynolds number is 566 and the Mach number is 0.368 are presented in Figure 78. The predictions of blocked load pressure are seen to be reasonably accurate for small values of x_r/b while considerably in error for larger values of x_r/b. The experimental data in comparison to either of the prediction models demonstrate a much larger decrease in this parameter with the separation distance. The calculated values of open load flow rate are again quite accurate near the nozzle exit plane. With increasing values of x_r/b, the experimental data again diminish rapidly in comparison to the prediction.

Comparisons are presented in Figures 79 through 81 of typical measured and predicted values of open load flow rate and blocked load pressure recovery with the receiver offset at 10°. These data were obtained at a receiver location of $x_r/b = 5.5$ for the same flow cases

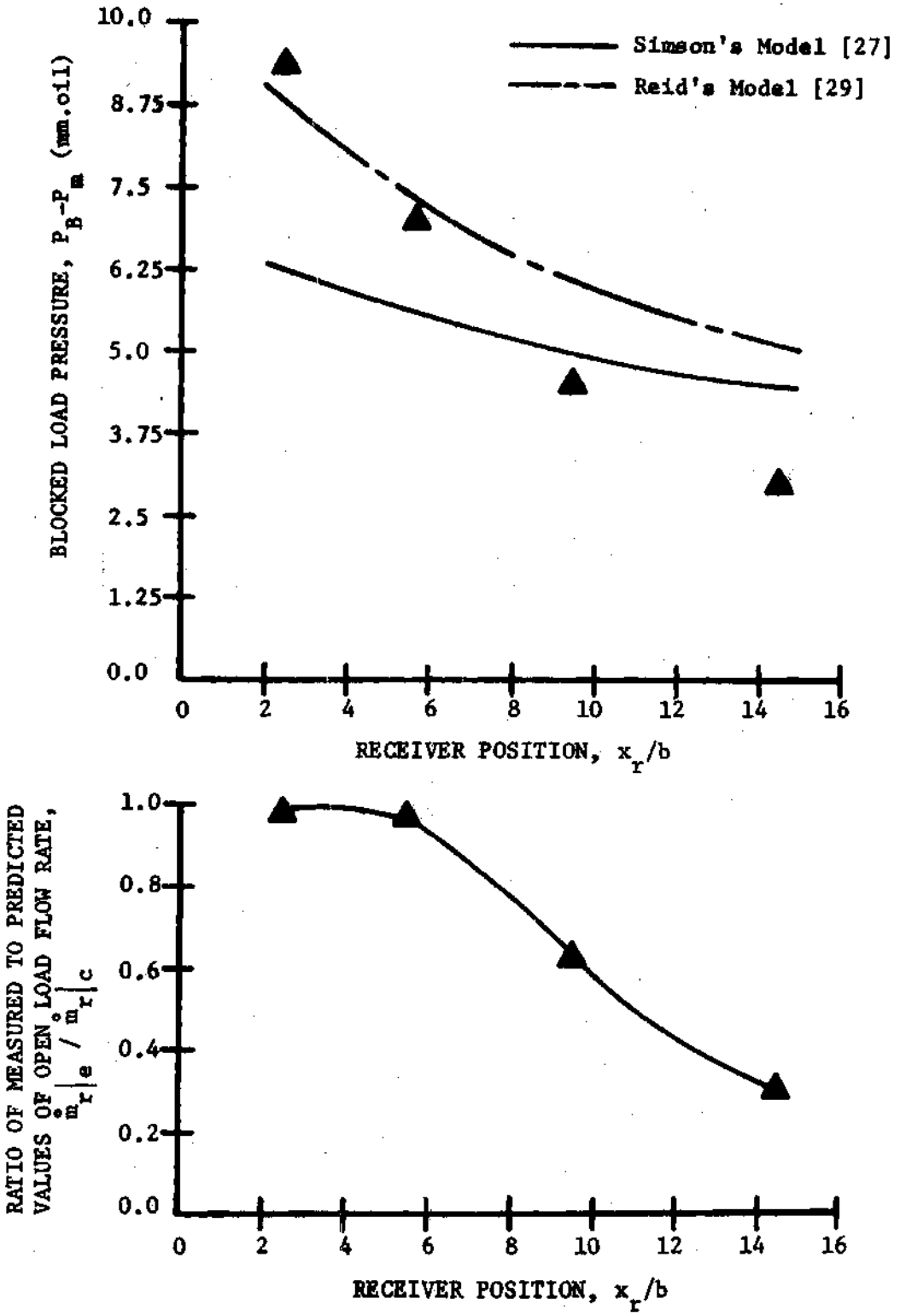

Figure 77. Comparison of Measured and Predicted Values of Receiver Characteristics for R_e = 252, M = 0.763 and $\theta_r = 0°$

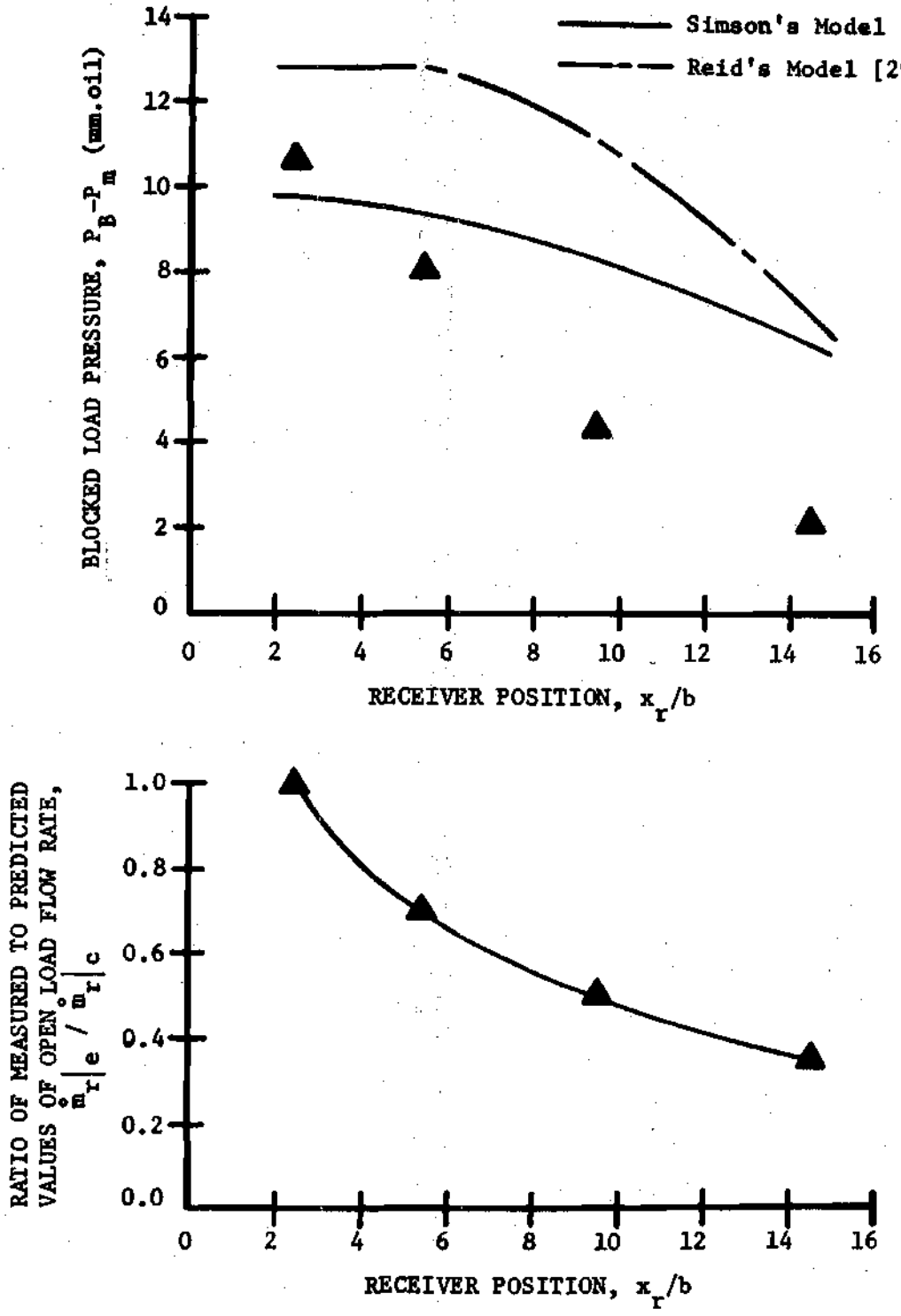

Figure 78. Comparison of Measured and Predicted Values of Receiver Characteristics for R_e = 566, M = 0.368 and θ_r = 0°

presented in Figures 76 through 78. Two methods were employed to calculate the blocked load pressures shown in these figures. In the former the blocked load pressure was calculated based on the method suggested by Simson. That is the average of the total pressure profile across the receiver inlet. In the latter this parameter was estimated to be equal to the total pressure at the center of mass flow rate of the velocity profile coincident to the receiver inlet. This method may be viewed as an extension of Reid's "cowl" streamline approach to asymmetric velocity profiles at the receiver inlet. The open load flow rate was again computed from the appropriate form of expression (200). The calculation of the predictions was performed by the computer program described in Appendix I.

The blocked load pressure and open load flow characteristics are presented in Figure 79 for a power jet operating at a Reynolds number of 107 and a Mach number of 0.653. The blocked load pressure and the open load flow rate are presented as a function of control port pressure at the top and bottom of this figure, respectively. It may be observed that in this flow case both methods for predicting blocked load pressure give a reasonable description of the data. The experimental values are observed, however, to reach a maximum at a larger control port pressure. This trend could stem from error in predicting the power jet deflection angle. The measured values of the open load flow rate are found to be much smaller than those predicted. This trend was also observed in Figure 76 for the case where $\theta_r = 0°$. The measured values of open load flow rate would appear to reach a maximum at higher control port pressure.

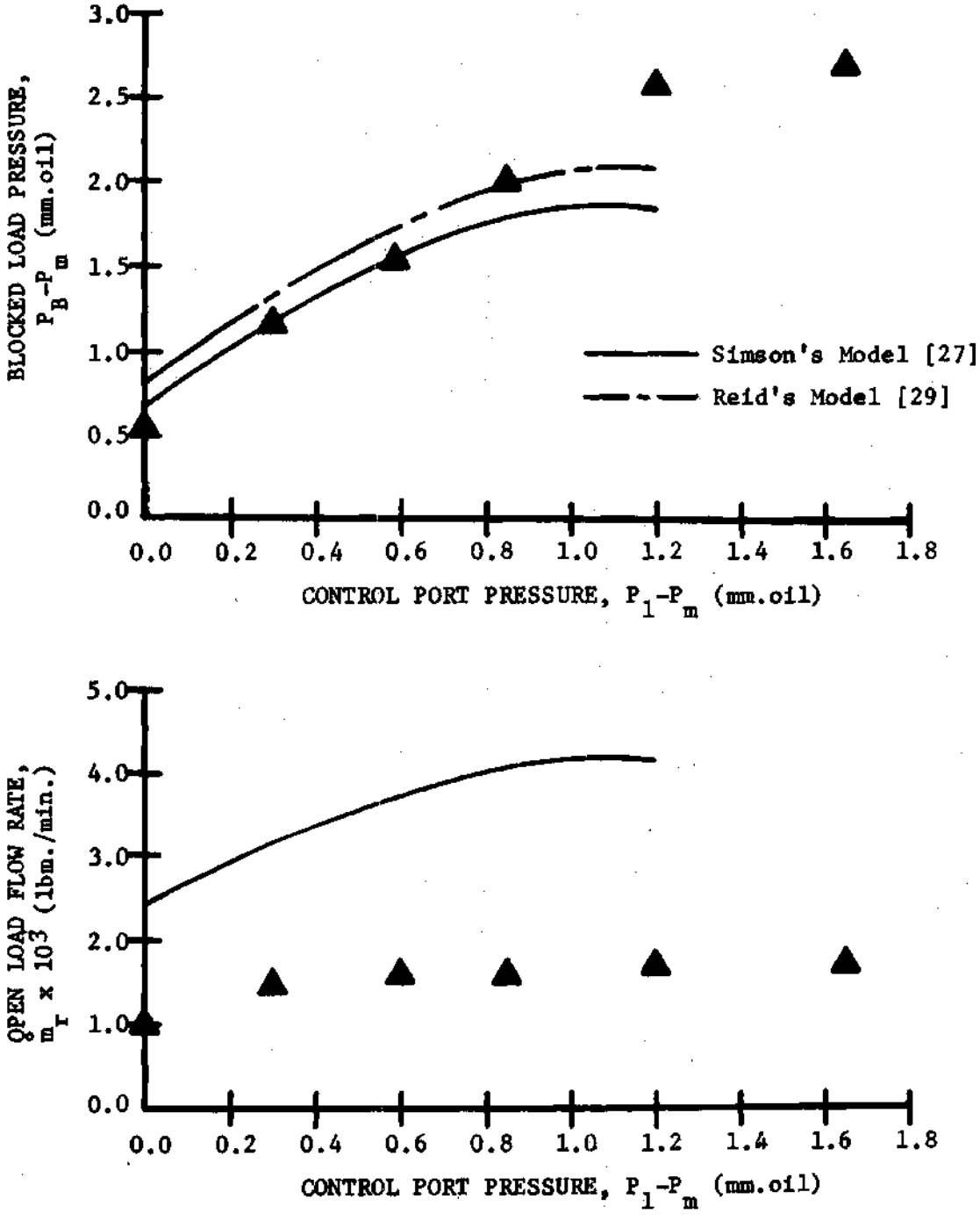

Figure 79. Comparison of Measured and Predicted Values of Receiver Characteristics for R_e = 107, M = 0.653, x_r/b = 5.5 and θ_r = 10°

The characteristics of a flow case are presented in Figure 80 in which the Reynolds number is 252 and the Mach number is 0.763. The predicted values of open load flow rate are shown to be reasonably accurate with respect to these data. This fact is in agreement with information found in Figure 77. The experimental data are observed, however, to obtain a maximum value at a higher control port pressure. Both methods of predicting blocked load pressure would also be reasonable estimates of the experimental data. The measured values of blocked load pressure, as in the case of the open load flow rate, obtain a maximum value at a higher control port pressure. If the predictions were shifted such that maximum values coincided, the method based on total pressure at the center of mass would be the more accurate.

Characteristics of a flow case in which the Reynolds number is 566 and the Mach number is 0.368 are presented in Figure 81. The predicted values of open load flow rate are found to be in fair agreement with experimental data. The data in comparison to the predictions demonstrate a much faster rise of flow rate with control port pressure and are observed to obtain a maximum at a lower value of this parameter. The blocked load pressure data demonstrate the same trend in that the pressure rises more quickly with control port pressure and reaches a maximum at a lower value of this variable. In this flow case, the technique based on the total pressure at the center of mass of the profile would be the more accurate estimate of blocked load pressure.

In summary, the correlation of measured and predicted values of open load flow rate demonstrated several trends. Firstly, the prediction

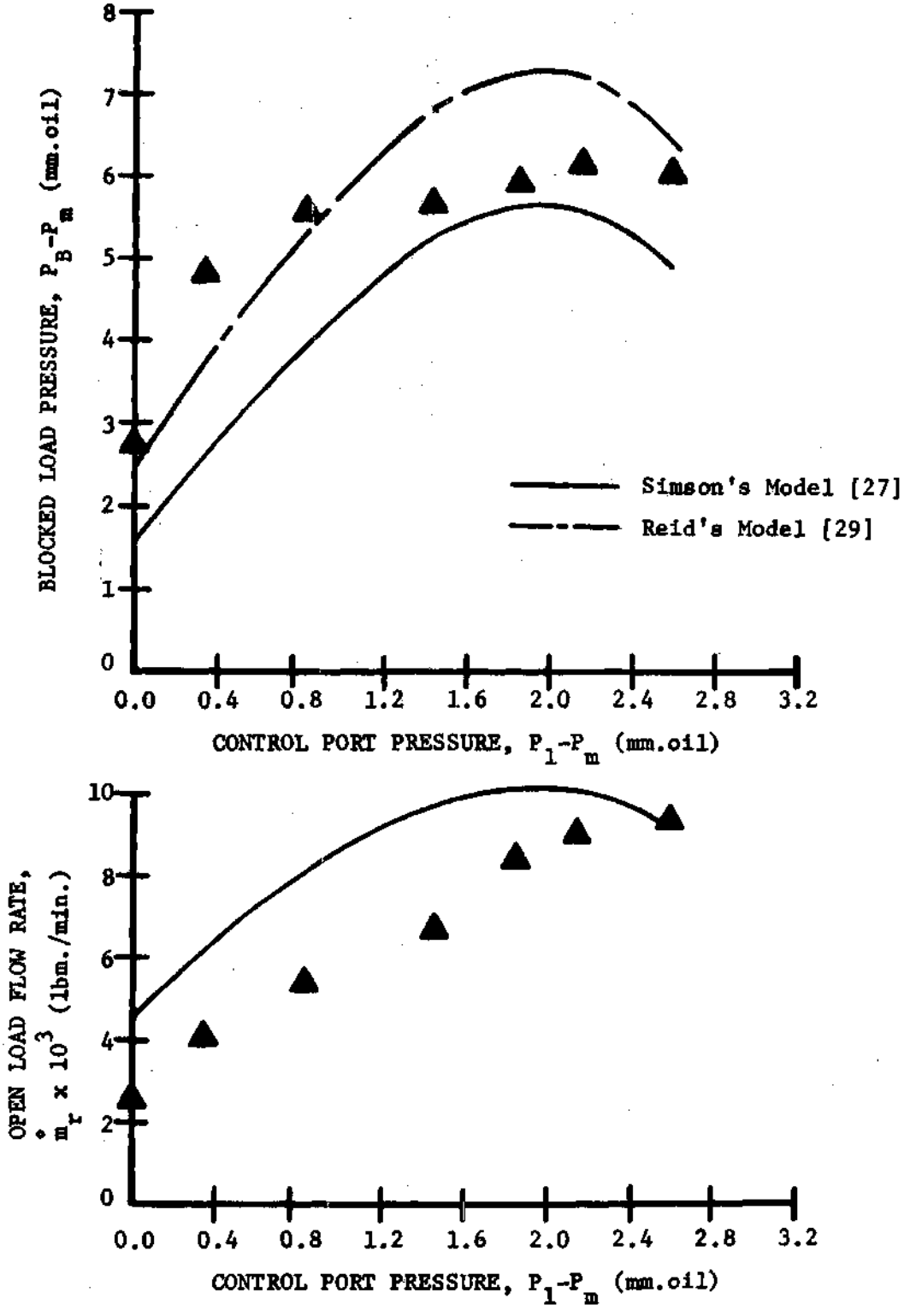

Figure 80. Comparison of Measured and Predicted Values of Receiver Characteristics for R_e = 252, M = 0.763, x_r/b = 5.5 and θ_r = 10°

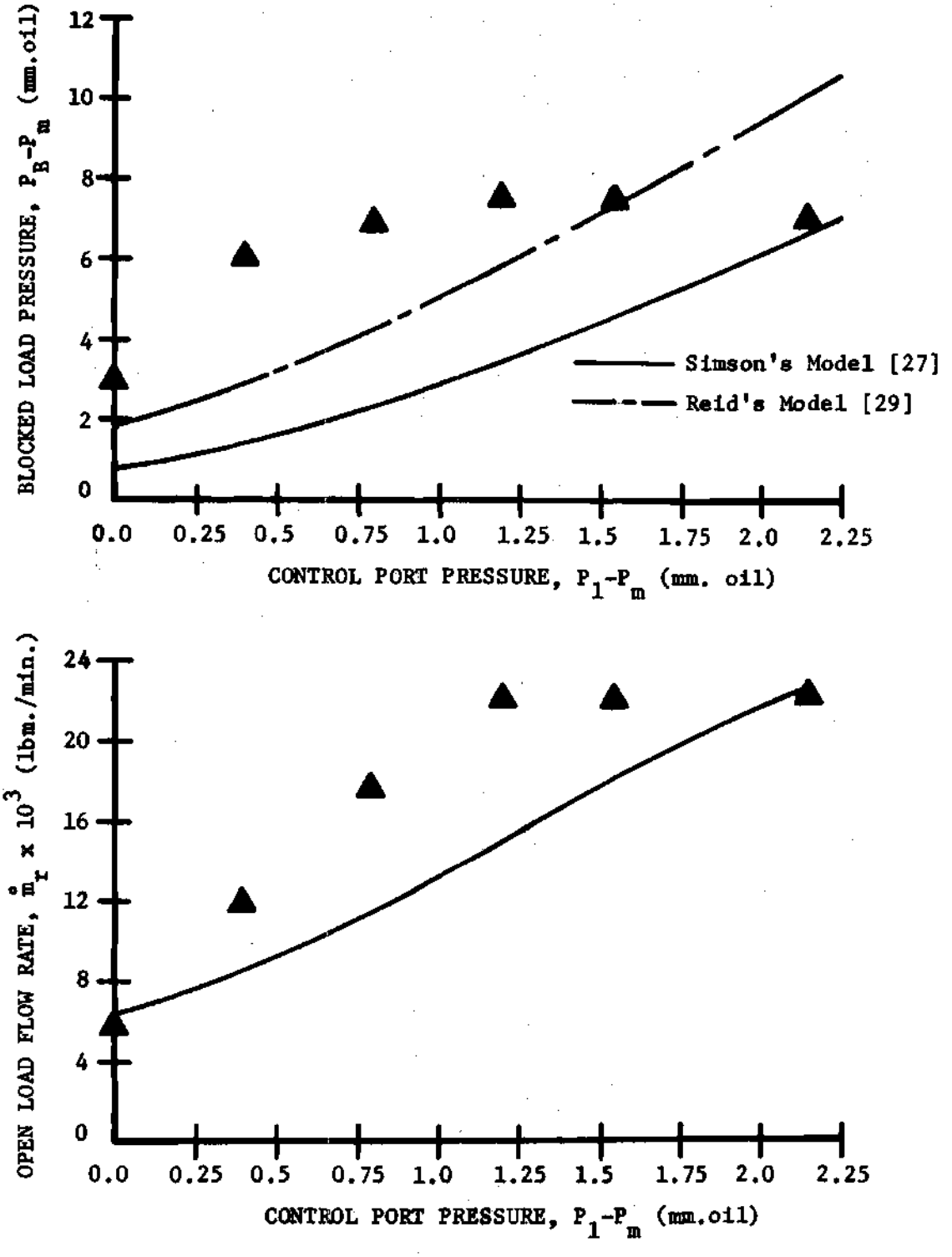

Figure 81. Comparison of Measured and Predicted Values of Receiver Characteristics for R_e = 566, M = 0.368, x_r/b = 5.5 and $\theta_r = 10°$

technique was better for short receiver power jet separation distances. The measured values of open load flow rate were found to diminish rapidly in comparison to those predicted as x_r/b was increased. This information would suggest that the jet boundary layers adjacent to the top and bottom plates of the experimental apparatus were significant in width at larger values of x_r/b. Considering the numerical values, it would appear that the low velocity boundary layer regions could provide a leakage path back out of the receiver inlet. Secondly, the predictions of open load flow rate when the receiver was offset with respect to the power nozzle centerline were better for the lower Reynolds number flow cases. The receiver flow rate was found to increase more rapidly with control port pressure than was predicted. It is assumed that the better correlation between analysis and data for the lower Reynolds number flow cases was the result of wider more uniform velocity profiles which occur at these conditions.

The comparison of predicted and measured values of blocked load pressure recovery demonstrated several trends. Firstly, fair correlation was achieved for both the respective models of Simson and Reid at receiver positions near the power jet exit plane. For larger receiver separation distances and higher Reynolds number flow cases, the measured values of this parameter were much lower than predicted. It should be noted that this effect might again suggest power jet boundary layer growth upon the constraining plates of the experimental apparatus. Secondly, the predictions of blocked load pressure when the receiver was offset with respect to the power nozzle centerline were again better

for the lower Reynolds number flow cases. The blocked load pressure was found to increase more rapidly than predicted with control port pressure in the higher Reynolds number flow cases.

Considering the present research, it would appear the computation of open load flow rate and blocked load pressure from the respective models of Simson and Reid is justified where two conditions are met. That is, when the flow is substantially two-dimensional and the coincident power jet velocity profile is fairly large and uniform. For conditions in which the jet flow was suspected of being three-dimensional, the measured values diminished rapidly in comparison to those predicted. The one exception to this rule was the blocked load pressure recovery for large separation distances at low Reynolds numbers. The correlation was observed to be poor for situations in which the power jet was small in comparison to the receiver inlet or the coincident velocity profile was very nonuniform. It should be pointed out that these conclusions are generally in agreement with Reid's experimental results. Reid indicated that Simson's predictions of open load flow rate and blocked load pressure were better for larger power jet receiver separation distances. That is, at positions where the jet profiles were wider and more uniform over the receiver inlet plane.

CHAPTER VII

CONCLUSIONS AND SUGGESTIONS FOR FURTHER RESEARCH

Conclusion

Steady state and fluctuating plane jet characteristics were compared to analytical theories and experimental data from previously investigated flow regimes. The comparison of high Reynolds number flow cases from the present research with a turbulent incompressible plane jet [8] demonstrated somewhat similar steady state characteristics. The propagation and growth of the turbulent shear layers, however, is much slower for even the highest Reynolds number case considered in this investigation.

The comparison of a low Reynolds number case from this research to a laminar incompressible jet with approximately the same Reynolds number [18] indicated very similar characteristics. Steady state jet characteristics from the present research were compared to flow data from the investigation of Anderson [21]. These data exhibited similarities as to the qualitative effect of Reynolds and Mach number upon the time-average velocity profiles. The centerline velocity decay and jet spread rates were found, however, to be quite different at approximately the same flow conditions. A possible explanation of these differences could be the respective nozzles used in the investigations. This would suggest nozzle geometry is important to the velocity distribution in this regime.

The experimental data indicated the following conclusions upon the structure of a plane jet in this regime:

1. Lower Reynolds number and higher Mach number flow conditions retard the growth of turbulent free shear layers; this observation is in agreement with the predictions from stability theory by Curle [23] and Pai [24].
2. The power profile solution of Schlichting [15] is not in agreement with the latter up to 20 nozzle widths from the exit plane for the lower Reynolds number jet flows, although it would appear to approach this distribution in the limit.
3. Jet flows in this regime may be composed of a potential core regime, a laminar transition regime where the turbulent shear layers have not met and their effect is small, a turbulent transition region beyond the coalescence of the free turbulent layers and a fully turbulent zone.
4. Not all four regions may be present in a single case. This is apparent since no laminar transition region existed for high Reynolds number conditions. Likewise, no core regions were found for low Reynolds number flows.

The experimental data demonstrated the jet's longitudinal velocity profile could be described by the Gaussian distribution

$$\bar{u}/\bar{u}_c = e^{-4.6\,\eta^2} \quad \text{for} \quad -y_c \geq y \geq -\infty \qquad (215)$$

$$y_c \leq y \leq \infty$$

$$\bar{u}/\bar{u}_c = 1 \quad \text{for} \quad -y_c \leq y \leq y_c$$

where the profile shape parameter η is defined as

$$\eta = \frac{y/b - y_c/b}{y^*/b - y_c/b} \tag{216}$$

A correlation of the time-average component of velocity in the longitudinal direction was formulated based on this velocity distribution. The correlation employs only simple calculations and graphs to describe the jet's centerline velocity and profile shape. The predictions of the data correlation up to 10 nozzle widths downstream are expected to be within approximately five percent for the centerline velocity and 10 percent for the jet width parameter η. The correlation is expected to be of sufficient accuracy for design purposes.

The data from the interaction portion of this research were compared to the predictions of Simson's [27] model. The calculated values of jet deflection angle, using this model in conjunction with the free jet data correlation, are reasonably accurate. The maximum and average errors in the jet deflection angles were found to be 1.9° and 1°, respectively. This good agreement suggests the interaction process is not significantly affected by molecular effects in the regime

$$1 \times 10^{-2} \geq K_n \geq 5 \times 10^{-4} \tag{217}$$

where K_n is the Knudsen number based on nozzle width.

Considering the simplicity of Simson's interaction model, the prediction of the control port mass flow rate using the measured value of power nozzle flow is reasonably accurate. The maximum error in the

control port mass flow rate is approximately 20 percent of the maximum control port flow. If the predicted values of power nozzle flow are employed in the calculations, the maximum error in the control port mass flow rate increases to approximately 26 percent of the maximum control port flow. Better agreement between measured and predicted control port mass flow rates is found for low control port pressures. This is to be expected since the mathematical model is restricted to small deflection angles.

A technique is presented for predicting the power nozzle mass flow rate and thus making the expression for control port flow useful for design. This procedure is based on the free jet data correlation and an assumed velocity profile at the nozzle exit plane. The maximum and average error in this prediction is approximately 10 percent and 4.6 percent, respectively.

The deflected power jet's velocity profiles are found to be distorted by the control port for positions near the interaction region. However, through diffusion with the fluid at rest, the velocity profiles smoothed rapidly and were in good agreement with the data correlation beyond a streamwise station three nozzle widths from the exit plane.

The data from the jet receiver interaction investigation were compared to the predictions based upon the respective models of Simson [27] and Reid [29]. Attempts to compute the blocked load pressure and open load flow rate characteristics from these models in conjunction with the free jet data correlation have produced mixed results. The correlation of measured and predicted values of open load flow rate and

blocked load pressure were generally better for short receiver power jet separation distances and decreased in accuracy for larger separation distances. This effect was attributed to boundary layer growth on the top and bottom plates of the experimental apparatus.

For situations in which the receiver was offset with respect to the power nozzle centerline, the correlation was better for lower Reynolds number conditions. The receiver's flow rate and pressure characteristics for the higher Reynolds number flow cases were found to increase more rapidly with control port pressure than was predicted. It is assumed the better correlation between analysis and data for the lower Reynolds number cases was the result of the wider more uniform velocity profiles which occur at these conditions.

In summary, neither the models of Simson or Reid are generally adequate to describe the blocked load pressure and open load flow characteristics. For situations in which the flow was assumed to be substantially two-dimensional and fairly uniform over the receiver inlet, the predictions were adequate descriptions of the results.

Suggestions for Further Research

Further experiments which could result in a better description of a plane jet in this flow regime are recommended in the paragraphs that follow.

Studies of plane jet characteristics at supersonic Mach numbers are suggested. Such studies would indicate the effect of an increased degree of compressibility upon the free jet's structure. Of special interest is the effect of higher Mach number conditions upon the

transition process from laminar to turbulent flow. Equipment which is more accurate and sensitive would be required to maintain the flow and measure the flow field in such a research.

Further experiments are suggested to determine the effects of nozzle radius of curvature and aspect ratio upon the flow field. The poor correlation in steady state characteristics between the present research and that of Anderson [21] could suggest the nozzle radius of curvature is an important parameter. Measurements of the boundary layer growth on the top and bottom plates of the apparatus would provide useful information. These data are required to describe the overall energy in a jet flow. It would also be useful in interpreting the experimental results of the power jet receiver interaction study.

Experimental measurements of the x and y-components of the steady state and fluctuating velocity field are suggested. The evaluation and comparison of these data to similar characteristics from high Reynolds number turbulent jets could provide further information on turbulent transition.

Jet interaction experiments at higher values of Knudsen number are recommended. Such experiments would indicate the flow regime in which molecular effects become important to the interaction process. It is anticipated, at sufficiently rarefied flow conditions, these experiments would demonstrate the control flow substantially passing through the power jet without deflecting it. More sensitive equipment would be required for such an investigation.

Experimental studies of the physical phenomena resulting from the interaction of two and three-dimensional velocity distributions upon a rectangular receiver are suggested. It is hoped this investigation would lead to a more rational model of flow and pressure recovery than is presently available. It would be suggested such experiments first be performed at flow conditions consistent with operational fluidic devices.

APPENDIX A

ANEMOMETER CALIBRATION

The anemometer sensing element was maintained at a constant temperature during the calibration procedure and the subsequent research. This was accomplished by an electronic bridge circuit which was found in the anemometer module. A high gain amplifier which was connected across the center of the bridge controlled the current flow through the bridge such that the resistance of the sensor was maintained equal to that of a control resistor. The electronic circuit thus controlled the resistance and hence the temperature of the anemometer sensor in the flow field. The voltage drop across the sensor is proportional to both the electrical current flowing through as well as the heat transfer from this device. This heat transfer is a function of the velocity of the fluid passing the sensor. The voltage drop across the sensor thus may be used to measure velocity, however, a calibration procedure is required to establish the relationship between the voltage drop and the velocity in the flow field.

The heat transfer, H, from a sensor in a gas is in general a function of the fluid velocity, V, as well as the sensor's geometry, static pressure in the gas, P, static temperature in the gas, T, density of the gas, ρ, the temperature of the sensor, T_w, as well as properties of the gas, μ, C_p, k and $\bar{R}$. This assumes that the radiation heat transfer between the sensor and surroundings does not vary with

position in the experimental model. This assumption was checked by evacuating the model to a low absolute pressure and then determining the heat transfer rate from the sensor in still air as a function of various positions in the model. No detectable variation in heat transfer rate was found. In the present research a single sensor was employed which was held at a constant temperature. This served to simplify the calibration procedure.

If the gas flowing past the sensor is assumed to be ideal and the flow process in the jet is assumed to be isoenergetic, then the static temperature in the gas is

$$T = T_T - V^2/2g_c\ C_p \tag{218}$$

where T_T is the stagnation temperature of the flow.

For an ideal gas at a constant static pressure, density is only a function of temperature, thus

$$\rho = \rho(T) \tag{219}$$

The properties of the gas and consequently the heat transfer from a constant temperature sensor in air is a function of only velocity for a fixed stagnation temperature and a fixed ambient pressure

$$H = H(V) \tag{220}$$

In summary, the voltage drop across the anemometer sensor is proportional to only velocity for flow about a single sensor for a fixed gas, stagnation temperature and ambient pressure.

Based on the preceding discussion it is apparent that both the ambient pressure as well as the total temperature must be maintained constant between the calibration procedure and subsequent research. The velocity field used in the calibration was obtained by allowing air to flow from the supply reservoir through the supply port into the experimental model. The control port and the receiver diffuser were removed from the apparatus during calibration. Calibration data were taken for static pressure levels in the model of approximately 0.51 mm. hg., 1 mm. hg., 2 mm. hg., 5 mm. hg., 10 mm. hg., and 20 mm. hg. These pressures were maintained constant to within ±0.0115 mm. hg. and ±0.0038 mm. hg. for static pressure levels of 5 mm. hg. and above and 2 mm. hg. and below, respectively.

Measurements of the stagnation temperature in the supply reservoir of the experimental model indicated that during a particular experimental run the total temperature was essentially constant. However, over a period of several months the upstream total temperature was found to vary as much as 5°F about the valve 72°F. The stagnation temperature was considered constant, at least with respect to a particular experimental run. As a check on the assumption of constant stagnation enthalpy in the flow, measurements were made of the stagnation temperature in the test model. The anemometer was used to measure the temperature near the jet flow by determining the change of resistance of the unheated sensor. Thermocouples were used to measure the temperature in fixed position taps in the supply reservoir and experimental model. These measurements indicated the stagnation temperature

in the model was essentially identical to the supply chamber temperature.

Two techniques were employed in the calibration of the anemometer. The first method of calibration consisted of measuring the velocity at various positions in the jet flow with an impact probe. The anemometer sensor would then be positioned in the same locations and the voltage drop across the sensor determined as a function of the known velocity. A cathetometer was used in conjunction with reference marks on the model's base plate to insure the locations were matched. The second method consisted of determining the velocity of the potential core at the exit plane of the jet and then measuring the voltage drop across the sensor as a function of this known velocity. The velocity in the potential core was determined from inviscid perfect gas relationships by using the pressure drop across the nozzle, the upstream stagnation temperature and the model pressure.

Of the two methods described, the velocity calibration in the potential core was considered the more exact. This was due to the large relative size of the impact probe used in the calibration in comparison to the jet flow in which it was positioned. This large size was required to maintain the probe's Reynolds number sufficiently high in order to insure the validity of the calculation of velocity from inviscid perfect gas relationships. Sherman [30] studied the effect of low Reynolds number on impact probe operation. He concluded the shape of the probe employed in this research was the best for low Reynolds number conditions. However, for Reynolds numbers of less than 70 based on free

stream conditions and probe diameter the use of perfect gas relationships to calculate velocity was in error. This error was found to be very significant for Reynolds numbers lower than 20.

Experimental studies demonstrated that the optimum location of the impact probe during calibration was a position on the centerline of the jet flow several nozzle widths downstream of the exit plane. If the probe was positioned nearer the exit plane, it was found to block the flow from the nozzle. Velocity measurements made at positions farther downstream of this optimum location demonstrated considerable scatter. It is assumed that this scatter resulted from the interaction of the probe and the highly turbulent flow in this region.

The primary concern in employing the pressure ratio technique for calibration was insuring the existence of a potential core at the jet's exit plane. Two rather simple tests were employed to insure the existence of this core. First, a scan was made across the exit plane to insure the existence of a constant voltage and hence a constant velocity region. Secondly, the probe was moved downstream of the exit plane to insure the core existed a sufficient distance downstream of the nozzle's exit. Data were not taken unless both of the criterion were satisfied.

Two techniques were utilized for measuring the steady state voltage drop across the anemometer sensor. This was necessary since as the model pressure decreases the sensitivity of voltage drop across the sensor to velocity also diminishes. For model pressures of 5 mm. hg. and above the standard voltmeter in the anemometer module provided

sufficient sensitivity, however, for ambient pressures of 2 mm. hg. and lower this voltage was amplified. For these low pressure conditions the anemometer voltage signal was introduced into one input of an oscilloscope. A potentiometer which was calibrated to the voltage drop across the sensor in still air at that model pressure was introduced into the other oscilloscope input. These two voltages were measured differentially and amplified. A low pass filter was employed to smooth the anemometer voltage input to the oscilloscope. The break frequency on this filter was 50 Hertz.

In order to illustrate how the anemometer calibration data were obtained, a sample calculation for the impact probe will be presented.

Calculation of the velocity from the impact pressure at one condition may be illustrated with the following data:

measured impact pressure above model pressure = 5.5 mm. oil

model static pressure = 66.21 mm. oil

$$P_m/P_i = 66.21/71.71 = 0.9233 \qquad (221)$$

From isentropic flow tables for the pressure ratio of 0.9233 the following relationships are defined:

$$M = 0.34 \quad ; \quad T/T_T = 0.9774 \qquad (222)$$

From the definition of the speed of sound and the Mach number

$$c = \sqrt{k \bar{R} T g_c} \quad ; \quad M = V/c \qquad (223)$$

For this test T_T = 532°R where R denotes degrees Rankine. The sonic velocity for air may be determined from the previous relation and is

$$c = \sqrt{(T/T_T)\ k\ \bar{R}\ T_T\ g_c} \tag{224}$$

$$c = \sqrt{(0.9774)(1.4)(53.34)(532)(32.2)}$$

$$c = 1118 \text{ ft./sec.}$$

The velocity is thus

$$V = Mc \tag{225}$$

$$V = (0.34)(1118)$$

$$V = 380 \text{ ft./sec.}$$

APPENDIX B

CALCULATION OF STEADY STATE AND FLUCTUATING COMPONENTS OF VELOCITY

Both steady state and fluctuating components of velocity were determined by means of the hot film anemometer. The calibration of this instrument was described in Appendix A. A typical calibration curve which was obtained for a model pressure of 5 mm. hg. may be seen in Figure 82. Employing this curve it is possible to demonstrate the calculation of both steady state and fluctuating components of velocity from the measured voltage drops.

Calculation of Steady State Velocity

The calculation of the steady state velocity may be illustrated with the following data:

measured voltage at point of unknown velocity = 2.46 volts

measured voltage at point of zero velocity = 2.185 volts

$$\Delta e_1 = 2.46 - 2.185 = 0.275 \text{ volts} \qquad (226)$$

From Figure 82 the steady state velocity is 477 ft./sec.

Uncertainty in Steady State Velocity Measurements

The factors influencing the accuracy of the steady state velocity measurements would include the sensitivity and reading error of the instrumentation as well as variations in the model static pressure

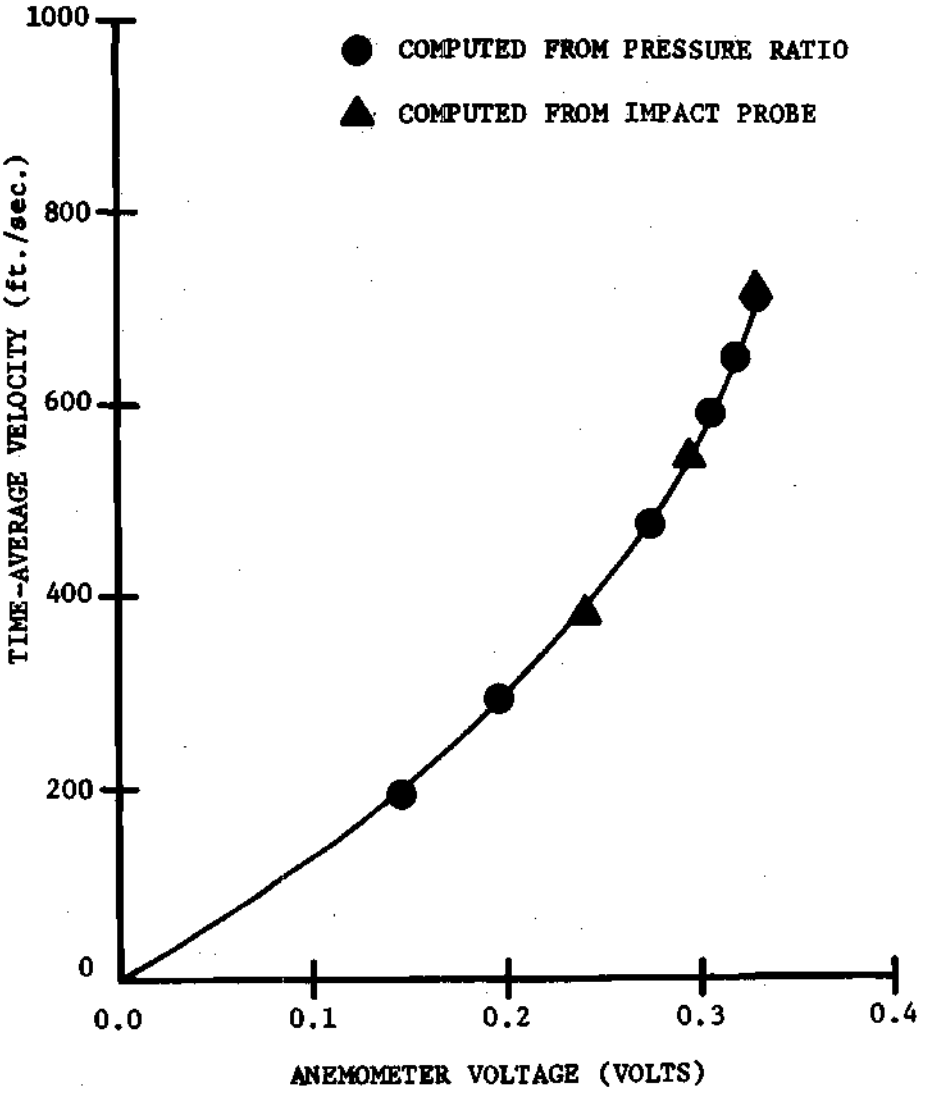

Figure 82. Anemometer Calibration Curve for P_m = 5.0 mm. hg.

during an experimental run. It should be noted that changes of total temperature between runs should not affect the accuracy of these measurements. That is since the anemometer readings were made with respect to the voltage level in the gas at rest, the effect of changes of total temperature between runs is eliminated.

It may be assumed that the measured value of steady state velocity, $\bar{u}$, is a function of the voltage drop across the sensor, e_1, and the static pressure in the model, P_m

$$\bar{u} = \bar{u}\ (e_1, P_m) \tag{227}$$

The effect of variations of voltage drop and model pressure from their true values upon the velocity may be written as

$$\Delta\bar{u} = \left.\frac{\partial\bar{u}}{\partial e_1}\right|_{P_m} \Delta e_1 + \left.\frac{\partial\bar{u}}{\partial P_m}\right|_{e_1} \Delta P_m \tag{228}$$

The previous expression represents the error in the computed steady state velocity as a function of the errors in voltage and model pressure. If it is assumed that an infinite number of velocity measurements are made, the uncertainty in this measurement may be expressed as

$$w_{\bar{u}} = \left[\left(\left.\frac{\partial\bar{u}}{\partial e_1}\right|_{P_m} w_e\right)^2 + \left(\left.\frac{\partial e_1}{\partial P_m}\right|_{\bar{u}} \left.\frac{\partial\bar{u}}{\partial e_1}\right|_{P_m} w_{pm}\right)^2\right]^{1/2} \tag{229}$$

$w_{\bar{u}}$, w_e and w_{pm} represent the uncertainties in velocity, voltage and model pressure, respectively.

Shown in Table 6 is the computed uncertainties associated with the steady velocity measurements in this research. These values were

computed for both zero velocity and the maximum velocity for each of the model pressure levels considered. These data indicate the uncertainty associated with the range of experimentation.

Table 6. Uncertainty in Steady State Velocity Measurements

Model Pressure, P_m (mm. hg.)	Uncertainty in Speed at $\bar{u}=0$ (ft./sec.)	Uncertainty in Speed at $\bar{u}=\bar{u}_{max}$ (ft./sec.)
20.0	0.745	3.125
10.0	2.04	12.51
5.0	5.52	22.31
2.0	2.77	19.26
1.0	8.75	10.32
0.51	22.03	13.51

It could be argued that the uncertainties presented in Table 6 are optimistic, since they assume the anemometer calibration data are absolutely correct. It is rather difficult to estimate the uncertainty associated with the calibration procedure, however, it should be more accurate than the actual measurement of an unknown velocity. This is true since the calibration curves are based on the weighted average of a number of individual data points and, therefore, are more accurate than a single velocity measurement. A pessimistic appraisal of the total experimental uncertainty in the measured value of velocity would be to assume that the same uncertainty existed in the calibration and subsequent use of the anemometer. If the calibration and use of the device are uncorrelated, the uncertainties found in Table 6 would increase by approximately 41 percent for this pessimistic assumption.

Calculation of the uncertainties in Table 6 from expression (229) may be illustrated by the following data. For a model pressure of 5 mm. hg. and for a steady state velocity of zero

$$\left.\frac{\partial \bar{u}}{\partial e_1}\right|_{P_m} = 1100 \frac{\text{ft./sec.}}{\text{volt}} \quad ; \quad \left.\frac{\partial e_1}{\partial P_m}\right|_{\bar{u}} = 0.04 \frac{\text{volts}}{\text{mm. hg.}} \tag{230}$$

uncertainty in voltage, $w_e = 0.005$ volts

uncertainty in model pressure, $w_{pm} = 0.0115$ mm. hg.

Introducing the previous data into equation (229), yields

$$w_{\bar{u}} = \{[(1100)(0.005)]^2 + [(0.04)(1100)(0.0115)]^2\}^{1/2} = 5.52 \text{ ft./sec.} \tag{231}$$

Calculation of the Fluctuating Component of Velocity

A true rms voltmeter was employed in this research to measure the fluctuating component of velocity in the free jet. An explanation of how the fluctuating component of velocity was calculated may be made by considering the factors influencing this voltage.

The electrical output from the anemometer is composed of two fluctuating signals, that is electronic noise and the fluctuation of voltage due to turbulence in the jet flow. This may be expressed as

$$e_f = e_s + e_n \tag{232}$$

where e_s and e_n represent the signal and noise voltages, respectively.

Since the signal and noise are uncorrelated the output of the voltmeter is

$$\sqrt{\overline{e_f^2}} = \sqrt{\overline{e_s^2} + \overline{e_n^2}} \tag{233}$$

The rms value of the signal from the previous expression is

$$\sqrt{\overline{e_s^2}} = \sqrt{\left(\sqrt{\overline{e_f^2}}\right)^2 - \left(\sqrt{\overline{e_n^2}}\right)^2} \tag{234}$$

With the signal separated from the electronic noise it is possible to obtain the rms value of the velocity fluctuations. The fluctuating component of velocity may be expressed as

$$\sqrt{\overline{u'^2}} = f\left(\sqrt{\overline{e_s^2}}, P_m, \bar{u}\right) \tag{235}$$

For constant values of $\bar{u}$ and P_m the preceding expression may be simplified to

$$\sqrt{\overline{u'^2}} = \left.\frac{\partial \bar{u}}{\partial e_1}\right|_{P_m, \bar{u}} \sqrt{\overline{e_s^2}} \tag{236}$$

That is, the rms values of velocity and voltage are related by the slope of the anemometer calibration curve at the appropriate static pressure and average velocity.

Calculation of the fluctuating component of velocity from experimental data may be illustrated with the following data for a static pressure level of 5 mm. hg.:

rms value of voltage reading $\sqrt{\overline{e_f^2}}$ = 0.0092 volts

rms value of electronic noise $\sqrt{\overline{e_n^2}}$ = 0.0046 volts

The value of the true signal from expression (234) is

$$\sqrt{\overline{e_s^2}} = \sqrt{(0.0092)^2 - (0.0046)^2} = 0.00795 \text{ volts} \tag{237}$$

The average value of velocity at which this data point was taken is 162 ft./sec. From Figure 82

$$\left.\frac{\partial \bar{u}}{\partial e_1}\right|_{P_m, \bar{u}} = 1490 \ \frac{\text{ft./sec.}}{\text{volt}} \tag{238}$$

The value of $\sqrt{\overline{u'^2}}$ from expression (236) is thus

$$\sqrt{\overline{u'^2}} = (1490)(0.00795) = 11.8 \text{ ft./sec.} \tag{239}$$

Uncertainty in Fluctuating Component of Velocity Measurements

The measured value of the fluctuating component of velocity may be expressed as

$$\sqrt{\overline{u'^2}} = K_e \sqrt{\overline{e_s^2}} \tag{240}$$

where K_e is represented by

$$K_e = \left.\frac{\partial \bar{u}}{\partial e_1}\right|_{P_m, \bar{u}} \tag{241}$$

The effect of errors in the rms value of voltage, the model pressure and the average velocity upon the fluctuating component of velocity may be written as

$$\Delta\sqrt{\overline{u'^2}} = K_e \Delta\sqrt{\overline{e_s^2}} + \left(\sqrt{\overline{e_s^2}}\right)\left(\left.\frac{\partial K_e}{\partial P_m}\right|_{\bar{u}}\right)\Delta P_m + \left(\sqrt{\overline{e_s^2}}\right)\left(\left.\frac{\partial K_e}{\partial \bar{u}}\right|_{P_m}\right)\Delta\bar{u} \tag{242}$$

The previous expression represents the error in the computed rms value of the velocity as a function of errors in the rms value of voltage, the model pressure and the average velocity. If it is assumed that an infinite number of measurements of the fluctuating component of velocity are made, then the uncertainty in this parameter may be expressed as

$$w^2\sqrt{\overline{u'^2}} = \left(K_e\, w\sqrt{\overline{e_s^2}}\right)^2 + \left(\sqrt{\overline{e_s^2}}\left.\frac{\partial K_e}{\partial P_m}\right|_{\bar{u}} w_{pm}\right)^2 + \left(\sqrt{\overline{e_s^2}}\left.\frac{\partial K_e}{\partial \bar{u}}\right|_{P_m} w_{\bar{u}}\right)^2 \tag{243}$$

$w\sqrt{\overline{u'^2}}$, $w\sqrt{\overline{e_s^2}}$, w_{pm} and $w_{\bar{u}}$ represent the uncertainties in the rms value of velocity, rms value of voltage, the model pressure and the average velocity, respectively. If the preceding expression is divided through by the mean square velocity (expression (240) squared), an expression for the normalized uncertainty in the fluctuating component of velocity results

$$\frac{w\sqrt{\overline{u'^2}}}{\sqrt{\overline{u'^2}}} = \left\{\left(\frac{w\sqrt{\overline{e_s^2}}}{\sqrt{\overline{e_s^2}}}\right)^2 + \left[\left.\frac{\partial K_e}{\partial P_m}\right|_{\bar{u}}\left(\frac{1}{K_e}\right)(w_{pm})\right]^2 + \left[\left.\frac{\partial K_e}{\partial \bar{u}}\right|_{P_m}\left(\frac{1}{K_e}\right) w_{\bar{u}}\right]^2\right\}^{1/2} \tag{244}$$

Shown in Table 7 is the computed percentage uncertainties associated with the fluctuating component of velocity. These values are computed for both the maximum and minimum steady state velocity for each of the model pressure levels considered. These data thus indicate the uncertainty associated with the range of experimentation. It should be noted that in the calculation of the information in Table 7 the percentage uncertainty in the rms value of voltage has been assumed to be five percent for each case. The rms voltmeter and the reading error associated with this device are certainly not that large; however, the main error associated with obtaining the fluctuating component of voltage is the separation of the noise and true signal voltages.

Table 7. Percentage Uncertainty in Root Mean Square Velocity Measurements

Model Pressure, P_m (mm. hg.)	Percentage Uncertainty in $\sqrt{\overline{u'^2}}$ at $\bar{u} = 0$	Percentage Uncertainty in $\sqrt{\overline{u'^2}}$ at $\bar{u} = \bar{u}_{max}$
20.0	5.45	5.01
10.0	5.03	6.05
5.0	5.07	7.17
2.0	5.01	8.18
1.0	5.05	5.01
0.51	5.06	5.44

Calculation of the uncertainties in Table 7 from expression (244) may be illustrated by the following data. For a model pressure of 5 mm. hg. and a steady state velocity of zero

$$\left.\frac{\partial K_e}{\partial P_m}\right|_{\bar{u}} = -370 \frac{\text{ft./sec.}}{\text{volt mm. hg.}} ; \quad \left.\frac{\partial K_e}{\partial \bar{u}}\right|_{P_m} = 1.47/\text{volt} \tag{245}$$

$$K_e = 1100 \frac{\text{ft./sec.}}{\text{volt}} ; \quad \frac{w\sqrt{e_s^2}}{\sqrt{e_s^2}} = 0.05$$

$$w_{pm} = 0.0115 \text{ mm. hg.} ; \quad w_{\bar{u}} = 5.52 \text{ ft./sec.}$$

Introducing the previous data into expression (244) yields

$$\frac{w\sqrt{u'^2}}{\sqrt{u'^2}} = \{(0.05)^2 + [(-370)(\tfrac{1}{1100})(0.0115)]^2 + [(1.47)(\tfrac{1}{1100})(5.52)]^2\}^{1/2} \tag{246}$$

$$\frac{w\sqrt{u'^2}}{\sqrt{u'^2}} = 0.0507$$

Thus the uncertainty associated with this measurement is 5.07 percent.

APPENDIX C

FREE JET DATA

Flow Conditions

A tabulation of the flow conditions considered in the free jet investigation is presented in Table 8. The absolute pressure in the experimental model and the differential pressure across the supply nozzle serves to identify these cases. The Reynolds and Mach number based on the width of the supply nozzle and measured conditions at the centerline of the nozzle exit plane are also presented.

The calculation of the Reynolds and Mach numbers found in Table 8 from the measured values of velocity at the centerline of the nozzle exit plane, $\bar{u}_0$, model ambient pressure, P_m, and upstream total temperature, T_T, may be summarized by the following equations.

If it is assumed that the flow is isoenergetic, the static temperature, T, at the centerline of the nozzle exit plane may be expressed as

$$T = T_T - \bar{u}_0^2/2g_c\, C_p \tag{247}$$

The sonic velocity of the flow is given by

$$c = \sqrt{k\, \bar{R}\, T\, g_c} \tag{248}$$

The value of the Mach number may be found from the definition

$$M = \bar{u}_0/c \tag{249}$$

The value of the Reynolds number may be determined from the definition

$$R_e = \rho \bar{u}_0 b/\mu \tag{250}$$

If it is assumed the gas is ideal, then density may be expressed as

$$\rho = P_m/\bar{R}T \tag{251}$$

Assuming the viscosity of the gas is proportional to the square root of temperature, then viscosity may be expressed as

$$\mu = \mu_*(T/T_*)^{1/2} \tag{252}$$

The calculation of the Mach number and Reynolds number may be illustrated with data from the third flow case in Table 8.

measured velocity = 725 ft./sec.

model pressure = 1.0 mm. hg.

upstream total temperature = 532°R

From expression (247) the static temperature may be determined

$$T = 532 - (725)^2 / (2)(32.2)(778)(0.24) = 488°R \tag{253}$$

Inserting the value of static temperature into expression (248) yields the speed of sound

$$c = \sqrt{(1.4)(53.34)(488)(32.2)} = 1083 \text{ ft./sec.} \tag{254}$$

The value for the Mach number may be computed from equation (249)

$$M = 725/1083 = \underline{0.67} \tag{255}$$

The density of the gas may be computed from expression (251) and is

$$\rho = (1.0)(2.783) \;/\; (53.34)(488) = 1.069 \times 10^{-4} \text{ lbm./ft.}^3 \tag{256}$$

The viscosity of the gas from expression (252) is

$$\mu = 0.37 \times 10^{-6} \sqrt{\frac{488}{492}} = 0.3686 \times 10^{-6} \text{ lbf.sec./ft.}^2 \tag{257}$$

Introducing the values of density and viscosity into expression (250), yields

$$R_e = (1.069 \times 10^{-4})(725)(0.0167) \;/\; (0.3686 \times 10^{-6})(32.2)$$

$$\underline{R_e = 109} \tag{258}$$

Free Jet Velocity Data

A tabulation of the time-averaged and fluctuating components of velocity which were measured in the free jet investigation is presented in Tables 9 through 23. A description of how this information was obtained from anemometer data and a discussion of experimental error associated with these measurements is presented in Appendix B.

The free jet data have been presented in a nondimensional form in that all length units and velocities have been divided by nozzle width, b, and steady state velocity at the centerline of the nozzle exit plane, $\bar{u}_0$, respectively. Values of x represent distance downstream of the nozzle's exit plane and values of y represent distance from the centerline of the jet. It should be noted that the centerlines

of the experimental jet and experimental apparatus did not exactly correspond. This asymmetry was attributed to slight imperfections in the nozzle blocks. The maximum offset angle between the jet and apparatus centerline was found to be -1.9°. No attempt was made to correct the experimental data for the slight error associated with traversing the jet profiles normal to the device's centerline rather than the jet's centerline.

Free Jet Static Pressure Measurements

Static pressure traverses are presented for several flow cases in Tables 24 through 26. Differential pressure measurements between the model ambient and the jet are expressed in mm. of oil which has a specific gravity of 1.04.

Free Jet Velocity Vector Measurements

Velocity vector traverses are presented for several flow cases in Tables 27 through 29. The angle of the jet's velocity vector with respect to the centerline of the apparatus is presented as a function of the nondimensional distance from the jet's centerline. The sign convention established in these data is such that a positive y-value produces a vector whose angle is 90° to the apparatus centerline.

Table 8. Experimental Free Jet Conditions

Model Pressure, P_m (mm. hg.)	Differential Nozzle Pressure (mm. hg.)	Reynolds Number	Mach Number
0.51	0.199	47.7	0.591
1.0	0.149	64.2	0.416
1.0	0.406	109	0.670
1.0	0.780	152	0.885
2.0	0.321	142	0.457
2.0	0.937	255	0.761
2.0	1.600	336	0.956
5.0	0.436	262	0.347
5.0	0.666	325	0.426
5.0	1.645	515	0.646
10.0	0.410	359	0.240
10.0	0.981	558	0.368
10.0	1.542	705	0.458
20.0	0.478	546	0.183
20.0	0.658	645	0.216

Table 9. Free Jet Velocity Measurements;
R_e = 47.7, M = 0.591, $\bar{u}_0$ = 645 ft./sec.

x/b	y/b	$\bar{u}/\bar{u}_0$	$\bar{u}/\bar{u}_c$	$\sqrt{\overline{u'^2}}/\bar{u}_0 \times 10^2$
0.0	0.0	1.0		0.0
0.25	0.0	0.884		0.0
1.0	0.0	0.807		0.0
2.5	0.0	0.721		0.0
5.0	0.0	0.674		0.0
7.5	0.0	0.626		0.0
10.0	0.0	0.572		0.0
15.0	0.0	0.481		0.0
20.0	0.0	0.426		0.0

*No turbulence was detected in the jet.

Table 10. Free Jet Velocity Measurements;
$R_e = 64.2$, $M = 0.416$, $\bar{u}_0 = 463$ ft./sec.

x/b	y/b	$\bar{u}/\bar{u}_0$	$\bar{u}/\bar{u}_c$	$\sqrt{\overline{u'^2}}/\bar{u}_0 \times 10^2$
0.0	0.0	1.0		0.0
0.25	-0.66		0.309	0.0
	-0.52		0.448	0.0
	-0.48		0.558	0.0
	-0.39		0.751	0.0
	-0.33		0.820	0.0
	-0.29		0.890	0.0
	-0.18		0.945	0.0
	-0.07		0.971	0.0
	0.0	0.959	1.0	0.0
	0.08		1.0	0.0
	0.18		0.971	0.0
	0.23		0.890	0.0
	0.27		0.834	0.0
	0.35		0.695	0.0
	0.44		0.585	0.0
0.25	0.54		0.475	0.0
	0.71		0.309	0.0
0.50	0.0	0.933		0.0
1.0	0.0	0.892		0.0
2.0	0.0	0.868		0.0
3.0	-0.97		0.304	0.0
	-0.77		0.503	0.0
	-0.69		0.603	0.0
	-0.54		0.767	0.0
	-0.36		0.884	0.0
	-0.23		0.899	0.0
	-0.10		0.966	0.0
	0.05	0.810	1.0	0.0
	0.20		0.966	0.0
	0.31		0.915	0.0
	0.41		0.833	0.0
	0.53		0.767	0.0
	0.62		0.651	0.0
	0.78		0.471	0.0
	0.92		0.370	0.0
	1.11		0.206	0.0
	1.39		0.106	0.0
4.0	0.0	0.759		0.0

Table 10. (Continued)

x/b	y/b	$\bar{u}/\bar{u}_0$	$\bar{u}/\bar{u}_c$	$\sqrt{\overline{u'^2}}/\bar{u}_0 \times 10^2$
6.0	-1.54		0.156	0.0
	-1.17		0.376	0.0
	-0.90		0.597	0.0
	-0.67		0.797	0.0
	-0.52		0.871	0.0
	-0.44		0.891	0.0
	-0.23		0.965	0.0
	-0.02	0.718	1.0	0.0
	0.19		0.965	0.0
	0.35		0.926	0.0
	0.49		0.871	0.0
	0.67		0.779	0.0
	0.78		0.706	0.0
	1.04		0.559	0.0
	1.33		0.376	0.0
	1.66		0.156	0.0
10.0	-2.02		0.214	0.0
	-1.56		0.431	0.0
	-1.19		0.645	0.0
	-0.93		0.711	0.0
	-0.61		0.883	0.0
	-0.27		0.949	0.0
	0.0	0.637	1.0	0.0
	0.01		0.990	0.0
	0.29		0.969	0.0
	0.53		0.904	0.0
	0.80		0.818	0.0
	1.02		0.731	0.0
	1.22		0.604	0.0
	1.53		0.473	0.0
	1.74		0.345	0.0
	2.19		0.173	0.0
15.0	0.0	0.569		0.0
20.0	-2.42		0.277	0.0
	-1.77		0.547	0.0
	-1.07		0.820	0.0
	-0.59		0.940	0.0
	-0.07	0.503	1.0	0.0
	0.51		0.97	0.0
	1.29		0.70	0.0
	1.75		0.547	0.0
	2.37		0.306	0.0

Table 11. Free Jet Velocity Measurements;
R_e = 109, M = 0.67, $\bar{u}_0$ = 725 ft./sec.

x/b	y/b	$\bar{u}/\bar{u}_0$	$\bar{u}/\bar{u}_c$	$\sqrt{\overline{u'^2}}/\bar{u}_0 \times 10^2$
0.0	0.0	1.0		0.0
0.25	-0.70		0.317	0.0
	-0.60		0.413	0.0
	-0.49		0.588	0.0
	-0.36		0.807	0.0
	-0.27		0.866	0.0
	-0.17		0.916	0.0
	-0.11		0.980	0.0
	-0.03	0.945	1.0	0.0
	0.07		1.0	0.0
	0.20		0.916	0.0
	0.26		0.866	0.0
	0.34		0.826	0.0
	0.48		0.627	0.0
	0.57		0.413	0.0
	0.76		0.237	0.0
0.5	0.0	0.910		0.0
1.0	0.0	0.865		0.0
2.0	0.0	0.814		0.0
3.0	-1.43		0.071	0.0
	-1.17		0.183	0.0
	-1.01		0.292	0.0
	-0.86		0.425	0.0
	-0.78		0.558	0.0
	-0.69		0.690	0.0
	-0.50		0.847	0.0
	-0.40		0.922	0.0
	-0.27		0.946	0.0
	0.0	0.79	1.0	0.0
	0.34		0.946	0.0
	0.56		0.823	0.0
	0.75		0.624	0.0
	0.98		0.381	0.0
	1.35		0.183	0.0
	1.85		0.071	0.0
4.0	0.0	0.776		0.0
6.0	-1.59		0.126	0.0
	-1.15		0.394	0.0
	-0.95		0.563	0.0

Table 11. (Continued)

x/b	y/b	$\bar{u}/\bar{u}_0$	$\bar{u}/\bar{u}_c$	$\sqrt{\overline{u'^2}}/\bar{u}_0 \times 10^2$
6.0	-0.68		0.782	0.0
	-0.46		0.903	0.0
	0.0	0.727	1.0	0.0
	0.25		0.980	0.0
	0.45		0.928	0.0
	0.71		0.782	0.0
	0.93		0.612	0.0
	1.18		0.417	0.0
	1.55		0.200	0.0
10.0	-1.70		0.258	0.0
	-1.25		0.537	0.0
	-0.86		0.791	0.0
	-0.61		0.893	0.0
	-0.28		0.945	0.0
	0.0	0.669	1.0	0.0
	0.41		0.945	0.0
	0.88		0.765	0.0
	1.10		0.588	0.0
	1.39		0.436	0.0
	1.72		0.258	0.0
	2.16		0.132	0.0
15.0	0.0	0.635		0.0
20.0	0.0	0.593		0.0

Table 12. Free Jet Velocity Measurements;
R_e = 152, M = 0.885, $\bar{u}_0$ = 930 ft./sec.

x/b	y/b	$\bar{u}/\bar{u}_0$	$\bar{u}/\bar{u}_c$	$\sqrt{\overline{u'^2}}/\bar{u}_0 \times 10^2$
0.0	0.0	1.0		0.0
0.25	0.0	0.930		0.0
0.5	0.0	0.940		0.0
1.0	0.0	0.918		0.0
2.0	0.0	0.854		0.0
4.0	0.0	0.724		0.0
6.0	0.0	0.690		0.0
10.0	0.0	0.642		0.0
15.0	0.0	0.592		0.0
20.0	0.0	0.553		0.0

*No turbulence was detected in the jet.

Table 13. Free Jet Velocity Measurements;
R_e = 142, M = 0.457, $\bar{u}_0$ = 507 ft./sec.

x/b	y/b	$\bar{u}/\bar{u}_0$	$\bar{u}/\bar{u}_c$	$\sqrt{\overline{u'^2}}/\bar{u}_0 \times 10^2$
0.0	0.0	1.0		0.0
0.5	0.0	0.976		0.0
1.0	0.0	0.943		0.0
2.0	0.0	0.917		0.0
4.0	0.0	0.838		0.0
6.0	0.0	0.785		0.0
10.0	0.0	0.709		0.0
15.0	0.0	0.661		0.0
20.0	0.0	0.605		0.0

*Turbulence detected in the jet at x/b = 10.0.

Table 14. Free Jet Velocity Measurements;
R_e = 255, M = 0.761, $\bar{u}_0$ = 811 ft./sec.

x/b	y/b	$\bar{u}/\bar{u}_0$	$\bar{u}/\bar{u}_c$	$\sqrt{\overline{u'^2}}/\bar{u}_0 \times 10^2$
0.0	0.0	1.0		0.0
0.25	-0.72		0.119	0.0
	-0.55		0.290	0.0
	-0.52		0.390	0.0
	-0.48		0.520	0.0
	-0.28		0.853	0.0
	-0.18		0.932	0.0
	-0.08	0.967	1.0	0.0
	0.08		0.983	0.0
	0.17		0.941	0.0
	0.24		0.887	0.0
	0.49		0.505	0.0
	0.53		0.377	0.0
	0.57		0.232	0.0
	0.75		0.113	0.0
0.5	0.0	0.927		0.0
1.0	0.0	0.908		0.0
2.0	0.0	0.888		0.0
3.0	-0.92		0.159	0.0
	-0.79		0.280	0.0
	-0.72		0.473	0.0
	-0.61		0.562	0.0
	-0.54		0.685	0.0
	-0.45		0.818	0.0
	-0.37		0.872	0.0
	-0.11		0.964	0.0
	0.11	0.840	1.0	0.0
	0.26		0.946	0.0
	0.44		0.818	0.0
	0.53		0.720	0.0
	0.63		0.580	0.0
	0.71		0.473	0.0
	0.80		0.340	0.0
	0.91		0.207	0.0
	1.11		0.100	0.0
4.0	0.0	0.800		0.0
6.0	-0.93		0.250	0.488
	-0.79		0.404	0.758
	-0.70		0.548	0.868
	-0.59		0.693	1.058

Table 14. (Continued)

x/b	y/b	$\bar{u}/\bar{u}_0$	$\bar{u}/\bar{u}_c$	$\sqrt{\overline{u'^2}}/\bar{u}_0 \times 10^2$
6.0	-0.47		0.817	0.888
	-0.35		0.937	0.0
	-0.15		0.990	0.0
	-0.01	0.755	1.0	0.0
	0.31		0.937	0.0
	0.45		0.846	0.932
	0.55		0.737	1.129
	0.68		0.616	0.947
	0.79		0.491	0.821
	0.95		0.308	0.505
	1.13		0.154	0.477
10.0	-1.15		0.170	0.679
	-0.96		0.310	1.02
	-0.79		0.450	1.49
	-0.65		0.650	1.90
	-0.52		0.770	1.78
	-0.38		0.910	1.28
	-0.18	0.708	1.0	0.0
	0.21		0.975	0.0
	0.36		0.880	2.06
	0.53		0.750	2.07
	0.68		0.620	1.77
	0.76		0.530	1.58
	0.96		0.340	1.17
	1.19		0.170	0.837
15.0	0.0	0.683		0.0
20.0	0.0	0.664		0.0

Table 15. Free Jet Velocity Measurements;
R_e = 336, M = 0.956, $\bar{u}_0$ = 985 ft./sec.

x/b	y/b	$\bar{u}/\bar{u}_0$	$\bar{u}/\bar{u}_c$	$\sqrt{\overline{u'^2}}/\bar{u}_0 \times 10^2$
0.0	0.0	1.0		0.0
0.25	-0.63		0.180	0.416
	-0.56		0.293	0.462
	-0.52		0.438	0.855
	-0.35		0.775	1.78
	-0.24		0.875	0.0
	-0.16		0.970	0.0
	-0.04		1.0	0.0
	0.05	0.950	1.0	0.0
	0.13		0.970	0.0
	0.23		0.875	0.0
	0.35		0.716	1.58
	0.53		0.492	0.961
	0.57		0.331	0.490
	0.63		0.215	0.425
0.5	0.0	0.965		0.0
1.0	0.0	0.950		0.0
2.0	0.0	0.908		0.0
3.0	-0.97		0.204	0.416
	-0.83		0.336	0.472
	-0.41		0.742	0.990
	-0.37		0.821	1.15
	-0.33		0.900	0.0
	-0.14		0.970	0.0
	0.0	0.850	1.0	0.0
	0.44		0.766	1.04
	0.56		0.641	0.814
	0.75		0.352	0.481
4.0	0.0	0.822		0.0
6.0	-1.09		0.193	0.579
	-0.97		0.325	0.778
	-0.84		0.465	1.19
	-0.66		0.702	1.76
	-0.50		0.903	2.47
	-0.26		0.973	1.73
	-0.01	0.743	1.0	0.0
	0.09		0.973	0.0
	0.30		0.903	1.54
	0.65		0.770	1.99
	0.79		0.623	1.36
	0.95		0.422	0.998
	1.12		0.220	0.713

Table 15. (Continued)

x/b	y/b	$\bar{u}/\bar{u}_0$	$\bar{u}/\bar{u}_c$	$\sqrt{\overline{u'^2}}/\bar{u}_0 \times 10^2$
10.0	-1.27		0.228	0.953
	-1.13		0.352	1.24
	-0.90		0.570	1.95
	-0.77		0.723	2.79
	-0.65		0.820	2.79
	-0.21		0.955	0.0
	0.0	0.698	1.0	0.0
	0.55		0.880	3.24
	0.77		0.673	2.77
	0.86		0.588	2.43
	1.02		0.422	1.78
	1.19		0.255	1.34
15.0	0.0	0.653		0.0
20.0	0.0	0.593		0.0

Table 16. Free Jet Velocity Measurements;
$R_e = 262$, $M = 0.347$, $\bar{u}_0 = 389$ ft./sec.

x/b	y/b	$\bar{u}/\bar{u}_0$	$\bar{u}/\bar{u}_c$	$\sqrt{\overline{u'^2}}/\bar{u}_0 \times 10^2$
0.0	0.0	1.0		0.0
1.75	0.0	1.0		0.0
3.0	0.0	0.974		0.0
4.0	0.0	0.961		0.0
6.0	0.0	0.928		0.0
10.0	0.0	0.868		0.0
15.0	0.0	0.819		0.0
20.0	0.0	0.681		5.51

*Turbulence detected in the jet at x/b = 3.0.

Table 17. Free Jet Velocity Measurements;
R_e = 325, M = 0.426, $\bar{u}_0$ = 468 ft./sec.

x/b	y/b	$\bar{u}/\bar{u}_0$	$\bar{u}/\bar{u}_c$	$\sqrt{\overline{u'^2}}/\bar{u}_0 \times 10^2$
0.0	0.0	1.0		0.0
0.25	-0.58		0.095	0.440
	-0.46		0.375	0.571
	-0.38		0.695	0.729
	-0.31		0.873	0.520
	-0.23		0.966	0.0
	-0.11	1.0	1.0	0.0
	0.17		1.0	0.0
	0.27		0.932	0.0
	0.34		0.847	0.510
	0.40		0.644	0.530
	0.51		0.254	0.561
	0.70		0.064	0.300
2.25	0.0	1.0		0.0
3.0	-0.84		0.107	0.0
	-0.64		0.256	0.274
	-0.53		0.441	0.479
	-0.39		0.625	0.880
	-0.25		0.842	0.0
	-0.14		0.953	0.0
	-0.06		0.985	0.0
	0.03	0.982	1.0	0.0
	0.12		0.985	0.0
	0.19		0.908	0.0
	0.26		0.857	0.0
	0.29		0.810	0.971
	0.35		0.672	0.918
	0.46		0.507	0.821
	0.54		0.377	0.390
	0.67		0.149	0.220
	1.04		0.032	0.0
4.0	0.0	0.961		0.0
6.0	-1.13		0.044	
	-0.96		0.122	0.505
	-0.73		0.299	0.715
	-0.61		0.459	0.842
	-0.39		0.698	0.929
	-0.26		0.882	0.817
	-0.20		0.922	0.600
	-0.11		0.991	0.0
	-0.05	0.952	1.0	0.0

Table 17. (Continued)

x/b	y/b	$\bar{u}/\bar{u}_0$	$\bar{u}/\bar{u}_c$	$\sqrt{\overline{u'^2}}/\bar{u}_0 \times 10^2$
6.0	0.14		0.965	0.0
	0.23		0.896	0.583
	0.36		0.754	0.861
	0.50		0.565	0.986
	0.61		0.426	1.02
	0.81		0.233	0.884
	1.03		0.067	
10.0	-1.13		0.106	1.01
	-0.89		0.248	1.45
	-0.71		0.418	1.98
	-0.57		0.563	2.42
	-0.41		0.693	2.46
	-0.28		0.858	1.60
	-0.13		0.955	1.00
	0.08	0.902	1.0	0.0
	0.12		0.983	1.03
	0.19		0.950	1.44
	0.30		0.858	1.79
	0.39		0.745	2.28
	0.60		0.525	2.67
	0.73		0.383	2.46
	0.90		0.225	1.79
	1.22		0.047	0.804
15.0	0.0	0.833		1.78
20.0	0.0	0.592		

Table 18. Free Jet Velocity Measurements;
R_e = 515, M = 0.646, $\bar{u}_0$ = 701 ft./sec.

x/b	y/b	$\bar{u}/\bar{u}_0$	$\bar{u}/\bar{u}_c$	$\sqrt{\overline{u'^2}}/\bar{u}_0 \times 10^2$
0.0	0.0	1.0		0.0
0.25	-0.715		0.068	0.0
	-0.485		0.291	1.16
	-0.415		0.757	0.500
	-0.335		0.885	0.0
	-0.255		0.955	0.0
	-0.165	1.0	1.0	0.0
	0.245		0.970	0.0
	0.325		0.910	0.0
	0.385		0.861	0.0
	0.475		0.576	1.29
	0.535		0.194	0.603
	0.785		0.068	0.0
0.5	0.0	1.0		0.0
1.0	0.0	1.0		0.0
2.0	0.0	1.0		0.0
3.0	-0.96		0.041	0.160
	-0.84		0.103	0.227
	-0.66		0.240	0.463
	-0.55		0.412	0.655
	-0.44		0.660	0.729
	-0.38		0.784	0.356
	-0.31		0.852	0.0
	-0.25		0.903	0.0
	-0.16		0.947	0.0
	0.0	0.997	1.0	0.0
	0.04		0.965	0.0
	0.18		0.926	0.0
	0.31		0.838	0.0
	0.36		0.777	0.0
	0.43		0.660	0.729
	0.50		0.540	0.763
	0.60		0.345	0.799
	0.73		0.135	0.379
	0.94		0.050	0.133
4.0	0.0	0.987		0.0
6.0	-1.08		0.029	0.0
	-0.84		0.147	0.530
	-0.73		0.272	1.19
	-0.60		0.497	1.50

Table 18. (Continued)

x/b	y/b	$\bar{u}/\bar{u}_0$	$\bar{u}/\bar{u}_c$	$\sqrt{\overline{u'^2}}/\bar{u}_0 \times 10^2$
6.0	-0.48		0.672	1.29
	-0.34		0.843	0.0
	-0.30		0.915	0.0
	-0.14		0.974	0.0
	-0.05	0.977	1.0	0.0
	0.05		1.0	0.0
	0.15		0.965	0.0
	0.19		0.928	0.0
	0.30		0.849	1.03
	0.44		0.714	1.82
	0.53		0.518	2.37
	0.69		0.295	1.82
	0.86		0.147	0.953
	1.17		0.044	0.266
10.0	0.0	0.937		2.61
15.0	0.0	0.612		7.05

Table 19. Free Jet Velocity Measurements;
R_e = 359, M = 0.24, $\bar{u}_0$ = 270 ft./sec.

x/b	y/b	$\bar{u}/\bar{u}_0$	$\bar{u}/\bar{u}_c$	$\sqrt{\overline{u'^2}}/\bar{u}_0 \times 10^2$
0.0	0.0	1.0		0.0
3.5	0.0	1.0		0.0
4.0	0.0	0.996		0.0
6.0	0.0	0.978		0.0
10.0	0.0	0.930		0.326
12.5	0.0	0.886		
15.0	0.0	0.818		5.88
17.5	0.0	0.675		
20.0	0.0	0.608		

*Turbulence detected in the jet at x/b = 0.25.

Table 20. Free Jet Velocity Measurements;
R_e = 558, M = 0.368, $\bar{u}_0$ = 410 ft./sec.

x/b	y/b	$\bar{u}/\bar{u}_0$	$\bar{u}/\bar{u}_c$	$\sqrt{\overline{u'^2}}/\bar{u}_0 \times 10^2$
0.0	0.0	1.0		0.0
5.0	0.0	1.0		0.0
5.5	0.0	1.0		
7.5	0.0	0.983		
10.0	0.0	0.967		13.0
12.5	0.0	0.794		
15.0	0.0	0.639		13.3
17.5	0.0	0.594		
20.0	0.0	0.566		11.7

*Turbulence detected in the jet at x/b = 0.25.

Table 21. Free Jet Velocity Measurements;
R_e = 705, M = 0.458, $\bar{u}_0$ = 507 ft./sec.

x/b	y/b	$\bar{u}/\bar{u}_0$	$\bar{u}/\bar{u}_c$	$\sqrt{\overline{u'^2}}/\bar{u}_0 \times 10^2$
0.0	0.0	1.0		0.0
5.0	0.0	1.0		0.0
6.5	0.0	1.0		
7.5	0.0	0.987		
10.0	0.0	0.904		15.2
12.5	0.0	0.710		
15.0	0.0	0.634		13.1
17.5	0.0	0.606		
20.0	0.0	0.579		11.1

*Turbulence detected in the jet at x/b = 0.25.

Table 22. Free Jet Velocity Measurements;
R_e = 546, M = 0.183, $\bar{u}_0$ = 206 ft./sec.

x/b	y/b	$\bar{u}/\bar{u}_0$	$\bar{u}/\bar{u}_c$	$\sqrt{\overline{u'^2}}/\bar{u}_0 \times 10^2$
0.0	0.0	1.0		0.0
0.25	-0.60		0.027	0.172
	-0.57		0.071	0.243
	-0.54		0.130	0.576
	-0.50		0.337	0.977
	-0.46		0.570	1.00
	-0.38		0.870	0.571
	-0.29		1.0	0.0
	0.0	1.0	1.0	0.0
	0.33		0.967	0.0
	0.38		0.777	0.777
	0.45		0.505	1.07
	0.48		0.321	0.977
	0.52		0.185	0.878
	0.55		0.082	0.305
	0.62		0.027	0.117
3.0	-0.83		0.011	0.200
	-0.73		0.055	0.290
	-0.63		0.188	0.523
	-0.55		0.343	0.636
	-0.47		0.580	0.820
	-0.35		0.790	0.650
	-0.26		0.945	0.033
	0.0	1.0	1.0	0.033
	0.20		0.983	0.033
	0.35		0.790	0.833
	0.48		0.470	0.829
	0.57		0.254	0.595
	0.62		0.155	0.562
	0.68		0.088	0.318
	0.75		0.033	0.243
6.0	-0.90		0.032	0.397
	-0.80		0.109	0.655
	-0.66		0.212	2.16
	-0.52		0.440	3.14
	-0.43		0.640	3.20
	-0.33		0.777	2.92
	-0.15		0.967	3.27
	-0.05	1.0	1.0	2.78

Table 22. (Continued)

x/b	y/b	$\bar{u}/\bar{u}_0$	$\bar{u}/\bar{u}_c$	$\sqrt{\overline{u'^2}}/\bar{u}_0 \times 10^2$
6.0	0.16		0.967	3.16
	0.26		0.804	3.49
	0.44		0.505	2.68
	0.57		0.310	1.99
	0.66		0.163	1.55
	0.81		0.060	1.11
10.0	-0.86		0.103	4.04
	-0.69		0.264	7.03
	-0.47		0.489	11.8
	-0.37		0.707	14.2
	-0.16		0.920	11.1
	-0.03	0.945	1.0	10.4
	0.18		0.954	10.4
	0.29		0.822	12.7
	0.39		0.667	11.8
	0.50		0.448	9.38
	0.60		0.328	7.73
	0.74		0.224	4.03
	0.92		0.075	2.33
	1.11		0.029	1.80
15.0	0.0	0.680		11.9
20.0	0.0	0.587		10.1

Table 23. Free Jet Velocity Measurements;
$R_e = 645$, $M = 0.216$, $\bar{u}_0 = 244$ ft./sec.

x/b	y/b	$\bar{u}/\bar{u}_0$	$\bar{u}/\bar{u}_c$	$\sqrt{\overline{u'^2}}/\bar{u}_0 \times 10^2$
0.0	0.0	1.0		0.0
0.25	-0.58		0.048	0.0
	-0.53		0.144	0.413
	-0.49		0.328	1.65
	-0.44		0.631	2.06
	-0.40		0.932	1.19
	-0.35		0.968	0.0
	0.0	1.0	1.0	0.0
	0.37		0.902	0.470
	0.41		0.755	1.40
	0.44		0.620	1.96
	0.47		0.307	2.27
	0.51		0.123	1.02
	0.56		0.053	0.474
	0.67		0.010	0.097
3.0	-0.69		0.066	0.675
	-0.63		0.139	1.11
	-0.56		0.254	1.32
	-0.49		0.414	1.55
	-0.45		0.566	1.79
	-0.38		0.755	1.16
	-0.26		0.935	0.473
	-0.09	1.0	1.0	0.0
	0.15		1.0	0.0
	0.24		0.935	0.473
	0.36		0.778	1.17
	0.41		0.681	1.56
	0.46		0.524	1.75
	0.51		0.336	1.61
	0.61		0.181	1.17
	0.69		0.045	0.533
6.0	-0.76		0.065	0.926
	-0.67		0.131	1.51
	-0.59		0.242	2.49
	-0.49		0.431	3.29
	-0.36		0.700	3.05
	-0.25		0.901	1.43
	0.0	1.0	1.0	0.0
	0.10		0.968	0.473
	0.27		0.837	2.03

Table 23. (Continued)

x/b	y/b	$\bar{u}/\bar{u}_0$	$\bar{u}/\bar{u}_c$	$\sqrt{\overline{u'^2}}/\bar{u}_0 \times 10^2$
6.0	0.43		0.567	3.60
	0.52		0.365	3.02
	0.58		0.242	2.57
	0.67		0.139	1.89
	0.74		0.074	1.22
7.5	0.0	1.0		
10.0	-0.61		0.298	3.84
	-0.51		0.460	4.90
	-0.39		0.649	5.51
	-0.19		0.834	5.68
	-0.05	0.934	1.0	5.26
	0.18		0.896	5.47
	0.29		0.781	5.85
	0.42		0.583	5.27
	0.50		0.482	4.78
	0.59		0.342	3.96
	0.77		0.180	2.80
	0.91		0.070	1.92
15.0	0.0	0.681		14.1
20.0	0.0	0.566		12.4

Table 24. Free Jet Static Pressure Measurements; R_e = 336, M = 0.956, $\bar{u}_0$ = 985 ft./sec.

x/b	y/b	$P - P_m$ (mm.oil)
3.0	-0.71	-0.05
	-0.47	-0.20
	-0.27	-0.40
	-0.12	-0.70
	0.05	-0.75
	0.19	-0.50
	0.39	-0.35
	0.52	-0.10
	0.71	0.0
6.0	-0.73	0.0
	-0.49	-0.20
	-0.29	-0.35
	-0.15	-0.70
	0.01	-0.80
	0.17	-0.65
	0.37	-0.35
	0.50	-0.15
	0.89	0.0
10.0	-1.09	0.0
	-0.78	-0.15
	-0.53	-0.40
	-0.29	-0.55
	0.02	-0.75
	0.36	-0.55
	0.41	-0.45
	0.60	-0.25
	0.83	-0.10

Table 25. Free Jet Static Pressure Measurements; R_e = 325, M = 0.426, $\bar{u}_0$ = 468 ft./sec.

x/b	y/b	$P - P_m$ (mm. oil)
3.0	-0.91	0.0
	-0.62	-0.05
	-0.50	-0.15
	-0.18	-0.40
	0.04	-0.55
	0.17	-0.45
	0.27	-0.30
	0.41	-0.15
	0.61	-0.05
	0.86	0.0
6.0	-0.78	0.0
	-0.61	-0.05
	-0.46	-0.15
	-0.22	-0.30
	-0.07	-0.55
	0.05	-0.60
	0.22	-0.45
	0.42	-0.25
	0.62	-0.10
	0.99	0.0
10.0	-0.95	0.0
	-0.80	-0.05
	-0.50	-0.15
	-0.34	-0.30
	-0.03	-0.55
	0.12	-0.45
	0.36	-0.30
	0.56	-0.15
	0.84	0.0

Table 26. Free Jet Static Pressure Measurements; $R_e = 705$, $M = 0.458$, $\bar{u}_0 = 507$ ft./sec.

x/b	y/b	$P - P_m$ (mm. oil)
3.0	-0.56	0.0
	-0.41	-0.25
	-0.28	-0.65
	-0.17	-0.90
	-0.11	-1.05
	-0.01	-1.15
	0.18	-0.95
	0.26	-0.80
	0.34	-0.45
	0.48	-0.15
	0.55	-0.05
6.0	-0.78	-0.05
	-0.66	-0.15
	-0.47	-0.25
	-0.30	-0.55
	-0.24	-0.70
	-0.05	-1.05
	0.09	-1.20
	0.22	-1.00
	0.39	-0.50
	0.48	-0.30
	0.69	0.0

Table 27. Free Jet Velocity Vector Measurements; R_e = 336, M = 0.956, $\bar{u}_0$ = 985 ft./sec.

x/b	y/b	θ (degree)
3.0	-2.32	67.5
	-1.60	25.5
	-1.18	11.5
	-0.85	5.0
	-0.65	4.0
	0.29	2.5
	0.85	- 4.0
	0.96	- 7.0
	1.09	-10.0
	1.23	-15.0
	1.39	-20.0
	1.66	-42.0
6.0	-2.55	64.0
	-1.98	35.0
	-1.60	18.0
	-1.47	13.5
	-1.22	7.5
	-0.87	2.5
	-0.68	- 1.5
	-0.30	- 1.0
	-0.08	0.0
	0.12	- 0.5
	0.32	0.5
	0.75	- 2.0
	1.03	- 6.0
	1.15	-10.0
	1.44	-17.0
	1.71	-32.0
	2.31	-58.0
10.0	-2.38	37.0
	-2.13	26.0
	-1.90	20.0
	-1.74	13.0
	-1.36	10.0
	-1.24	6.5
	-0.99	3.5
	-0.79	0.0
	-0.31	- 2.5

Table 27. (Continued)

x/b	y/b	θ (degree)
10.0	0.02	0.0
	0.10	0.5
	0.30	0.0
	0.51	0.0
	0.67	- 2.0
	0.86	- 2.5
	1.05	- 4.5
	1.26	- 6.5
	1.36	- 8.5
	1.54	-12.0
	1.96	-27.0
	2.39	-46.0

Table 28. Free Jet Velocity Vector Measurements; R_e = 325, M = 0.426, $\bar{u}_0$ = 468 ft./sec.

x/b	y/b	θ (degree)
3.0	-2.05	50.0
	-1.53	20.0
	-1.34	15.5
	-1.17	9.5
	-0.95	5.0
	-0.64	4.0
	-0.09	0.0
	0.66	- 3.0
	1.01	- 9.0
	1.14	-15.0
	1.35	-25.5
	1.91	-57.0
6.0	-2.01	40.0
	-1.66	25.5
	-1.59	16.0
	-1.45	13.5
	-1.16	10.0
	-0.90	5.0
	-0.21	0.0
	0.18	0.0
	0.61	0.0
	1.04	- 5.0
	1.23	-10.0
	1.38	-13.5
	1.52	-22.0
	2.04	-47.0
10.0	-2.44	31.0
	-2.13	24.5
	-1.75	12.5
	-1.67	11.5
	-1.49	9.0
	-1.29	7.5
	-0.80	4.0
	-0.68	0.0
	-0.08	0.0
	0.28	0.0
	0.90	- 1.0
	1.44	- 8.5
	1.64	-14.5
	1.73	-21.0
	2.12	-42.0

Table 29. Free Jet Velocity Vector Measurements; R_e = 705, M = 0.458, $\bar{u}_0$ = 507 ft./sec.

x/b	y/b	θ (degree)
3.0	-1.70	33.0
	-1.37	20.5
	-1.10	13.0
	-0.73	3.0
	0.48	- 4.0
	0.59	- 5.0
	0.82	- 8.0
	1.04	-20.0
	1.64	-45.0
	2.46	-56.0
6.0	-1.26	22.0
	-1.10	13.5
	-0.90	10.5
	-0.68	6.5
	-0.25	4.0
	0.54	0.5
	0.86	- 5.5
	0.99	- 9.0
	1.48	-17.5
	1.76	-44.0
	2.64	-50.0

APPENDIX D

JET INTERACTION DATA

Flow Conditions

A tabulation of the power jet flow conditions considered in the jet interaction investigation is presented in Table 30. The absolute pressure in the experimental model and the differential pressure across the primary nozzle serves to identify these data cases. The Reynolds and Mach numbers of the power jets which are calculated from the free jet correlation are also presented.

Jet Deflection Data

A tabulation of measured steady state velocity profiles and centerline positions of the deflected power jets is presented in Tables 31 through 38. These data are presented for a constant power jet flow as a function of the control port differential pressure above the model ambient. The indicating fluid has a specific gravity of 1.04. Values of the power jet and control port mass flow rates which were obtained with calibrated rotameters are also presented. A discussion of the method of obtaining the steady state velocity profiles from anemometer data and a description of the experimental error associated with these measurements is presented in Appendix B. The deflected power jet's centerline position was located by taking partial velocity profiles. The jet's centerline was established as the mid-point of these profiles.

Values of x represent parallel distance downstream of the power nozzle's exit plane and values of y represent normal distance from the apparatus or power nozzle centerline. It should be noted that the centerlines of the deflected jet and the power nozzle were offset. The lateral probe traverses cut across different axial stations in the deflected jet. The axial station of the deflected jet profiles, s/b, at the arbitrary probe traverse coordinates x/b and y/b may be expressed as

$$s/b = (x/b-1/2) \cos \theta - y/b \sin \theta + 1/2 \qquad (259)$$

where θ represents the deflection angle of the jet with respect to the power nozzle centerline. Applying the previous expression to the velocity profile data indicates the variation of s/b across the experimental profiles increases with downstream distance. The maximum magnitude of this variation for deflection angles of less than 10° was found to be 0.45 nozzle widths at the station x/b = 10.0. The axial distance traveled at the centerline of the profile which is intersected by the probe traverse is within two percent of the longitudinal traverse coordinate, x/b, for deflection angles restricted to less than 10°. It should also be noted that the normal distance from the deflected jet's centerline differs by the cosine of the deflection angle from the distance to the centerline of the lateral traverse coordinate, y/b.

Deflected Jet Static Pressure Measurements

Static pressure traverses of the deflected power jet are presented for several flow cases in Tables 39 and 40. Differential pressure

measurements between the model ambient are expressed in mm. of oil which has a specific gravity of 1.04.

Deflected Jet Velocity Vector Measurements

Velocity vector traverses are presented for several flow cases in Tables 41 and 42. The deflection angle of the jet with respect to the power nozzle centerline is presented as a function of normal distance from the apparatus or power nozzle centerline. The sign convention established is such that a positive y value produces a vector whose angle is 90° to the apparatus centerline.

Table 30. Experimental Jet Interaction Conditions

Model Pressure, P_m (mm.hg.)	Differential Nozzle Pressure (mm.hg.)	Reynolds Number	Mach Number
1.0	0.443	114	0.691
1.0	0.815	155	0.892
2.0	0.939	252	0.763
2.0	1.639	341	0.970
5.0	0.673	326	0.434
5.0	1.720	534	0.662
20.0	0.478	546	0.183
20.0	0.742	700	0.222

Table 31. Deflected Jet Velocity Measurements;
R_e = 114, M = 0.691, $\dot{m}_i$ = 0.00544 lbm./min.

x/b	y/b	$\bar{u}_c$ (ft./sec.)	$\bar{u}/\bar{u}_c$	P_1-P_m (mm.oil)	$\dot{m}_c$ (lbm./min.)
6.0	-0.74		1.0	1.10	0.000611
10.0	-1.30		1.0		
15.0	-1.94		1.0		
1.0	-1.62		0.087	1.90	0.001130
	-1.23		0.199		
	-0.98		0.379		
	-0.84		0.597		
	-0.73		0.800		
	-0.64		0.876		
	-0.50		0.920		
	-0.33		0.979		
	-0.15	633	1.0		
	0.04		0.979		
	0.27		0.920		
	0.39		0.856		
	0.56		0.813		
2.0	-1.90		0.131		
	-1.56		0.239		
	-1.35		0.434		
	-1.24		0.587		
	-1.11		0.760		
	-0.99		0.912		
	-0.85		0.978		
	-0.64	582	1.0		
	-0.50		1.0		
	-0.38		0.978		
	-0.30		0.954		
	-0.19		0.931		
	-0.05		0.890		
	0.12		0.824		
	0.29		0.613		
	0.40		0.367		
	0.54		0.218		
4.0	-2.61		0.096		
	-2.32		0.239		
	-2.05		0.453		
	-1.91		0.619		
	-1.75		0.810		
	-1.59		0.928		

Table 31. (Continued)

x/b	y/b	$\bar{u}_c$ (ft./sec.)	$\bar{u}/\bar{u}_c$	P_1-P_m (mm.oil)	$\dot{m}_c$ (lbm./min.)
4.0	-1.31	532	1.0		
	-1.15		0.974		
	-0.90		0.974		
	-0.71		0.953		
	-0.44		0.904		
	-0.26		0.737		
	-0.07		0.522		
	0.27		0.192		
7.5	-3.87		0.101		
	-3.54		0.251		
	-3.28		0.399		
	-3.05		0.600		
	-2.84		0.774		
	-2.69		0.901		
	-2.47	506	1.0		
	-1.96		0.976		
	-1.76		0.976		
	-1.31		0.901		
	-0.98		0.676		
	-0.71		0.476		
	-0.50		0.300		
	-0.20		0.124		
				0.30	0.000215
				0.60	0.000392
				0.85	0.000559
				1.20	0.000753
				1.65	0.000998
				0.40	0.000262
				0.85	0.000559
				1.15	0.000753
				1.65	0.000998

Table 32. Deflected Jet Velocity Measurements;
R_e = 155, M = 0.892, $\dot{m}_i$ = 0.00796 lbm./min.

x/b	y/b	$\bar{u}_c$ (ft./sec.)	$\bar{u}/\bar{u}_c$	P_1-P_m (mm.oil)	$\dot{m}_c$ (lbm./min.)
6.0	-0.43		1.0	1.10	0.000452
10.0	-0.68		1.0		
15.0	-1.14		1.0		
6.0	-0.87		1.0	2.00	0.000770
10.0	-1.47		1.0		
15.0	-2.19		1.0		

Table 33. Deflected Jet Velocity Measurements;
R_e = 252, M = 0.763, $\dot{m}_i$ = 0.0120 lbm./min.

x/b	y/b	$\bar{u}_c$ (ft./sec.)	$\bar{u}/\bar{u}_c$	P_1-P_m (mm.oil)	$\dot{m}_c$ (lbm./min.)
6.0	-0.85			2.20	0.001358
10.0	-1.51				
15.0	-2.22				
6.0	-1.41			3.60	0.002123
10.0	-2.41				
15.0	-3.67				
				0.85	0.000523
				1.45	0.000679
				1.85	0.000888
				2.15	0.001150
				2.60	0.001280
				0.75	0.000340
				1.15	0.000549
				1.65	0.000758
				2.30	0.001098
				2.55	0.001411

Table 34. Deflected Jet Velocity Measurements;
R_e = 341, M = 0.970, $\dot{m}_i$ = 0.01586 lbm./min.

x/b	y/b	$\bar{u}_c$ (ft./sec.)	$\bar{u}/\bar{u}_c$	P_1-P_m (mm.oil)	$\dot{m}_c$ (lbm./min.)
3.0	-1.49		0.070	3.40	0.001510
	-1.35		0.204		
	-1.21		0.336		
	-0.79		0.742		
	-0.75		0.821		
	-0.61		0.900		
	-0.52		0.970		
	-0.38	817	1.0		
	0.06		0.766		
	0.18		0.641		
	0.37		0.352		
	0.46		0.204		
	0.63		0.063		
6.0	-0.79		1.0		
10.0	-2.98		0.070		
	-2.69		0.228		
	-2.55		0.352		
	-2.32		0.571		
	-2.19		0.723		
	-2.07		0.820		
	-1.63		0.955		
	-1.42	690	1.0		
	-0.87		0.880		
	-0.65		0.673		
	-0.56		0.588		
	-0.40		0.422		
	-0.23		0.255		
	-0.02		0.091		
15.0	-2.22		1.0		
6.0	-1.20		1.0	5.05	0.002123
10.0	-2.08		1.0		
15.0	-3.14		1.0		

Table 35. Deflected Jet Velocity Measurements;
R_e = 326, M = 0.434, $\dot{m}_i$ = 0.01640 lbm./min.

x/b	y/b	$\bar{u}_c$ (ft./sec.)	$\bar{u}/\bar{u}_c$	P_1-P_m (mm.oil)	$\dot{m}_c$ (lbm./min.)
0.0	-0.44		0.523	1.55	0.001660
	-0.40		0.772		
	-0.28		0.970		
	-0.21	470	1.0		
	0.26		0.970		
	0.32		0.937		
	0.42		0.670		
1.0	-0.93		0.044		
	-0.78		0.180		
	-0.67		0.389		
	-0.54		0.692		
	-0.45		0.904		
	-0.37		0.965		
	0.0	456	1.0		
	0.19		0.904		
	0.31		0.692		
	0.39		0.522		
	0.52		0.329		
3.0	-1.34		0.044		
	-1.16		0.154		
	-1.03		0.329		
	-0.91		0.522		
	-0.79		0.720		
	-0.65		0.902		
	-0.45	456	1.0		
	-0.34		1.0		
	-0.12		0.902		
	0.01		0.747		
	0.09		0.643		
	0.19		0.487		
	0.28		0.329		
	0.39		0.180		
	0.56		0.044		
10.0	-2.73		0.049		
	-2.37		0.231		
	-2.19		0.393		
	-2.04		0.539		
	-1.85		0.764		
	-1.65		0.940		

Table 35. (Continued)

x/b	y/b	$\bar{u}_c$ (ft./sec.)	$\bar{u}/\bar{u}_c$	P_1-P_m (mm.oil)	$\dot{m}_c$ (lbm./min.)
10.0	-1.45	412	1.0		
	-1.22		0.940		
	-1.02		0.793		
	-0.79		0.539		
	-0.63		0.379		
	-0.45		0.199		
	-0.19		0.049		
15.0	-3.74		0.080		
	-3.34		0.280		
	-3.09		0.472		
	-2.81		0.680		
	-2.43		0.968		
	-2.32	375	1.0		
	-2.14		0.968		
	-1.91		0.840		
	-1.58		0.592		
	-1.33		0.400		
	-1.14		0.253		
	-0.71		0.053		
6.0	-1.12		1.0	2.30	0.002280
10.0	-2.07		1.0		
15.0	-3.13		1.0		

Table 36. Deflected Jet Velocity Measurements;
$R_e = 534$, $M = 0.662$, $\dot{m}_i = 0.02796$ lbm./min.

x/b	y/b	$\bar{u}_c$ (ft./sec.)	$\bar{u}/\bar{u}_c$	P_1-P_m (mm.oil)	$\dot{m}_c$ (lbm./min.)
6.0	-0.43		1.0	2.30	0.001842
10.0	-0.80		1.0		
15.0	-1.29		1.0		
6.0	-0.82		1.0	3.80	0.002460
10.0	-1.39		1.0		
15.0	-2.03		1.0		
6.0	-1.03		1.0	5.40	0.003425
10.0	-1.83		1.0		
15.0	-2.76		1.0		
				0.85	0.001019
				1.40	0.001437
				2.45	0.001829
				3.15	0.002195
				4.40	0.002979
				4.95	0.003397
				0.25	0.000627
				1.10	0.001098
				1.60	0.001385
				2.35	0.001803
				2.85	0.002038
				4.00	0.002665

Table 37. Deflected Jet Velocity Measurements;
R_e = 546, M = 0.183, $\dot{m}_1$ = 0.0292 lbm./min.

x/b	y/b	$\bar{u}_c$ (ft./sec.)	$\bar{u}/\bar{u}_c$	P_1-P_m (mm.oil)	$\dot{m}_c$ (lbm./min.)
6.0	-0.46		1.0	0.80	0.001986
10.0	-0.93		1.0		
15.0	-1.51		1.0		
6.0	-0.96		1.0	1.60	0.003660
10.0	-1.82		1.0		
15.0	-2.84		1.0		
				0.35	0.001359
				0.50	0.001777
				0.75	0.002038
				1.05	0.002613
				1.30	0.003293
				2.10	0.005017
				0.85	0.002300
				1.15	0.003031
				1.40	0.003554
				1.75	0.004207

Table 38. Deflected Jet Velocity Measurements;
R_e = 700, M = 0.222, $\dot{m}_1$ = 0.0388 lbm./min.

x/b	y/b	$\bar{u}_c$ (ft./sec.)	$\bar{u}/\bar{u}_c$	P_1-P_m (mm.oil)	$\dot{m}_c$ (lbm./min.)
6.0	-0.56		1.0	1.35	0.002505
10.0	-1.16		1.0		
15.0	-1.86		1.0		
0.0	-0.44		0.712	1.85	0.003480
	-0.39		0.935		
	-0.33	244	1.0		
	-0.15		0.967		
	0.0		0.950		
	0.14		0.935		
	0.36		0.902		
	0.40		0.836		
	0.44		0.631		
3.0	-1.12		0.045		
	-1.05		0.131		
	-0.98		0.254		
	-0.87		0.545		
	-0.77		0.778		
	-0.65		0.967		
	-0.58	244	1.0		
	-0.29		1.0		
	-0.14		0.967		
	-0.02		0.778		
	0.08		0.545		
	0.16		0.348		
	0.26		0.209		
	0.34		0.106		
	0.42		0.033		
6.0	-1.68		0.045		
	-1.56		0.139		
	-1.46		0.266		
	-1.37		0.431		
	-1.26		0.681		
	-1.14		0.902		
	-1.00		0.983		
	-0.88	244	1.0		
	-0.69		0.967		
	-0.51		0.780		
	-0.42		0.632		
	-0.32		0.431		
	-0.22		0.266		

Table 38. (Continued)

x/b	y/b	$\bar{u}_c$ (ft./sec.)	$\bar{u}/\bar{u}_c$	P_1-P_m (mm.oil)	$\dot{m}_c$ (lbm./min.)
6.0	-0.09		0.123		
	0.01		0.041		
10.0	-3.04		0.034		
	-2.64		0.068		
	-2.46		0.152		
	-2.31		0.250		
	-2.16		0.394		
	-2.00		0.606		
	-1.76		0.932		
	-1.60	236	1.0		
	-1.33		0.834		
	-1.17		0.652		
	-0.99		0.407		
	-0.84		0.250		
	-0.71		0.123		
	-0.55		0.055		
	-0.34		0.025		
6.0	-1.04		1.0	2.55	0.004710
10.0	-1.97		1.0		
15.0	-3.11		1.0		

Table 39. Deflected Jet Static Pressure Measurements; R_e = 341, M = 0.97, $\dot{m}_i$ = 0.01440 lbm./min.

x/b	y/b	P_1-P_m (mm.oil)	$P-P_m$ (mm.oil)
3.0	-1.08	3.40	0.0
	-0.97		-0.10
	-0.86		-0.30
	-0.70		-0.50
	-0.52		-0.80
	-0.34		-0.75
	-0.19		-0.65
	0.02		-0.35
	0.19		-0.15
	0.35		0.0
10.0	-2.63		0.0
	-2.30		-0.10
	-2.09		-0.30
	-1.86		-0.50
	-1.60		-0.70
	-1.39		-0.80
	-1.18		-0.70
	-0.96		-0.40
	-0.72		-0.25
	-0.53		-0.05

Table 40. Deflected Jet Static Pressure Measurements; R_e = 326, M = 0.434, $\dot{m}_i$ = 0.01574 lbm./min.

x/b	y/b	P_1-P_m (mm.oil)	$P-P_m$ (mm.oil)
3.0	-1.03	1.55	0.0
	-0.88		-0.05
	-0.76		-0.20
	-0.65		-0.35
	-0.54		-0.45
	-0.42		-0.55
	-0.30		-0.50
	-0.13		-0.35
	-0.03		-0.25
	0.10		-0.15
	0.19		-0.05
	0.40		0.0
10.0	-2.31		0.0
	-2.17		-0.05
	-1.99		-0.15
	-1.89		-0.25
	-1.66		-0.40
	-1.50		-0.55
	-1.33		-0.60
	-1.22		-0.45
	-1.12		-0.40
	-1.00		-0.30
	-0.82		-0.15
	-0.73		-0.05

Table 41. Deflected Jet Velocity Vector Measurements; R_e = 341, M = 0.97, $\dot{m}_i$ = 0.01440 lbm./min.

x/b	y/b	P_1-P_m (mm.oil)	θ (degree)
3.0	-2.72	3.40	49.0
	-2.25		25.5
	-2.13		19.5
	-1.94		11.5
	-1.74		6.0
	-1.38		- 2.5
	-1.16		- 7.0
	-0.51		- 7.5
	0.22		-10.5
	0.50		-12.5
	0.75		-17.5
	0.92		-25.0
10.0	-4.41		28.5
	-4.00		25.5
	-3.71		18.5
	-3.55		13.0
	-3.30		9.0
	-2.90		0.0
	-2.39		- 3.0
	-2.25		- 8.0
	-2.03		-11.0
	-1.96		-12.0
	-1.85		-13.0
	-1.25		-12.5
	-0.67		- 8.0
	-0.22		-13.0
	0.08		-20.0
	0.40		-30.5

Table 42. Deflected Jet Velocity Vector Measurements; R_e = 326, M = 0.434, $\dot{m}_1$ = 0.01574 lbm./min.

x/b	y/b	P_1-P_m (mm. oil)	θ (degree)
3.0	-2.08	1.55	23.5
	-1.73		12.5
	-1.48		4.5
	-1.27		- 2.5
	-1.10		- 4.0
	-0.60		- 9.0
	-0.15		- 8.0
	0.16		- 9.5
	0.43		-12.0
	0.63		-15.5
	0.93		-22.5
10.0	-3.93		23.5
	-3.51		18.5
	-3.29		11.5
	-3.02		8.5
	-2.78		1.5
	-2.57		0.0
	-2.26		- 2.5
	-2.00		- 6.0
	-1.81		- 7.5
	-1.27		- 4.5
	-1.00		- 4.5
	-0.78		- 5.5
	-0.52		- 8.5
	-0.36		-12.5
	0.10		-18.0
	0.38		-32.5
	0.78		-41.0

APPENDIX E

JET RECEIVER IMPINGEMENT DATA

Flow Conditions

A tabulation of the power jet flow conditions in the jet receiver impingement investigation is presented in Table 43. The absolute pressure in the experimental model and the differential pressure across the primary nozzle identify these cases. The Reynolds and Mach numbers of the power jet flows presented in this table are calculated using the free jet data correlation.

Receiver Interaction Data

A tabulation of measured receiver jet interaction data is presented in Tables 44 through 48. These data are presented for a constant power jet flow as a function of the control port differential pressure, receiver location and receiver loading.

In the interaction region of the device, the power nozzle and control port mass flow rates were obtained with calibrated rotameters. The control port pressure above the model ambient is presented in terms of mm. of oil (specific gravity 1.04). The positions of the control and supply ports are identical to that in the interaction study.

The position of the receiver was determined by its radial location and offset angle. The receiver's centerline was located upon a radius of length x_r which emanated from the intersection of the control and supply port centerlines; see Figure 29. This distance

nondimensionalized by the power nozzle width is represented by $x_{r/b}$. The offset angle of the receiver's centerline with respect to the power nozzle centerline is θ_r. Receiver offset angles of 0° and 10° were considered in this research. At a receiver offset angle of 0° the control port pressure was adjusted to a zero value and thus the power jet and receiver centerlines were coincident. At a receiver offset angle of 10° the control port pressure was varied through a range of values and consequently the power jet was positioned at a number of offset angles with respect to the receiver inlet.

The receiver loading was established by modulating the distance separating a circular disk and the hole in the back plate of the receiver; see Figure 35. A load of zero revolutions indicated the hole was closed tight and the receiver was blocked. The load was varied in integer turns of the disk. The static pressure at the receiver exit was measured by a differential manometer. Its value above the model ambient pressure (P_r-P_m) is presented in terms of mm. of oil (specific gravity 1.04). The mass flow rate through the receiver, $\dot{m}_r$, was determined as a function of receiver pressure and loading by calibration. Previous to this investigation the nozzle blocks were removed from the supply port of the experimental apparatus. The receiver inlet was then sealed into the supply port and measured quantities of flow were passed through the device. Calibration curves were established at constant values of model pressure which relate the mass flow rate through the receiver exit as a function of receiver exit pressure and receiver load. These calibration data were subsequently used to compute the receiver flow rate in the experimental study.

Table 43. Experimental Jet Receiver Impingement Conditions

Model Pressure P_m (mm.hg.)	Differential Nozzle Pressure (mm.hg.)	Reynolds Number	Mach Number
1.0	0.394	107	0.653
2.0	0.939	252	0.763
5.0	1.683	530	0.657
10.0	0.980	566	0.368
20.0	0.482	549	0.184

Table 44. Receiver Interaction Measurements;

$R_e = 107$, $M = 0.653$, $\dot{m}_i = 0.00532$ lbm./min.

P_1-P_m (mm.oil)	$\dot{m}_c \times 10^3$ (lbm./min.)	θ_r (degree)	x_r/b	Load (Revolutions)	$\dot{m}_r \times 10^3$ (lbm./min.)	P_r-P_m (mm.oil)
0.0		0.0	2.5	0	0.0	3.25
				2	0.69	2.75
				3	1.06	1.80
				4	1.44	1.25
				6	2.04	0.95
			5.5	0	0.0	2.60
				2	0.57	2.25
				3	0.95	1.60
				4	1.23	1.10
				6	1.70	0.75
			9.5	0	0.0	1.90
				2	0.38	1.50
				3	0.57	0.95
				4	0.84	0.70
				6	1.10	0.45
			14.5	0	0.0	1.35
				2	0.26	1.00
				3	0.43	0.70
				4	0.61	0.50
				6	0.75	0.30
0.0		10.0	5.5	0	0.0	0.55
0.30	0.206				0.0	1.15
0.60	0.390				0.0	1.55
0.85	0.555				0.0	2.00
1.20	0.740				0.0	2.55
1.65	0.981				0.0	2.70

Table 44. (Continued)

P_1-P_m (mm.oil)	$\dot{m}_c \times 10^3$ (lbm./min.)	θ_r (degree)	x_r/b	Load (Revolutions)	$\dot{m}_r \times 10^3$ (lbm./min.)	P_r-P_m (mm.oil)
0.0				3	0.21	0.35
0.30	0.206				0.45	0.75
0.60	0.390				0.54	0.90
0.85	0.555				0.66	1.10
1.20	0.740				0.89	1.50
1.65	0.981				0.89	1.50
0.0				6	0.61	0.25
0.30	0.206				0.98	0.40
0.60	0.390				1.10	0.45
0.85	0.555				1.10	0.45
1.20	0.740				1.40	0.60
1.65	0.981				1.40	0.60
0.0		10.0	9.5	0	0.0	0.35
0.40	0.261				0.0	0.55
0.85	0.555				0.0	0.80
1.15	0.740				0.0	1.35
1.65	0.981				0.0	1.70
0.0				3	0.14	0.25
0.40	0.261				0.18	0.30
0.85	0.555				0.30	0.50
1.15	0.740				0.42	0.70
1.65	0.981				0.51	0.85
0.0				6	0.13	0.05
0.40	0.261				0.25	0.10
0.85	0.555				0.50	0.20
1.15	0.740				0.50	0.20
1.65	0.981				0.87	0.35

Table 45. Receiver Interaction Measurements;

$R_e = 252$, $M = 0.763$, $\dot{m}_i = 0.0120$ lbm./min.

P_1-P_m (mm.oil)	$\dot{m}_c \times 10^3$ (lbm./min.)	θ_r (degree)	x_r/b	Load (Revolutions)	$\dot{m}_r \times 10^3$ (lbm./min.)	P_r-P_m (mm.oil)
0.0		0.0	2.5	0	0.0	9.35
				2	2.93	9.30
				3	5.35	6.40
				4	6.65	4.65
				6	8.05	3.20
			5.5	0	0.0	6.90
				2	2.20	6.70
				3	5.00	5.85
				4	6.45	4.50
				6	7.55	2.90
			9.5	0	0.0	4.50
				2	1.32	3.75
				3	2.75	2.75
				4	3.55	2.00
				6	4.30	1.45
			14.5	0	0.0	3.05
				2	0.87	2.35
				3	1.65	1.55
				4	1.75	0.90
				6	2.20	0.70
0.0		10.0	5.5	0	0.0	2.75
0.35	0.261				0.0	4.85
0.85	0.523				0.0	5.60
1.45	0.680				0.0	5.70
1.85	0.863				0.0	5.95
2.15	1.155				0.0	6.15
2.60	1.307				0.0	6.05

Table 45. (Continued)

P_1-P_m (mm.oil)	$\dot{m}_c \times 10^3$ (lbm./min.)	θ_r (degree)	x_r/b	Load (Revolutions)	$\dot{m}_r \times 10^3$ (lbm./min.)	P_r-P_m (mm.oil)
0.0				3	1.17	1.10
0.35	0.261				2.45	2.40
0.85	0.523				3.40	3.55
1.45	0.680				3.85	4.20
1.85	0.863				4.52	5.15
2.15	1.155				4.85	5.65
2.60	1.307				5.20	6.15
0.0				6	2.10	0.65
0.35	0.261				2.95	0.95
0.85	0.523				4.40	1.50
1.45	0.680				5.45	1.90
1.85	0.863				6.80	2.50
2.15	1.155				7.40	2.80
2.60	1.307				7.55	2.90
0.0		10.0	9.5	0	0.0	0.75
0.75	0.340				0.0	2.25
1.15	0.523				0.0	3.20
1.65	0.732				0.0	4.20
2.30	1.124				0.0	4.80
2.50	1.333				0.0	4.90
0.0				3	0.55	0.50
0.75	0.340				1.28	1.20
1.15	0.523				1.80	1.70
1.65	0.732				2.22	2.15
2.30	1.124				2.70	2.70
2.50	1.333				2.75	2.75

Table 45. (Continued)

P_1-P_m (mm.oil)	$\dot{m}_c \times 10^3$ (lbm./min.)	θ_r (degree)	x_r/b	Load (Revolutions)	$\dot{m}_r \times 10^3$ (lbm./min.)	P_r-P_m (mm.oil)
0.0				6	1.00	0.30
0.75	0.340				2.10	0.65
1.15	0.523				2.50	0.80
1.65	0.732				3.20	1.05
2.30	1.124				3.75	1.25
2.50	1.333				3.90	1.30

Table 46. Receiver Interaction Measurements;
R_e = 530, M = 0.657, $\dot{m}_i$ = 0.0276 lbm./min.

P_1-P_m (mm.oil)	$\dot{m}_c \times 10^3$ (lbm./min.)	θ_r (degree)	x_r/b	Load (Revolutions)	$\dot{m}_r \times 10^3$ (lbm./min.)	P_r-P_m (mm.oil)
0.0		0.0	2.5	0	0.0	19.45
				2	8.70	18.05
				3	14.20	13.55
				4	18.30	10.90
				6	22.10	7.25
			5.5	0	0.0	15.45
				2	7.30	14.45
				3	13.70	12.75
				4	18.45	11.00
				6	20.20	6.35
			9.5	0	0.0	8.45
				2	4.20	6.55
				3	7.75	4.70
				4	9.65	3.60
				6	11.20	2.35
			14.5	0	0.0	4.80
				2	2.72	3.65
				3	5.00	2.30
				4	6.10	1.65
				6	7.60	1.15
0.0	0.261	10.0	5.5	0	0.0	2.50
0.85	0.967				0.0	10.10
1.40	1.360				0.0	11.10
2.45	1.777				0.0	10.90
3.15	2.170				0.0	11.10
4.40	2.930				0.0	12.05
4.95	3.450				0.0	13.75

Table 46. (Continued)

P_1-P_m (mm.oil)	$\dot{m}_c \times 10^3$ (lbm./min.)	θ_r (degree)	x_r/b	Load (Revolutions)	$\dot{m}_r \times 10^3$ (lbm./min.)	P_r-P_m (mm.oil)
0.0	0.261			3	3.70	1.50
0.85	0.967				8.00	4.95
1.40	1.360				10.80	8.45
2.45	1.777				11.70	9.75
3.15	2.170				12.40	10.80
4.40	2.930				14.75	14.40
4.95	3.450				14.90	14.65
0.0	0.261			6	6.00	0.80
0.85	0.967				11.30	2.40
1.40	1.360				14.35	3.65
2.45	1.777				16.70	4.70
3.15	2.170				18.00	5.30
4.40	2.930				20.30	6.40
4.95	3.450				20.60	6.55
0.25	0.601	10.0	9.5	0	0.0	0.50
1.10	1.122				0.0	6.55
1.60	1.360				0.0	7.60
2.35	1.777				0.0	8.35
2.85	2.065				0.0	8.50
0.25	0.601			3	1.10	0.40
1.10	1.122				6.80	3.75
1.60	1.360				7.40	4.35
2.35	1.777				7.90	4.90
2.85	2.065				8.25	5.25
0.25	0.601			6	1.60	0.15
1.10	1.122				10.10	1.95
1.60	1.360				11.00	2.25
2.35	1.777				11.30	2.40
2.85	2.065				12.10	2.70

Table 47. Receiver Interaction Measurements;
R_e = 566, M = 0.368, $\dot{m}_i$ = 0.03045 lbm./min.

P_1-P_m (mm.oil)	$\dot{m}_c \times 10^3$ (lbm./min.)	θ_r (degree)	x_r/b	Load (Revolutions)	$\dot{m}_r \times 10^3$ (lbm./min.)	P_r-P_m (mm.oil)
0.0		0.0	2.5	0	0.0	10.70
				2	9.15	10.50
				3	16.00	8.40
				4	19.60	6.80
				6	22.50	4.30
			5.5	0	0.0	8.10
				2	7.80	7.90
				3	11.50	4.80
				4	13.70	3.75
				6	16.10	2.25
			9.5	0	0.0	4.40
				2	4.70	3.55
				3	8.10	2.65
				4	9.53	1.95
				6	11.20	1.30
			14.5	0	0.0	2.15
				2	2.35	1.60
				3	4.23	1.05
				4	5.60	0.75
				6	6.70	0.55
0.0	0.418	10.0	5.5	0	0.0	3.00
0.40	0.901				0.0	6.05
0.80	1.098				0.0	6.85
1.20	1.648				0.0	7.45
1.55	2.040				0.0	7.35
2.15	2.613				0.0	7.10
0.0	0.418			3	3.60	0.85

Table 47. (Continued)

P_1-P_m (mm.oil)	$\dot{m}_c \times 10^3$ (lbm./min.)	θ_r (degree)	x_r/b	Load (Revolutions)	$\dot{m}_r \times 10^3$ (lbm./min.)	P_r-P_m (mm.oil)
0.40	0.901				7.50	2.35
0.80	1.098				9.70	3.60
1.20	1.648				11.10	4.50
1.55	2.040				11.20	4.60
2.15	2.613				12.30	5.40
0.0	0.418			6	4.90	0.35
0.40	0.901				10.10	1.10
0.80	1.098				13.40	1.70
1.20	1.648				16.10	2.25
1.55	2.040				16.30	2.30
2.15	2.613				17.20	2.50
0.0	0.522	10.0	9.5	0	0.0	2.20
0.50	1.150				0.0	3.20
0.90	1.462				0.0	3.50
1.35	2.040				0.0	3.95
2.00	2.535				0.0	4.25
2.35	2.872				0.0	4.25
0.0	0.522			3	4.70	1.20
0.50	1.150				6.30	1.80
0.90	1.462				7.00	2.10
1.35	2.040				7.50	2.35
2.00	2.535				7.80	2.50
2.35	2.872				8.10	2.65
0.0	0.522			6	8.70	0.85
0.50	1.150				9.80	1.05
0.90	1.462				10.40	1.15
1.35	2.040				10.70	1.20
2.00	2.535				11.50	1.35
2.35	2.872				11.20	1.30

Table 48. Receiver Interaction Measurements;
$R_e = 549$, $M = 0.184$, $\dot{m}_i = 0.0293$ lbm./min.

P_1-P_m (mm.oil)	$\dot{m}_c \times 10^3$ (lbm./min.)	θ_r (degree)	x_r/b	Load (Revolutions)	$\dot{m}_r \times 10^3$ (lbm./min.)	P_r-P_m (mm.oil)
0.0		0.0	2.5	0	0.0	5.65
				2	9.40	5.35
				3	15.80	4.15
				4	19.20	3.30
				6	21.40	2.10
			5.5	0	0.0	4.65
				2	7.70	3.75
				3	12.90	2.85
				4	15.90	2.30
				6	18.70	1.50
			9.5	0	0.0	3.65
				2	4.90	2.05
				3	8.20	1.30
				4	9.70	1.00
				6	11.70	0.70
			14.5	0	0.0	2.45
				2	4.50	1.85
				3	7.80	1.25
				4	9.30	0.95
				6	10.40	0.60
0.0	0.417	10.0	5.5	0	0.0	0.35
0.35	1.360				0.0	3.70
0.50	1.777				0.0	4.15
0.75	2.065				0.0	4.20
1.05	2.613				0.0	3.85
1.30	3.290				0.0	3.85
2.10	5.040				0.0	4.00

Table 48. (Continued)

P_1-P_m (mm.oil)	$\dot{m}_c \times 10^3$ (lbm./min.)	θ_r (degree)	x_r/b	Load (Revolutions)	$\dot{m}_r \times 10^3$ (lbm./min.)	P_r-P_m (mm.oil)
0.0	0.417			3	1.63	0.20
0.35	1.360				6.85	1.05
0.50	1.777				11.10	2.15
0.75	2.065				12.82	2.80
1.05	2.613				13.40	3.05
1.30	3.290				12.60	2.70
2.10	5.040				13.05	2.90
0.0	0.417			6	2.00	0.05
0.35	1.360				9.60	0.55
0.50	1.777				15.10	1.00
0.75	2.065				16.80	1.20
1.05	2.613				19.25	1.60
1.30	3.290				17.20	1.25
2.10	5.040				18.40	1.45
0.0	0.261	10.0	9.5	0	0.0	0.65
0.80	2.245				0.0	1.80
1.15	2.925				0.0	1.90
1.40	3.480				0.0	1.80
1.75	4.180				0.0	1.55
0.0	0.261			3	3.40	0.45
0.80	2.245				7.32	1.15
1.15	2.925				7.80	1.25
1.40	3.480				7.57	1.20
1.75	4.180				6.35	0.95
0.0	0.261			6	4.80	0.25
0.80	2.245				13.00	0.80
1.15	2.925				11.00	0.65
1.40	3.480				10.30	0.60
1.75	4.180				10.30	0.60

APPENDIX F

DERIVATION OF FREE JET MOMENTUM AND MASS FLOW INTEGRALS

The experimental data demonstrated the plane jet's steady state longitudinal velocity profile could be described by a simple Gaussian distribution. The form of this expression is

$$\bar{u}/\bar{u}_c = e^{-4.6\eta^2} \quad \text{for} \quad -y_c \geq y \geq -\infty \qquad y_c \leq y \leq \infty \tag{260}$$

$$\bar{u}/\bar{u}_c = 1 \quad \text{for} \quad -y_c \leq y \leq y_c$$

The value of η is given by

$$\eta = \frac{y/b - y_c/b}{y^*/b - y_c/b} \tag{261}$$

A sketch of the profile is presented in Figure 57.

Momentum Integral

The momentum per unit height of the jet in the x-direction from arbitrary positions y_1 to y_2 may be written as

$$J = \int_{y_1}^{y_2} \rho \, \bar{u}^2 \, dy \tag{262}$$

For an ideal gas with constant specific heats within an isoenergetic mixing process (constant total temperature), the relationship between

static and total temperature in the jet is

$$T = T_T \left(1 - \frac{\bar{V}^2}{2 g_c C_p T_T}\right) \tag{263}$$

$\bar{V}$ in the previous expression represents the average speed of the velocity vector. The expression above may be simplified by introducing an identity for constant pressure specific heat

$$T = T_T \left[1 - \left(\frac{k-1}{2}\right)\left(\frac{\bar{V}^2}{k\ g_c\ \bar{R}\ T_T}\right)\right] \tag{264}$$

Using the ideal gas equation of state ρ may be written as

$$\rho = \rho_T\ (P/P_T)\,(T_T/T) \tag{265}$$

Solving for ρ yields

$$\rho = \frac{\rho_T\ (P/P_T)}{\left[1 - \left(\frac{k-1}{2}\right)\left(\frac{\bar{V}}{C_T}\right)^2\right]} \tag{266}$$

where C_T is the sonic velocity based on the total temperature.

For a single flow case the density at any position in the jet is a function only of the velocity at that point. Experimental studies have indicated the x-component of velocity, $\bar{u}$, can be substituted for $\bar{V}$ in expression (266) with a maximum error in the value of ρ of 0.02 percent. After this substitution equation (262) may be written as

$$J = \int_{y_1}^{y_2} \frac{\rho_T \, (P/P_T) \, \bar{u}^2}{\left[1 - (\frac{k-1}{2})\left(\frac{\bar{u}}{C_T}\right)^2\right]} \, dy \tag{267}$$

Nondimensionalizing the preceding equation gives

$$J = \rho_T \, (P/P_T) \, \bar{u}_c^{\,2} \int_{y_1}^{y_2} \frac{(\bar{u}/\bar{u}_c)^2}{[1 - B(\bar{u}/\bar{u}_c)^2]} \, dy \tag{268}$$

$$B = \frac{k-1}{2}\left(\frac{\bar{u}_c}{C_T}\right)^2$$

The nondimensional velocity profiles given in equations (260) and (261) may be inserted into the previous expression and the result integrated. The most general case of this integration is from a position at the centerline of the jet to some arbitrary position beyond the potential core region.

$$J = \rho_T(P/P_T) \, \bar{u}_c^{\,2} \left[\int_0^{y_c} \frac{1}{1-B} \, dy + \int_{y_c}^{y_2} \frac{(e^{-4.6\eta^2})^2}{1-B(e^{-4.6\eta^2})^2} \, dy\right] \tag{269}$$

The variables of integration may be transformed to

$$\eta = \frac{y/b - y_c/b}{y^*/b - y_c/b} \tag{270}$$

$$dy = (y^* - y_c) \, d\eta$$

The resulting momentum integral becomes

$$J = \rho_T (P/P_T)\ \bar{u}_c^{\,2} \left[\frac{y_c}{1-B} + (y^*-y_c) \int_0^{\eta_2} \frac{e^{-9.2\eta^2}}{1 - B\ e^{-9.2\eta^2}}\, d\eta \right] \qquad (271)$$

$$\eta_2 = \frac{y_2/b - y_c/b}{y^*/b - y_c/b}$$

The integrand of the preceding expression may be transformed into a power series by simple division

$$J = \rho_T (P/P_T)\ \bar{u}_c^{\,2} \left[\frac{y_c}{1-B} + (y^*-y_c) \int_0^{\eta_2} \left(\sum_{m=0}^{\infty} B^m\ e^{-(m+1)9.2\eta^2} \right) d\eta \right] \qquad (272)$$

In order to interchange the order of integration and summation in expression (272), the series $\sum_{m=0}^{\infty} B^m\ e^{-(m+1)9.2\eta^2}$ must be shown to be a uniformly convergent series of continuous functions in the region $0 \leq \eta \leq \infty$. It is evident that $B^m\ e^{-(m+1)9.2\eta^2}$ is continuous for $0 \leq \eta \leq \infty$. The Weirstrass M-test may be applied to show uniform convergence. By this test if for all values of η in the region $0 \leq \eta \leq \infty$, the absolute value of a series of the form $M_0 + M_1 + M_2 \cdots$ are, respectively, less than the corresponding terms in a convergent series of constant terms. Then the series converges uniformly in the region $0 \leq \eta \leq \infty$. The test series for this proof is $\sum_{m=0}^{\infty} B^m$.

The following is true:

$$\left| B^m \, e^{-(m+1)9.2\eta^2} \right| \leq B^m \quad \text{for } -\infty \leq \eta \leq \infty \tag{273}$$

The power series $\sum_{m=0}^{\infty} B^m$ converges for all B where $|B| < 1$, thus the order of integration and summation may be interchanged for $B < 1$. From the definition of B it is apparent that for subsonic air this condition is satisfied. Equation (272) consequently may be written as

$$J = \rho_T (P/P_T) \, \bar{u}_c^{\,2} \left[\frac{y_c}{1-B} + (y^* - y_c) \sum_{m=0}^{\infty} B^m \int_0^{\eta_2} e^{-(m+1)9.2\eta^2} \, d\eta \right] \tag{274}$$

The integrand of equation (274) may be converted into the form

$$\phi(\gamma) = \int_0^{\gamma_2} \frac{1}{\sqrt{2\pi}} e^{-\gamma^2/2} \, d\gamma \tag{275}$$

This is the cumulative distribution function which may be found in mathematical handbooks. Rewriting equation (274) in this form gives

$$J = \rho_T (P/P_T) \, \bar{u}_c^{\,2} \left[\frac{y_c}{1-B} + (y^* - y_c) \sum_{m=0}^{\infty} B^m \frac{\sqrt{2\pi}}{A_1} \int_0^{A_1 \eta_2} \frac{1}{\sqrt{2\pi}} e^{-\gamma^2/2} \, d\gamma \right] \tag{276}$$

$$\gamma = A_1 \eta$$

$$A_1 = \sqrt{18.4(m+1)}$$

Simplifying yields

$$J = PB \left(\frac{2k}{k-1}\right) b \left[\frac{y_c/b}{1-B} + \sqrt{\frac{\pi}{9.2}} (y^*/b - y_c/b) \sum_{m=0}^{\infty} \frac{B^m}{\sqrt{m+1}} \phi(A_1\eta_2)\right] \quad (277)$$

The series $\sum_{m=0}^{\infty} \frac{B^m}{\sqrt{m+1}} \phi(A_1\eta_2)$ may be evaluated if B and η_2 are known.

The results of the momentum integration may be summarized

$$J = PB \left(\frac{2k}{k-1}\right) b \left[\frac{y_c/b}{1-B} + \sqrt{\frac{\pi}{9.2}} (y^*/b - y_c/b) \Gamma_1 (B,\eta_2)\right] \quad (278)$$

$$B = \frac{k-1}{2} \left(\frac{\bar{u}_c}{C_T}\right)^2$$

$$\eta_2 = \frac{y_2/b - y_c/b}{y^*/b - y_c/b}$$

$$\Gamma_1 (B,\eta_2) = \sum_{m=0}^{\infty} \frac{B^m}{\sqrt{m+1}} \phi (A_1\eta_2)$$

The momentum of one half of a free jet may be determined by setting $\eta_2 = \infty$ in equation (278). The momentum of a free jet may be determined by doubling the half jet momentum. The expression for the momentum of a plane jet is

$$J_\infty = 2\ PB \left(\frac{2k}{k-1}\right) b \left[\frac{y_c/b}{1-B} + 0.292\ (y^*/b - y_c/b) \sum_{m=0}^{\infty} \frac{B^m}{\sqrt{m+1}}\right] \quad (279)$$

Mass Flow Integral

The mass flow rate per unit height through a surface normal to the x-axis of the supply jet is

$$\mathring{m} = \int_{y_1}^{y_2} \rho \bar{u}\, dy \tag{280}$$

where y_1 and y_2 are two arbitrary positions on this surface. The expression for density found in equation (266) may be substituted into the equation above to give

$$\mathring{m} = \rho_T (P/P_T)\ \bar{u}_c \int_{y_1}^{y_2} \frac{\bar{u}/\bar{u}_c}{[1 - B(\bar{u}/\bar{u}_c)^2]}\, dy \tag{281}$$

The nondimensional velocity profiles may again be substituted into the preceding equation and the result integrated. The most general case again will be considered; that is, from a position at the centerline to some arbitrary position beyond the potential core region.

$$\mathring{m} = \rho_T (P/P_T)\ \bar{u}_c \left[\int_0^{y_c} \frac{1}{1-B}\, dy + \int_{y_c}^{y_2} \frac{e^{-4.6\eta^2}}{[1 - B(e^{-4.6\eta^2})^2]}\, dy \right] \tag{282}$$

Changing variables of integration and simplifying gives

$$\mathring{m} = \rho_T (P/P_T)\ \bar{u}_c \left[\frac{y_c}{1-B} + (y^* - y_c) \int_0^{\eta_2} \frac{e^{-4.6\eta^2}}{1 - B\, e^{-9.2\eta^2}}\, d\eta \right] \tag{283}$$

The integrand of the above may be converted into a power series by division.

$$\mathring{m} = \rho_T (P/P_T)\ \bar{u}_c \left[\frac{y_c}{1-B} + (y^* - y_c) \int_0^{\eta_2} \sum_{m=0}^{\infty} B^m\, e^{-(2m+1)4.6\eta^2}\, d\eta \right] \tag{284}$$

As in the previous case, uniform convergence of the series $\sum_{m=0}^{\infty} B^m e^{-(2m+1)4.6\eta^2}$ must be demonstrated in order to interchange the order of integration and summation. It is evident that $B^m e^{-(2m+1)4.6\eta^2}$ is continuous for $0 \leq \eta \leq \infty$ and thus the Weirstrass M-test may be used to show uniform convergence. Using the same test series $\sum_{m=0}^{\infty} B^m$, it is apparent that

$$\left| B^m e^{-(2m+1)4.6\eta^2} \right| \leq B^m \quad \text{for} \quad -\infty \leq \eta \leq \infty \tag{285}$$

Thus the series $\sum_{m=0}^{\infty} B^m e^{-(2m+1)4.6\eta^2}$ converges uniformly in the interval $0 \leq \eta \leq \infty$ for $|B| < 1$. Equation (284) may be written as

$$\mathring{m} = \rho_T (P/P_T) \bar{u}_c \left[\frac{y_c}{1-B} + (y^* - y_c) \sum_{m=0}^{\infty} B^m \int_0^{\eta_2} e^{-(2m+1)4.6\eta^2} \, d\eta \right] \tag{286}$$

Again the above integrand may be converted to the cumulative distribution function which is computed and tabulated in handbooks dealing with probability. Simplifying expression (286) yields

$$\mathring{m} = \frac{bP \bar{u}_c}{\bar{R} T_T} \left[\frac{y_c/b}{1-B} + \sqrt{\frac{\pi}{4.6}} (y^*/b - y_c/b) \sum_{m=0}^{\infty} \frac{B^m}{\sqrt{2m+1}} \phi (A_2 \eta_2) \right] \tag{287}$$

$$A_2 = \sqrt{9.2(2m+1)}$$

The series $\sum_{m=0}^{\infty} \frac{B^m}{\sqrt{2m+1}} \phi (A_2 \eta_2)$ may be evaluated if B and η are known. This series has been evaluated as a function of B and η and the results are shown in Figure 71.

The results of the mass flow integration may be summarized

$$\dot{m} = \frac{bP\ \bar{u}_c}{\bar{R}\ T_T}\left[\frac{y_c/b}{1-B} + \sqrt{\frac{\pi}{4.6}}\ (y^*/b - y_c/b)\ \Gamma_2\ (B,\eta_2)\right] \qquad (288)$$

$$\Gamma_2\ (B,\eta_2) = \sum_{m=0}^{\infty} \frac{B^m}{\sqrt{2m+1}}\ \phi\ (A_2\eta_2)$$

$$B = \frac{k-1}{2}\ (\tilde{u}_c/C_T)^2$$

$$\eta_2 = \frac{y_2/b - y_c/b}{y^*/b - y_c/b}$$

APPENDIX G

ESTIMATION OF THE SUPPLY NOZZLE MASS FLOW RATE

The experimental data indicated the supply jet's velocity profile at the exit plane of the nozzle could be represented by a power law distribution of the form

$$\bar{u}/\bar{u}_c = 1 \qquad \text{for} \quad 0 \leq y \leq y_c \tag{289}$$

$$\bar{u}/\bar{u}_c = 1 - \left(\frac{y/b - y_c/b}{1/2 - y_c/b}\right)^n \qquad \text{for} \quad y_c \leq y \leq b/2$$

The profile distribution coefficient, n, was found to vary with the flow condition in order to provide the best fit to the experimental data.

Assuming the supply jet's x-component of momentum is conserved, the flow rate at the nozzle exit plane may be estimated based on the free jet data correlation and the assumed velocity profile. The procedure which was developed for computing the nozzle flow consists of three steps. Firstly, the momentum and the core width at the nozzle exit plane are calculated from the free jet correlation. Secondly, the profile distribution coefficient, n, is calculated from the known momentum and core width. Thirdly, the nozzle flow rate is computed based on the assumed velocity profile. The following two sections will develop the momentum and mass flow rate expressions for the velocity profile

presented in equation (289). The third section will employ these expressions to calculate the nozzle flow rate.

Momentum Integral

The momentum per unit height in the x-direction of one half the supply jet at the nozzle exit plane is

$$J = \int_0^{b/2} \rho \bar{u}^2 \, dy \tag{290}$$

As was demonstrated previously, the density of an ideal gas with constant specific heats within an isoenergetic mixing process is

$$\rho = \frac{\rho_T (P/P_T)}{[1 - (\frac{k-1}{2})(\bar{u}/C_T)^2]} \tag{291}$$

Introducing the previous expression for density into (290), results in

$$J = \int_0^{b/2} \frac{\rho_T (P/P_T) \, \bar{u}^2}{[1 - (\frac{k-1}{2})(\bar{u}/C_T)^2]} \, dy \tag{292}$$

Nondimensionalizing the previous equation gives

$$J = \rho_T (P/P_T) \, \bar{u}_c^{\,2} \int_0^{b/2} \frac{(\bar{u}/\bar{u}_c)^2}{[1 - B(\bar{u}/\bar{u}_c)^2]} \, dy \tag{293}$$

The nondimensional velocity profiles given in equation (289) may be inserted into equation (293) and the result integrated.

$$J = \rho_T (P/P_T) \, \bar{u}_c^{\,2} \left[\int_0^{y_c} \frac{1}{1-B} \, dy + \int_{y_c}^{b/2} \frac{(1 - \tau_1^{\,n})^2}{[1 - B(1-\tau_1^{\,n})^2]} \, dy \right] \tag{294}$$

$$\tau_1 = \frac{y/b - y_c/b}{1/2 - y_c/b}$$

The variables of the integration are changed to

$$\tau_1 = \frac{y/b - y_c/b}{1/2 - y_c/b} \tag{295}$$

$$dy = (b/2 - y_c)\, d\tau_1$$

The resulting momentum integral is

$$J = \rho_T (P/P_T)\, \bar{u}_c^{\,2} \left[\frac{y_c}{1-B} + (\frac{b}{2} - y_c) \int_0^1 \frac{(1 - \tau_1^{\,n})^2}{[1 - B(1-\tau_1^{\,n})^2]}\, d\tau_1 \right] \tag{296}$$

The integrand of the above expression may be transformed into a power series by simple division

$$J = \rho_T (P/P_T)\, \bar{u}_c^{\,2} \left[\frac{y_c}{1-B} + (\frac{b}{2} - y_c) \int_0^1 \sum_{m=0}^{\infty} B^m (1-\tau_1^{\,n})^{2(m+1)}\, d\tau_1 \right] \tag{297}$$

In order to interchange the order of integration and summation in expression (297), the series $\sum_{m=0}^{\infty} B^m (1-\tau_1^{\,n})^{2(m+1)}$ must be shown to be a uniformly convergent series of continuous functions in the region $0 \leq \tau_1 \leq 1$. It is evident that $B^m (1-\tau_1^{\,n})^{2(m+1)}$ is continuous for $0 \leq \tau_1 \leq 1$ and thus the Weirstrass M-test may be used to show uniform convergence. The test series $\sum_{m=0}^{\infty} B^m$ may be used to demonstrate uniform convergence. It is apparent that

$$\left| B^m (1-\tau_1^{\,n})^{2(m+1)} \right| \leq B^m \qquad 0 \leq \tau_1 \leq 1 \tag{298}$$

$$n \geq 0$$

The test series $\sum_{m=0}^{\infty} B^m$ converges for all B where $|B| < 1$, thus uniform convergence is demonstrated and the order of integration and summation may be interchanged. Equation (297) may be written as

$$J = \rho_T (P/P_T)\ \bar{u}_c^{\,2} \left[\frac{\bar{y}_c}{1-B} + \left(\frac{b}{2} - y_c\right) \sum_{m=0}^{\infty} B^m \int_0^1 (1-\tau_1^{\,n})^{2(m+1)}\ d\tau_1 \right] \qquad (299)$$

The series $\sum_{m=0}^{\infty} B^m \int_0^1 (1-\tau_1^{\,n})^{2(m+1)}\ d\tau_1$ may be determined if B and n are known. This series has been evaluated as a function of B and n and the results are shown in Figure 73. In summary, the momentum of the power jet per unit height at the exit plane of the nozzle is

$$J_\infty = 4 \left(\frac{k}{k-1}\right) P\ Bb \left[\frac{\bar{y}_c/b}{1-B} + \left(\frac{1}{2} - y_c/b\right) \phi_1\ (B,n) \right] \qquad (300)$$

$$\phi_1\ (B,n) = \sum_{m=o}^{\infty} B^m \int_0^1 (1-\tau_1^{\,n})^{2(m+1)}\ d\tau_1$$

$$B = \frac{k-1}{2} \left(\bar{u}_c/C_T\right)^2$$

Mass Flow Integral

The mass flow per unit height through a surface normal to the x-axis of the supply jet is

$$\dot{m} = \int_{y_1}^{y_2} \rho \bar{u}\ dy \qquad (301)$$

After introducing the expression for density found in equation (291), the preceding expression may be evaluated to determine the flow rate

at the exit plane of the nozzle.

$$\dot{m} = 2\rho_T \, (P/P_T) \, \bar{u}_c \int_0^{b/2} \frac{\bar{u}/\bar{u}_c}{[1 - B(\bar{u}/\bar{u}_c)^2]} \, dy \tag{302}$$

The nondimensional velocity profiles given in equation (289) may be substituted into the preceding expression and the result integrated

$$\dot{m} = 2\rho_T \, (P/P_T) \, \bar{u}_c \left[\int_0^{y_c} \frac{1}{1-B} \, dy + \int_{y_c}^{b/2} \frac{(1-\tau_1^n)}{[1 - B(1-\tau_1^n)^2]} \, dy \right] \tag{303}$$

Changing variables of integration and simplifying gives

$$\dot{m} = 2\rho_T \, (P/P_T) \, \bar{u}_c \left[\frac{y_c}{1-B} + (\frac{b}{2} - y_c) \int_0^1 \frac{(1-\tau_1^n)}{[1 - B(1-\tau_1^n)^2]} \, d\tau_1 \right] \tag{304}$$

The integrand of the preceding expression may also be transformed into a power series by simple division

$$\dot{m} = 2\rho_T \, (P/P_T) \, \bar{u}_c \left[\frac{y_c}{1-B} + (\frac{b}{2} - y_c) \int_0^1 \sum_{m=0}^{\infty} B^m \, (1-\tau_1^n)^{2m+1} \, d\tau_1 \right] \tag{305}$$

Uniform convergence of the series $\sum_{m=0}^{\infty} B^m \, (1-\tau_1^n)^{2m+1}$ must be demonstrated in order to interchange the order of integration and summation in the preceding expression. It is evident that $B^m \, (1-\tau_1^n)^{2m+1}$ is continuous for $0 \leq \tau_1 \leq 1$. The Weirstrass M-test may again be used to demonstrate uniform convergence. Using the same test series $\sum_{m=0}^{\infty} B^m$, it is evident

$$\left|B^m\ (1-\tau_1{}^n)^{2m+1}\right| \leq B^m \qquad 0 \leq \tau_1 \leq 1 \qquad (306)$$

$$n > 0$$

Thus the series $\sum_{m=0}^{\infty} B^m\ (1-\tau_1{}^n)^{2m+1}$ converges uniformly for $|B| < 1$.

Equation (305) may be written as

$$\dot{m} = 2\rho_T\ (P/P_T)\ \bar{u}_c \left[\frac{y_c}{1-B} + (\frac{b}{2} - y_c) \sum_{m=0}^{\infty} B^m \int_0^1 (1-\tau_1{}^n)^{2m+1}\ d\tau_1\right] \qquad (307)$$

The series $\sum_{m=0}^{\infty} B^m \int_0^1 (1-\tau_1{}^n)^{2m+1}\ d\tau_1$ may be calculated if B and n are known. This series has been evaluated as a function of B and n and the results are presented in Figure 74. In summary, the mass flow per unit height exiting the nozzle is

$$\dot{m} = \frac{2P\ \bar{u}_c\ b}{\bar{R}\ T_T} \left[\frac{y_c/b}{1-B} + (1/2 - y_c/b)\ \phi_2\ (B,n)\right] \qquad (308)$$

$$\phi_2\ (B,n) = \sum_{m=0}^{\infty} B^m \int_0^1 (1-\tau_1{}^n)^{2m+1}\ d\tau_1$$

where $\bar{R}$ and T_T are the gas constant and total temperature, respectively.

Calculation of Nozzle Flow Rate

The expression for the momentum of the jet at the nozzle exit plane was presented in equation (300). Solving for $\phi_1\ (B,n)$ from that expression yields

$$\phi_1 (B,n) = \left[\frac{J_\infty/b}{4 \left(\frac{k}{k-1}\right) PB} - \frac{y_c/b}{1-B} \right] \left(\frac{1}{1/2 - y_c/b} \right) \Bigg|_{x=0} \qquad (309)$$

where J_∞ is determined from the free jet data correlation and the jet characteristics are evaluated at the nozzle exit plane. With ϕ_1 (B,n) and B both known, the profile distribution coefficient, n, may be computed from Figure 73. The value of ϕ_2 (B,n) may be determined from Figure 74 and the mass flow rate per unit height from the nozzle exit may be evaluated from equation (308).

APPENDIX H

SAMPLE CALCULATIONS

Calculation of Free Jet Parameters

The calculation of free jet parameters which are required in the determination of interaction and receiver characteristics may be illustrated with data from flow case six of Table 30. The pressure and temperature in the stagnation tank upstream of the supply nozzle is 6.72 mm. hg. and 532°R, respectively. The pressure in the experimental model is 5.0 mm. hg. The pressure ratio across the nozzle is

$$P_m/P_T = 5/6.72 = 0.745 \tag{310}$$

From one-dimensional perfect gas relationships the following parameters are determined at the nozzle exit:

$$M = 0.662 \quad ; \quad T/T_T = 0.9197 \tag{311}$$

The static temperature at the nozzle exit is calculated to be 489°R.

From the definition of speed of sound and Mach number

$$\bar{u}_0 = M \sqrt{k \bar{R} T g_c} \tag{312}$$

The potential velocity at the centerline of the nozzle exit plane may be computed from the previous expression with $k = 1.4$ and $\bar{R} = 53.34 \frac{\text{ft.lbf.}}{\text{lbm.}\ ^\circ\text{R}}$ for air and the gravitational constant equal to $32.2 \frac{\text{ft.lbm.}}{\text{lbf.sec.}^2}$

$$\bar{u}_0 = 0.662 \sqrt{(1.4)(53.34)(489)(32.2)} = 717 \text{ ft./sec.} \quad (313)$$

The Reynolds number at the centerline of the nozzle exit is defined as

$$R_e = \rho \bar{u}_0 \, b/\mu \quad (314)$$

If it is assumed the gas is ideal, the density, ρ, may be expressed as

$$\rho = P_m/\bar{R} \, T \quad (315)$$

The density at the nozzle exit plane is

$$\rho = \frac{(5.0 \text{ mm.hg.}) \left(2.783 \frac{\text{lbf.}}{\text{ft.}^2 \text{ mm.hg.}}\right)}{\left(53.34 \frac{\text{ft.lbf.}}{\text{lbm.} \, ^\circ\text{R}}\right)(489^\circ\text{R})} \quad (316)$$

$$\rho = 5.33 \times 10^{-4} \text{ lbm./ft.}^3$$

Assuming the viscosity of the gas, μ, is proportional to the square root of temperature

$$\mu = 0.37 \times 10^{-6} \, (T/492)^{1/2} \text{ lbf.sec./ft.}^2 \quad (317)$$

The viscosity at the centerline of the nozzle exit plane is

$$\mu = 0.37 \times 10^{-6} \, (489/492)^{1/2} = 0.369 \times 10^{-6} \text{ lbf.sec./ft.}^2 \quad (318)$$

Introducing the values of density and viscosity into the expression for Reynolds number where b is equal to 0.0167 feet, yields

$$R_e = \frac{(5.33 \times 10^{-4})(717)(0.0167)}{(0.369 \times 10^{-6})(32.2)} = 534 \qquad (319)$$

The Reynolds number and Mach number based upon potential flow conditions at the nozzle exit plane are thus 534 and 0.662, respectively. Entering the plot to the right in Figure 59 with these parameters, it is determined the core length is $x_c/b = 3.55$. Entering the plot to the left of the nomograph with $x_c/b = 3.55$, the core width at $x/b = 0.25$ is found to be $y_c/b = 0.22$. The jet width parameter, y^*/b, at the position $x/b = 0.25$ is found as a function of Reynolds and Mach number in Figure 63 to be $y^*/b = 0.83$.

With the centerline velocity, core width and jet width parameter known at the position $x/b = 0.25$, the free jet momentum nondimensionalized by the nozzle width may be computed from equation (153)

$$J_\infty/b = 4 \left(\frac{k}{k-1}\right) P_m B \left[\frac{y_c/b}{1-B} + 0.292 \, (y^*/b - y_c/b) \sum_{m=0}^{\infty} \frac{B^m}{\sqrt{m+1}}\right] \qquad (320)$$

The required value of B is calculated from equation (154)

$$B = \frac{k-1}{2} (\bar{u}_c/C_T)^2$$

$$B = \left(\frac{1.4-1}{2}\right) \left[717 \, / \, \sqrt{(1.4)(53.34)(532)(32.2)}\right]^2 = 0.0838 \qquad (321)$$

Introducing the value of B into the expression for free jet momentum and evaluating

$$J_\infty/b = 4\left(\frac{1.4}{1.4-1}\right)(5.0\ \text{mm.hg.})\left[2.783\ \frac{\text{lbf.}}{\text{ft.}^2\text{mm.hg.}}\right](0.08038)$$

$$\left[\frac{0.22}{1-0.08038} + 0.292\ (0.83-0.22)(1.06095)\right] \qquad (322)$$

$$J_\infty/b = 6.65\ \text{lbf./ft.}^2$$

The value of $\sum_{m=0}^{\infty} B^m/\sqrt{m+1}$ in the preceding expression was found in Figure 64 to be 1.06095.

Calculation of Jet Deflection Angle

The calculation of the power jet deflection angle as a function of control port pressure may be illustrated by the following data. Upon the power jet flow considered previously, a control port pressure of 2.30 mm. oil above model ambient (specific gravity of the oil 1.04) is imposed. The control port width, X, is equal to the power nozzle width, b. The power jet deflection angle may be computed from equation (115)

$$\theta = \frac{X/b\ (P_1-P_m)}{J_\infty/b} \qquad (323)$$

$$\theta = \frac{(1)(2.30\ \text{mm. oil})\left(\frac{1.04\ \text{mm.hg.}}{13.6\ \text{mm. oil}}\right)\left(2.783\ \frac{\text{lbf.}}{\text{ft.}^2\text{mm.hg.}}\right)}{6.65\ \text{lbf./ft.}^2}$$

$$\theta = 0.0736\ \text{rd.} = 4.22°$$

Calculation of Power Nozzle Mass Flow Rate

The computation of the power nozzle flow may be illustrated by the following example. The core width at the exit plane of the power jet is found from Figure 59 to be $y_c/b = 0.237$. The value of ϕ_1 (B,n) may be computed from expression (195) using the previously defined values of J_∞/b and B

$$\phi_1 (B,n) = \left[\frac{J_\infty/b}{4\left(\frac{k}{k-1}\right) P_m B} - \frac{y_c/b}{1-B}\right]\left(\frac{1}{1/2 - y_c/b}\right) \tag{324}$$

$$\phi_1 (B,n) = \left[\frac{6.65 \text{ lbf./ft.}^2}{4\left(\frac{1.4}{1.4-1}\right)(5.0 \text{ mm.hg.})\left(2.783 \frac{\text{lbf.}}{\text{ft.}^2 \text{mm.hg.}}\right)(0.08038)} - \frac{0.237}{1-0.08038}\right]\left[\frac{1}{0.5-0.237}\right]$$

$$\phi_1 (B,n) = 0.635$$

The profile distribution parameter, n, is plotted as a function of ϕ_1 (B,n) and B in Figure 73. From this figure n is found to be equal to 2.5. The mass flow rate from the power nozzle is computed from expression (198)

$$\dot{m}_1 = \frac{2P_m \bar{u}_c bh}{\bar{R} T_T}\left[\frac{\bar{y}_c/b}{1-B} + \left(\frac{1}{2} - y_c/b\right) \phi_2 (B,n)\right] \tag{325}$$

The function ϕ_2 (B,n) is found from Figure 74 to be equal to 0.764. Evaluating the previous expression with a model height of one inch, yields

$$\dot{m}_i = \frac{2(5.0)(2.783)(717)(0.0167)(0.0833)}{(53.34)(532)} \left[\frac{0.237}{1-0.08038} + (0.5-0.237)(0.764)\right] \quad (326)$$

$$\dot{m}_i = 0.000445 \text{ lbm./sec.} = 0.02668 \text{ lbm./min.}$$

Calculation of Control Port Mass Flow Rate

The calculation of control port mass flow rate may be illustrated with the previously considered power jet flow and control port pressure. The nondimensional distance at which the deflected power jet passes the control port knife edge is determined from equation (190). For a control port set back of $y_e/b = 0.6$, the value of s'/b is

$$s'/b = \frac{(J_\infty/b)(X/b)}{(y_e/b)(P_1-P_m) + J_\infty/b} \quad (327)$$

$$s'/b = \frac{(6.65 \text{ lbf./ft.}^2)(1)}{(0.6)(2.30 \text{ mm.oil})\left(\frac{1.04 \text{ mm.hg.}}{13.6 \text{ mm. oil}}\right)\left(2.783 \frac{\text{lbf.}}{\text{ft.}^2 \text{mm.hg.}}\right) + 6.65 \frac{\text{lbf.}}{\text{ft.}^2}}$$

$$s'/b = 0.958$$

The core width at the position $x/b = 0.958$ is determined from Figure 59 to be $y_c/b = 0.173$. The jet width parameter y^*/b at this axial position may be determined from equation (167). Introducing the jet parameters which were calculated for $x/b = 0.25$ into this expression yields

$$\left.\frac{y^*}{b}\right|_x = \left.\frac{y_c}{b}\right|_x + \frac{\left\{B\left[\frac{y_c/b}{1-B} + 0.292\left(\frac{y^*}{b} - \frac{y_c}{b}\right)\sum_{m=0}^{\infty}\frac{B^m}{\sqrt{m+1}}\right]\right\}\Bigg|_{x/b=1/4} - \left.\frac{y_c}{b}\left(\frac{B}{1-B}\right)\right|_x}{\left.0.292\ B\sum_{m=0}^{\infty}\frac{B^m}{\sqrt{m+1}}\right|_x} \tag{328}$$

$$\left.\frac{y^*}{b}\right|_{x/b=0.958} = 0.173 + \frac{\left\{0.08038\left[\frac{0.22}{1-0.08038} + 0.292\ (0.83-0.22)(1.06095)\right]\right\}}{0.292\ (0.08038)(1.06095)}$$

$$- 0.173\left[\frac{0.08038}{1-0.08038}\right] / 0.292\ (0.08038)(1.06095)$$

$$\left.\frac{y^*}{b}\right|_{x/b=0.958} = 0.944$$

The parameter η_2 necessary for the calculation of control port flow rate may be computed from equation (188)

$$\eta_2 = \frac{y_e/b + \frac{(X/b)^2(P_1-P_m)}{2(J_\infty/b)} - y_c/b}{y^*/b - y_c/b} \tag{329}$$

$$\eta_2 = \frac{0.6 + \frac{(1)^2(2.30)\left(\frac{1.04}{13.6}\right)(2.783)}{2(6.65)} - 0.173}{0.944 - 0.173}$$

$$\eta_2 = 0.602$$

The control port mass flow rate now may be computed from equation (187)

$$\dot{m}_c = \frac{hb\ P_m\ \bar{u}_c}{\bar{R}\ T_T}\left[\frac{y_c/b}{1-B} + 0.8264\ (y^*/b - y_c/b)\ \Gamma_2(B,\eta_2)\right]$$

$$+ \frac{hb\ \sqrt{\rho(P_1 - P_m)}}{2}\ (y^*/b - y_c/b)\ \eta_2^{\,2} - \dot{m}_i/2 \qquad (330)$$

$$\dot{m}_c = \frac{(0.0833)(0.0167)(5.0)(2.783)(717)}{(53.34)(532)}\left[\frac{0.173}{1-0.08038}\right.$$

$$\left. + 0.8264(0.944 - 0.173)(0.491)\right]$$

$$+ \frac{(0.0833)(0.0167)\ \sqrt{(5.33\times10^{-4})(2.30)(\frac{1.04}{13.6})(2.783)(32.2)}}{2}\ (0.944$$

$$- 0.173)(0.602)^2 - \dot{m}_i/2$$

$$\dot{m}_c = 0.0002628 \text{ lbm./sec.} - \dot{m}_i/2 = 0.01577 \text{ lbm./min.} - \dot{m}_i/2$$

The value of $\Gamma_2(B,\eta_2)$ was determined from Figure 71. The measured value of supply nozzle flow for this condition is found in Table 5 to be 0.02796 lbm./min. The control port flow rate is thus

$$\dot{m}_c = 0.01577 - 0.01398 = 0.00179 \text{ lbm./min.} \qquad (331)$$

Calculation of Open Load Flow Rate and Blocked Load Pressure Recovery

The calculation of open load flow rate and blocked load pressure may be illustrated with the previously considered power jet flow condition. The control port pressure for this example as well as the

receiver offset angle is zero. The power nozzle receiver separation distance is x/b = 3.0.

The core width of the power jet at the downstream position of the receiver, x/b = 3.0, is determined from Figure 59 to be y_c/b = 0.034. The jet width parameter at this axial position may be determined from equation (167)

$$\left.\frac{y^*}{b}\right|_{x/b=3} = 0.034 + \frac{\left\{0.08038\left[\frac{0.22}{1-0.08038} + 0.292(0.83-0.22)(1.06095)\right]\right\}}{0.292\ (0.08038)(1.06095)} - 0.034\left\{\frac{0.08038}{1-0.08038}\right\} / 0.292\ (0.08038)(1.06095) \tag{332}$$

$$\left.\frac{y^*}{b}\right|_{x/b=3} = 1.297$$

The power jet deflection distance is calculated from equation (201) to be ℓ = 0. For the present example in which the receiver offset angle is equal to 0° and the receiver and supply nozzle widths are equal, the value of e is determined to be 0.5 b. The potential core lies within the lower and upper edges of the receiver and thus the open load flow rate is computed from expression (209)

$$\dot{m}_r = \frac{hb\ P_m\ \bar{u}_c}{\bar{R}\ T_T}\left\{\frac{2y_c/b}{1-B} + 0.8264\ (y^*/b - y_c/b)\left[\Gamma_2(B,\eta_3)+\Gamma_2(B,\eta_4)\right]\right\} \tag{333}$$

The values of η_3 and η_4 required for the evaluation of the previous

expression are

$$\eta_3 = \frac{(e+d-\ell)/b - y_c/b}{y^*/b - y_c/b} \tag{334}$$

$$\eta_3 = \frac{0.5 - 0.034}{1.297 - 0.034} = 0.369$$

$$\eta_4 = \frac{-(e-\ell)/b - y_c/b}{y^*/b - y_c/b}$$

$$\eta_4 = \frac{-(-0.5) - 0.034}{1.297 - 0.034} = 0.369$$

$\Gamma_2(B,\eta_3)$ and $\Gamma_2(B,\eta_4)$ are found to be equal to 0.38 from Figure 71. Evaluating the expression for open load flow rate gives

$$\dot{m}_r = \frac{(0.0833)(0.0167)(5.0)(2.783)(717)}{(53.34)(532)} \left[\frac{0.068}{1-0.08038} \right. \tag{335}$$

$$\left. + 0.8264\ (1.297-0.034)(0.38+0.38)\right]$$

$$\dot{m}_r = 0.0004241 \text{ lbm./sec.} = 0.02545 \text{ lbm./min.}$$

The blocked load pressure recovery based on Reid's model may be computed from the expression

$$P_B = P_m \left[1 + \left(\frac{k-1}{2k\ \bar{R}\ T}\right) \bar{u}_c^2\right]^{k/k-1} \tag{336}$$

Introducing the numerical values of the centerline velocity and temperature and then evaluating yields

$$P_B = 5.0 \left[1 + \frac{(1.4-1)(717)^2}{2(1.4)(53.34)(32.2)(489)}\right]^{1.4/1.4-1} = 6.705 \text{ mm.hg.} \tag{337}$$

APPENDIX I

COMPUTER PROGRAM FOR JET PARAMETERS

The calculation of free jet parameters, control and supply jet interaction parameters as well as open load flow rate and blocked load pressure are rather laborious computations. A digital computer program was written to expedite the calculation of this information.

The following is a Fortran IV computer program which was devised to calculate the previously described variables. Following the program listing is a sample set of input data and output results. The calculations were performed upon a Control Data Corporation 6400 Digital Computer at the Phoenix Division of AiResearch Manufacturing Company. The program plan, firstly, is to numerically compute the required free jet parameters from the known flow condition, nozzle geometry and the free jet data correlation. The power jet deflection angle and the control port mass flow rate are then computed based on the free jet parameters, the power nozzle mass flow rate, control port pressure and geometry. Finally, the open load flow rate and blocked load pressure recovery are calculated from the power jet description, receiver location and geometry.

The evaluation of $\Gamma_1(B,\eta)$ and $\Gamma_2(B,\eta)$ was accomplished by numerically summing 10 terms of each of these series. The error resulting from truncating these rapidly converging series was assumed to be less than 0.1 percent. The numerical value of the normal curve of

error which was required in these summations was provided by Subroutine Cubic. This subroutine interpolated a map of the numerical values of the normal curve of error. Subroutine Cubic's method of interpolation consisted of forming a cubic equation through grid points on either side of the required ordinate. This cubic equation was then evaluated at the required ordinate in order to determine the value of the function.

The blocked load pressure recovery based on Simson's analytical model was calculated by integrating the power jet's total pressure profile across the inlet plane of the receiver and then dividing this value by the receiver inlet width. The integration was accomplished by computing the total pressure at 20 equally spaced increments across the receiver inlet and then summing according to the trapezoid rule. Included in the computer output data is a listing of the function η, x-component of steady state velocity, static temperature and total pressure at 10 equally spaced increments across the receiver inlet plane. The summation of power jet mass flow rate and momentum with respect to the edge of the receiver was presented at each of these stations. Interpolation was used to determine the center of the mass flow rate profile coincident to the receiver inlet. The blocked load pressure based on Reid's analytical model was then calculated by interpolating the total pressure profile to the centroid of the mass flow rate profile. Logic statements were employed in the computer program to determine the appropriate expression for calculating open load flow rate. Power jet parameters, receiver geometry and expressions

(203), (206), (208) and (211) were used to select which of the four flow regimes were appropriate.

The input and output variables for this computer program along with the dimensions of these parameters will be identified in Tables 49 and 50. The identification of these parameters will follow the order of appearance within the input-output portion of the program. Provisions are made in the program by means of Do Loops to introduce multiple values of receiver positions, x_r, and control port pressure, P_1. The map of the normal curve of error is introduced in 40 evenly spaced grid points which represents ordinates of from 0 to 3.9.

Table 49. Computer Program Input Variables

Variable	Description	Dimensions
PM	experimental model absolute pressure	mm. hg.
PT	upstream stagnation tank absolute pressure	mm. hg.
TT	total temperature in stagnation tank	°R
GAMMA	ratio of specific heats	dimensionless
R	gas constant	ft.lbf./lbm.°R
CP	constant pressure specific heat	BTU/lbm.°R
B	power nozzle width	in.
H	power nozzle height	in.
XX	control port width divided by power nozzle width	dimensionless
YE	setback distance of control port from power nozzle centerline divided by power nozzle width	dimensionless
XMSUP	power nozzle mass flow rate	lbm./min.
THETAR	receiver offset angle	radians
D	receiver inlet width	in.
XR	radial distance from point of intersection of control and supply port centerlines to the receiver inlet divided by power nozzle width	dimensionless
PC	control port pressure	mm. oil (S.G.= 1.04)

Table 50. Computer Program Output Variables

Variable	Description	Dimensions
XMACH	power jet Mach number at centerline of nozzle exit plane	dimensionless
REYND	power jet Reynolds number at centerline of nozzle exit plane	dimensionless
UO	power jet centerline velocity at nozzle exit plane	ft./sec.
XCORE	nondimensional core length	dimensionless
XTRAN	nondimensional transition parameter	dimensionless
XTURB	nondimensional separation distance between laminar and turbulent flow regions	dimensionless
YCORJ	nondimensional core width at x/b = 0.25	dimensionless
YWIDJ	nondimensional profile width at x/b = 0.25	dimensionless
XJJET	power jet momentum per unit area	$lbf./ft.^2$
THETAJ	power jet deflection angle	radians
SCONT	nondimensional distance along power jet centerline from power nozzle exit to control port knife edge	dimensionless
UCLS	power jet centerline velocity at control port edge	ft./sec.
YCORS	nondimensional core width at control port edge	dimensionless
YWIDS	nondimensional profile width at control port edge	dimensionless
XNEW2	the function η_2 evaluated at control port edge	dimensionless

Table 50. (Continued)

Variable	Description	Dimensions
GAM2	the function $\Gamma_2(B,\eta_2)$ evaluated at control port edge	dimensionless
XMPROF	component of control port mass flow rate passing through power jet velocity profile	lbm./min.
XMATMO	component of control port mass flow rate to atmosphere	lbm./min.
XMCONT	control port mass flow rate	lbm./min.
UCLXR	power jet centerline velocity at receiver inlet	ft./sec.
YCORXR	nondimensional power jet core width at receiver inlet	dimensionless
YWIDXR	nondimensional profile width at receiver inlet	dimensionless
E	nondimensional position of receiver's upper edge with respect to power nozzle centerline	dimensionless
XL	nondimensional power jet deflection distance	dimensionless
XNEW3	the function η_3	dimensionless
XNEW4	the function η_4	dimensionless
GAM2N3	the function $\Gamma_2(B,\eta_3)$	dimensionless
GAM2N4	the function $\Gamma_2(B,\eta_4)$	dimensionless
XMOPRC	open load mass flow rate through the receiver	lbm./min.
XNEWXR	the function η determined at positions across the receiver inlet	dimensionless

Table 50. (Continued)

Variable	Description	Dimensions
UXR	the x-component of velocity at positions across the receiver inlet	ft./sec.
TXR	static temperature at positions across the receiver inlet	°R
POXR	total pressure at positions across the receiver inlet	mm. oil (S.G.= 1.04)
SUMMAS	summation of mass flow rate coincident to receiver inlet up to this position	lbm./min.
SUMMOM	summation of momentum per unit height coincident to receiver inlet up to this position	lbf./ft.
GAM1N3	the function $\Gamma_1(B,\eta_3)$	dimensionless
GAM1N4	the function $\Gamma_1(B,\eta_4)$	dimensionless
XMOMEN	calculated value of power jet momentum per unit height coincident to receiver inlet	lbf./ft.
PBAV	blocked load pressure resulting from determining average of total pressure across the receiver inlet	mm. oil (S.G.= 1.04)

```
PROGRAM     JET                                   CDC 6400 6UF V3.0-P348 OPT=0

            PROGRAM JET(INPUT,OUTPUT,TAPE60=INPUT,TAPE61=OUTPUT)
            DIMENSION XRR(30),PCC(30),ERFN(50),XNENXR(21),TXR(21),UXR(21),
           +POXR(21),DENSXR(21),XMASR(21),XMOM(21),SUMMAS(21),SUMMOM(21)
            COMMON/CBIVAR/NIXX,NIXZ,DCDX,DCDY
 5        5  IF (EOF(60))400,10
          10 WRITE(61,50)
             READ(60,830)PM,PT,TT,GAMMA,R,CP
             WRITE(61,1000)PM,PT,TT,GAMMA,R,CP
             READ(60,830)B,H,XX,YE,XMSUP,THETAR,D
10           WRITE(61,1010)B,H,XX,YE,XMSUP,THETAR
             WRITE(61,1015)D
             READ(60,810)M
             READ(60,830)(XRR(I),I=1,M)
             WRITE(61,1020)(XRR(I),I=1,M)
15           READ(60,810)N
             READ(60,830)(PCC(I),I=1,N)
             WRITE(61,1030)(PCC(I),I=1,N)
             READ(60,830)(ERFN(I),I=1,3)
             K=ERFN(1)+3.0
20           READ(60,830)(ERFN(I),I=4,K)
             WRITE(61,1040)(ERFN(I),I=1,K)
             WRITE(61,55)
          50 FORMAT (1H1,27X,*INPUT DATA*/)
          55 FORMAT(1H1,27X,*OUTPUT RESULTS*/)
25        830 FORMAT(6E12.5)
          810 FORMAT(I3)
          1000 FORMAT(5X,2HPM,11X,2HPT,11X,2HTT,11X,5HGAMMA,8X,1HR,12X,2HCP/
              +6(3X,E10.4)/)
          1010 FORMAT(5X,1HB,12X,1HH,12X,2HXX,11X,2HYE,11X,5HXMSUP,6X,6HTHETAR
30            +/6(3X,E10.4)/)
          1015 FORMAT(5X,1HD/3X,E10.4/)
          1020 FORMAT(5X,*POSITION XR*/8(3X,E10.4)/)
          1030 FORMAT(5X,*CONTROL PORT PRESSURE*/8(3X,E10.4)/)
          1040 FORMAT(5X,*NORMAL CURVE OF ERROR*/3(3X,E10.4)/6(3X,E10.4)/
35            +6(3X,E10.4)/6(3X,E10.4)/6(3X,E10.4)/6(3X,E10.4)/6(3X,E10.4)/
              +6(3X,E10.4)/)
          C      CALCULATE FLOW CONDITIONS
                 CT=SQRT(GAMMA*R*TT*32.174)
                 XMACH=SQRT(((PT/PM)**((GAMMA-1.0)/GAMMA)-1.0)*2.0/(GAMMA-1.0))
40               T=TT/(1.0+(GAMMA-1.0)*XMACH*XMACH/2.0)
                 U0=XMACH*SQRT(GAMMA*R*T*32.174)
                 DENS=PM*2.7834/(R*T)
                 VISC=0.00000037*SQRT(T/492.0)
                 REYND=DENS*U0*B/(12.0*VISC*32.174)
45               XCORE=(REYND**0.75)/(10.3*(1.0+XMACH*XMACH))-3.95
                 IF(XCORE)100,110,110
          100    CV=0.845+(0.00382*REYND**0.75)/(1.0+XMACH*XMACH)
                 U0=CV*U0
                 T=TT-U0*U0/(2.0*32.174*CP*778.0)
50               XMACH=U0/SQRT(GAMMA*R*T*32.174)
                 DENS=PM*2.7834/(R*T)
                 VISC=0.00000037*SQRT(T/492.0)
                 REYND=DENS*U0*B/(12.0*VISC*32.174)
                 XCORE=0.0
55        110    CONTINUE
```

```
PROGRAM     JET                                          CDC 6400 GUF V3.0-P348 OPT=0

            C     CALCULATE POWER JET MOMENTUM
                  XTRAN=0.0036*REYND/(1.0+1.25*XMACH**4.0)
                  XTURB=545.0*(1.0+0.6*XMACH**4.0)/REYND**0.65
                  IF(XCORE-0.25)120,130,130
 60           120 UCLJ=U0*2.7183**((1.0-((0.25+XTRAN)/(XCORE+XTRAN)))**0.45)/9.0)
                  GO TO 132
              130 UCLJ=U0
              132 BBJ=((GAMMA-1.0)/2.0)*(UCLJ/CT)**2.0
                  SUMJ=1.0
 65               DO 135 MM=1,10
                  XMM=MM
                  TERM=(BBJ**XMM)/SQRT(XMM+1.0)
              135 SUMJ=SUMJ+TERM
                  YCORJ=0.5*((XCORE-0.25)*(10.3*(1.0+XMACH*XMACH)/(REYND**0.75)))
 70               YCORJ=AMAX1(0.0,YCORJ)
                  YWIDJ=(6.73/REYND**0.45-0.125)*(1.0+2.3*XMACH*XMACH)*(0.25)**
                 +(0.00808*SQRT(REYND)+0.185)+0.5
                  XJETI=BBJ*(YCORJ/(1.0-BBJ)+0.292*(YWIDJ-YCORJ)*SUMJ)
                  XJJET=4.0*GAMMA/(GAMMA-1.0)*PM*2.7834*XJETI
 75               WRITE(61,1200)XMACH,REYND,U0,XCORE,XTRAN,XTURB
              1200 FORMAT(5X,5HXMACH,8X,5HREYND,8X,2HU0,11X,5HXCORE,8X,5HXTRAN,8X,
                 +5HXTURB/6(3X,E10.4)/)
                  WRITE(61,1210)YCORJ,YWIDJ,XJETI,XJJET
              1210 FORMAT(5X,5HYCORJ,8X,5HYWIDJ,8X,5HXJETI,8X,5HXJJET/4(3X,E10.4)/)
 80               DO 300 I=1,M
                  XR=XRR(I)
                  DO 200 JJ=1,N
                  PC=PCC(JJ)
            C     CONTROL PORT CHARACTERISTICS
 85               THETAJ=XX*PC*0.212846/XJJET
                  SCONT=XX*XJJET/(YE*PC*0.212846+XJJET)
                  IF(XCORE-SCONT)140,150,150
              140 UCLS=U0*2.7183**((1.0-((SCONT+XTRAN)/(XCORE+XTRAN)))**0.45)/9.0)
                  GO TO 152
 90           150 UCLS=U0
              152 BBS=((GAMMA-1.0)/2.0)*(UCLS/CT)**2.0
                  SUMS=1.0
                  DO 155 NN=1,10
                  XNN=NN
 95               TERM=(BBS**XNN)/SQRT(XNN+1.0)
              155 SUMS=SUMS+TERM
                  YCORS=0.5*((XCORE-SCONT)*(10.3*(1.0+XMACH*XMACH)/(REYND**0.75)))
                  YCORS=AMAX1(0.0,YCORS)
                  YWIDS=YCORS+(XJETI-YCORS*BBS/(1.0-BBS))/(0.292*BBS*SUMS)
100               XNEW2=(YE+XX*XX*PC*0.212846/(2.0*XJJET)-YCORS)/(YWIDS-YCORS)
                  GAM2=0.0
                  DO 159 LL=1,10
                  XLL=LL-1
                  TERM=(BBS**XLL)/SQRT(2.0*XLL+1.0)*CUBIC(ERFN,SQRT(9.2*(2.0*XLL+1.0
105              +))*XNEW2)
              159 GAM2=GAM2+TERM
                  XMPROF=(M*B/144.0*PM*2.7834*UCLS/(R*TT))*(YCORS/(1.0-BBS)+0.8264
                 +*(YWIDS-YCORS)*GAM2)*60.0
                  XMATMO=M*B/144.0*SQRT(DENS*PC*0.212846*32.174)/2.0*(YWIDS-YCORS)*
110              +XNEW2*XNEW2*60.0
```

```
      PROGRAM     JET                                          CDC 6400 GUF V3.0-P348 OPT=0

                      XMCONT=XMPROF+XMATMO-XMSUP/2.0
                C     RECEIVER CHARACTERISTICS
                      IF((XR+XX/2.0)-XCORE)160,160,170
                160   UCLXR=U0
      115             GO TO 190
                170   IF((XR+XX/2.0)-XTURB)180,180,185
                180   UCLXR=U0*2.7813**((1.0-((XR+XX/2.0+XTRAN)/(XCORE+XTRAN))**0.45)/9.
                     +0)
                      GO TO 190
      120       185   US=U0*2.7813**((1.0-((XTURB+XTRAN)/(XCORE+XTRAN))**0.45)/9.0)
                      UCLXR=US*((XR+XX/2.0)/XTURB)**(-0.5)
                190   BBXR=((GAMMA-1.0)/2.0)*(UCLXR/CT)**2.0
                      SUMXR=1.0
                      DO 195 KK=1,10
      125             XKK=KK
                      TERM=(BBXR**XKK)/SQRT(XKK+1.0)
                195   SUMXR=SUMXR+TERM
                      YCORXR=0.5*((XCORE-XR-XX/2.0)*(10.3*(1.0+XMACH*XMACH)/REYND**0.75)
                     +)
      130             YCORXR=AMAX1(0.0,YCORXR)
                      YWIDXR=YCORXR+(XJETI-YCORXR*BBXR/(1.0-BBXR))/(0.292*BBXR*SUMXR)
                      DD=D/8
                      XL=XR*THETAJ
                      E=XR*THETAR-DD/2.0
      135             IF((E-XL)-YCORXR)500,450,450
                C     REGIME 1
                450   XNEW3=((E+DD-XL)-YCORXR)/(YWIDXR-YCORXR)
                      XNEW4=((E-XL)-YCORXR)/(YWIDXR-YCORXR)
                      GAM2N3=0.0
      140             DO 455 LL=1,10
                      XLL=LL-1
                      TERM=(BBXR**XLL)/SQRT(2.0*XLL+1.0)*CUBIC(ERFN,SQRT(9.2*(2.0*XLL+1.
                     +))*XNEW3)
                455   GAM2N3=GAM2N3+TERM
      145             GAM2N4=0.0
                      DO 460 LL=1,10
                      XLL=LL-1
                      TERM=(BBXR**XLL)/SQRT(2.0*XLL+1.0)*CUBIC(ERFN,SQRT(9.2*(2.0*XLL+1.
                     +))*XNEW4)
      150   460   GAM2N4=GAM2N4+TERM
                      XMOPRC=(H*B/144.0*PM*2.7834*UCLXR/(R*TT))*(0.8264*(YWIDXR-YCORXR)
                     +*(GAM2N3-GAM2N4))*60.0
                      GAM1N3=0.0
                      DO 465 LL=1,10
      155             XLL=LL-1
                      TERM=(BBXR**XLL)/SQRT(XLL+1.0)*CUBIC(ERFN,SQRT(18.4*(XLL+1.0))*
                     +XNEW3)
                465   GAM1N3=GAM1N3+TERM
                      GAM1N4=0.0
      160             DO 470 LL=1,10
                      XLL=LL-1
                      TERM=(BBXR**XLL)/SQRT(XLL+1.0)*CUBIC(ERFN,SQRT(18.4*(XLL+1.0))*
                     +XNEW4)
                470   GAM1N4=GAM1N4+TERM
      165             XMOMEN=PM*2.7834*BBXR*2.0*GAMMA*B/12.0/(GAMMA-1.0)*(0.58436*
```

```
      PROGRAM     JET                                    CDC 6400 GUF V3.0-P348 OPT=0

                 +(YWIDXR-YCORXR)*(GAM1N3-GAM1N4))
                  GO TO 750
                500  IF((E+DD-XL)-YCORXR)600,550,550
                C    REGIME 4
170             600  XMOPRC=(H*B/144.0*PM*2.7834*UCLXR/(R*TT))/(1.0-BBXR)*60.0
                     XMOMEN=PM*2.7834*BBXR*2.0*GAMMA*B/12.0/(1.0-BBXR)
                     GO TO 750
                550  IF(ABS(E-XL)-YCORXR)650,700,700
                C    REGIME 2
175             650  XNEW3=((E+DD-XL)-YCORXR)/(YWIDXR-YCORXR)
                     GAM2N3=0.0
                     DO 655 LL=1,10
                     XLL=LL-1
                     TERM=(BBXR**XLL)/SQRT(2.0*XLL+1.0)*CUBIC(ERFN,SQRT(9.2*(2.0*XLL+1.
180                 +))*XNEW3)
                655  GAM2N3=GAM2N3+TERM
                     XMOPRC=(H*B/144.0*PM*2.7834*UCLXR/(R*TT))*(((YCORXR-(E-XL))/(1.0-
                    +BBXR)+0.6264*(YWIDXR-YCORXR)*GAM2N3)*60.0
                     GAM1N3=0.0
185                  DO 665 LL=1,10
                     XLL=LL-1
                     TERM=(BBXR**XLL)/SQRT(XLL+1.0)*CUBIC(ERFN,SQRT(18.4*(XLL+1.0))*
                    +XNEW3)
                665  GAM1N3=GAM1N3+TERM
190                  XMOMEN=PM*2.7834*BBXR*2.0*GAMMA*B/12.0/(GAMMA-1.0)*(((YCORXR-(E-XL
                    +))/(1.0-BBXR)+0.58436*(YWIDXR-YCORXR)*GAM1N3)
                     GO TO 750
                C    REGIME 3
                700  XNEW3=((E+DD-XL)-YCORXR)/(YWIDXR-YCORXR)
195                  XNEW4=(-(E-XL)-YCORXR)/(YWIDXR-YCORXR)
                     GAM2N3=0.0
                     DO 705 LL=1,10
                     XLL=LL-1
                     TERM=(BBXR**XLL)/SQRT(2.0*XLL+1.0)*CUBIC(ERFN,SQRT(9.2*(2.0*XLL+1.
200                 +))*XNEW3)
                705  GAM2N3=GAM2N3+TERM
                     GAM2N4=0.0
                     DO 710 LL=1,10
                     XLL=LL-1
205                  TERM=(BBXR**XLL)/SQRT(2.0*XLL+1.0)*CUBIC(ERFN,SQRT(9.2*(2.0*XLL+1.
                    +))*XNEW4)
                710  GAM2N4=GAM2N4+TERM
                     XMOPRC=(H*B/144.0*PM*2.7834*UCLXR/(R*TT))*(2.0*YCORXR/(1.0-BBXR)
                    ++0.6264*(YWIDXR-YCORXR)*(GAM2N3+GAM2N4))*60.0
210                  GAM1N3=0.0
                     DO 715 LL=1,10
                     XLL=LL-1
                     TERM=(BBXR**XLL)/SQRT(XLL+1.0)*CUBIC(ERFN,SQRT(18.4*(XLL+1.0))*
                    +XNEW3)
215             715  GAM1N3=GAM1N3+TERM
                     GAM1N4=0.0
                     DO 720 LL=1,10
                     XLL=LL-1
                     TERM=(BBXR**XLL)/SQRT(XLL+1.0)*CUBIC(ERFN,SQRT(18.4*(XLL+1.0))*
220                 +XNEW4)
```

```
PROGRAM      JET                                          CDC 6400 GUF V3.0-P348 OPT=0

             720  GAM1N4=GAM1N4+TERM
                  XMOMEN=PM*2.7834*BBXR*2.0*GAMMA*B/12.0/(GAMMA-1.0)*(2.0*YCORXR/
                 +(1.0-BBXR)+0.58436*(YWIDXR-YCORXR)*(GAM1N3+GAM1N4))
             750  POMOM=PM*(1.0+((GAMMA-1.0)/(2.0*GAMMA*PM*2.7834*D/12.0))*XMOMEN)
225                 +**(GAMMA/(GAMMA-1.0))
                  POMOM=(POMOM-PM)*13.6/1.04
                C     TOTAL PRESSURE ACROSS RECEIVER
                  DO 800 J=1,21
                  XJ=J-1
230               IF((E-XL)+DD*XJ/20.0)820,820,840
             820  XNEWXR(J)=(-((E-XL)+DD*XJ/20.0)-YCORXR)/(YWIDXR-YCORXR)
                  XNEWXR(J)=AMAX1(0.0,XNEWXR(J))
                  GO TO 850
             840  XNEWXR(J)=(((E-XL)+DD*XJ/20.0)-YCORXR)/(YWIDXR-YCORXR)
235               XNEWXR(J)=AMAX1(0.0,XNEWXR(J))
             850  UXR(J)=UCLXR*2.7183**(-4.6*XNEWXR(J)**2.0)
                  TXR(J)=TT-UXR(J)*UXR(J)/(2.0*32.174*CP*778.0)
                  DENSXR(J)=PM*2.7834/(R*TXR(J))
                  XMASR(J)=DENSXR(J)*UXR(J)*60.0
240               XMOM(J)=DENSXR(J)*UXR(J)*UXR(J)/32.174
                  POXR(J)=PM*(1.0+(GAMMA-1.0)*UXR(J)*UXR(J)/(2.0*GAMMA*R*TXR(J)*
                 +32.174))**(GAMMA/(GAMMA-1.0))
             860  POXR(J)=(POXR(J)-PM)*13.6/1.04
                  SUMPOR=0.0
245               SUMMAS(1)=0.0
                  SUMMOM(1)=0.0
                  DO 950 KK=1,20
                  XMASTE=(XMASR(KK)+XMASR(KK+1))/2.0*D*H/(20.0*144.0)
                  XMOMTE=(XMOM(KK)+XMOM(KK+1))/2.0*D/(20.0*12.0)
250               SUMMAS(KK+1)=XMASTE+SUMMAS(KK)
                  SUMMOM(KK+1)=XMOMTE+SUMMOM(KK)
                  TERM=(POXR(KK)+POXR(KK+1))/2.0*D/20.0
             950  SUMPOR=SUMPOR+TERM
                  PBAV=SUMPOR/D
255               WRITE(61,1300)XR,PC
             1300 FORMAT(5X,2HXR,11X,2HPC/2(3X,E10.4)//)
                  WRITE(61,1400)THETAJ,SCONT,UCLS,YCORS,YWIDS,XNEW2
             1400 FORMAT(5X,*INTERACTION REGION PARAMETERS*/5X,6HTHETAJ,7X,5HSCONT
                 +,8X,4HUCLS,9X,5HYCORS,8X,5HYWIDS,8X,5HXNEW2,8X/6(3X,E10.4)/)
260               WRITE(61,1410)GAM2,XMPROF,XMATMO,XMCONT
             1410 FORMAT(5X,4HGAM2,9X,6HXMPROF,7X,6HXMATMO,7X,6HXMCONT/4(3X,E10.4)/)
                  WRITE(61,1500)UCLXR,YCORXR,YWIDXR,E,XL,XNEW3
             1500 FORMAT(5X,*RECEIVER PARAMETERS*/5X,5HUCLXR,8X,6HYCORXR,7X,6HYWIDXR
                 +,7X,1HE,12X,2HXL,11X,5HXNEW3/6(3X,E10.4)/)
265               WRITE(61,1510)XNEW4,GAM2N3,GAM2N4,XMOPRC
             1510 FORMAT(5X,5HXNEW4,,8X,6HGAM2N3,7X,6HGAM2N4,7X,6HXMOPRC/4(3X,E10.4
                 +)//)
                  WRITE(61,1525)
             1525 FORMAT(5X,6HXNEWXR,7X,3HUXR,10X,3HTXR,10X,4HPOXR,9X,6HSUMMAS,7X,
270                 +6HSUMMOM)
                  DO 1550 J=1,11
                  NN=J*2-1
             1550 WRITE(61,1600)XNEWXR(NN),UXR(NN),TXR(NN),POXR(NN),SUMMAS(NN),
                 +SUMMOM(NN)
275          1600 FORMAT(1X,6(3X,E10.4)/)
```

```
PROGRAM     JET                                          CDC 6400 GUF V3.0-P348 OPT=0

            WRITE(61,1650)GAM1N3,GAM1N4,XMOMEN,POMOM,PBAV
          1650 FORMAT(5X,6HGAM1N3,7X,6HGAM1N4,7X,6HXMOMEN,7X,5HPOMOM,8X,4HPBAV/
           +5(3X,E10.4)//)
          200  CONTINUE
280       300  CONTINUE
            GO TO 5
          400  CONTINUE
            STOP
            END


FUNCTION    CUBIC                                        CDC 6400 GUF V3.0-P348 OPT=0

              FUNCTION CUBIC(Y,X)
              COMMON/CBIVAR/NIXX,NIXZ,DCDX,DCDY
              DIMENSION Y(20)
              NIXX=0
 5            NI=Y(1)
              IF (X-Y(3))10,20,30
           10 NIXX=-1
           20 CUBIC=Y(4)
              DCDX=(Y(5)-Y(4))/Y(2)
10            RETURN
           30 I=(X-Y(3))/Y(2)+4.0
              A=I-4
              DX=X-Y(3)-A*Y(2)
              IF (DX)40,40,60
15         40 IF (I-NI-3)120,50,100
           50 CUBIC=Y(I)
              DCDX=(Y(I)-Y(I-1))/Y(2)
              RETURN
         120  CUBIC=Y(I)
20            DCDX=(Y(I+1)-Y(I-1))/(2.*Y(2))
           60 E=DX/Y(2)
              IF (I-4)70,70,80
           70 B=-1.5*Y(I)+2.0*Y(I+1)-0.5*Y(I+2)
              C=0.5*(Y(I)+Y(I+2))-Y(I+1)
25            CUBIC=Y(I)+E*(B+E*C)
              DCDX=(B+2.0*E*C)/Y(2)
              RETURN
           80 IF (I-(NI+2))90,110,100
           90 B=(2.0*Y(I-1)+3.0*Y(I)-6.0*Y(I+1)+Y(I+2))/6.0
30            C=(Y(I-1)-2.0*Y(I)+Y(I+1))/2.0
              D=(Y(I-1)-3.0*Y(I)+3.0*Y(I+1)-Y(I+2))/6.0
              CUBIC=Y(I)+E*(-B+E*(C-E*D))
              DCDX=(-B+E*(2.*C-3.*E*D))/Y(2)
              RETURN
35         100 NIXX=+1
              CUBIC=Y(NI+3)
              DCDX=(Y(NI+3)-Y(NI+2))/Y(2)
              RETURN
           110 B=0.5*(Y(NI+3)-Y(NI+1))
40            C=0.5*(Y(NI+1)+Y(NI+3))-Y(NI+2)
              CUBIC=Y(NI+2)+E*(B+E*C)
              DCDX=(B+2.*E*C)/Y(2)
              RETURN
              END
```

INPUT DATA

PM	PT	TT	GAMMA	R	CP
.5000E+01	.6720E+01	.5320E+03	.1400E+01	.5334E+02	.2400E+00

B	H	XX	YE	XMSUP	THETAR
.2000E+00	.1000E+01	.1000E+01	.6000E+00	.2796E-01	0.

D
.2000E+00

POSITION XR
.2500E+01

CONTROL PORT PRESSURE
0.

NORMAL CURVE OF ERROR

.4000E+02	.1000E+00	0.			
0.	.3980E-01	.7930E-01	.1179E+00	.1554E+00	.1915E+00
.2258E+00	.2580E+00	.2881E+00	.3159E+00	.3413E+00	.3643E+00
.3849E+00	.4032E+00	.4192E+00	.4332E+00	.4452E+00	.4554E+00
.4641E+00	.4713E+00	.4773E+00	.4821E+00	.4861E+00	.4893E+00
.4918E+00	.4938E+00	.4953E+00	.4965E+00	.4974E+00	.4981E+00
.4987E+00	.4990E+00	.4993E+00	.4995E+00	.4997E+00	.4998E+00
.4998E+00	.4999E+00	.4999E+00	.5000E+00		

OUTPUT RESULTS

XMACH	REYND	U0	XCORE	XTRAN	XTURB
.6639E+00	.5393E+03	.7195E+03	.3591E+01	.1562E+01	.1020E+02

YCORJ	YWIDJ	XJETI	XJJET
.2215E+00	.8266E+00	.3472E-01	.6764E+01

XR	PC
.2500E+01	0.

INTERACTION REGION PARAMETERS

THETAJ	SCONT	UCLS	YCORS	YWIDS	XNEW2
0.	.1000E+01	.7195E+03	.1718E+00	.9515E+00	.5492E+00

GAM2	XMPROF	XMATMO	XMCONT
.477CE+00	.1453E-01	0.	.5544E-03

RECEIVER PARAMETERS

UCLXR	YCORXR	YWIDXR	E	XL	XNEW3
.7195E+03	.3920E-01	.1284E+01	-.5000E+00	0.	.3700E+00

XNEN4	GAM2N3	GAM2N4	XMOPRC
.3700E+00	.3928E+00	.3928E+00	.2628E-01

XNEWXR	UXR	TXR	POXR	SUMMAS	SUMMOM
.3700E+00	.3833E+03	.5198E+03	.5543E+01	0.	0.
.2897E+00	.4890E+03	.5121E+03	.9337E+01	.1838E-02	.5023E-02
.2094E+00	.5880E+03	.5032E+03	.1405E+02	.4150E-02	.1281E-01
.1291E+00	.6664E+03	.4950E+03	.1874E+02	.6891E-02	.2355E-01
.4882E-01	.7117E+03	.4898E+03	.2191E+02	.9945E-02	.3668E-01
0.	.7195E+03	.4889E+03	.2249E+02	.1313E-01	.5091E-01
.4882E-01	.7117E+03	.4898E+03	.2191E+02	.1632E-01	.6513E-01
.1291E+00	.6664E+03	.4950E+03	.1874E+02	.1938E-01	.7826E-01
.2094E+00	.5880E+03	.5032E+03	.1405E+02	.2212E-01	.8900E-01
.2897E+00	.4890E+03	.5121E+03	.9337E+01	.2443E-01	.9679E-01
.3700E+00	.3833E+03	.5198E+03	.5543E+01	.2627E-01	.1018E+00

GAM1N3	GAM1N4	XMOMEN	POMOM	PBAV
.4737E+00	.4737E+00	.1019E+00	.1552E+02	.1565E+02

LITERATURE CITED

1. Pai, S. I., Fluid Dynamics of Jets, D. Van Nostrand Co., Inc., New York, 1954, p. 96.

2. Schlichting, H., Boundary Layer Theory, McGraw-Hill Book Co., Inc., New York, 4th ed., 1960, pp. 458-465.

3. Schlichting, H., ibid., pp. 477-482.

4. Tollmien, W., "Berechnung der turbulenten Ausbreitungsvorgänge," ZAMM, Bd. VI, 1926, pp. 468-478.

5. Görtler, H., "Berechnung von Aufgaben der freien Turbulenz auf Grund eines neum Näherungsansatzes," ZAMM, Bd. 22, 1942, pp. 245-254.

6. Schlichting, H., op.cit., pp.590-608.

7. Liepmann, H. W. and Laufer, J., Investigations of Free Turbulent Mixing, NACA Technical Note TN 1257.

8. Miller, D. R. and Comings, E. W., "Static Pressure Distribution in the Free Turbulent Jet," Journal of Fluid Mechanics, Vol. III, 1957, pp. 1-16.

9. Albertson, M. L. and Dai, Y. B., "Diffusion of Submerged Jets," American Society of Civil Engineers Proceedings, Vol. 74, No. 10, Dec., 1948.

10. Pai, S. I., op.cit., p.139.

11. Pai, S. I., op.cit., p.217.

12. Abramovich, G. N., The Theory of a Free Jet of a Compressible Gas, NACA Technical Memorandum TM 1058, 1944.

13. Olson, R. E. and Miller, D. P., "Aerodynamic Studies of Free and Attached Jets," Prepared for Harry Diamond Laboratories under Contract DA-49-186-ORD-912, Oct., 1963.

14. Pai, S. I., op.cit., pp. 79-81.

15. Schlichting, H., "Laminar Strahlausbreitung," ZAMM, Bd. 13, 1933.

16. Bickley, W., "The Plane Jet," Phil. Mag. 7, 23, 1937, p. 156.

17. Andrade, E. N. da C., "Velocity Distribution in a Liquid to Liquid Jet, Part II, The Plane Jet," Proc. Phys. Soc. 51, 1939, p. 784.

18. Chanaud, R. C. and Powell, A., "Experiments Concerning the Sound-Sensitive Jet," The Journal of the Acoustical Society of America, Vol. 34, No. 7, July, 1962, p. 907.

19. Chapman, D. R., Laminar Mixing of a Compressible Fluid, NACA Technical Note TN 1800, Feb., 1949.

20. Pai, S. I., op.cit., pp. 81-89.

21. Anderson, D. C., An Experimental Investigation of Compressible Jet Wall Attachment at Low Reynolds Numbers, Ph D Thesis, School of Mechanical Engineering, Georgia Institute of Technology, March, 1969.

22. Schlichting, H., op.cit., pp. 382-386.

23. Curle, N., "On Hydrodynamic Stability in Unlimited Fields of Viscous Flow," Proc. Royal Society (London), Vol. 238, 1957, pp. 489-500.

24. Pai, S. I., op.cit., pp. 193-208.

25. Moynihan, F. A. and Reilly, R. J., "Deflection and Relative Flow of Three Interacting Jets," Proceedings of the Harry Diamond Laboratories Fluid Amplification Symposium, Vol. I, 1964, pp. 123-146.

26. Chiu, P. C. and Man, C. P., "An Approximate Analysis of Three Two-Dimensional Interacting Jets," ASME Technical Paper No. 67-WA/FE-32, 1967.

27. Simson, A. K., A Theoretical Study of the Design Parameters of Subsonic Pressure Controlled, Fluid-Jet Amplifiers, Ph D Thesis, Department of Mechanical Engineering, Massachusetts Institute of Technology, July, 1963.

28. Kline, S. J. and Abbott, D. E., "Optimum Design of Straight-Walled Diffusers," Journal of Basic Engineering, Transactions of the ASME, Sept., 1959, p. 321.

29. Reid, K. N., Static and Dynamic Interaction of a Fluid Jet and a Receiver-Diffuser, Ph D Thesis, Department of Mechanical Engineering, Massachusetts Institute of Technology, Sept., 1964.

30. Sherman, F. S., New Experiments on Impact-Pressure Interpretation in Supersonic and Subsonic Rarefied Air Streams, NACA Technical Note TN 2995, Sept., 1953.

VITA

Dale Edward Jensen was born in Chicago, Illinois on April 15, 1943. He attended Texas public schools and graduated from Brewer High School, Ft. Worth, Texas in June, 1961. He attended the University of Texas at Arlington and graduated with a Bachelor of Science degree in Mechanical Engineering in January, 1965. In January, 1965 he entered Arizona State University and completed the requirements for a Master of Science degree in Mechanical Engineering in June, 1968. In September, 1966 he entered the Georgia Institute of Technology. Mr. Jensen was married in May, 1968 to the former Mary Jo Whitt. In December, 1969 he became employed by AiResearch Manufacturing Company, Phoenix, Arizona where he is presently employed.